Karlsruher Institut für Technologie

3D TOMOGRAPHY BASED ON THE AFTERSHOCK SEQUENCE OF THE 2016 MW 7.8 PEDERNALES, ECUADOR EARTHQUAKE

Dissertation to obtain the degree of
Doctor of Natural Sciences
from the KIT Faculty of Physics

by

SERGIO LEÓN-RÍOS

ADVISOR:
Prof. Dr. Andreas Rietbrock

REVISOR:
apl. Prof. Dr. Joachim Ritter

KARLSRUHE
2020

Karlsruher Institut für Technologie

3D TOMOGRAPHY BASED ON THE AFTERSHOCK SEQUENCE OF THE 2016 MW 7.8 PEDERNALES, ECUADOR EARTHQUAKE

Zur Erlangung des akademischen Grades eines
DOKTORS DER NATURWISSENSCHAFTEN (Dr. rer. nat.)
von der KIT-Fakultät für Physik des
Karlsruher Instituts für Technologie (KIT)
angenommene

Dissertation

von

M. Sc. León-Ríos, Sergio

Tag der mündlichen Prüfung: 30.10.2020

Referent: Prof. Dr. Andreas Rietbrock

Korreferent: apl. Prof. Dr. Joachim Ritter

Hasta que la dignidad
se haga costumbre

Abstract

Based on the seismicity recorded by the permanent Ecuadorian seismic network and our large emergency network installed shortly after the 2016 Mw 7.8 Pedernales earthquake, I derive a 3D seismic velocity model for central coastal Ecuador based on local earthquake tomography (LET). I manually analyzed seismic waveforms recorded on our combined amphibious network to determine high quality arrival times of seismic phases. I inverted the seismic travel times simultaneously for earthquake locations and three-dimensional (3D) velocity structure (Vp and Vp/Vs) using a staggered approach that increases complexity from 1D to finally obtaining a detailed 3D model.

While our 1D velocity model highlights the first-order structures of the studied margin through the analysis of the relocated seismicity, station correction terms and regional moment tensors (RMT), the resulting three-dimensional tomographic images show an area that is widely affected by the subducting topography and small- to large-scale faults at the surface. The oceanic Nazca plate is well imaged down to ∼40 km depth by an eastward dipping high Vp velocity feature. I also identify a low Vp (∼5.5 km/s) region along strike in the marine forearc, which I interpret as a thermal anomaly that might be caused either the rocks coming from the Galapagos Hot Spot or by shallow serpentinization. The marine forearc region also shows differences to the North and to the South of the Equator line, with a prominent seamount, imaged by a Vp ∼5.0 km/s, coming from the Atacames seamount chain in the northern region and, based on the elevated Vp/Vs ratios (>1.84), a deeply fractured oceanic crust in the South caused by the subduction of the Carnegie Ridge. The elevated Vp/Vs ratios (>1.84) also suggests a large presence of fluids. In the oceanic crust, this is associated to a combination of extensional faults formed prior to subducting and highs in topography that contribute to fracturing within the downgoing plate. In contrast, elevated Vp/Vs ratios (>1.84) in the upper continental crust are expressions of a highly fractured marine forearc and the presence of small- to large-scale faults that help fluids to circulate along the overriding plate.

The relocated seismicity shows several clusters, mostly organized along the plate interface, but also occurring in both, oceanic and continental plates. Clustered aftershocks in the oceanic crust are located on the flanks of a subducting seamount which promotes active faulting. On the other hand, seismicity observed in the upper plate is related to the (re)activation of several crustal faults following the 2016 Pedernales earthquake. The imaged three-dimensional seismic velocity structures were associated with the seismotectonical and geological context of the Ecuadorian margin to give insights about the main features controlling the occurrence of large megathrust

earthquakes in the region.

I also explore the relation between the observed physical properties of the rocks along the slab interface and the spatial distribution of the coseismic slip of the Pedernales earthquake. Our findings suggest a strong correlation between domains with normal Vp/Vs ratios (1.78-1.84) and the areas where the rupture propagated. In contrast, the areas with elevated Vp/Vs ratios (>1.84) can be colocated with the up- and down-dip limits of the Pedernales earthquake and might have contributed to stop the rupture. Furthermore, a grid search analysis shows that the 2016 event occurred in the only area of the margin capable to host an earthquake with the observed magnitude.

Finally, this study contributes to a better understanding of the processes occurring in subduction zones. Especially, I remark the importance of having a complete seismic velocity structure that includes both Vp and Vp/Vs ratios which complement with each other in order to give a full interpretation for the features observed along the study margin. Furthermore, the analysis of the seismic velocities of the rocks along the seismic interface, together with information derived from geodetic studies and the rupture area grid search approach designed in this work, can provide valuable data neccesary for the estimation of seismic hazard.

About the author

Sergio León-Ríos holds the degrees of Bachelor of Science in Physics from Universidad Católica del Norte, in Antofagasta, Chile and Master of Science in Geophysics from Universidad de Chile, in Santiago, Chile. From 2016 to 2018, León-Ríos conducted his doctorate studies at the University of Liverpool in the United Kingdom. Since 2018, he moved to Germany and continued his doctoral research in the Geophysical Institute at the Karlsruhe Institute of Technology. A list with the publications, related and unrelated to this work, and the collaborations in projects during his doctoral studies are listed below:

Publications

Related to this work

- **León-Ríos, S.**, Agurto-Detzel, H., Rietbrock, A., ... & Lynner, C. (2019). 1D-velocity structure and seismotectonics of the Ecuadorian margin inferred from the 2016 Mw7. 8 Pedernales aftershock sequence. *Tectonophysics*, 767, 228165.

- Meltzer, A., Beck, S., ..., **León-Ríos, S.**, ... & Hernandez, S. (2019). The 2016 Mw 7.8 Pedernales, Ecuador, earthquake: rapid response deployment. *Seismological Research Letters*, 90(3), 1346-1354.

- Agurto-Detzel, H., Font, Y., ..., **León-Ríos, S.**, ... & De Barros, L. (2019). Ridge subduction and afterslip control aftershock distribution of the 2016 Mw 7.8 Ecuador earthquake. *Earth and Planetary Science Letters*, 520, 63-76.

- **León-Ríos, S.**, Bie, L., Agurto-Detzel, H., ... & Woollam, J. (2020). 3D local earthquake tomography of the Ecuadorian margin in the source area of the 2016 Mw 7.8 Pedernales earthquake. *Earth and Space Science Open Archive*; submitted to *Journal of Geophysical Research*.

- Soto-Cordero, L., Meltzer, A., ..., **León-Ríos, S.**, ... & Hayes, G. P. (2020). Structural Control on Megathrust Rupture and Slip Behavior: Insights From the 2016 Mw 7.8 Pedernales Ecuador Earthquake. *Journal of Geophysical Research: Solid Earth*, 125(2), e2019JB018001.

- Hoskins, M., Meltzer, ..., **León-Ríos, S.**, ... & Rietbrock, A. (*accepted, October 2020*). Triggered crustal earthquake swarm across subduction segment boundary after the 2016 Pedernales, Ecuador megathrust earthquake. *Earth and Planetary Science Letters*.

Not related to this work

- **León-Ríos, S.**, Ruiz, S., Maksymowicz, A., ... & Madariaga, R. (2016). Diversity of the 2014 Iquique's foreshocks and aftershocks: clues about the complex rupture process of a Mw 8.1 earthquake. *Journal of Seismology*, 20(4), 1059-1073.

- **León-Ríos, S.**, Espinoza González, R., Fuentes, S., ... & Zárate, R. A. (2016). One-dimensional TiO2-B crystals synthesised by hydrothermal process and their antibacterial behaviour on *escherichia coli*. *Journal of Nanomaterials*, 2016.

Seismic networks: deployments and collaborations

- Service to the United Kingdom North-West (UKNW) seismic network. University of Liverpool, 2016–2017.

- Deployment and service of the UK portion, comprising 10 broadband and 10 short period seismic sensors, for the emergency network installed after the 2016 Pedernales, Ecuador earthquake. University of Liverpool, 2016–2017.

- Deployment of the inland portion of 50 seismic stations for the PICTURES project in northern Chile. University of Liverpool, October 2016.

- Collection and shipping of the inland portion of 50 seismic stations for the CEVICHE project in southern Chile. University of Liverpool, January 2017.

- Emergency deployment of 67 short period instruments in the area affected by the seismic swarm and the Mw 7.0 earthquake in Valparaíso, Chile. University of Liverpool, April 2017.

- Collaboration in the deployment of 5 broadband stations for the study of the Albstadt shear zone in southwest Germany. Karlsruhe Institute of Technology, 2018.

– Deployment and logistics for the KIT-UChile mobile seismic array, comprising 88 short period sensors, installed in central and northern Chile. Karlsruhe Institute of Technology, 2018–2020.

– Deployment and logistics for the inland portion of the HIPER project, comprising 50 broadband and 100 short period instruments, installed in the rupture area of the 2016 Pedernales earthquake in Ecuador. Karlsruhe Institute of Technology, 2020.

Acknowledgments

First of all I would to aknowledge the support of Agencia Nacional de Investigacion (ANID) under the Programa Formación de Capital Humano Avanzado, Becas de Doctorado en el extranjero, BECAS CHILE (grant 8068/2015). To the several groups that supported the large collaborative emergency network deployment: Instituto Geofísico de la Escuela Politécnica Nacional and all the staff involved in the project, thanks for its unvaluable contribution to the project. Geoazur in France, Lehigh University and University of Arizona in United States and to the University of Liverpool in United Kingdom, many thanks. To the people in Ecuador who allowed us to install our stations in their houses, big thanks for your hospitality, patience and help when was needed.

To Andreas Rietbrock, many thanks for the tremendous support during the whole period. It is not easy to change program and country in the middle of the way and moreover it was not easy to wrap up all this during a pandemic, so thanks again for all your help during this time. Also, many thanks to the people in Liverpool, Nice, Quito, Santiago and here in Karlsruhe that contributed to this work through discussion and comments during the whole process.

Last but not least, to my family, *jefe*, *ewok*, *negro & coloraa*, gracias por estar y los tkm. Finally, to the old friends in Chile, the new ones that made during this crazy experience and to all the people who crossed at different stages of this journey, *salud!*.

Contents

List of Figures

List of Tables

Chapter 1

Introduction

The regions where two tectonic plates interact with each other, with the denser one moving under the other, are known as subduction zones. These zones are responsible for triggering large megathrust earthquakes with high tsunamigenic potential and therefore it is critical to understand the involved structures, mechanisms and processes. Since the beginning of the 20^{th} century when the hypothesis of continental drift was proposed by Alfred Wegener (Wegener, 1912) and later with the development of the theory of plate tectonics between 1950's - 1970's, several areas where these lithospheres interact and are dragged into the Earth's interior have been discovered (see Figure 1.1). Besides having caused the largest earthquakes ever recorded (eg. Mw 9.5 Valdivia, Chile 1960; Mw 9.2 Alaska, US 1964; Mw 9.2 Sumatra, Indonesia 2004), subduction zones also cause deformation in the upper crust, volcanism and diverse types of seismicity (Pilger, 1984; Cahill and Isacks, 1992). Its characteristics are shown in Figure 1.2. Prior subducting, the incoming plate bends forming the outer rise area (A) with extensional faulting and shallow seismicity. After crossing the trench axis, which identifies the beginning of the subduction, the contact between the downgoing and upper plates creates a locked area (B), called seismogenic zone, that eventually unlocks causing earthquakes with a broad range of magnitudes (M$\sim$1-9) along the interface. As the sinking plate reaches greater depths, gravity pulls the slab down triggering intraplate seismicity (C). On the other hand, due to the large stress caused by the subduction process, the upper crust is deformed promoting shallow seismicity (D). Although the main characteristics of subduction zones are the same along most active margins, there are considerable differences influencing the nucleation of megathurust earthquakes that need to be addressed. Following that, the high rate of seismicity along the South American subduction zone place this region as an ideal natural laboratory to study the mechanisms of earthquakes and the physical properties of the structures involved in an oceanic-continental convergent margin. In this region, the relative motion between the downgoing Nazca oceanic plate and the overriding South American continental plate is in average 6.0 - 6.5 mm/yr (Kendrick et al., 2003) and caused several megathrust earthquakes during the last century, as shown in Figure 1.3.

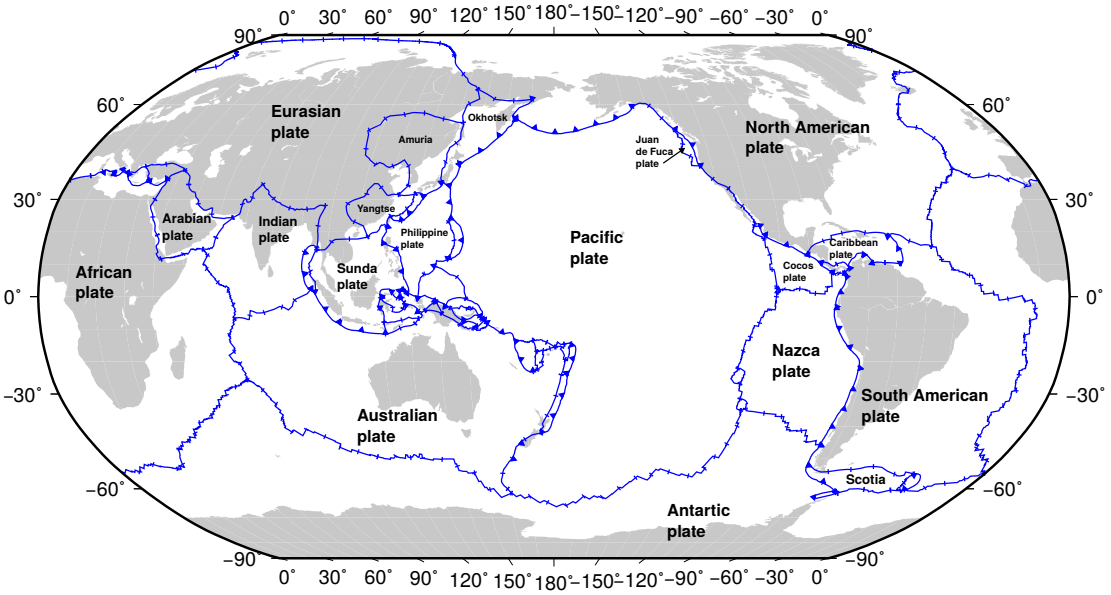

Figure 1.1: Distribution of active subduction zones and convergent margins (triangles) and spreading centers (tick) around the world. Solid blue lines represents the fault trace at surface derived by Bird (2003) and edited by Heine (2019).

As it is described by Bilek (2010), the diversity of earthquake magnitudes is related to the heterogenities and complexities in both plates. Quoting the author "features such as seamounts, ridges, fracture zones, and variable sediment supply enter the trench. In addition, there are various upper plate features such as transverse faults and forearc basins observed along the South American Plate". All these features affect the nucleation and extension of large megathrust earthquakes. In this context, on the 16^{th} April, 2016, a Mw 7.8 earthquake occurred in central coastal Ecuador close to the city of Pedernales. The Pedernales event affected an area of 200 km^2 (Nocquet et al., 2017) killing more than 600 people ((Lanning et al., 2016)). Despite the overwhelming losses, the Pedernales earthquake also gave us a big opportunity to characterize the subduction zone along the Ecuadorian margin by analyzing its unfolding aftershock sequence.

1.1 Motivation

The main goal of this study is to characterize the velocity structure along the coastal central Ecuadorian margin based on local earthquake tomography (LET) using data recorded by a dense emergency network installed shortly after the 2016 Pedernales earthquake. Previous studies regarding velocity structures in Ecuador have been conducted in small areas highlighting local heterogenities, however there is still an absence of a regional scale velocity model showing the three-dimensionality of the margin on a larger scale. By taking advantage of the unfolding aftershock sequence recorded on the permanent Ecuadorian seismic network (Alvarado et al., 2018) and the Pedernales rapid response deployment (Meltzer et al., 2019), together comprising more than 60 inland stations and 10 ocean bottom seismometers (OBS), I focus on the following

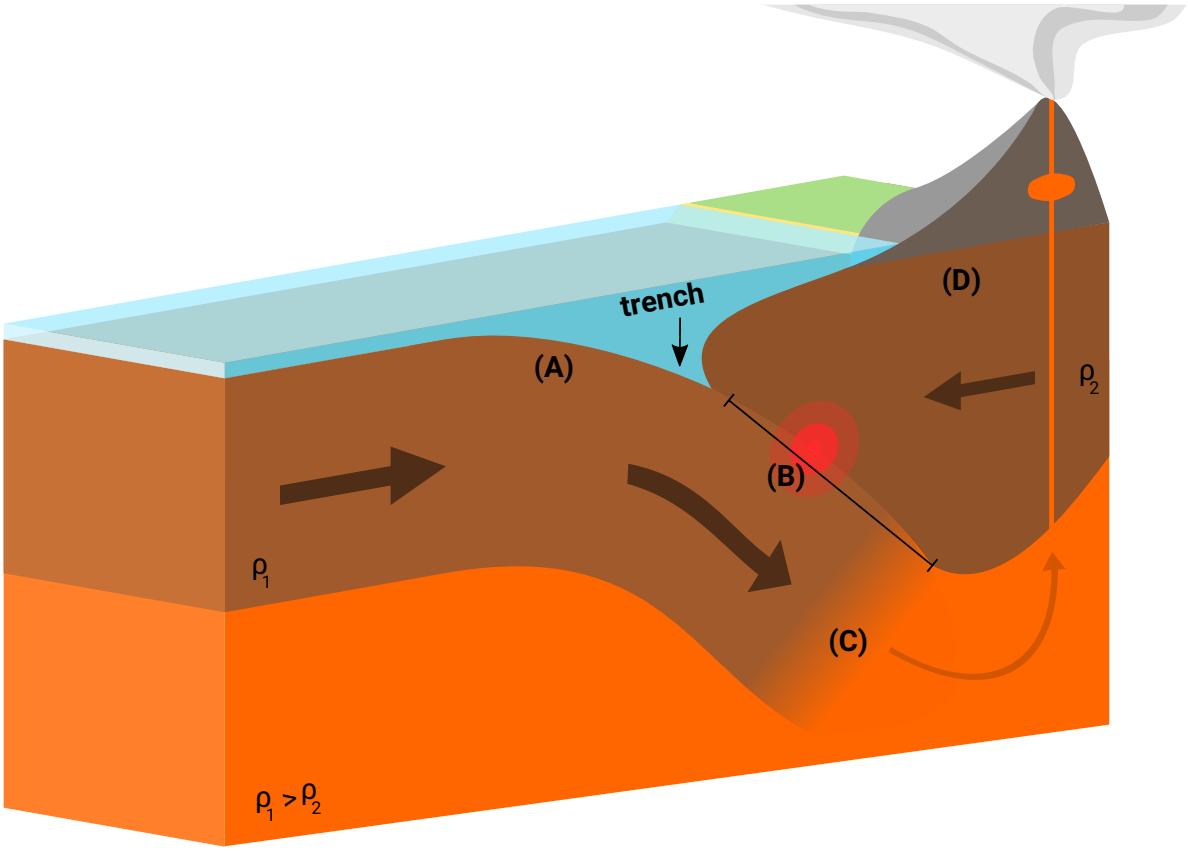

Figure 1.2: Schematic representation of a subduction zone. The oceanic plate with a density ρ_1 sinks below the continental plate which has a density ρ_2 (ρ_2<ρ_1). Characters A-D identify the different areas where seismicity occurs due to the interaction of the downgoing and upper plates. (A) outer rise region, (B) seismogenic zone where large megathrust earthquakes occur, (C) intraplate earthquakes and (D) crustal seismicity. Imaged edited from Domdomegg (2015) under the common creations license CC BY 4.0.

questions about the Ecuadorian margin:

1. What is the three-dimensional (3D) velocity structure at a regional scale of the area affected by the 2016 Pedernales earthquake?

2. How are Vp and Vp/Vs ratios related to the regional geology and the seismotectonic context?

3. What are the main structural and tectonic features controlling the seismic activity in the region?

The next chapters summarize the steps conducted to obtain a novel three-dimensional seismic velocity model (3DVM) for the Ecuadorian margin based on LET derived using a staggered approach. Results and interpretations for each stage are shown in the following chapters of the thesis and are confronted with the questions above in the final chapter.

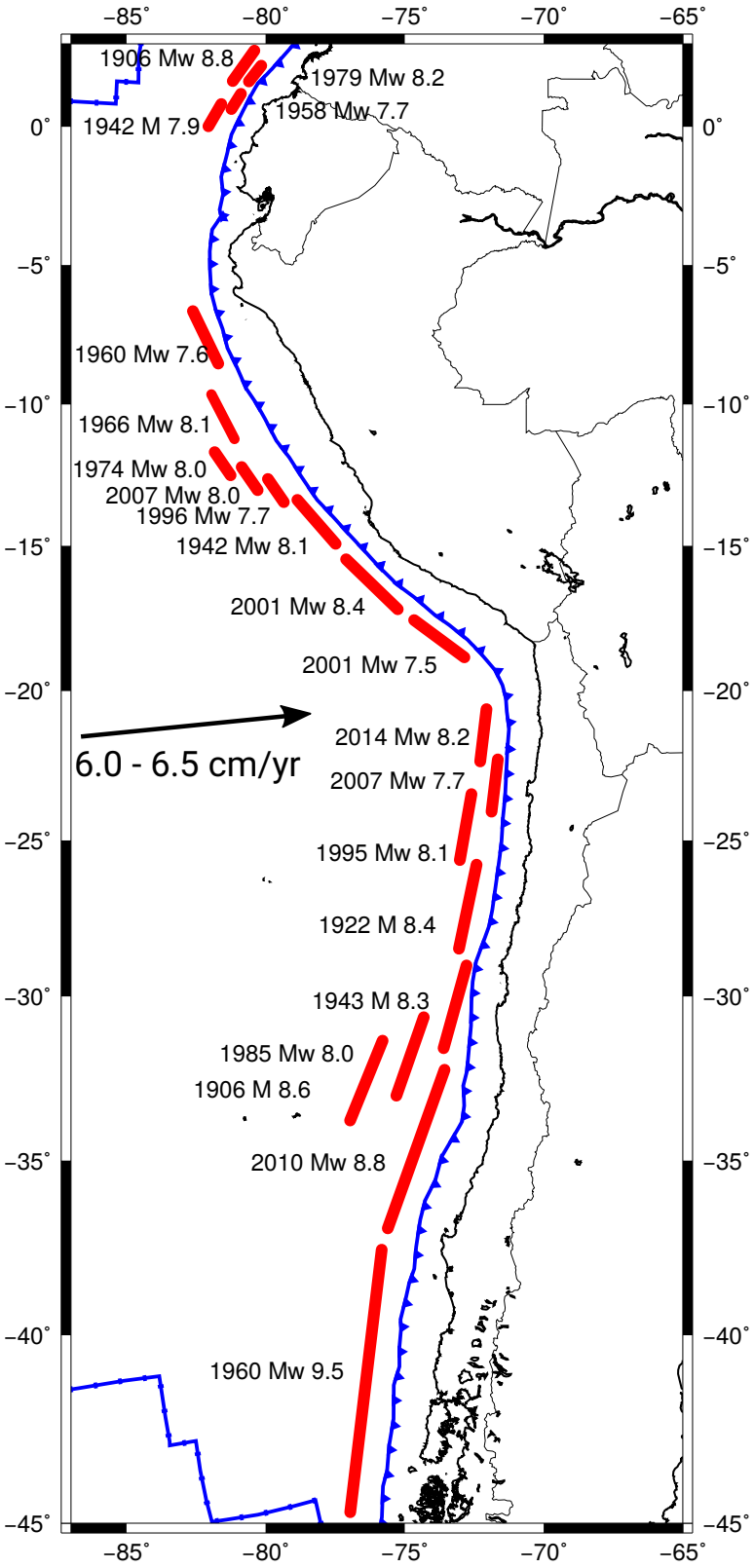

Figure 1.3: Overview map of the South American subduction zone. Rupture areas of significant earthquakes M>7.5 Bilek (2010) are shown in solid red lines. Convergence rate from Kendrick et al. (2003). Trench derived by Bird (2003) and edited by Heine (2019).

1.2 Dissertation outline

The structure of this thesis comprises a theoretical frame for the inverse problem, given in **chapter 2**, including the hypocentre-velocity coupled problem, the moment tensor inverse problem and a detailed description of the computational packages used to calculate their corresponding solutions. The seismotectonic and geological setting for the Ecuadorian margin and the main characteristics of the 2016 Pedernales earthquake are described in **chapter 3**. The rapid scientific response after the mainshock, with the installation of a large emergency network and its subsequently data processing methodology is described in **chapter 4**. The one-dimesional velocity structure derived with the recorded dataset together with its seismotectonic implications are shown in **chapter 5**. Following, **chapter 6** describes the results and interpretations for the three-dimensional velocity model. A detailed inspection of the physiscal properties along the slab interface and its implicances on the 2016 Pedernales rupture extent are included in **chapter 7**. **Chapter 8** summarizes the main steps followed in this work. The major findings are addressed in order to answer the questions proposed in the motivation section. Finally, comments on a possible implementation of the 3DVM at the seismological service in Ecuador (IGEPN) and future work in the Ecuadorian margin are given.

Chapter 2

Inverse problems in seismology

Since the end of the 60's, based on studies from (Backus and Gilbert, 1967, 1968, 1969, 1970) and due to the almost always indirect nature of the observations of the Earth's interior, the generalized inverse method has been widely used in Geophysics, and particularly in Seismology (Sambridge, 2006; Cañas and Ledesma, 1984). Usually, inversion techniques are used when a large dataset is available. In that case, a linearized problem between the observables (e.g. seismograms records, gravity measurements, etc.) and unknowns (e.g. velocity or density structure of the Earth) arises. Keilis-Borok and Yanovskaja (1967) summarizes the inverse problem as follows:

- Given: a combination of observations and a priori information regarding the unknowns to resolve.
- To be found: a set of parameters which are in agreement with the background formulation and the given data.

In this chapter I give an overview of the inverse problems for the velocity-hypocenter couple and for the moment tensor. Furthermore, the computational packages used in this thesis to solve the unknowns of each problem are described.

2.1 The velocity-hypocenter coupled problem

To obtain reliable earthquake locations, it is imperative to have a seismic velocity model capable of describing the study area in details. As we mentioned in the previous chapter, the seismic velocity structure in Ecuador is still under discussion and no consensus has been reached. In this context, we then need to determine both the velocity structure and the earthquake hypocenters, which is known as the velocity-hypocenter coupled problem. To solve this problem, we must use the principles of inverse theory which help us to derive the hypocenters and the velocity structure of the area of

interest, using the observed arrival times. Following the seismic ray theory by Thurber (1983), we can express the travel time *(t)* of a body wave released from a certain source *(i)* and traveling to the receiver *(j)* though a path *(s)* and slowness *(u)* as the follow:

$$t_{ij} = \int_{source}^{station} u \mathrm{d}s \tag{2.1}$$

The observed time (T_{ij}) can be then expressed as a function of the origin time t_o , the travel time t_{ij} from the source x_i, y_i, z_i to the station (x_j, y_j, z_j) and the velocity $v(s)$ along the path.

$$T_{ij} = t_o + t_{ij}(x_i, y_i, z_i, v(s), x_j, y_j, z_j) \tag{2.2}$$

From equation 2.2 we only know the observed time and the station location. The remaining parameters are unknowns that contribute to the problem. However, we can find a solution by estimating the predicted travel times (T_{ij}^{pre}) by using a trial origin and its respective rays travelling from the source to the receiver through a reference velocity model. The difference between the obtained (T_{ij}^{pre}) and the observed times (T_{ij}^{obs}) will be the travel time residuals (ΔT_{ij}). They represent the differences between the predicted and observed hypocenters caused by the variations in the seismic velocity structure of the rocks along the path.

$$\Delta T_{ij} = T_{ij}^{obs} - T_{ij}^{pre} \tag{2.3}$$

To estimate the perturbations in the velocities and hypocenters and therefore reduce the travel time residuals, we need to know how the observed times depend on all the parameters that are part of the inversion problem. Although the arrival time of a seismic ray is a non-linear function of the hypocenter and velocity parameters, we can follow a linear approach by applying a Taylor series expansion in its first order (Thurber, 1983).

$$\Delta T_{ij} = \Delta T_o + \sum_{k=1}^{3}[\frac{\partial t_{ij}}{\partial x_{kj}} \Delta x_{kj}] + \sum_{l=1}^{L}[\frac{\partial t_{ij}}{\partial v_l} \Delta v_l] \tag{2.4}$$

where ΔT_o and Δx_{kj} are the perturbations to the hypocentral parameters in time and space. Δv_l considers the variations of the L parameters of the velocity model. For a given observation, the velocity partial derivatives in equation 2.4 represent the influence of each model parameter on that specific datum. The system of equations that group the time partial derivatives is contained in the Jacobi matrix *G* in equation 2.5. The vector with the model corrections in both velocities and hypocenters is represented by *m*. Finally, travel time residuals are considered in vector *d*

$$d = Gm \tag{2.5}$$

In the case where the number of observations is equal to the unknowns number, it is possible to derive a single solution. However, in the majority of cases we have a larger number of observations than unknowns and therefore we can estimate a reliable solution that fits best the observed data. We can define the best model as the one which shows the smallest difference between the observed and predicted data. This difference or misfit (*E*) can be calculated as follows

$$E = d^{obs} - d^{pre} = d^{obs} - Gm \tag{2.6}$$

To estimate a realistic solution, we aim for model parameters minimizing the misfit. In the most common way this is achieve by forcing the derivative of the squared misfit with respect to the model parameters to be equal to zero

$$\frac{\partial E^2}{\partial v_l} = \frac{\partial}{\partial v_l}(d^{obs} - Gm)^2 = 0 \tag{2.7}$$

Equation 2.7 leads to the least squares solution (Lay and Wallace, 1995) in which m^{est} represents the best solution of the estimated model corrections to minimize the error

$$m^{est} = (G^T G)^{-1} G^T d \tag{2.8}$$

Because of the irregular distribution of the data, there will be regions with less observations than unknowns (e.g. regions in the marine forearc where it is difficult and expensive to have a large number of seismic stations), creating a mixed determined problem (Husen et al., 1999). In other words, some of the model parameters cannot be independently resolved and others are unable to be resolved at all. To make the solution more stable and to avoid strong fluctuations in the model, a damping factor is introduced. By adding this term, the damped least squares solution becomes

$$m^{est} = (G^T G + \varepsilon^2 I)^{-1} G^T d \tag{2.9}$$

The damping parameter ε^2 gives more importance to the norm of the model corrections which, in combination with the squared misfit, helps to minimize the damped least squares solution at each iteration (Evans et al., 1994). Due to the inherently non-linear nature of the inverse problem (Norton, 1988), the solution for the model corrections must be obtained by an iterative process that minimize the mean-square-error between the observed and calculated data. This means that after each run, the estimated model m^{est} and vectors d and G are updated. The equation 2.9 is solved again until a stop criterion, such as predefined minimum in the residuals or a threshold in the parameter changes, is reached. Finally, the solutions for the model corrections are incorporated into the initial model and the absolute velocity structure and earthquake localizations are derived. This methodology provides the theoretical foundation for the programs VELEST (Kissling et al., 1994), for minimum 1D seismic velocity structure calculation and SIMULPS (Thurber, 1983; Thurber and Atre, 1993; Eberhart-Phillips, 1990; Evans et al., 1994), for 3D seismic velocity model inversion, which were used in this work to obtain the 1D, 2D and 3D structure for the Ecuadorian margin.

2.1.1 VELEST: package and parameters

To have a reliable 1D velocity structure for the study area is a critical step when the main goal is to achieve a 3D velocity representation of the region. Because of the complexity of the problem and its non-linearity, it is not recommended to derive a 3D model from scratch. Therefore, intermediate steps are needed to gradually increase the complexity of the model from 1D, 2D and finally the 3D velocity model. The VELEST program calculate a minimum 1D velocity model based on an iterative process where both P and S arrival times are included in a simultaneous inversion

for hypocentral parameters and velocities. Beside the velocity model and hypocentral locations, another output from the inversion are the station corrections. These terms are related to the site effects in the station's neighbourhood and can be used as a control mechanism when they are compared with large-scale geological features. When a large dataset is well spread along a region of interest, the minimum 1D model will considerably improve the initial velocity structure and the earthquake locations. In general, to obtain a good minimum 1D velocity model, it is important to fulfill certain conditions:

- **Reference model:** when available it has to be a general representation of the area. Also, depth gradient must be positive.
- **Station distribution:** it is expected to have a homogeneous distribution of instruments to ensure a good azimuthal coverage for the events (usually <180°) and seismic ray distribution.
- **Dataset:** a large amount of seismicity spread along the area of study is the ideal scenario. Quality of the observed data should be good enough to allow reliable onset detections.
- **Damping:** different damping values should be tested in order to allow the optimal calculation of the velocities and station correction terms.
- Vp/Vs **ratio:** reference value for Vp/Vs must be incorporated during the first stage. In the later stages, it is possible to derive the actual value from observations.
- **Reference station:** to calculate the station corrections, it is necessary to define a station which, ideally, is located in the centre of the network and has a large number of observations.

2.2 Three-dimensional seismic tomography

The first three-dimensional travel time inversions in seismology were presented in the 70s by Keiiti Aki (Aki and Lee, 1976; Aki et al., 1977) and since then it has become a very popular tool to examinate and reveal the heterogeneous nature of Earth's interior. Calculation of a 3D velocity model and accurate earthquake locations follow, in terms of the coupled hypocenter-velocity problem, the damped least squares principles described for the minimum 1D model. Therefore, it is possible to obtain a well constraint solution by using high quality travel time data which allow us to invert for a larger number of unknowns as we increase the model paremeters that need to be calculated. With the improvement of computational power and the acquisition of large volumes of high-quality data, seismic tomography has seen great advances in terms of how to resolve inverse problems with thousands of unknowns (e.g. Burdick et al. (2014)). However, it is necessary to meet certain conditions to obtain meaningful solutions.

- **High quality dataset:** initial data needs to be carefully selected by considering events with

a homogeneous coverage along the area of interest and initial locations which are close to its true hypocenter. A way to achieve this conditions is to include earthquakes with a large number of reliable observations for both, P- and S-phases, and a small gap (largest azimuthal distance between two observations). Events relocated using a minimum 1D model ensure an high quality dataset and subsequent processes will help to refine their true locations.

- **Realistic model parameters:** similar to the earthquake dataset, the initial velocity model must be a good representation of the true model to ensure the iterative process to converge to reliable solutions. Also, the model parametrization has to be fine enough to illuminate structures present in the study region, but coarse enough to allow to incorporate model corrections into the final output.

- **Well defined damping values:** the computation of stable solutions for inverse problems usually involve a trade-off between the data variance (how good is the data fitted by the solution) and the model variance (how good is the obtained model). The damping factor relates both quantities and is selected empirically by analyzing the trade-off curve (L-curve due to its characteristic shape). After testing several damping factors in a sequence of reduced-step inversions, the optimal value is the one that best balances the data and model variances. The trade-off analysis has to be done prior to each inversion (i.e. 1D Vp, 1D Vp/Vs, ..., 3D Vp, 3D Vp/Vs)

2.2.1 SIMULPS: program and parameters

SIMULPS was introduced in the 80s by Thurber (1983) as a tool to calculate a seismic tomography based on local earthquake data. It is based on the travel time inversion strategy described by Aki and Lee (1976) and due to constant improvements during the last three decades by Eberhart-Phillips (1986); Um and Thurber (1987); Eberhart-Phillips (1990, 1993); Thurber and Atre (1993) it is widely used for the calculation of LET. The program settings and input data are controlled by 4 main files described as follows:

MOD. This file refers to the characteristics of the model space, such as grid extension, initial Vp and Vp/Vs models and fixed or linked nodes. SIMULPS works with a 3D grid scheme in which the velocities and ratios can vary along all directions by a B-spline interpolation performed in the vicinity of the 8 closest grid points (Thurber, 1983), allowing a smooth transition rather than sharp velocity contrast. The version used in this study allows flexible gridding (Thurber and Eberhart-Phillips, 1999) by having poor-sampled nodes linked to those which are well covered. This contributes to compensate the under-determination in certain areas with a reduced number of observations. The organization and spacing of the nodes in the grid is given by the area of interest. The x-y distribution aims to have as many ray paths as possible passing through its central region

where the station network is located, while the vertical disposition is, in most of the cases, following the layering of the reference model.

CNTL. The control file sets the main parameters for the inversion. In here, it is possible to define the type (earthquakes, shots, blasts) and number of events to be used but also the number of iterations, cutoff value, weights and the maximum variation, between the inital and final value, of the velocities. Damping values for Vp, Vp/Vs and station corrections can also be modified in this file.

STNS. This file gives the number and the list of stations to be used, including their code, latitude, longitude, elevation and station corrections terms (when available). It also sets the origin of the 3D grid, based on a left-handed reference system (i.e. x-axis positive to the West, y-axis positive North, z-axis positive downward), by giving a latitude, longitude and a counterclockwise, North referenced, rotation angle of the axises.

EQKS. File containing the list of events to be included in the inversion and their corresponding arrival times.

Using the configuration defined by the files described above, SIMULPS performs a ray tracing method that follows a two step approach. First, source and receivers are connected by circular arcs with different radii that explore and sample the entire volume of interest. The travel time with the shortest ray path is then selected as the first arrival (Thurber, 1983). Second step is to minimize each segment of the selected ray path by applying a pseudo bending technique (Um and Thurber, 1987) that allows to find the fastest source-receiver travel time. The reduction in quality of the S-wave travel times, mainly caused by the difficulty on the onset detection in the seismograms, can cause artifacts in the solution of the P- to S-wave ratio (Vp/Vs). To avoid this issue, SIMULPS calculates directly the Vp/Vs ratio by using t_p and t_{s-p} times (Thurber and Atre, 1993). The expected P-phase arrival times are calculated using directly the initial Vp velocity model. On the other hand, the predicted S-onsets come from the calculation over a S-wave velocity model built from the combination of both initial Vp and Vp/Vs models contained in MOD file. Later, and assuming that the differences between the P and S ray paths is negectable, the S-P travel time residuals can be calculated along the S-wave path as follow:

$$\Delta t_{sp}^{obs} - \Delta t_{sp}^{pre} = \int_{S-wave} \frac{\partial(Vp/Vs) - 1}{Vp} \mathrm{d}s \tag{2.10}$$

where Δt_{sp} corresponds to the observed and predicetd S-P times and $\partial(Vp/Vs)$ is the perturbations at the Vp/Vs model. Finally, the full system is inverted for Vp and Vp/Vs together with hypocentral locations and the resulting velocity at an arbitrary point of the grid will be an average of the velocities of all the ray paths that crossed that point.

2.2.2 Assessment of the model robustness

The studies that defined the framework for geophysical inverse problems (Gilbert and Backus, 1966; Backus and Gilbert, 1967, 1968, 1969, 1970) and seismic tomography (Aki and Lee, 1976; Aki et al., 1977) discussed the importance of proving the reliability of the calculated models. Furthermore, a review by Rawlinson et al. (2014) about the analysis of uncertainties mentioned that the fact of simply producing a model that satisfies certain set of data is not meaningful, if the results cannot be associate to error bounds that define a region of confidence. These bounds are strongly related to the geometry of the area of interest, as well as the distribution of the data and the available seismic stations. As the actual source and receiver locations are, in general, organized with a certain degree of heterogenity, it is expected for the resulting model to have areas better resolved than others, which are necessary to identify. Several methods are available to account for well-constrained regions of a tomographic inversion. This chapter summarizes the analysis of the Model Resolution Matrix (MRM) by exploring its diagonal elements (Toomey and Foulger, 1989), as well as synthetic tests that examinates the resolution capability of a model by using synthetic data.

Model Resolution Matrix (MRM)

The MRM provides insights on how well resolved the model parameters are at each grid node and how much is the smearing, or level of dependancy, between the closest nodes in the inversion grid. Following the description given by Thurber and Atre (1993) and the notes on this matter by Collings (2012) and Rawlinson et al. (2014), the MRM R estimates the average between the estimated δm model and the true model δm_{True} by

$$\delta m = R\delta m_{True} \tag{2.11}$$

where R it is defined by

$$R = ([G^T C_d^{-1} + C_m^{-1}]^{-1} G^T C_d^{-1})G = G^{-g}G \tag{2.12}$$

with the term in rounded brackets known as the generalized inverse G^{-g} which contains the terms that reflects the uncertainties associated with the data (C_d) and the initial model C_m (Rawlinson et al., 2010). More in detail, following Tarantola (1987), by including the covariance matrix C_M which is an indicator of how two model unknowns depend on each other, the resolution matrix R can be re-writen as

$$R = I - C_M C_m^{-1} \tag{2.13}$$

The diagonal elements of the C_M matrix predicts the uncertainties associated to each parameter (Rawlinson et al., 2014). Therefore, a valid estimation for well-resolved model parameters is given by considering the resolution diagonal elements (RDE). In general, large RDE (close to 1) and small off diagonal elements indicate good resolution. A visual way to investigate the MRM is

by using the spread function (SF), which takes into account the ratio between off-diagonal and diagonal elements of the MRM (Toomey and Foulger, 1989). It is defined by

$$SF(r_p) = \|r_p\|^{-1} \sum_{q=1}^{m} \Omega(p,q) R_{p,q}^2 \tag{2.14}$$

where r_p is the averaging vector of the p^{th} parameter, $R_{p,q}$ is an element of the resolution matrix, $\Omega(p,q)$ is a weighting function for the distance between the p^{th} and q^{th} nodes and m is the number of parameters. The SF will be low, meaning a well-resolved grid node, when low smearing and large RDE are present. However, there is no unique value that defines what is acceptable or not, as the SF values will vary depending on the initial settings (e.g. grid spacing and damping) considered for each inversion. Another item that can be explored by the MRM is the level of smearing at each grid point. This value indicates the dependance of the solution at a certain node with respect to its closest neighbours. Smearing is strongly related to the quantity of ray paths and can be visualized by contouring each row of the MRM. By using an arbitrary value, usually around 70 - 75%, it is possible to obtain a surface around the model parameter where the value of the averaging vector, contained in the MRM, decays below the selected threshold. This visual quantification for the smearing can be interpreted by analyzing the shape and extension of the surface, where small and rounded contour lines indicate well-resolved nodes. Although the analysis of the MRM is widely used for solution robustness estimation, it can show problems to identify model parametrization artifacts and thus misleading the resolution assessment (e.g. Iyer and Hirahara (1993)). For this reason, the MRM analysis must be necessarily complemented with other numerical tests.

Synthetic tests

The use of synthetic data is another approach to assess the quality of a solution. Because this technique starts with an arbitrary model where the actual data is forward-modelled to create synthetic travel times, it can provide information about the restoring capability of the data and the model parametrization. Here, the criterion for well-resolved regions is based on the similarities between the final model and the arbitrary model where the synthetic data was created (Lévěque et al., 1993). A classic tool to explore this matter is the checkerboard test. This type of analysis was firstly introduced by Aki and Lee (1976) and then improved by Spakman and Nolet (1988). Here, synthetic travel times are calculated, using the observed dataset and station distribution, over a known structure that it is usually an alternating pattern of positive and negative anomalies. Then, the inversion method is applied to recover the original structure. Finally, by evaluating the differences (dv) between the initial and final models it is possible to assess the resolution capability of a certain dataset. Lévěque et al. (1993) highlight the problems of this technique to restore large-size anomalies included in the arbitrary model, suggesting that a complete synthetic test have to include tests on different sizes of velocity anomalies and changes in the grid node configuration (coarser and smaller grids) and in the distribution of the sources and receivers. Other technique based on synthetic data is the restoring resolution test (Zhao et al., 1992). Here, an

arbitrary model is built based on the velocity structure derived by inverting the actual data. Changes in the geometry and the sign of the velocity anomalies are incorporated to the model and the forward modelling produces the synthetic travel times which are subsequently inverted over the reference input model. The resulting model will show areas that are unable to be resolved by the initial model.

2.3 The moment tensor inverse problem

Moment tensors give a general description of a seismic source based on generalized force couples. Due to the simple formulation and flexibility to process different type of data, this method has been widely applied to represent the focal mechanism of earthquakes based on the inversion of the Earth free oscillations (Gilbert and Dziewonski, 1975), long periodic waves (Strelitz, 1980; Sipkin, 1982), surface waves (Dziewonski and Woodhouse, 1983; Sipkin, 1987; Sipkin and Needham, 1994) and also by using regional data (Dreger and Helmberger, 1993; Mao et al., 1994; Ichinose et al., 1998). This section comprises the theory behind the calculations of regional moment tensors (RMT) compiled from Stein and Wysession (2003), Dahm and Krüger (2014) and personal notes collected during my master and doctoral thesis. Also, main characteristics of the ISOLA package (Sokos and Zahradnik, 2008; Sokos and Zahradník, 2013), used in this study to derive RMT for the aftershock sequence of the Pedernales earthquake, are given.

2.3.1 Seismic source representation

By considering a seismic source as a punctual representation, it is necessary to ensure the conservation of momentum. Then, a pair of forces with equal magnitude, opposite direction acting over a single point are needed. Other option is to represent the source by two pairs of forces acting perperdicular to each other. In here, each pair have two force vectors with opposite direction acting over single points separated by a small distance d (see Figure 7.3). This configuration ensures the conservation of the angular momentum and it is known as double couple forces (Aki and Richards, 2002; Stein and Wysession, 2003).

It is possible to define M_{ij}, with i, j=1,2,3, as a force couple pointing in the direction i and with a separation between them along the j direction. Then, the moment tensor M, a symmetric 3x3 matrix, will contain all the possible combination of the force couples (six independent components, see Figure 2.2). The diagonal elements of M represent linear vector dipoles while the off-diagonal elements indicate the force couples.

This representation allows not only to describe seismic sources but a vast type of sources such as explosions, landslides and even meteorite falling into the Earth (Dahm and Krüger, 2014).

Therefore, it is relevant to understand the components of the tensor M in order to give a proper geological and/or physical interpretation of the observed process. In that line, a decomposition of the moment tensor is often applied in order to evaluate the contribution of different source components to the main framework. The moment tensor of a dislocation can be expressed by the general dislocation source equation proposed by Aki and Richards (2002),

$$M_{pq} = NA(n_p D_q + n_q D_p) + \eta A n_k D_k \delta_{pq} \tag{2.15}$$

where D represents the dislocation vector in an arbitrary direction, A is the area or plane where the dislocation ocurrs, n is an unitary vector indicating the direction of the fault and N and η are elastic constants. This equation can be decompose by several techniques depending on the interpretation that authors aim to achieve. Jost and Herrmann (1989) give a nice overview of various types of decomposition for the moment tensor that it is briefly describe in the following lines. The moment tensor M is decomposed through its eigenvalues and eigenvectors forming the matrix

$$M = \begin{pmatrix} a_{1x} & a_{2x} & a_{3x} \\ a_{1y} & a_{2y} & a_{3y} \\ a_{1z} & a_{2z} & a_{3z} \end{pmatrix} \begin{pmatrix} m_1 & 0 & 0 \\ 0 & m_2 & 0 \\ 0 & 0 & m_3 \end{pmatrix} \begin{pmatrix} a_{1x} & a_{2y} & a_{3z} \\ a_{1x} & a_{2y} & a_{3z} \\ a_{1x} & a_{2y} & a_{3z} \end{pmatrix} \tag{2.16}$$

with a_i representing the eigenvectors of the eigenvalues m_i. The equation 2.16 can also be written as

$$M = \begin{bmatrix} a_1 & a_2 & a_3 \end{bmatrix} m \begin{pmatrix} a_1^T \\ a_2^T \\ a_3^T \end{pmatrix} \tag{2.17}$$

where m is a diagonalized moment tensor and the elements of m are the eigenvalues of M. The diagonalized tensor m can be now decomposed as follow:

$$m = \frac{1}{3} \begin{pmatrix} tr(M) & 0 & 0 \\ 0 & tr(M) & 0 \\ 0 & 0 & tr(M) \end{pmatrix} + \begin{pmatrix} m_1^* & 0 & 0 \\ 0 & m_2^* & 0 \\ 0 & 0 & m_3^* \end{pmatrix} \tag{2.18}$$

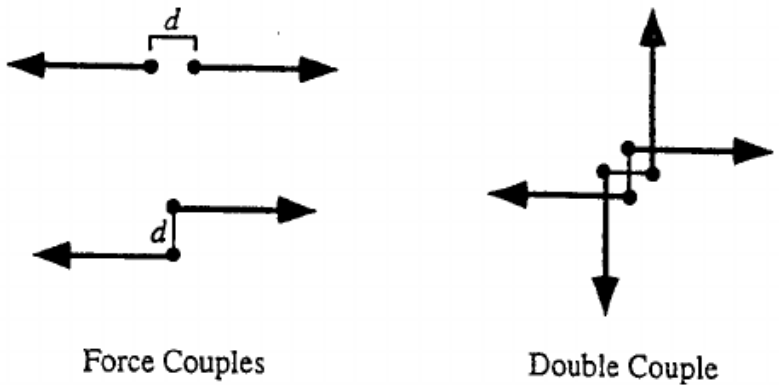

Figure 2.1: (Left) Force couples represented by two vectors with equal magnitude and opposite direction and separated by a distance d. (right) Double couple representation with a complementary pair of force couples producing a total momentum equal to zero.

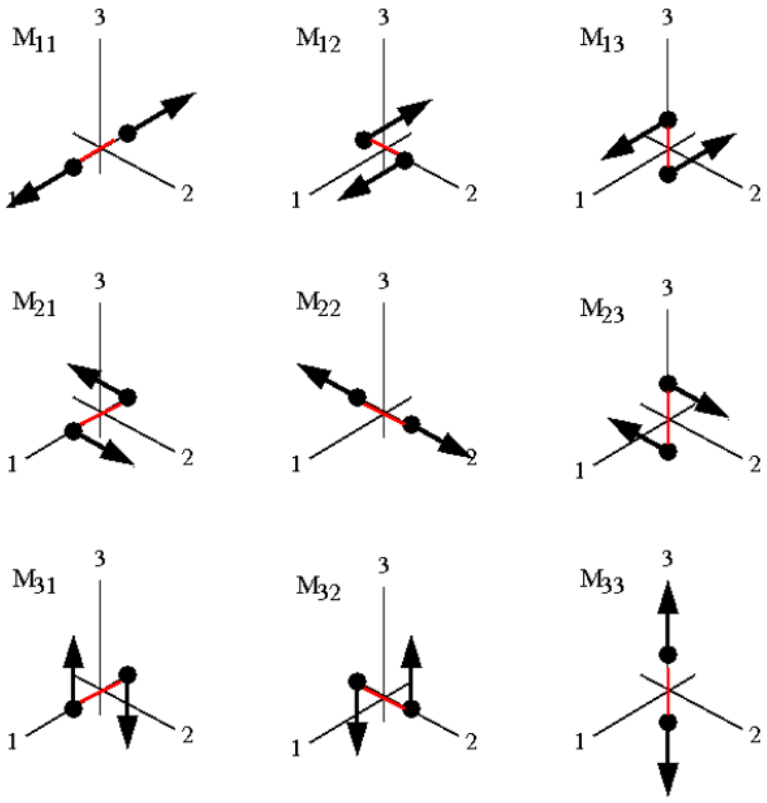

Figure 2.2: Graphic representation of a system of force couples in a Cartesian moment tensor. Diagonal elements of the moment tensor represent linear vector dipoles, while off-diagonal elements represent force couples with moment.

with tr(M) being the trace of tensor M and $m_i^* = m_i - \frac{1}{3}tr(M)$. The two matrixes above represent the isotropic and deviatoric part of the moment tensor M.

$$M = M^{ISO} + M^{DEV} \tag{2.19}$$

As the isotropic part (M^{ISO}) radiates only P and Rayleigh waves, plus the spheirodal normal modes with no preferred direction, it is often associated to changes in the volume. On the other side, the deviatoric tensor (M^{DEV}) has no direct geological meaning, however further decompositions lead to different information broadly used for geophysical interpretations. Following that, Jost and Herrmann (1989) listed two options that can be applied to (M^{DEV}). First, a best double couple (DC) and a compensated linear vector dipole (CLVD); and second, a strike-slip, a pure dip-slip and a vertical CLVD. Regarding seismotectonic interpretations, the DC+CLVD method which maximize the DC part seems to be the most relevant in the majority of cases and it is broadly used in seismology by the visualization of the results using focal mechanisms.

2.3.2 Moment tensor calculation

Dahm and Krüger (2014) provide an excellent description for the problem of moment tensor calculations. The inversion problem for moment tensors requires the availability of digital time

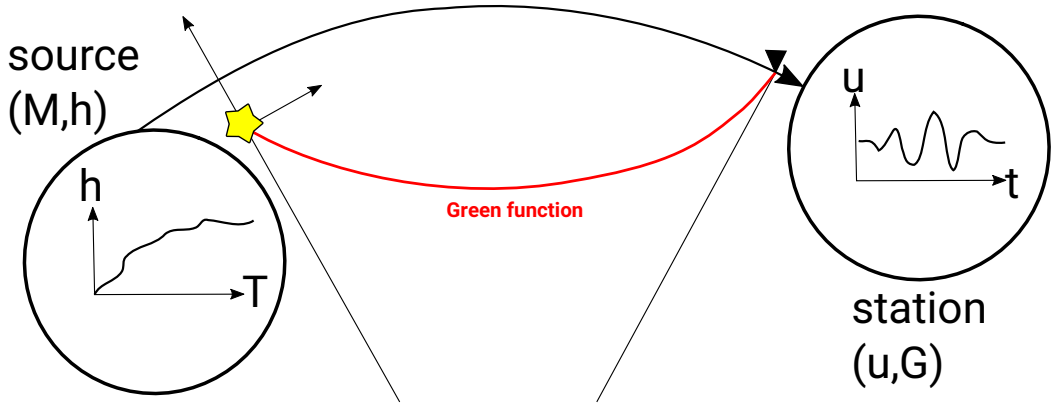

Figure 2.3: Setting for the inverse problem which summarizes the response of the Earth represented by the Green's functions G measured in a station at the surface after being affected by a perturbation from a point source.

series of observed data, e.g. full seismograms. It is also required to have calibrated systems for predictable data acquisition. This translates in the necessity of having the instrument response (eg. poles and zeros) of each sensor that collected the data. Finally, capacity of calculation (or availability) of accurate synthetic seismograms of the Earth (i.e. Green's functions). Figure 2.3 shows the geometry of the problem in which the Green's functions (G) represent the Earth response at a certain station x after been affected by a perturbation source ξ. The point source can be described by a moment tensor M and a source function $h(t)$ while the displacement at the surface is indicated by u. The difference between source ($h(t)$) and ground motion ($u(t)$) can be explained by the heterogenities of the Earth along the ray path. The moment tensor M can be obtained by solving the point source moment tensor representation of ground displacement

$$u_n(x,t) = M_{pq}(\xi,t) * \frac{\partial}{\partial \xi_q} G_{np}(x,\xi)|_{\xi_0} = M_{pq}(\xi,t) * G_{np,q}(x,\xi,t) \tag{2.20}$$

where u_n represents the displacement at location x and time t. The moment tensor at location ξ is given by M. Partial derivatives of the Green's tensor are indicated by $G_{np,q}$. By considering a Dirac delta function as a source, $G_{np,q}$ can be written as $G_{\gamma}^{\alpha\beta}$ which represents the displacement field calculated in the direction γ given a certain point source at a known time and space. Therefore, the only non-null component that remains is $M_{\alpha\beta}$ that is equal to 1 or to a amplitude factor with physical units (eg. Nm). Then, it is possible to write the equation 2.20 as a matrix by

$$\begin{pmatrix} u_x(t) \\ u_y(t) \\ u_z(t) \end{pmatrix} = \begin{pmatrix} G_x^{xx}(t) & G_x^{yy}(t) & G_x^{zz}(t) & G_x^{xy}(t) & G_x^{xz}(t) & G_x^{yz}(t) \\ G_y^{xx}(t) & G_y^{yy}(t) & G_y^{zz}(t) & G_y^{xy}(t) & G_y^{xz}(t) & G_y^{yz}(t) \\ G_z^{xx}(t) & G_z^{yy}(t) & G_z^{zz}(t) & G_z^{xy}(t) & G_z^{xz}(t) & G_z^{yz}(t) \end{pmatrix} \begin{pmatrix} M_{xx} \\ M_{yy} \\ M_{zz} \\ M_{xy} \\ M_{xz} \\ M_{yz} \end{pmatrix} \tag{2.21}$$

This equation has the same shape as the $d = Gm$ discussed in the velocity-hypocenter problem. Considering the observed data and the Green's functions (i.e synthetic seismograms) as knowns,

it is possible to find the 6 components of M by the least squares method. In that matter, there are several programs available to calculate moment tensor solutions (eg. computers program in seismology (Herrmann, 2013), ISOLA (Sokos and Zahradnik, 2008; Sokos and Zahradník, 2013), among others). In this study, we used the ISOLA package which allows the calculation of moment tensors at a regional to local scale (RMT) and provides an interactive viewing that allows to check the processes prior the inversion.

2.3.3 The ISOLA package

The ISOLA package (Sokos and Zahradnik, 2008; Sokos and Zahradník, 2013) comprises two programs working together. First, the ISOLA Fortran code is the responsible to perform the calculations for data preparation, filtering, instrumental response and moment tensor inversion. All these utilities can be operated by the user through an interactive graphical tool controlled by the ISOLA-GUI MATLAB code. ISOLA is capable to calculate moment tensors in a regional to local scale (RMT) following a full waveform inversion adapted from the work of Kikuchi and Kanamori (1991) for teleseismic data. Based on the discrete wavenumber method from Bouchon (1981) and Coutant (1989) the equation 2.20 can be written in a discrete form by

$$u_i(t) = \sum_{p=1}^{3} \sum_{q=1}^{3} M_{pq} * G_{ip,q} \tag{2.22}$$

Moreover, the moment tensor M_{pq} can be expressed by a linear combination of six elementary tensors M^i that represent five DC combinations and a pure isotropic source (i.e. explosion), as shown in Figure 2.4. The equation for M_{pq} is defined as

$$M_{pq} = \sum_{i=1}^{6} a_i M_{pq}^i \tag{2.23}$$

where a_i represents the coefficients of the linear combination. By combining 2.22 and 2.23, the ground displacement $u_i t$ becomes

$$u_i(t) = \sum_{p=1} \sum_{q=1} (\sum_{j=1}^{6} M_{pq}^j) * G_{ip,q} \tag{2.24}$$

which leads to

$$u_i(t) = \sum_{j=1}^{6} a_j (\sum_{p} \sum_{q} M_{pq}^j * G_{ip,q}) = \sum_{j=1}^{6} a_j E_i^j(t) \tag{2.25}$$

with E^j denoting the j-th elementary seismogram corresponding to the j-th elementary moment tensor (ISOLA user manual). ISOLA includes a Dirac delta function as source function and therefore the only remaining unknowns are the coefficients a_j which denoted in matrix is $u = Ea$ and can be solved by the least squares method included in the Fortran code

$$a_{opt} = (E^T E)^{-1} E^T u$$

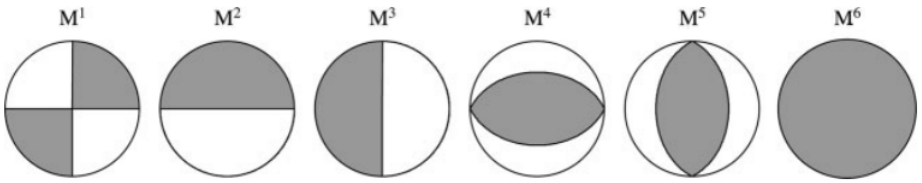

$$\mathbf{M^1} = \begin{pmatrix} 0 & 1 & 0 \\ 1 & 0 & 0 \\ 0 & 0 & 0 \end{pmatrix} \qquad \mathbf{M^2} = \begin{pmatrix} 0 & 0 & 1 \\ 0 & 0 & 0 \\ 1 & 0 & 0 \end{pmatrix}$$

$$\mathbf{M^3} = \begin{pmatrix} 0 & 0 & 0 \\ 0 & 0 & -1 \\ 0 & -1 & 0 \end{pmatrix} \qquad \mathbf{M^4} = \begin{pmatrix} -1 & 0 & 0 \\ 0 & 0 & 0 \\ 0 & 0 & 1 \end{pmatrix}$$

$$\mathbf{M^5} = \begin{pmatrix} 0 & 0 & 0 \\ 0 & -1 & 0 \\ 0 & 0 & 1 \end{pmatrix} \qquad \mathbf{M^6} = \begin{pmatrix} 1 & 0 & 0 \\ 0 & 1 & 0 \\ 0 & 0 & 1 \end{pmatrix}$$

Figure 2.4: Elementary moment tensors used in the inversion process by ISOLA. M^1-M^5 represent combinations of double couple and M^6 is a pure isotropic source (i.e. explosion).

2.3.4 ISOLA parameters and inversion

This section refers to the staggered process followed by ISOLA prior and during inversion. Options controlling each step are listed and described. More information can be found in the ISOLA user's manual.

Crustal model

First step required by ISOLA is to define a 1D velocity model with a maximum of 15 layers. Crustal Model provides the panel to create or load a velocity structure with Vp and Vs or Vp and a constant Vp/Vs ratio. Also density and attenuation for P- and S-waves are needed.

Event info

This section allows the user to include the information of the event to analize. Here the hypocentral data (i.e Lat, Lon, depth and origin time) are mandatory while magnitude and reporting agency are optional. On this step it is also possible to define the time length (in seconds) that will be used in the subsequent inversion.

Station selection

As stated in the title, this section gives the user the option to choose the stations to be included in the inversion. Graphical tool, ISOLA-GUI, can display a regional map with the available receivers on it allowing an interactive selection. During the inversion process, it is possible to discard stations with bad performance.

Data preparation

ISOLA accepts SAC files of velocity seismograms. It is important to check that all stations used have the same format to avoid misscalculations of the moment tensors. Data can be imported using the graphical tool. It is possible to check the quality of each component by a visual exploration of raw traces, signal to noise ratio and spectral plots. After decide which data will be considered in the inversion, a staggered preparation is performed by (1) doing the instrument correction by using poles and zeros files, (2) resampling the data by a predeterminated frequency (usually 50 Hz) and (3) aligning the origin time based on the event information. Corrected, aligned and resampled data is saved for the inversion stage.

Trial source definition

This item controls the number and location of the trial sources during the inversion. ISOLA offers the option to select a single or multiple source. In single source mode, user can vary the source location only in depth by defining a starting depth, a number of sources and a iteration step for the trial. On the other hand, multiple source mode allows the user to select sources along strike of the fault, along dip or in a plane. Besides trial sources and step, the fault strike and dip need to be defined.

Green's functions calculation

With all the available data already included in ISOLA, the Green's functions are computed. A maximum frequency is set and can be modified by the user. A terminal window monitors the creation of Green's functions and elementary seismograms. As mentioned before, ISOLA works under the assumption of a Dirac delta as source function.

Inversion

The last step for the calculation of RMT is the inversion itself. The options at this stage are related to the filtering that will be applied to the data, the number of subevents to be calculated, the type of inversion, time search window and weighting applied for each observable. Typical values for RMT calculations range between 0.02 and 0.1 Hz (eg. Herrmann (2013); Sokos and Zahradník (2013)). In relation to the type of inversion, we chose the deviatoric MT as this option leads to a more intuitive interpretation of the rupture plane. After the inversion is performed, it is possible to remove stations with bad performance (i.e. reduced correlation with the synthetic seismograms) and re-run the calculations.

Finally a complete visualization panel is offered where the most relevant are the display of the RMT solutionin a map view together with the stations used, the fitting between the observed and synthetic and a variance reduction plot comparing the variance of RMT at different trial sources. More options are available and can be found in the user's manual.

2.4 Application to this work

The theory and the computational programs presented in this chapter were applied in the Ecuadorian margin, along the area affected by the 2016 Mw 7.8 Pedernales earthquake. At first, I derived a minimum 1D velocity model, hypocentral locations and regional moment tensors using VELEST and ISOLA, respectively. Methodology, results and interpretations regarding these matters are shown in Chapters 5. Subsequently, using the resulting 1D structure and hipocentral locations as input for SIMULPS, I calculated a 3D seismic tomography based on local earthquake tomography. Chapters 6 and 7 provide detailed description about procedure, major findings and its relation with the regional tectonics.

Chapter 3

Seismotectonic and geological setting

This chapter contains a description of both the tectonical and geological settings along the Ecuadorian margin. The text included in the following sections is part of the research articles listed below:

- 1D-velocity structure and seismotectonics of the Ecuadorian margin inferred from the 2016 Mw7.8 Pedernales aftershock sequence, published in *Tectonophysics* (León-Ríos et al., 2019).
- 3D local earthquake tomography of the Ecuadorian margin in the source area of the 2016 Mw 7.8 Pedernales earthquake, submitted in *Journal of Geophysical Research* (León-Ríos et al., 2020).
- Ridge subduction and afterslip control aftershock distribution of the 2016 Mw 7.8 Ecuador earthquake, published in *Earth and Planetary Science Letters* (Agurto-Detzel et al., 2019) in which I am a co-author.
- Structural Control on Megathrust Rupture and Slip Behavior: Insights From the 2016 Mw 7.8 Pedernales Ecuador Earthquake, published in *Journal of Geophysical Research* (Soto-Cordero et al., 2020) in which I am a co-author.
- Triggered crustal earthquake swarm across subduction segment boundary after the 2016 Pedernales, Ecuador megathrust earthquake, accepted (October 2020) in *Earth and Planetary Science Letters* and in which I am a co-author.

3.1 Tectonics and geology of central coastal Ecuador

The Ecuadorian margin is controlled by the subduction of the oceanic Nazca plate beneath the continental South American plate. This process occurs with an east–west convergence rate ∼46 mm/yr (Trenkamp et al., 2002; Kendrick et al., 2003; Nocquet et al., 2009). The margin has been recognized as highly segmented and mainly of erosional type (Collot et al., 2002; Gailler et al., 2007; Marcaillou et al., 2016) which create diverse patterns in seismicity in the subducting and overriding plates as well as along the plate interface.

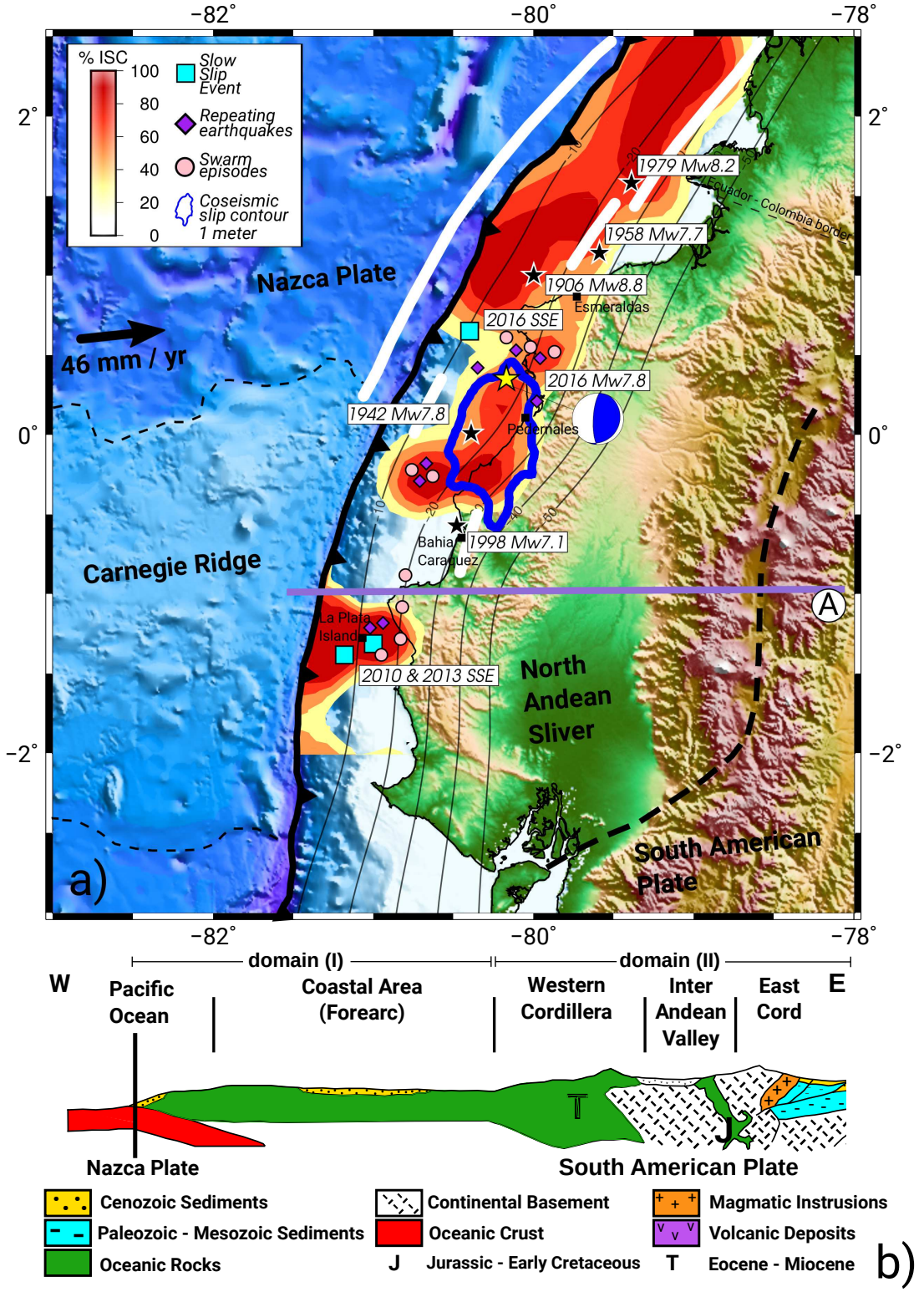

Figure 3.1: (a) Seismotectonic characteristics of the central coastal segment of the Ecuadorian margin. Inland and seafloor topography was derived by Michaud et al. (2006). Segmented line shows the Chingual-Cosanga-Pallatanga-Puna megashear fault (CCPP) that creates the North Andean Sliver. Bold arrow show the convergence rate between the Nazca plate and the North Andean Sliver. Black stars and white solid lines represents the epicenters and estimated ruptures of the last large subduction earthquakes occurred along the margin since 1906. Squares, diamonds and circles are showing the Slow Slip Events, repeating earthquakes and swarms sequence, respectively, reported by Rolandone et al. (2018). Interseismic coupling derived by Nocquet et al. (2014). Yellow star is showing the epicenter of the 2016 Mw 7.8 Pedernales earthquake. Coseismic slip contour, in blue solid line, was obtained by Nocquet et al. (2017). Trench data from Collot et al. (2005). Purple solid line shows the location of the projected profile. (b) Structural sketch of the Ecuadorian margin showing the main morphological structures. Figure edited from Jaillard et al. (2000).

The continental forearc is divided by the Chingual-Cosanga-Pallatanga-Puna (CCPP) fault zone which, in surface, extends from $\sim 2°$S to the Colombian border and towards Venezuela in the north (Alvarado et al., 2016). This long-scale structure creates the North Andean Sliver (NAS) shown in Figure 3.1a. In front of the NAS, the Nazca Plate is less than 26 Ma old (Lonsdale, 2005) and subducts at a relative rate of about 46 mm/yr (Chlieh et al., 2014).

Offshore, the study area is characterized by the presence of large bathymetric features, with volcanic rocks from the Cenozoic (Collot et al., 2009), such as the Carnegie Ridge (CR), the Atacames seamount chain (ASC) and the Yaquina graben farther north interpreted as a transform fault with an additional one closer to the trench, shifting extinct rifts (Lonsdale, 2005; Hardy, 1991). These significant along-strike and along-dip structural variations, which might also exist at greater depth on the subducted portion, may contribute to create diverse patterns of seismicity along strike (Gailler et al., 2007; Font et al., 2013; Agurto-Detzel et al., 2019).

The CR subducts beneath the Ecuadorian trench between latitude $\sim$1°and $\sim$2°S (see Figure 3.1 and 3.2). It is $\sim$280 km wide and $\sim$2 km high and is currently approaching to the margin with an ENE direction. The CR was formed by the Galapagos hot-spot (GHS) located about 1000 km west of the coastline of Ecuador. At the northern flank of the CR (see Figure 3.2), a series of seamounts, including the ASC, are subducting beneath the South American plate. Marcaillou et al. (2016) points out that the ASC plays an important role on promoting the stable sliding of the updip segment of the seismogenic zone and controlling the propagation of large subduction earthquakes towards the trench.

The thickness of the oceanic crust varies along strike - from 5 km in the north, close to Esmeraldas ($\sim$1°N), to 14 km in the south ($\sim$1°S), reaching its maximum of 19 km beneath the crest of the CR (Meissnar et al., 1976; Calahorrano et al., 2008; Sallarès et al., 2003, 2005; Graindorge et al., 2004; Gailler et al., 2007; Cano et al., 2014). In terms of the trench depth, variations from 3.7 km in the north to 2.8 km at the crest of the CR in the south have been observed (Collot et al., 2004).

To the coast, the Ecuadorian territory (1°N to 3°S) can be broadly divided into three main domains, as shown in Figure 3.1b, extending inland from the margin (Jaillard et al., 2000). Our study area comprises mainly domain I and part of domain II. The profile A, in Figure 3.1b, shows the nowadays marine forearc in central Ecuador. This formation is the result of subsequent accretion of lithospheric material and arc rocks that occurred between the late Cretaceous to the Paleocene/Eocene (Reynaud et al., 1999; Jaillard et al., 2009). In this domain, a thin layer of sediments of 500 m to 1000 m (Jaillard et al., 2000) covers most of the forearc.

Distributed along the coastline, as shown in Figure 3.2, magmatic outcrops have been associated to the Piñon formation (Reynaud et al., 1999; Luzieux et al., 2006; Reyes and Michaud, 2012) which used to be identified as "the Cretaceous igneous basement of western Ecuador"(Reynaud et al., 1999) and extends along the whole study area up to the CCPP fault to the east. In the Manta area, the San Lorenzo block, a mix of volcanic conglomerates, appears in conformity with the Piñon formation (Reynaud et al., 1999; Reyes and Michaud, 2012) creating the oceanic terranes. Sediments from Quaternary cover these geological features among other small formations developing several basins along the coast, such as the Borbon (Cantalamessa et al., 2007), Manta-Jama and Manabi basins (Reyes and Michaud (2012) - see Figure 3.2).

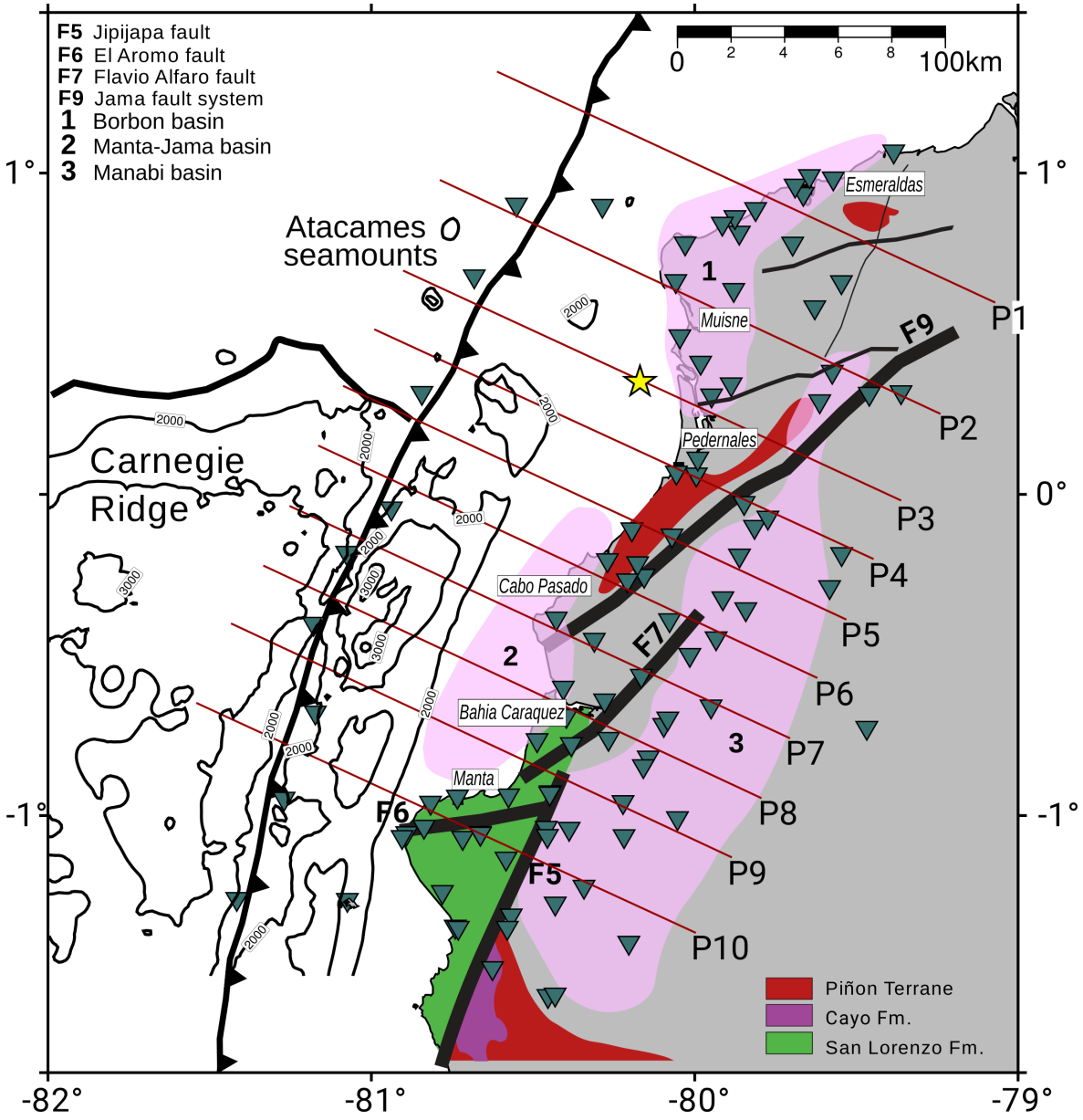

Figure 3.2: Geological context and recording network. Main formations, sedimentary basins and faults mapped by Reyes and Michaud (2012) are displayed by coloring forms and solid black lines. Offshore, residual bathymetry derived by Agurto-Detzel et al. (2019) is shown in solid black line. Permanent Ecuadorian network (RENSIG, Alvarado et al. (2018)) and emergency deployment (Meltzer et al., 2019) are shown in gray inverted triangles. Profiles, P1-P10, discussed in this work are plotted in solid red line. Yellow star represents the epicentre of the 2016 Pedernales earthquake (Nocquet et al., 2017).

The local tectonic and seismic activity is controlled by major faults that bound these basins (Reynaud et al., 1999; Luzieux et al., 2006; Reyes and Michaud, 2012; Font et al., 2013; Agurto-Detzel et al., 2019; León-Ríos et al., 2019). Reyes and Michaud (2012) updated the coastal geological map for Ecuador by (re)drawing the extension of several faults observed at the surface. Figure 3.2 summarizes the main geological structures and faults that, due to their extension, might contribute to the regional tectonic control but also to allow the circulation of fluids within the margin (e.g. the Jipijapa fault; Segovia et al. (2018)). The domain II is part of the Andean chain that involves the Western cordillera, with deformed rocks from accreted oceanic

crust, and the Eastern cordillera (Cordillera Real) which contains metamorphic rocks from the Paleozoic to Mesozoic (Litherland, 1994).

3.2 Historical earthquakes

During the last century, the Ecuadorian-Colombian margin has experienced several major earthquakes (Ramírez, 1975; Kelleher, 1972; Abe, 1979; Herd et al., 1981; Kanamori and McNally, 1982; Mendoza and Dewey, 1984; Beck and Ruff, 1984; Sennson and Beck, 1996). More recently, slow slip events have been observed (Mothes et al., 2013; Vallée et al., 2013; Chlieh et al., 2014; Segovia et al., 2015; Collot et al., 2017; Vaca et al., 2018; Rolandone et al., 2018), in addition to seismic swarms (Segovia, 2001; Segovia et al., 2009; Vaca et al., 2009) and repeating earthquakes (Rolandone et al., 2018) (see Figure 3.1).
In 1906 a megathrust earthquake Ms 8.7 (Kelleher, 1972), re-estimated to Mw 8.8 (Kanamori and McNally, 1982) and more recently to Mw 8.4 (Yoshimoto et al., 2017), ruptured the subduction segment along central and northern Ecuador and southern Colombia generating severe destruction which reached up to 100 km inland. The rupture extent of this earthquake is still under discussion. While Kanamori and McNally (1982) suggested a rupture of approximately 500 km length, Yoshimoto et al. (2017) proposed a smaller rupture area mainly located near the trench. The 1906 earthquake also caused permanent coastal uplift and generated a destructive tsunami (Ramírez, 1975; Kelleher, 1972; Abe, 1979; Herd et al., 1981; Kanamori and McNally, 1982). Subsequently, smaller earthquakes of diverse magnitudes (between Mw 7.0 to Mw 8.2) ruptured with thrust mechanisms, leading to several authors proposing a segmentation of the subduction zone along the northern Ecuadorian margin (e.g. Marcaillou et al. (2006); Gailler et al. (2007)).
In 1942, a Mw 7.8 earthquake occurred close to the coastal city of Pedernales affecting an area of ∼200 km x ∼90 km. The epicenter was located at the southern edge of the rupture region, suggesting that the event propagated to the NE (Kelleher, 1972; Sennson and Beck, 1996). In 1958, the Mw 7.7 Colombia-Ecuador earthquake (Kanamori and McNally, 1982) broke a small segment of the 1906 megathrust earthquake in the offshore portion of the Esmeraldas province to the North. Like the 1942 earthquake, the 1958 event showed a rupture propagation in the NE direction (Rothé, 1969; Kelleher, 1972; Mendoza and Dewey, 1984). Finally, in 1979, the largest event of this series of major earthquakes occurred close to the Ecuadorian-Colombian border with magnitude of Mw 8.2 also rupturing in a NE direction along ∼230 km of the margin (Herd et al., 1981; Kanamori and Given, 1981; Beck and Ruff, 1984).
Between the equator and south of the CR, there have been few large subduction earthquakes recorded (Egred, 1968; Dorbath et al., 1990; Bilek, 2010) with only two events of Mw>7.0 (in 1956 and 1998) occurring close to Bahia Caraquez (Storchak et al., 2013). However, a high rate of seismicity up to Mw 6.5 has been registered in this region (Vallée et al., 2013) suggesting that the accumulated stresses are released by different mechanisms than in the northern segment (White et al., 2003; Agurto-Detzel et al., 2019). Moreover, the area shows a complex slip behavior, with different types of seismic activity highlighted in Figure 3.1a.

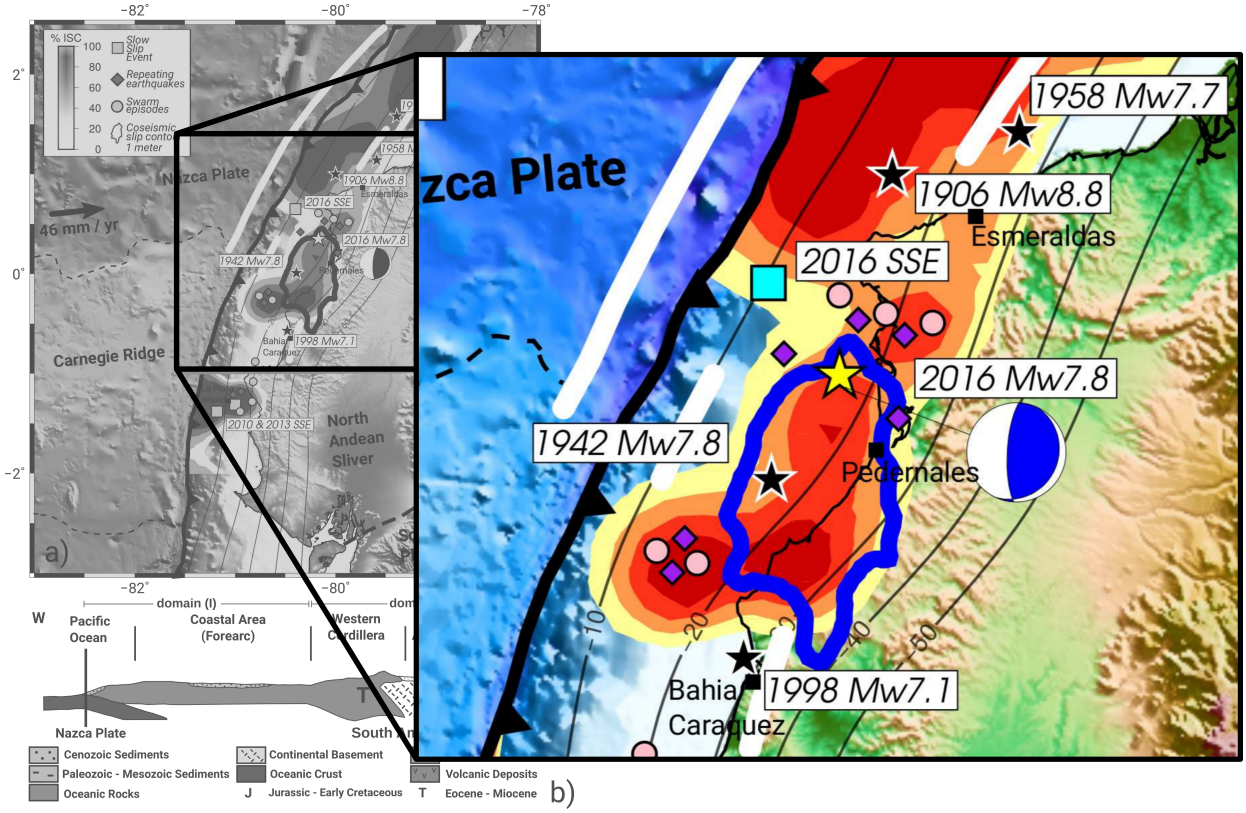

Figure 3.3: Zoom to Figure 3.1 to indicate the main characteristics (i.e. rupture, epicenter and focal mechanism) of the 2016 Pedernales earthquake. Slip model and focal mechanism were derived by Nocquet et al. (2017).

3.3 The 2016 Pedernales earthquake

On April 16th, 2016, a Mw 7.8 earthquake occurred in the central coast of Ecuador, close to the city of Pedernales (see Figure 3.1). The mainshock affected an area where large megathrust earthquakes, with magnitudes greater than 7, occurred in the past. Also, as it is shown in Figure 3.1, its occurrence correlates with a locked area of interseismic coupling derived by Chlieh et al. (2014); Nocquet et al. (2017). The focal depth estimated for the event was 17 km (Nocquet et al., 2017) and the rupture was characterized as a thrusting mechanism (see Figure 3.3) consistent with the megathrust on the plate interface.

The Pedernales earthquake ruptured an estimated area of 100 km x 40 km (Nocquet et al., 2017) and propagated along strike from north to south (Nocquet et al., 2017; Yi et al., 2018; Gombert et al., 2018). Although there are different rupture areas proposed for the 1906 earthquake (e.g. Kanamori and McNally (1982); Yoshimoto et al. (2017)), the edges of the 2016 mainshock appear to coincide with the southern boundaries of the 1906 earthquake. This segment of the subduction zone last ruptured in a Mw 7.8 earthquake in 1942 (Kelleher, 1972; Sennson and Beck, 1996). At the southern limit, the rupture coincides with the northern edge of the 1998 Mw 7.1 earthquake in Bahia Caraquez.

The 2016 mainshock led to the largest earthquake-related loss of life (668, Lanning et al. (2016)) in Ecuador since the 1987, Mw 7.1 Salado-Reventador event, which occurred in the Andean volcanic arc, killing around 1000 people (Bolton, 1991; Beauval et al., 2010). It also affected the Ecuadorian

Figure 3.4: Images from personal archive showing the destruction in the coastal Ecuadorian region: (left) Caleta de Manta, seafood market in Manta city; (center) building columns reinforced with bamboo timbers in Chone city; (right) six-storey building collapsed in Portoviejo city.

economy due to widespread destruction (see Figure 3.4) of houses, hotels and hospitals (Lanning et al., 2016).

In terms of geophysical research, the Pedernales earthquake triggered several studies for rupture characterization (Nocquet et al., 2017; Gombert et al., 2018; Yi et al., 2018), slow slip events related to the mainshock (Rolandone et al., 2018; Vaca et al., 2018) and analysis of seismic distribution and tectonics of the affected area (Agurto-Detzel et al., 2019; Meltzer et al., 2019; León-Ríos et al., 2019; Hoskins et al., 2018; Soto-Cordero et al., 2020; Koch et al., 2020; Lynner et al., 2020; León-Ríos et al., 2020).

Chapter 4

The Ecuador emergency network: Installation and data

This chapter details the collaboration triggered after the Pedernales earthquake to deliver a rapid deployment that records the unfolding aftershock sequence. As a Phd student at the University of Liverpool by that time (May 2016), I led the planning, installation, service and data collection for the UK stations deployed in Ecuador. Later, I created an aftershocks catalog with precise manually picked P- and S-onset times that was subsequently used in the staggered inversion process to obtain the velocity structure of the Ecuadorian margin. The installed network has contributed to produce several research articles which listed below:

- 1D-velocity structure and seismotectonics of the Ecuadorian margin inferred from the 2016 Mw7.8 Pedernales aftershock sequence, published in *Tectonophysics* (León-Ríos et al., 2019).
- The 2016 Mw 7.8 Pedernales, Ecuador, earthquake: rapid response deployment, published in *Seismological Research Letters* (Meltzer et al., 2019) in which I am a co-author.
- Ridge subduction and afterslip control aftershock distribution of the 2016 Mw 7.8 Ecuador earthquake, published in *Earth and Planetary Science Letters* (Agurto-Detzel et al., 2019) in which I am a co-author.
- 3D local earthquake tomography of the Ecuadorian margin in the source area of the 2016 Mw 7.8 Pedernales earthquake, submitted in *Journal of Geophysical Research* (León-Ríos et al., 2020).
- Structural Control on Megathrust Rupture and Slip Behavior: Insights From the 2016 Mw 7.8 Pedernales Ecuador Earthquake, published in *Journal of Geophysical Research* (Soto-Cordero et al., 2020) in which I am a co-author.
- Triggered crustal earthquake swarm across subduction segment boundary after the 2016 Pedernales, Ecuador megathrust earthquake, resubmitted to *Earth and Planetary Science Letters* in September 2020 and in which I am a co-author.

4.1 Emergency deployment

Although large subduction thrust earthquakes are well documented historically, occurring extensively throughout the entire South American margin, it is only over the last decade that dense monitoring seismic networks have been deployed to record the aftershock sequences of such events. This allows for highly accurate hypocentral relocations enabling detailed investigations into the physical processes occurring within the rupture zone.

Immediately after the 2016 Pedernales mainshock, an international collaboration of several institutions including; Instituto Geofísico de la Escuela Politécnica Nacional (IGEPN) from Ecuador, the French Centre d'études et d'expertise sur les risques, l'environnement, la mobilité et l'aménagement (CEREMA) and GEOAZUR institutes, Lehigh University and University of Arizona from the United States and the University of Liverpool from the United Kingdom, coordinated a rapid response effort to deploy a temporary seismic network. Within three days after the mainshock, IGEPN deployed 5 broadbands and 5 dual short period strong motion instruments in the vicinity of the epicenter of the Pedernales earthquake. Later, between 9-28 May, the institutions mentioned above installed 55 temporary inland stations comprising 35 broadbands, 14 intermediate and 6 short period seismometers. To extent the coverage region, 10 ocean bottom seismometers (OBS) were installed along the trench axis (Meltzer et al., 2019). As part of the University of Liverpool, I led the planning, installation, service and data collection of the UK portion by visiting the affected area in several occations during the first two years after the mainshock (see Figure 4.1).

The backbone of the emergency deployment is the RENSIG (Red Nacional de Sismografos) permanent Ecuadorian network (Alvarado et al., 2018) which is a mix of diverse instrumentation including CMG-3ESP, Trillium compact, Trillium 120p and TSM-1 Strong Motion instruments. The temporary network consists of: (i) short period seismometers Lennartz LE 3D-Lite recording at 100 Hz; (ii) intermediate period seismometers Güralp CMG-40T recording at 200 Hz; (iii) broadband Trillium Compact 120s, Güralp CMG-3T and Streckeisen STS-2 seismometers recording at 100 Hz (see inset in Figure 4.2). The temporary inland installation was fully operative from May 2016 to June 2017 with an in-between-spacing of $\sim$10-20 km. OBSs were recording between mid-May to mid-November in 2016 at 100 Hz. Figure 4.2 shows the spatial distribution of the full deployment including both temporary and permanent stations. Operation summary during the period May-December 2016 is shown in Figure 4.3. Finally, quality of the recorded

Figure 4.1: Images from personal archive during the stages of deployment, service and data collection of the UK portion of broadbands and short period inland stations. Installation was made between 16 May-28 May 2016. Services and data collection were carried out in August and November 2016. Finally, stations were removed in May-June 2017.

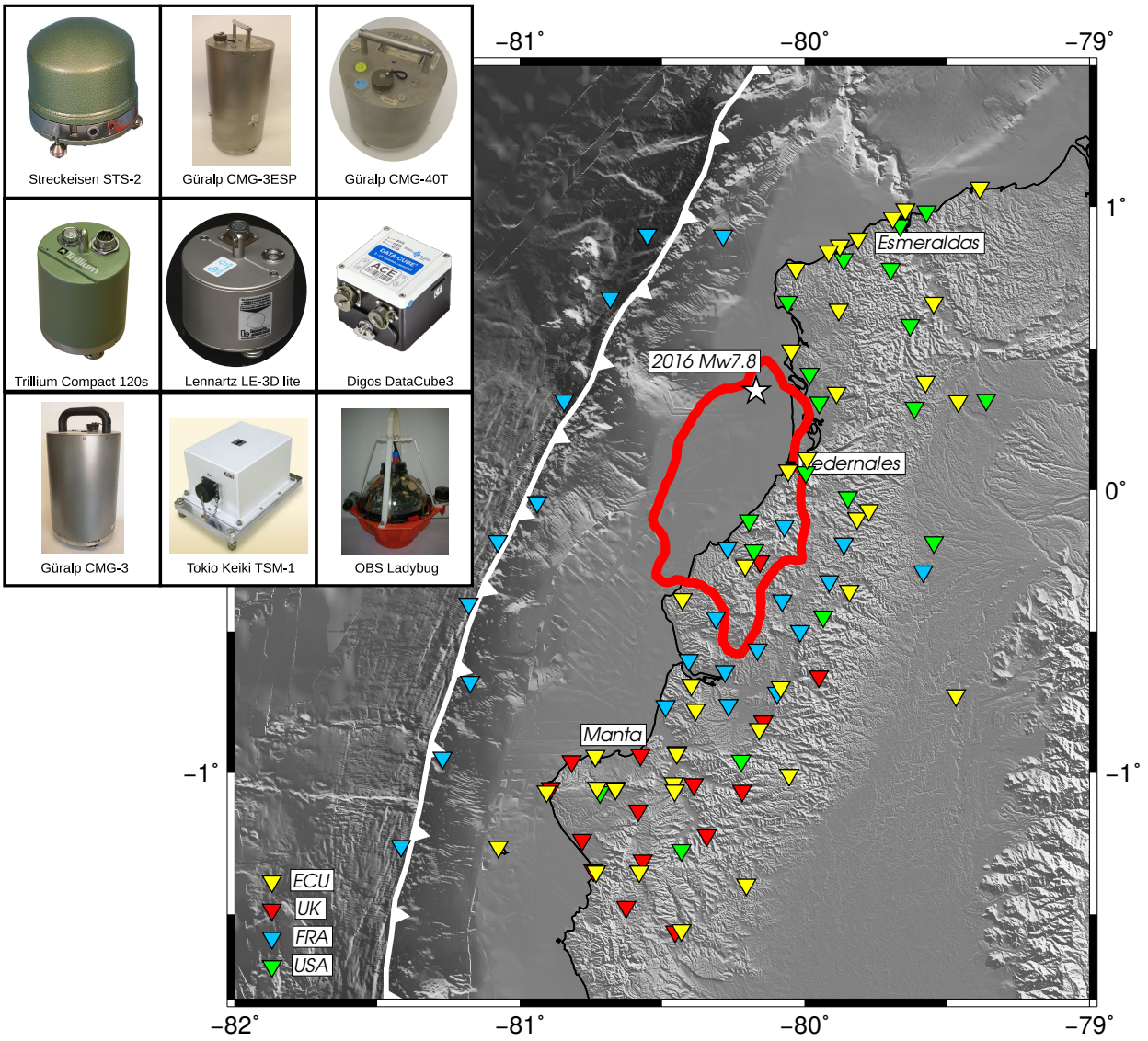

Figure 4.2: Seismic aftershock deployment. Inverted triangles represent the stations installed along the Ecuadorian margin. Yellow: backbone network including CMG-3ESP, Trillium compact, Trillium 120p, TSM-1 strong motion operated by the Instituto Geofisico de la Escuela Politecnica Nacional de Ecuador (IGEPN). Red: Broadband Trillium compact and short period Lennartz LE 3D-Lite instrumentation from the University of Liverpool, United Kingdom. Blue: intermediate period Güralp CMG-40T and OBSs from GeoAzur and IRD, France. Green: Broadband Güralp CMG-3T and Streckeisen STS-2 from IRIS-PASSCAL deployed by the University of Arizona and Lehigh University, United States. Most of the instruments deployed on site were recording at 100 Hz. White star is showing the epicenter of the 2016 Mw 7.8 Pedernales earthquake. Coseismic slip contour in red solid line was derived by Nocquet et al. (2017). Inland and seafloor topography was derived by Michaud et al. (2006). Trench data obtained from Collot et al. (2005).

traces is shown in Figure 4.4 by a representative sample of events in the northern, central and southern part of the study area.

4.2 Dataset and Processing

The initial catalog for the Pedernales sequence was provided by the IGEPN which included all the events detected by the RENSIG network (see Figure A1 in Appendix 1). Later, using an automatic location procedure over the Ecuador emergency network, Agurto-Detzel et al. (2019) derived a new catalog with more than 7000 events.

Figure 4.3: Summary for the station operation during the period from May-December 2016. Data retrieved from GeoAzur monitoring interface (David Ambrois and Jerome Chez) to check the available data of deployed networks.

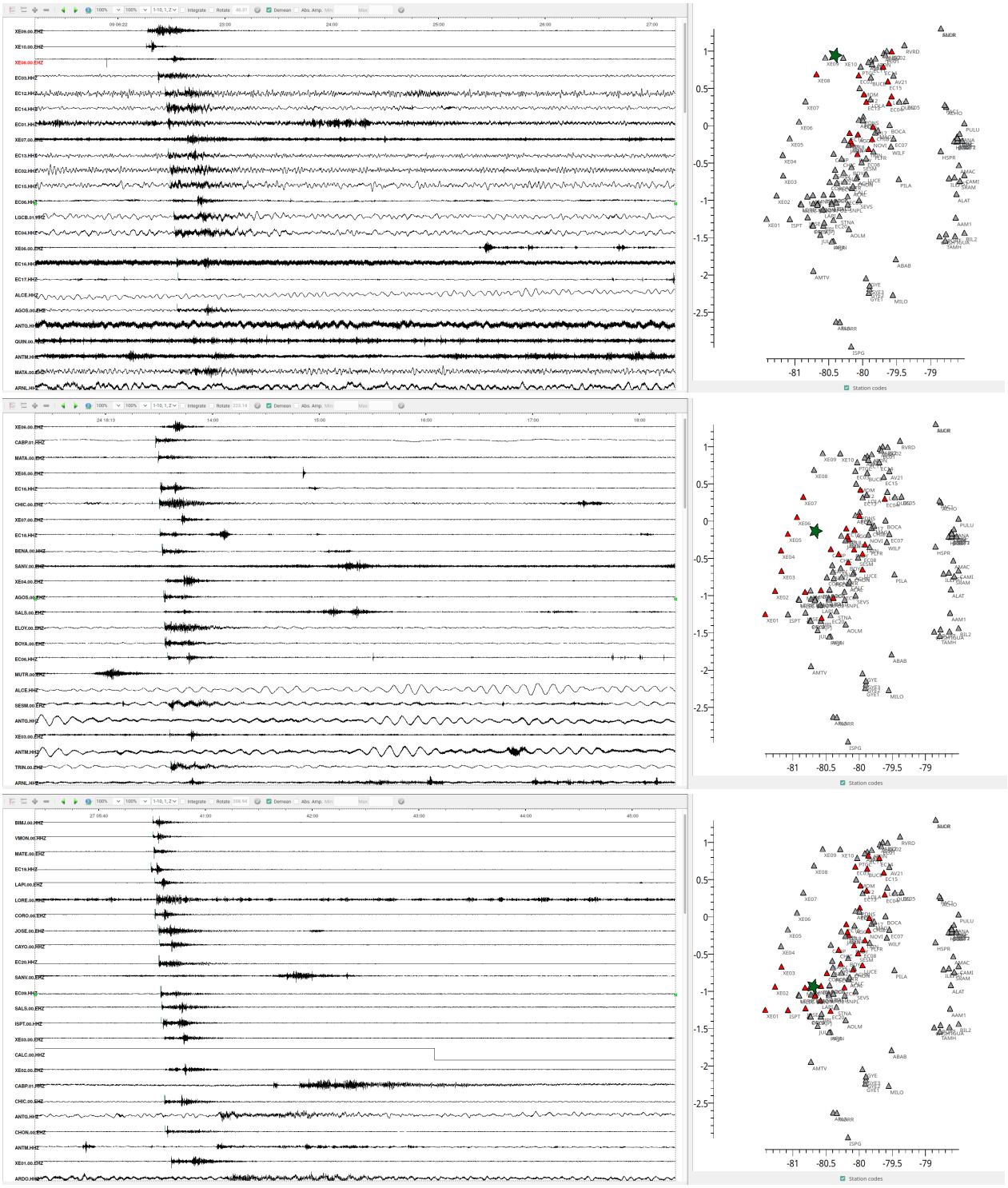

Figure 4.4: Representative sample for trace quality of three events recorded by our network in Ecuador. A map view is available for epicenter (green stars) and station distribution (gray triangle). Stations in red indicate detected onset observations. (top) Event in the northern part, offshore Esmeraldas occurred at UTC 2016.07.09T14:43:32; (center) Event in the central part, offshore Cabo Pasado occurred at UTC 2016.06.24T18:13:20 and (bottom) event in the southern part, close to Manta city occurred at UTC 2016.10.27T05:40:24.

Based on both catalogs, we created a high quality dataset to be used for the 1D inversion process. We first selected aftershocks with Ml > 3.5 located in the vicinity of the temporary network (see Figure A1, the latter in Appendix 1). To ensure optimal localizations we focused in the time period

when the whole network, with both OBS and inland stations, was recording. From this subset, P- and S-wave arrival times were manually picked for 345 aftershocks using the Seismic Data Explorer (SDX) software package. The events were located based on an average 1D velocity model derived from Font et al. (2013); SDX utilizes a modified hypo71 algorithm for hypocenter location (Lee and Lahr, 1972). Following the procedures from Agurto et al. (2012) and Hicks et al. (2014), we assigned pick error categories, referred as weights, from 0 to 4 to describe the quality of the selected arrival times. Each weight corresponds to the following time uncertainties: Weight 0 (< 0.04 s); Weight 1 (0.04 –0.1 s); Weight 2 (0.1 –0.2 s); Weight 3 (0.2 –1 s); Weight 4 (> 1 s). Figure 4.4 shows an example of the SDX visualization for three events.

To increase the resolution during the construction of our 3D velocity model, we incorporated more events with Ml > 2.5 by following the same procedure previously mentioned. In total, we analysed more than 800 events. By adding an azimuthal gap and number of observations criteria, these number were reduced to 227 events for the 1D velocity model and 568 aftershocks for the 3D modeling stages. Chapters 5 and 6 provide further details for the one- and three-dimensional stages, respectively.

Chapter 5

Minimum 1D velocity model

This chapter includes the methodology, results and interpretation of the minimum 1D velocity model derived for the Ecuadorian margin affected by the 2016 Pedernales earthquake. The text included in the following sections are part of the article:

- 1D-velocity structure and seismotectonics of the Ecuadorian margin inferred from the 2016 Mw7.8 Pedernales aftershock sequence, published in *Tectonophysics* (León-Ríos et al., 2019)

5.1 State-of-the-art at the Ecuadorian margin

Currently, the available velocity models for the Ecuadorian margin are usually focused in small areas or have limited resolution due to the lack of instruments monitoring the offshore and coastal portion of the country; they are also affected by along strike heterogeneities observed in the region. At present, the national network of seismographs of the Geophysical Institute (RENSIG) from IGEPN uses a five-layer model (called ASW; for detailed values see Font et al. (2013)) and is used by the IGEPN for locating tectonic events in Ecuador. It, therefore, results in large errors in hypocenter location, especially regarding depth of subduction related seismicity (See Supplementary Material A1 in Appendix 1). Font et al. (2013)) built an a-priori three-dimensional P-wave velocity model for the Ecuadorian subduction margin (4°N –6°S, 83°W –77°W), obtained via a joint compilation of marine seismics, gravimetric data, geological observations and seismicity of the region. The model is an improvement for the forearc and provides better hypocentral solutions for the coastal area but has limited capabilities due to the absence of an S-wave velocity model. Gailler et al. (2007) inverted wide-angle seismic data to describe deep structures present offshore of the Ecuadorian –Colombian border. In the same area, Agudelo et al. (2009) also improved the structural model using a combined data set of multichannel seismic reflection and wide-angle data. Cano et al. (2014) provide a 3D velocity model encompassing the rupture of the 1958 earthquake. Both models provide insights about offshore velocities.
Further to the south of our study area, Calahorrano (2001) developed a velocity model using marine seismic experiments representing the area close to the Gulf of Guayaquil. However, all three models are located outside of the Pedernales rupture area and outside the area covered by our temporary

seismic array. Finally, Graindorge et al. (2004) analyzed the velocity structure in the CR area using onshore and offshore wide-angle data to calculate a two-dimensional model. Although our array covers a portion of the CR, this model is not appropriate for the whole area covered by the array due to the anomalous structure of this bathymetric feature.
As it was mentioned in the introduction, there is still no consensus on a representative 1D velocity model and therefore an improved regional model will provide a better constrained seismic velocities in the area and, the foundation and starting model for a detailed 3D seismic imaging.

5.2 Building the model

From the manually picked catalog, we further filter to ensure only the highest quality events remain for the minimum 1D velocity model inversion. We selected earthquakes with at least 10 P- and 10 S-onset observations and an azimuthal gap < 200°. In total we obtained a dataset of 227 events with an average of 21 and 17 P- and S-onset times respectively, which contains 4939 P-phases and 3931 S-phases (see Supplementary Material A2 in Appendix 1).
To minimize the influence of strong topography changes and avoid bias due to the depth of the OBSs, we followed the strategy described by Husen et al. (1999) and Hicks et al. (2014) and set station elevation equal to zero. Station correction terms therefore account for both, the relative elevation and the site-specific velocity differences. Station correction terms were strongly damped (damping = 1000) during the Vp inversion, allowing for greater initial exploration of the Vp parameter space. For the Vs inversion, the damping was decreased (damping = 20), this allows the station-delay terms to absorb errors due to the velocity fluctuations near the stations.
We selected five starting models (see Supplementary Material A3 in Appendix 1) to cover a wide range of plausible cases: (1) the average model derived from Font et al. (2013), selected as it covers our entire study area with a 3D regional model, (2) an average offshore model based on previous studies by Gailler et al. (2007) and Agudelo et al. (2009), and (3-5) modified versions of the ASW model, used by IGEPN (Font et al., 2013). For models 3-5, we vary the Moho depth between the range of 40 to 60 km. To cover the entire range of feasible velocity models, we created 1000 random variations of each reference velocity model, sampling from a uniform distribution with bounds ± 0.5 km/s of the reference model velocity. We, therefore, explore 5000 starting models in total, derived from the five classes of models. From the 5000 starting models, the P-wave velocity model with the lowest overall misfit to the travel time picks (RMS 0.335 s) is assumed as our best Vp representation. The density plots in Figure 5.1d and 5.1e demonstrate how the best 200 solutions for the inverted Vp and Vs models have a clear convergence towards the best solution between 7.5 km and 40 km depth. The shallowest layers (down to 7.5 km) do also exhibit a convergence towards a minimum velocity solution, however, due to a lack of events occurring in this region, the solution shows a slightly wider range of possible velocities. For the deeper layers (> 40 km), absolute velocities cannot be constrained due to the lack of data and therefore several cluster of solutions can be observed. To detect picking outliers and to estimate an average Vp/Vs ratio for the region, we performed Wadati analysis (Wadati and Oki, 1933), displayed in Figure 5.1a. Onset times show a clear trend for (ts –tp) as a function of tp, a linear trend fit provides a Vp/Vs ratio

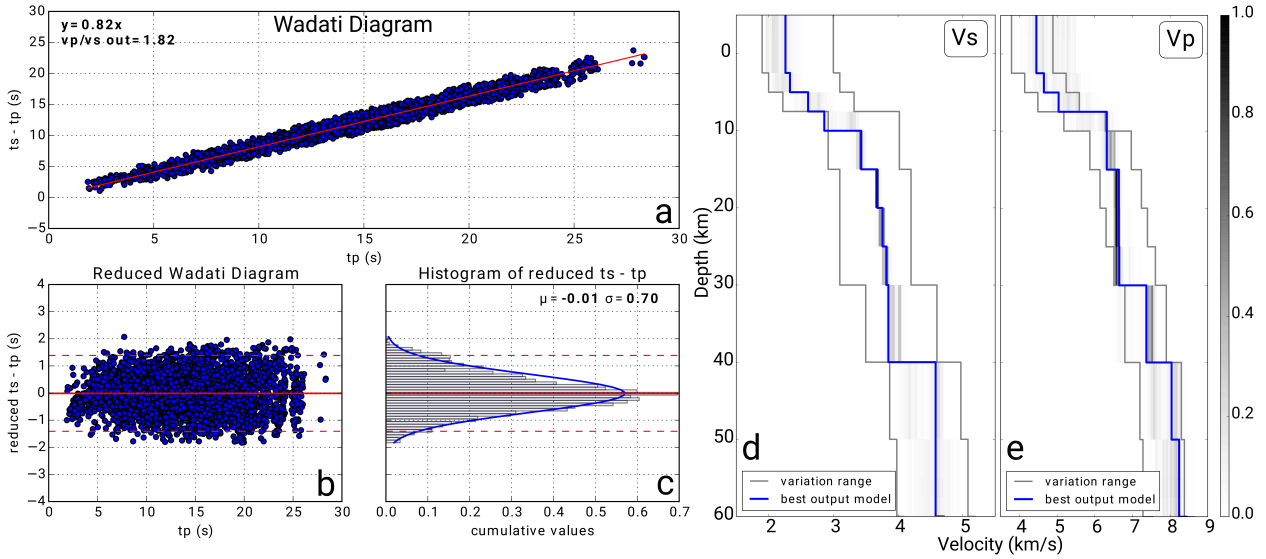

Figure 5.1: (a) Wadati Diagram (Wadati and Oki, 1933) used to compute the observed Vp/Vs ratio using all the available onsets. Red line shows the linear fit for the data which indicates a Vp/Vs ratio of 1.82. (b) Reduced Wadati Diagram used to remove outliers from onset times picked. $|Vp/Vs| > 2\sigma$ was used as a cutoff value. Solid red line: y = 0. Segmented red line: y = $\pm$ 2σ. (c) Reduced ts - tp histogram showing the distribution of picks in terms of its reduced time. Solid red line: y = 0. Segmented red line: y = $\pm$ 2σ. (d) and (e) Density plot for S-wave and P-wave velocity model, respectively, showing the best 200 solutions. Solid blue line shows the solution with the lowest rms. Gray lines are the perturbation range for each phase. Colorbar indicates the normalized hit count on each output model.

value of 1.82. A reduced Wadati diagram was also used to have a better control on the outliers in our dataset. Onsets greater than 2σ from the Vp/Vs trend were removed (see Figure 5.1b). The final dataset of arrival times is represented in a histogram in Figure 5.1c with a mean of ts-tp of 0.01 s and a variance of 0.70 s^2.

Finally, using our best Vp model and the Vp/Vs ratio (1.82) obtained via Wadati analysis, we built an initial 1D S-wave velocity model. The inversion for the optimum S-wave velocity model follows the same procedure as for the P-wave velocity model. We perturbed the S-wave velocities of the starting model within a range of $\pm$ 0.5 km/s, creating 1000 models where both P- and S-phases were simultaneously inverted for. In this step, we fixed the Vp velocities to avoid changes in the previously obtained Vp model by S-wave observations. The solution with the lowest RMS (0.303 s) was accepted as our final S-wave model along with the final set of station corrections and hypocentral locations. By using a Monte Carlo approach for selecting the starting model, we mitigate the dependency of the final model from starting model as we sample a much larger model space.

5.3 Regional Moment Tensors

A significant portion of the aftershocks are related to the megathrust faulting displaying reverse solutions consistent with the slip of the plate interface (Agurto-Detzel et al., 2019). We focus our RMT analysis on the seismicity recorded throughout offshore Bahia Caraquez and Cabo Pasado which exhibits various faulting mechanisms. In this area, we observe events distributed close to

the trench (5 km –10 km), however, due to the trade-off between hypocentral depth and origin time, depth location uncertainties in this region are larger than the average. These events could, therefore, be located at the interface, in the upper or in the downgoing plate. To better constrain the focal depth parameter for events in this region, we calculated RMT solutions for 14 events by performing a full waveform inversion using the isola package (Sokos and Zahradnik, 2008; Sokos and Zahradník, 2013). We analyzed events reported by IGEPN with Ml > 4.0. The location was fixed to the epicentral locations obtained from our relocation process with VELEST, and the depth is allowed to vary. Green′s functions are calculated from a simplified version of our minimum 1D model where the shallowest 8 layers are merged into 4 layers (see Supplementary Material A3 in Appendix 1). Seismic records were bandpass filtered between 0.04 and 0.09 Hz before the inversion, and between 4 to 10 broadband stations were used for the inversion process of each event.

5.4 Results

Our final minimum 1D model, represented by 12 layers, with P- and S-wave velocities and the Vp/Vs ratio are given in Table 5.1 and shown in Figure 5.2. The model is well constrained between 7.5 km and 40 km, where most of the seismicity is concentrated (see Figure 5.2). Although, most of the ray paths are concentrated in the shallower layers, we observe some rays down to 40 km depth, which help us to constrain the average of the oceanic and continental Moho depth. At shallower depths, the lack of crustal events (< 7.5 km depth) means we are not able to obtain reliable absolute velocities due to the trade-off with station corrections; at greater depths (30 km –40 km) the ray path distribution still shows rays passing through, however at depths > 40 km the limited extend does not allow a robust estimation of the average velocities.
The obtained model shows a Vp that fluctuates between 4.45 km/s and 5.04 km/s, in the top layers (down to 7.5 km). From 7.5 km depth to 25 km, Vp consistently increases from 6.3 km/s to 6.6

Depth (km)	Vp (km/s)	Vs(km/s)	Vp/Vs
-5.00	4.45	2.26	1.97
2.50	4.65	2.32	2.00
5.00	5.04	2.59	1.95
7.50	6.32	2.90	2.18
10.00	6.32	3.42	1.85
15.00	6.64	3.69	1.80
20.00	6.64	3.76	1.77
25.00	6.65	3.80	1.75
30.00	7.37	3.81	1.93
40.00	8.04	4.64	1.73
50.00	8.24	4.64	1.78
60.00	8.45	4.71	1.79

Table 5.1: Minimum 1D model. Absolute velocities and Vp/Vs ratio are listed in terms of depth.

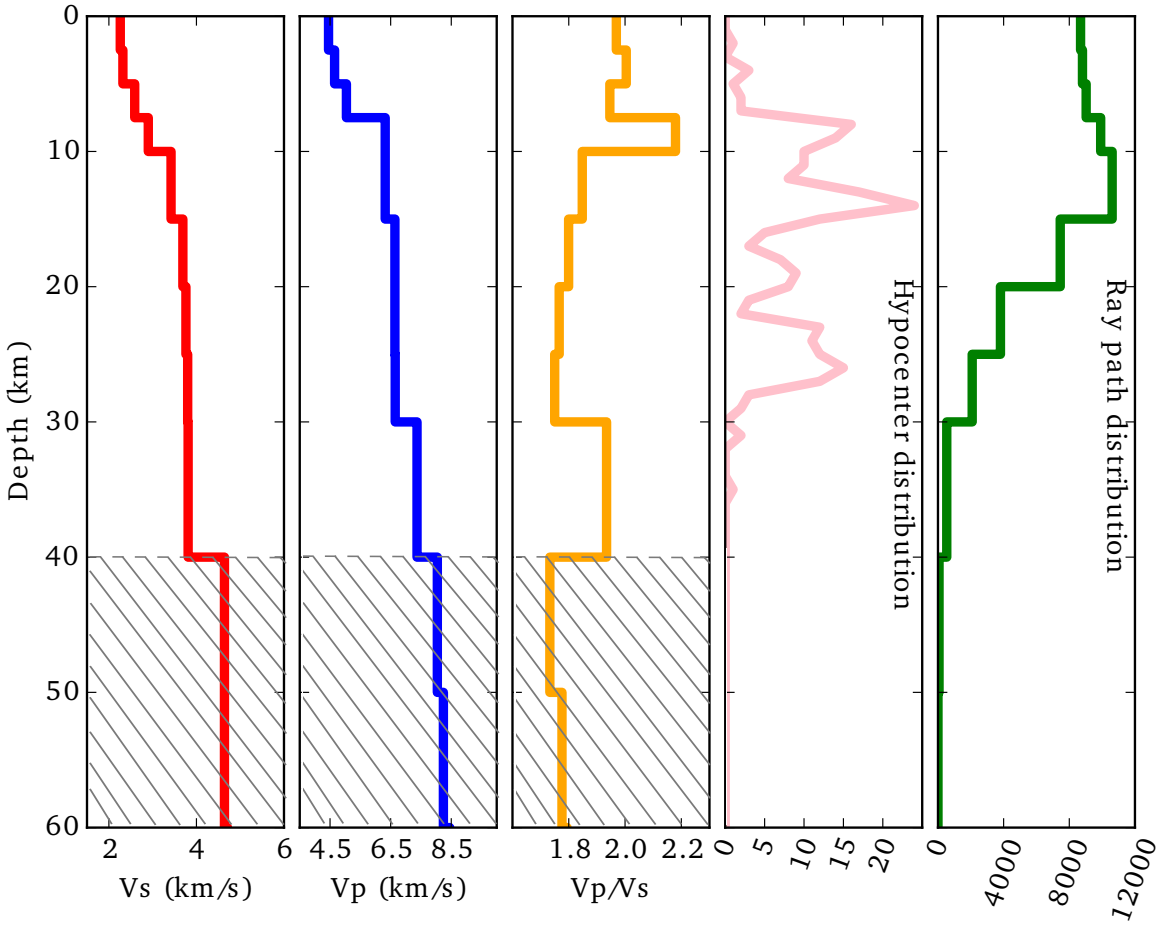

Figure 5.2: Final 1D velocity model showing the absolute Vp (solid blue line) and Vs (solid red line) velocities, Vp/Vs ratio (solid orange line) and a histogram of the seismicity distribution with depth. Dashed area indicates the area where our minimum 1D model is unconstrained. Velocity values for depths greater than 40 km were derived by Font et al. (2013) and were included in our initial reference model.

km/s. Between 30 km – 40 km the constant increase of Vp (from 7.37 km/s at 30 km to 8.04 km/s at 40 km) suggests an area of transition from crust to mantle. At 40 km Vp reaches 8.04 km/s, which can be related with continental upper mantle velocities. Finally, the absence of data between 40 km and 60 km depth, does not allow us to resolve the P-wave velocity, so the resulting values are mainly influenced by our reference model derived by Font et al. (2013) (see Figure 5.2).
Vp/Vs ratio shows a weighted arithmetic mean of 1.82 for the whole model. In the top layers (down to 7.5 km depth) we find a high Vp/Vs ratio that varies from 1.97 to 2.18. At 10 km depth, the Vp/Vs ratio decreases to 1.85 down to 30 km depth where it rises to 1.93. The Vp/Vs ratio is not well resolved at depths greater than 40 km as we do not have enough data to constrain that area (see Figure 5.2).
Statistics for the inversion also show the robustness of our model. Arrival time residuals were classified according to the weights described in the previous section. Histogram plots in Figure 5.3 indicate that most of the P- (99 %) and S- (88 %) phase picks are classified between weights 0 and 1. For high quality P-wave onsets (weight 0 and 1), the standard deviations of residuals is 0.24 s and 0.26 s, respectively. For the S phase, the deviation varies from 0.48 s, for weight 0, to 0.52 s for

weight 1. Observations for each station display residuals with a normal distribution concentrated between -1 to 1 seconds (See Supplementary Material A4 in Appendix 1). Overall, the obtained catalog has a variance of 0.084 s^2, which is above the variance based on the accuracy provided by the manual picking of 0.027 s^2 indicating that we are not overfitting our onset time data.

Our new minimum 1D-velocity model was then used to relocate the 227 manually-picked events (See Supplementary Material A5 in Appendix 1 for comparison with the original locations). To test the accuracy of the resulting hypocenters, we performed a stability test by randomly perturbing hypocenters starting locations by between 7.5 km –12.5 km in latitude, longitude and depth. We then relocated the events using our minimum 1-D velocity model and station corrections. The location of the recovered seismicity shifts only marginally respect to the original positions, leading to an estimation of the relocation uncertainties around 1 km in latitude and longitude, and 2.7 km in depth (See Supplementary Material A6 in Appendix 1). Overall, the relocated seismicity displays an average error of 1.38 km and 1.57 km for the horizontal and vertical component, respectively. As hypocentral uncertainty is shown to increase with distance offshore, we separately calculate the location errors for the offshore seismicity. For this data subset, we obtain average uncertainties of 1.53 km for the horizontal axis and 2.15 km for the vertical axis.

The relocated aftershocks are shown in Figure 5.4. The seismicity is distributed between 5 –10 km to 100 km eastward of the trench and between 2 km to 35 km in depth. The most important features are as follows:

(1) We observe that our epicentral distribution for the analyzed aftershocks are in agreement with other related studies (e.g. Meltzer et al. (2019), Agurto-Detzel et al. (2019)). We find that events with local magnitude greater than 3.5 are generally distributed outside the coseismic slip area of the 2016 Pedernales mainshock and skew towards the trench.

(2) Most of the seismicity along profiles AA′ and BB′ is located along the plate interface. Slab1.0 (Hayes et al., 2012) is used as a reference in Figure 5.4, however a comparison between both Slab1.0 (Hayes et al., 2012) and Slab2.0 (Hayes et al., 2018) is shown in Supplementary Material A7 in Appendix 1. The northern profile AA′ demonstrates the differences between the interface for both models, in the region, Slab2.0 is relatively deeper than the Slab1.0 interface; the located aftershocks are distributed between both Slab1.0 and Slab2.0. These relative changes in extensively used slab models further highlight the complexities the Ecuadorian margin along strike.

(3) Clustered activity in the overriding plate can be observed in both northern (AA′) and southern (BB′) profiles.

(4) Profiles AA′ and BB′ (see Figure 5.4) show that a portion of the aftershocks reach the trench. This has been demonstrated as a robust feature due to specific bias testing of the offshore relocated seismicity.

Although, the formal locations errors stated before are less than 3 km in depth, absolute locations errors can be significantly larger. To identify whether the events distributed close to the trench are located in the subducting or the overriding plate, we calculated RMT solutions to better constrain the hypocenter depth. We focus here on the offshore seismicity located close to profile BB′ and calculated 14 RMTs. This is an area where Agurto-Detzel et al. (2019) reported a single

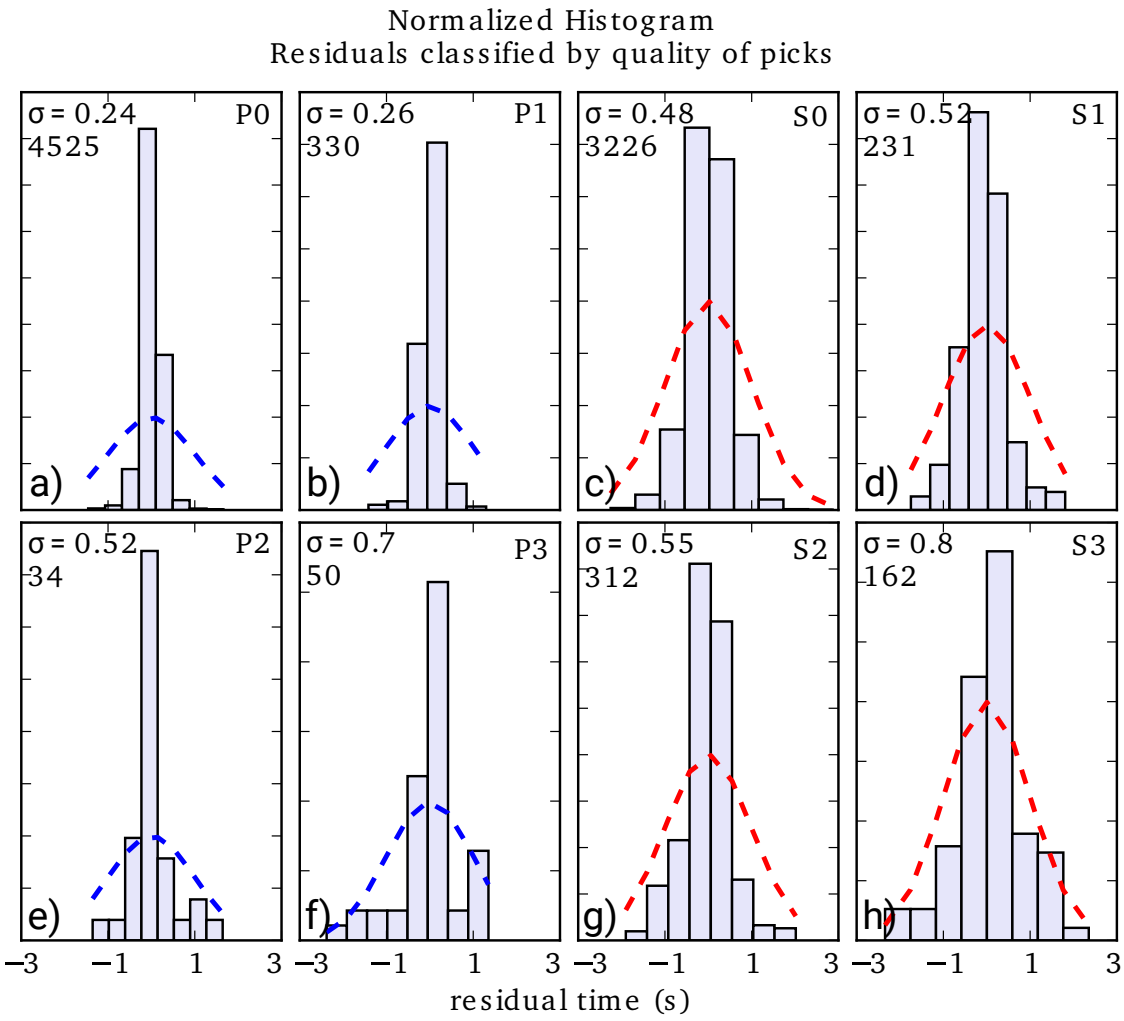

Figure 5.3: Histograms for the residuals obtained after the inversion of both Vp and Vs velocities. Plots were classified according to the quality of picks indicated in the top right corner. Each weight corresponds to the following time uncertainties: Weight 0 (< 0.04 s); Weight 1 (0.04 –0.1 s); Weight 2 (0.1 –0.2 s); Weight 3 (0.2 –1 s); Weight 4 (> 1 s). Segmented blue and red lines represent the fit of the data. Standard deviation and number of observation are displayed on the top left corner of each plot.

anomalous strike-slip event at about 10 km depth. Figure 5.4 shows the solutions superimposed over the relocated aftershock activity. Additional information about the waveform inversion fit and comparison with other MT catalogs are shown in Supplementary Material A8, A9 and A10 in Appendix 1. We also compare the difference between depths obtained from the velocity model inversion and isola. Events with depths between 5 km and 15 km, based on arrival times, show a small difference in their depth locations in comparison to the RMT solutions. For the offshore seismicity located with depths > 15 km using travel times, the RMT centroid depths are shallower than those of the hypocenters (see Table 5.2 and Supplementary Material A10 in Appendix 1). The majority of the aftershock RMTs for the Pedernales segment exhibit a thrust mechanism related to the subduction interface (e.g. Agurto-Detzel et al. (2019)). However, we also find events that display extensional and strike slip faulting mechanisms, distributed along the marine forearc. Table 5.2 summarizes our results listing the centroid information, nodal planes, magnitude, variance reduction and double-couple percentage.

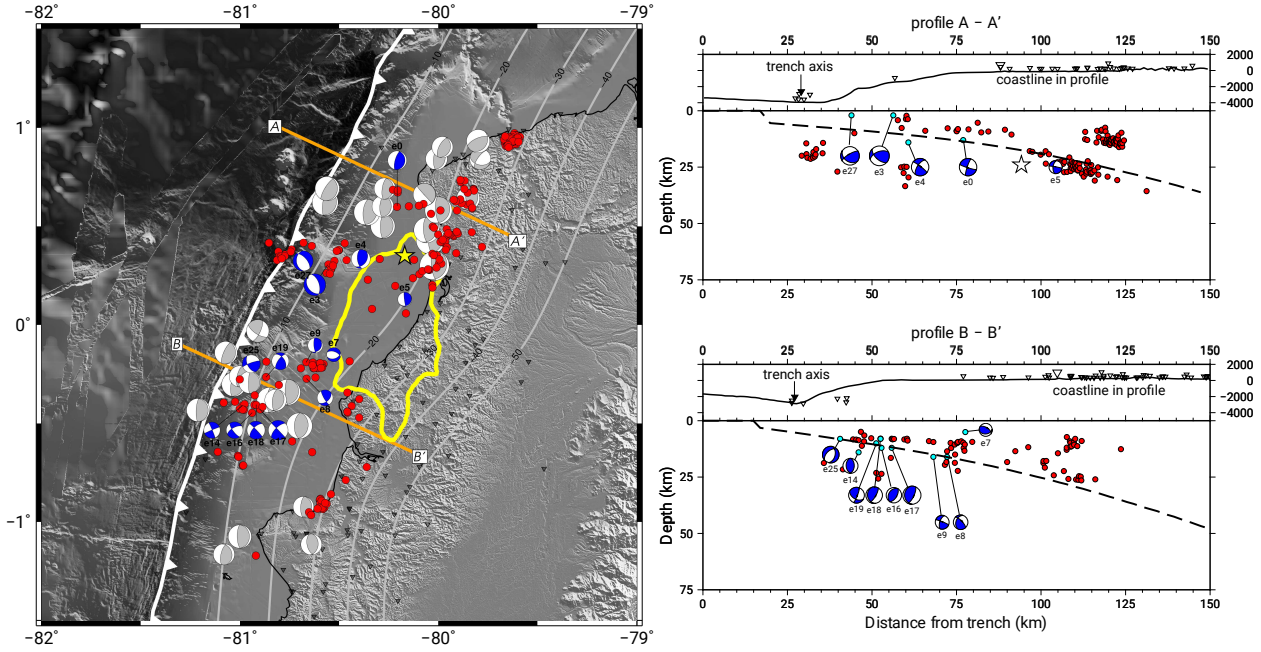

Figure 5.4: Mapview and cross sections, 60 km wide, of the relocated seismicity. Red circles indicate the aftershock locations after the inversion with VELEST. Blue beach balls represent the RMT calculated using isola superimposed over the gCMT catalog in gray. Star shows the location of the 2016 Mw 7.8 Pedernales earthquake. Slab1 from Hayes et al. (2012) is being used as a reference for the in-depth distribution. Inland and seafloor topography from Michaud et al. (2006). Coseismic slip contour derived byNocquet et al. (2017). Inland and seafloor topography from Michaud et al. (2006). Trench data obtained from Collot et al. (2005). Slab 1.0 km depth contours from Hayes et al. (2012) are shown in gray lines.

#	Lat (°)	Lon (°)	Centroid depth (km)	Arrival times depth (km)	Strike	Dip	Rake	Mag (Mw)	Var (%)	DC (%)	ID	Date
1	0.6330	-80.2077	13.00	8.24	196	72	94	4.4	80	82.3	e0	2016-06-06 16:45:08
2	0.2940	-80.5730	2.03	4.42	342	57	-79	5.1	68	89.5	e3	2016-06-01 10:05:16
3	0.3740	-80.4910	14.03	11.91	174	60	65	4.4	86	61.2	e4	2016-05-31 15:48:11
4	0.1295	-80.1691	25.03	25.53	173	84	81	3.3	28	63.8	e5	2016-05-30 05:48:56
5	-0.2000	-80.5770	5.00	18.37	290	54	-66	3.3	13	71.1	e7	2016-06-21 04:40:24
6	-0.2718	-80.6639	16.03	12.54	49	49	164	3.7	13	31.5	e8	2016-06-02 00:18:59
7	-0.1880	-80.6652	16.03	18.99	175	74	74	3.5	44	62.5	e9	2016-06-01 02:12:22
8	-0.4079	-80.9864	14.02	8.14	247	88	177	3.8	45	76.0	e14	2016-07-07 17:10:13
9	-0.4444	-80.9390	8.03	29.99	143	74	-27	3.9	18	99.1	e16	2016-07-08 04:41:34
10	-0.4268	-80.8981	12.03	7.88	316	89	24	4.6	66	55.6	e17	2016-07-08 07:03:48
11	-0.4047	-80.9177	12.03	22.99	316	86	29	4.2	61	43.3	e18	2016-07-08 07:35:15
12	-0.2629	-80.8675	10.03	22.35	324	50	28	4.0	57	10.4	e19	2016-07-10 06:44:34
13	-0.1967	-80.9427	8.03	-	250	80	35	4.2	23	70.0	e25	2016-05-05 16:06:40
14	0.3242	-80.6818	2.03	4.16	318	61	-110	4.7	57	65.9	e27	2016-06-01 15:00:51

Table 5.2: Summary of results for the obtained RMT. Depths calculated based on arrival times inversion were included for comparison.

5.5 Discussion

Velocity model

Figure 5.2 shows the best 1D velocity model. The histograms show depth distribution of the aftershock seismicity and help to demonstrate the resolution of our model at different depths. Although a more in-depth interpretation requires at least a 2D velocity model, our obtained 1D velocity model allows us to observe and discuss depth ranges and to first order the velocity

structure with depth. High Vp/Vs ratio obtained in the shallow layers can be related to hydrated sediments, non-consolidated soils and/or fractured oceanic crust (Peacock, 2001; Hacker et al., 2003; Kato et al., 2010; Pasten-Araya et al., 2018). The values in this section (up to 2.2 at 7.5 km depth) may reflect an upward migration of fluids coming from the dehydration of sediments subducting within the Nazca plate. Similar cases have been discussed in other areas such as northern Chile (Husen and Kissling, 2001), New Zealand (Barnes et al., 2010), Sumatra (Collings et al., 2012) and Costa Rica (Bangs et al., 2015). As we are dealing with P- and S- onsets coming from both OBS and inland stations, in the depth range between 10 km and 40 km, the subduction process of the Nazca plate descending beneath the South American plate produces an overlapping of velocities from both plates which do not allow us to address each plate individually in a one-dimensional model. However, there is a constant increase in velocities for both P- and S-wave indicating more consolidated rocks. We also identify another increase in the Vp/Vs ratio (Vp/Vs = 1.90) around 30 km depth. A change in Vp/Vs ratio at ∼30km depth agrees with the findings of Hacker et al. (2003) and Bloch et al. (2018) who associated these characteristics with the dehydration of the subducting oceanic plate. Between 30 km –40 km it is not possible to observe a sharp contrast. However, due to the rapid increase of Vp we suggest a transitional area where the oceanic Moho could be located. At depths greater than 40 km, Vp reaches values > 8 km/s that can be associated with velocities of the upper mantle (Gailler et al., 2007; Font et al., 2013; Araujo, 2016).

Station correction terms were also calculated in the inversion. Figure 5.5 shows the delays obtained for both P- and S-wave onsets. EC16 was used as a reference station because of itscentral location along the array and large number of observations (total= 384, P= 214, S=170). For the P-delay times, the standard deviation for all stations shows that values are concentrated around 0.50 s. Delays for the S phase show a distribution around 0.85 s. In both cases, the obtained values are coherent within the study region following a west to east change of sign that moves from negative to positive. This change is mainly associated with two factors: (1) The eastward dipping of the subducting Nazca plate that produces large residuals in the inversion as VELEST maps the 2D structure into the station correction terms; (2) the variations in topography of the area, from around 3000 meters below sea level at the trench to 700 meters above sea level in the coastal range. If we consider the difference in elevation of the array, a geological interpretation will only be valid for the inland stations as the reference station (EC16) is located in this area, and the delay in the OBS can mainly be explained due to the abrupt changes in topography from sea level to the trench (∼ 4000 m depth).

Taking this into account, the difference in elevation for the inland seismic stations range from sea level for stations installed close to the coast to 688 m for the stations deployed at the base of the coastal range. Station correction terms in Figure 5.5, especially for the S-phase, show a NE-SW variation in sign from negative to positive which might be related with changes in the geological conditions of the area. Those changes coincide with the Jama Fault System (JFS) mapped in coastal Ecuador (Michaud et al., 2006) and can be attributed to differences in the properties on both sides of the fault. Along the coast, it is possible to find Cretaceous formations (∼89 Ma, Luzieux et al. (2006)) with rocks from the oceanic crust that were accreted onto the margin and

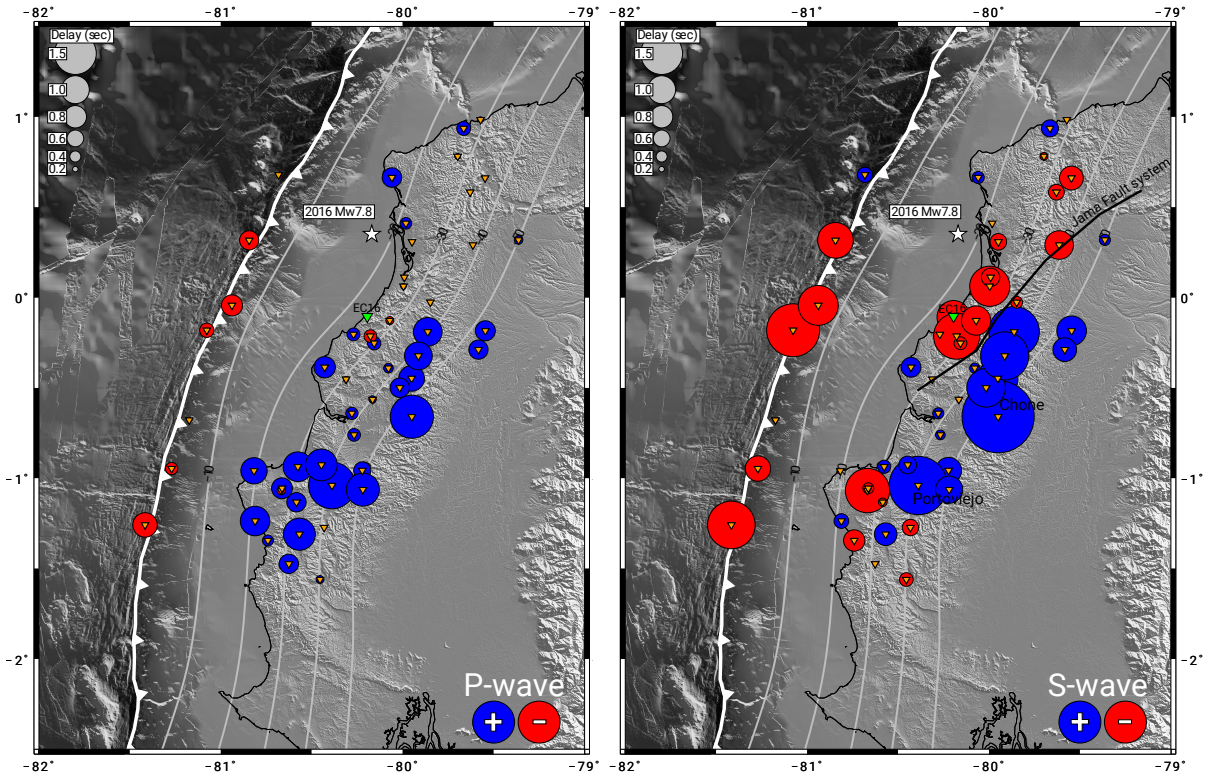

Figure 5.5: Map with station corrections for P- (right) and S- (left) phases obtained after the 1D inversion. Inverted green triangle represents the reference station EC16. White star is showing the epicenter of the 2016 Mw 7.8 Pedernales earthquake. Inland and seafloor topography from Michaud et al. (2006). Trench data obtained from Collot et al. (2005) Slab 1.0 km depth contours from Hayes et al. (2012) are shown in gray lines. Jama Fault System (JFS) trace extracted from Reyes and Michaud (2012).

could explain the negative delay in station terms. To the east side of the JFS, less consolidated formations such as conglomerates, volcanic sediments and alluvial formations from the Miocene, Pliocene and Quaternary, respectively, were mapped (Bristow, 1977; Cantalamessa and Di Celma, 2005) and can be correlated with the positive delay observed in our inversion. This difference in the geological structures is also consistent with the observation that cities far from the epicenter (> 100 km) suffered severe damage due to site effects such as Portoviejo and Chone where the vertical component of PGA reached up to 1.01 m/s^2 and 1.72 m/s^2 (IGEPN, 2016) and the delay terms for the S-phase calculated were 2.08 s and 2.57 s, respectively. The role of the fault system in the seismicity of the Central Coastal Ecuadorian margin will be discussed in detail in the next section.

Aftershock distribution

The majority of our relocated events with local magnitude greater than 3.5 are surrounding the coseismic slip area determined by Nocquet et al. (2017). This type of aftershock distribution concentrated on the updip part of the rupture has been previously observed in other megathrust earthquakes along the South American margin such as the Mw 8.8 Maule 2010 earthquake (Rietbrock et al., 2012) and the Mw 8.2 Iquique earthquake (León-Ríos et al., 2016).
The distribution of our relocated aftershocks along the margin are consistent with the observations

from Meltzer et al. (2019), Agurto-Detzel et al. (2019) that show seismicity streaks aligned perpendicular to the trench (see Supplementary Material A11 in Appendix 1). The seismicity distribution during the interseismic cycle (Font et al., 2013) is similar to the aftershock sequence of the Pedernales earthquake and suggests that this behavior could be a regular feature of the Ecuadorian subduction zone (see Supplementary Material A11 in Appendix 1).
Cross sections AA′ and BB′, in Figure 5.4, show that the depth distribution of the events is consistent with Slab1.0 from Hayes et al. (2012). While the northern section is in a good agreement with the projection of the slab at distances greater than 50 km eastward from the trench, the southern profile shows seismicity that could indicate a shallower plate interface (see profile BB′ in Figure A7 in Appendix 1). The subduction of the CR helps to explain this distribution due to the addition of a more buoyant oceanic crust which causes the raising of the seismogenic interface zone. This has been previously proposed by Collot et al. (2004) and Gailler et al. (2007) using active seismic methods in the forearc region of the Ecuadorian margin.
It is also possible to identify clustered seismicity in both sections, north and south, that are located in the overriding plate. This type of activity might be caused by the activation of crustal faults due to changes in Coulomb stress in the area surrounding the coseismic slip (e.g. Ryder et al. (2012)).
As previously mentioned, the aftershock seismicity, located in the northern profile AA′, occurs very close to the trench, up to ∼5 km –10 km, which we confirmed using the OBS stations offshore. Usually, seismicity along subduction margins does not extend up to areas close to the trench axis. Although this phenomena has been previously observed when an accretionary prism is present in the subduction zone, even in a erosional regime it is uncommon to observe seismicity with such proximity to the trench (i.e. 2010 Maule, Chile (Rietbrock et al., 2012; Lange et al., 2012); 2015 Mw 8.3 Illapel, Chile (Ruiz et al., 2016); 2014 Mw 8.2 Iquique, Chile (León-Ríos et al., 2016); New Zealand (Anderson and Webb, 1994); Japan (Asano et al., 2011)). This activity might be related to (1) intraplate deformation due to the bending of the oceanic crust that can causes seismicity in the subducting slab and/or to (2) the absence of a frontal accretionary prism that allows the locking of the megathrust to extend up to the trench, causing seismicity, even at shallow depths.
Finally, the presence of subducting seamounts acting as erosional agents, helps to create a scenario which might promote locking and allow seismicity to extend up to the trench along zones of weakness activated after large earthquakes.

Deformation in the marine forearc and upper crust

Previous studies by Agurto-Detzel et al. (2019) and Meltzer et al. (2019) have described the overall deformation caused by the Pedernales earthquake. As we now have developed a robust minimum 1D model for the area affected by the 2016 mainshock and also manually determined high precision onset times, we are able to constrain the hypocentral depths in greater detail. We, therefore, will concentrate our discussion on the offshore area close to Cabo Pasado (see Figure 5.6) and analyze the deformation in the marine forearc and upper crust based on the diverse seismicity found in this area. The distribution and mechanisms of the 14 calculated RMTs in this study are superimposed over our event locations in Figure 5.4. Thrusting focal mechanisms from the gCMT catalogs (Ekström et al., 2012) are also shown and highlight the diversity of our

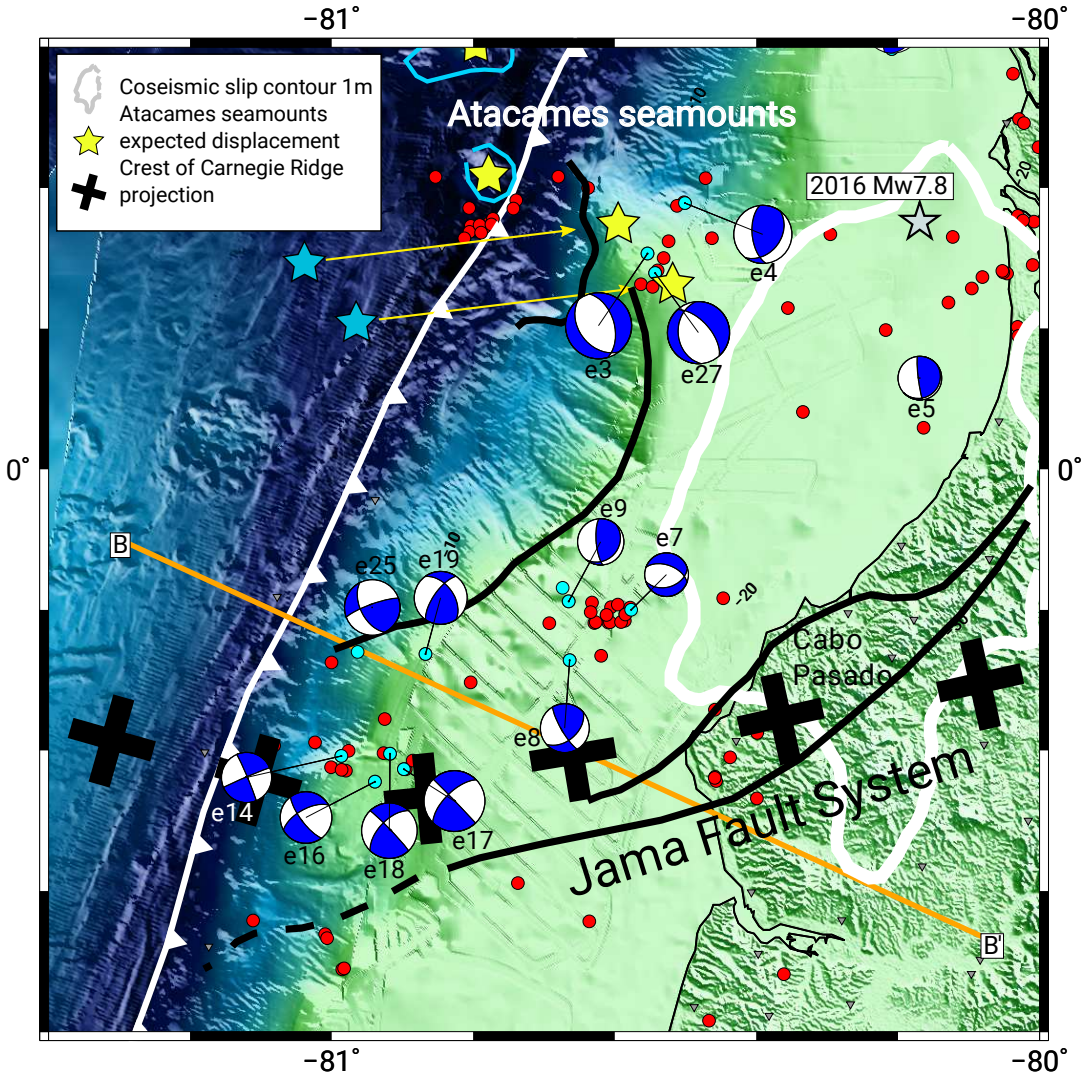

Figure 5.6: Zoom into the offshore Cabo Pasado area, where the strike-slip seismicity was detected. Red circles represents the seismicity relocated in the 1D inversion. Blue beach balls are the RMT solutions. Black crosses are the projection of the crest of the CR derived by Collot et al. (2004). Black solid lines show the Jama Fault System and its projection off shore from Collot et al. (2004) and Reyes and Michaud (2012), and the scarps in the marine forearc. Blue and yellow stars are the initial and final position of the Atacames seamounts proposed by Marcaillou et al. (2016). Grey star shows the epicenter of the 2016 Mw 7.8 Pedernales earthquake. Coseismic slip contour derived by Nocquet et al. (2017) is indicated in solid yellow line. Inland and seafloor topography from Michaud et al. (2006). Trench data obtained from Collot et al. (2005). Slab 1.0 km depth contours from Hayes et al. (2012) are shown in gray lines.

obtained solutions.

In profile AA′ we found two events with extensional components (e3 and e27 in Table 5.2) occurring in the overriding plate. Our RMT solutions agree with the suggestion by Marcaillou et al. (2016) who proposed that seamounts, part of the Atacames chain, could cause the activation of normal faults in the marine forearc of the overriding plate. Normal faulting in the marine forearc has been previously observed in the South American margin (Ruiz et al., 2014), especially in areas within erosive regime like in central Ecuador, where the overriding plate contains a small accretionary prism and a fractured, eroded and hydrated wedge that is easy to break.

Across profile BB′, we observed a clear pattern of strike-slip mechanisms distributed along the marine forearc (near the plate interface) and surrounding the scarps in front of Cabo Pasado. This

strike-slip sequence lasted for two days between the 7th and 8th July 2016. Figure 5.6 shows in detail the distribution of those events. This type of seismic activity in the area has been previously observed by Vaca et al. (2018) close to La Plata island ($\sim 1°$S).

Reactivation of preexisting normal faults in the upper crust after large megathrust earthquakes has been recently observed in many subduction zone settings (i.e. Farías et al. (2011); Ryder et al. (2012); Asano et al. (2011); Kato et al. (2011); Toda and Tsutsumi (2013)). Although normal fault mechanisms are also detected for the Pedernales aftershock sequence we observe a considerable amount of strike-slip seismicity that might be related to the following possible causes:

(1) The pattern followed by the strike-slip events is consistent with the projection of the crest of the CR derived by Pilger (1984) (see Figure 5.6). Around 80 km to the north of the CR, the forearc was affected by the subduction of the Atacames seamounts (Collot et al., 2005; Marcaillou et al., 2016) causing deformation on the margin and creating two scarps of 25 to 40 km wide separated by a shallow promontory (Collot et al., 2009) (see Figure 5.6). This suggests that subduction of the CR beneath the South American plate might create large scale deformation and reactivate transform faulting in the overriding plate.

(2) The location of the offshore Cabo Pasado seismicity is coincident with a rotational block system proposed by Daly (1989) that extends along the whole Pedernales segment. This system was created 45 Ma ago in the Mid-Late Eocene because of the rapid convergence rate between the Nazca and the South American plates. The interaction of the two convergent plates plus the presence of a major shear fault could have caused faulting in the forearc between the trench and the coast, creating several independent blocks in the Pedernales segment. Rapid changes in the relative velocities of these blocks could have caused both faults and blocks to have been rotated within the bounding shear zones, generating zones of strike-slip faulting at the edges of each block. These features remained inactive after the stabilization of convergence from the Late Miocene ($\sim$10 Ma) to the present day. Possible reactivation of the strike-slip faults might be related to the occurrence of large megathrust earthquake.

(3) Seismicity is associated with the possible extension offshore of the Jama Fault System (JFS) that also coincides with the area where the crest of the CR is located. The JFS could be explained as a large-scale system that was generated to release the stress accumulated by the interaction between the CCPP fault zone and the convergence margin. Collot et al. (2004) proposed the JFS as an active transcurrent fault that extends offshore which was confirmed by Hernández et al. (2011) and Michaud et al. (2015). It is possible that the occurrence of a large megathrust earthquake triggered the nucleation of seismicity along this fault.

In our opinion, a combination between hypothesis (1) and (3) is most likely to explain the observed activity because large-scale strike-slip system as the JFS normally do not extend in one single line but in several strands, covering an entire region as has been observed inland for the same system. In addition, the interaction between the CR and the upper crust where the JFS extends might contribute to the generation of this type of seismicity. These two factors, in addition to a large megathrust earthquake, such as the 2016 Pedernales event, could have provided the conditions to reactivate a strike-slip fault in the marine forearc. This offshore feature might have an important role as a barrier

for large megathrust earthquakes by absorbing the stress released during the reverse coseismic and transform it into strike-slip displacement (e.g. Collot et al. (2004)).
Whatever the cause is, the occurrence of seismicity associated with the reactivation of a strike-slip fault in the marine forearc is a remarkable observation. Upper crustal activity, related to normal faulting has been often documented: e.g. Pichilemu in central Chile (Farías et al., 2011), (Ryder et al., 2012) and also in Japan (Kato et al., 2011). It is therefore interesting to note that strike-slip faults can also be reactivated and should, therefore, be mapped in order to update the hazards map in the region.

5.6 Conclusions

We inferred a minimum 1D model for the Pedernales segment based on the aftershock sequence (Ml > 3.5) of the Mw 7.8 Pedernales earthquake. The velocity structure for both P- and S-phases was obtained after manually picking 345 events recorded by the permanent Ecuadorian seismic network and a temporary array that includes more than 70 inland and marine stations installed one month after the mainshock. P- and S- arrival times from 227 earthquakes with gap < 200°were inverted with VELEST to obtain absolute velocities, hypocentral locations and station correction terms.
The obtained minimum 1D velocity model shows a good resolution down to 40 km depth constrained with the ray paths and the earthquake distribution. The area has an average Vp/Vs ratio of 1.82 which varies with depth that may be related to hydration and serpentinization in the downgoing plate. The seismicity is distributed in streaks which align perpendicular to the trench. Cross sections allow us to identify the seismogenic contact between the Nazca and South American plates. Shallow seismicity was observed in both northern and southern segments of the rupture area suggesting the activation of faults in the overriding plate. Some of the observed seismicity reached the trench which suggests the absence of a frontal accretionary prism.
Regional moment tensors were calculated to analyze the source mechanism of some events offshore. Although the majority of the events show focal mechanisms consistent with the subduction process, we also observe extensional faulting in the marine forearc that can be associated to the subduction of already-mapped seamounts. We also found strike-slip faulting which might be related to the reactivation of a strike-slip structure after the 2016 Mw 7.8 Pedernales earthquake that, in combination with the subduction of the crest of the CR, might cause the nucleation of the observed seismicity along the marine forearc margin. The observation of this type of activity suggests the need to reevaluate the geological structures in the marine forearc and to update the seismic hazard map for this region including the possible scenario of a large strike-slip event.

Acknowledgments

This study was supported by IGEPN, IRD, the INSU-CNRS and the ANR grant ANR-15-CE04-0004. The UK portion of the temporary deployment was supported by NERC grant NE/P008828/1. The US portion of the temporary deployment was supported by IRIS PASSCAL and NSF RAPID Program Award EAR-1642498. SLR acknowledges partial support from Programa Formación de Capital Humano Avanzado, Becas de Doctorado en el extranjero, Becas CHile (Grant 8068/2015). HAD acknowledges support from ANR project ANR-15-CE04-0004 and UCA-JEDI project ANR-15-IDEX-01.

We are also indebted to Ben Yates, Davide Oregioni and Deny Malengros from Geoazur laboratories, INOCAR, Comandante Andrés Pazmino (INOCAR) and Captain Patricio Estupinian (Esmeraldas Coastguard) to operate OBSs at sea in very harsh environments.

Authors want to thanks to all involved in the deployment and data collection for his invaluable collaboration with this study. Finally, to all the people in Ecuador who allowed us to install our stations in their houses, big thanks for your hospitality, patience and help when was needed.

Chapter 6

3D seismic tomography for the Ecuadorian margin

The minimum 1D model described in the previous chapter was used as the initial reference to derive a novel three-dimensional velocity structure, at a regional scale, for the Ecuadorian margin. This chapter provides details about the methods and data used for the 3D inversion together with the results and interpretations based on the seismotectonic and geological context of the region. The text presented here is part of the research article:

- 3D local earthquake tomography of the Ecuadorian margin in the source area of the 2016 Mw 7.8 Pedernales earthquake, submitted to *Journal of Geophysical Research* (León-Ríos et al., 2020)

6.1 State-of-the-art: regional scale velocity models in the Ecuadorian margin

Although the Ecuadorian margin has been widely studied, there is still no consensus about a regional scale 3D velocity model, especially for the coastal area and the marine forerarc, where megathrust earthquakes pose high seismic hazard.
Previous small-scale studies in the Esmeraldas segment (Gailler et al., 2007; Agudelo et al., 2009; Cano et al., 2014), La Plata island (Gailler et al., 2007) and part of the Carnegie Ridge (CR) (Sallarès et al., 2003, 2005; Graindorge et al., 2004; Gailler et al., 2007) have contributed to our understanding of the first order characteristics of the physical properties of the margin. On a regional scale, Font et al. (2013) built a velocity model for the forearc by combining geodynamic, structural and velocity data, reproducing the slab geometry. Araujo (2016) derived a seismic velocity model and Moho depth for a larger area based on seismic data from the Ecuadorian permanent network (RENSIG, (Alvarado et al., 2018)); however, small-scale structures (i.e., seamounts) in the forearc region was not resolved. Lynner et al. (2020) and Koch et al. (2020) used ambient noise and joint ambient noise and receiver function methods, respectively, to image the coastal forearc but were unable to image the marine forearc.

Based on the aftershock activity of the 16th April 2016 Pedernales earthquake recorded by our temporary seismic network, which includes ocean bottom seismometers (OBS) installed along the trench axis (León-Ríos et al., 2019; Meltzer et al., 2019), we derive a novel three-dimensional velocity model for Vp and Vp/Vs together with precise hypocentral locations for the central coastal area of Ecuador. Local earthquake tomography images the physical properties of the margin which, together with the regional seismotectonic and geological settings, provide a descriptive interpretation of the major features involved in the Ecuadorian subduction process. Our findings highlight a very heteregeneous margin with seamounts and large bathymetric features within the oceanic crust, but also an overrding plate highly affected by large-scale faults. Finally, we discuss how these structures might contribute to controlling the seismic activity in the Ecuadorian margin.

6.2 Dataset

To extend the catalog used to obtain the 1D velocity model (León-Ríos et al., 2019), we incorporated more events from the refined aftershock catalog by Agurto-Detzel et al. (2019). Seismicity with ML > 2.5, recorded between May and November 2016, and located in the vicinity (300 x 200 km^2) of the temporary network was included in the 3D inversion process. From this catalog, P- and S-wave arrival times were manually picked using the Seismic Data Explorer (SDX) software package (http://doree.esc.liv.ac.uk:8080/sdx) that utilizes a modified hypo71 algorithm for the hypocenter location (Lee and Lahr, 1972). As described in chapter 3, we assigned picking error categories, referred as weights, from 0 to 4 to describe the quality of the selected arrival times. Each weight corresponds to the following time uncertainties: Weight 0 (< 0.04 s); Weight 1 (0.04 –0.1 s); Weight 2 (0.1 –0.2 s); Weight 3 (0.2 –1 s); Weight 4 (> 1 s). Events were located using the minimum 1D model and correction terms from León-Ríos et al. (2019). Finally, aftershocks with a median azimuthal gap of 123°, SDX location rms < 0.3 and at least 10 P- and 5 S-onset observations were included in the previous catalog to get a total of 568 earthquakes containing 10628 P-phases and 9134 S-phases.

6.3 Method: local earthquake tomography

Following the procedure detailed by Husen et al. (2000), Haberland et al. (2009) and Hicks et al. (2014), we performed a series of iterative travel time inversions to obtain Vp, Vp/Vs and hypocentral locations using SIMULPS (Thurber, 1983; Eberhart-Phillips, 1986; Um and Thurber, 1987; Eberhart-Phillips, 1993; Thurber and Atre, 1993; Thurber and Eberhart-Phillips, 1999). To compute the velocity and hypocentral solutions, this algorithm performs iterative travel time inversions within a 3D nodal grid defined by the user. For our inversion, we defined a grid of 200 x 250 x 60 km^3 (see Figure B1 in Appendix B) with several nodes organized in profiles perpendicular to the trench axis. The 1D model velocities (León-Ríos et al. (2019); see Figure B2 in Appendix B) reflect the margin structure below a coast reference station located approximately where northern limit of the CR subducts. To ensure this does not bias our 3D results, we invert for

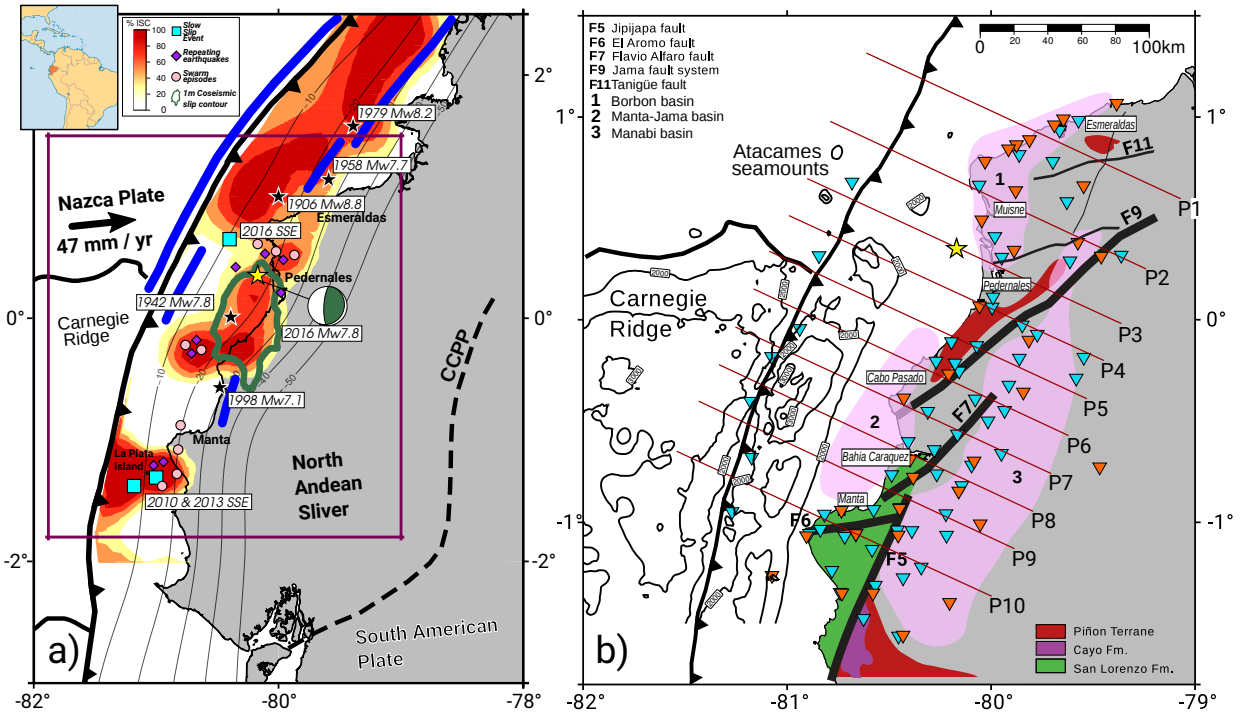

Figure 6.1: a) Seismotectonic setting of the study area. Solid blue lines represent the extension of historical earthquakes in the area. Epicentres of those events are indicated with a black star. Slow slip events, repeating earthquakes and seismic swarm episodes are also represented by squares, diamonds and circles, respectively. 2016 Pedernales earthquake is shown including its epicentre (yellow star), cosesimic slip by Nocquet et al. (2017) (solid green line) and focal mechanism (green beach ball). Distribution of the interseismic coupling by Nocquet et al. (2014). Chingual-Cosanga-Pallatanga-Puna fault (CCPP) that created the North Andean Sliver (NAS) is represented by a segmented line. b) Geological context and recording network. Main formations, sedimentary basins and faults mapped by Reyes and Michaud (2012) are displayed by coloring forms and solid black lines. Offshore, residual bathymetry derived by Agurto-Detzel et al. (2019) is shown in solid black line. Permanent Ecuadorian network (RENSIG, Alvarado et al. (2018)) and emergency deployment (Meltzer et al., 2019) are shown in orange and lightblue inverted triangles, respectively. Profiles, P1-P10, discussed in this work are plotted in solid red line.

two 2D models to represent the primary subducting structure north and south of the equator. We then merge these models to create a 3D starting model, but we also smooth/combine the two models to make a single 2D cross-section representing the subducting lithosphere, which is then itself extended along-strike to make a 3D starting model. Both 3D starting models are tested for inversion. For all stages, damping values were derived by analyzing trade-off curves (see Figure B3 in Appendix B). P-wave velocities were initially calculated and then used as input to perform the Vp/Vs inversion. Also, we applied a smoothing technique to improve our lateral resolution (Haberland et al., 2009; Hicks et al., 2014). A detailed description of each step is given in the following sections. Finally, the precise hypocentral locations and their corresponding arrival times resulting from the 2D inversions, were merged and subsequently inverted using a smooth 2D initial model projected over a grid that included more nodes to increase resolution along strike (see Supplementary Material B1 in Appendix A). Here, a damping curve was also calculated to obtain our final 3D velocity model. A detailed description of each step is given in the following sections.

		# events	P-phases	S-phases	Total phases	Damping		Model VAR		Localization VAR		RMS	
						Vp	Vp/Vs	Vp	Vp/Vs	Vp	Vp/Vs	Vp	Vp/Vs
1D*		229	4939	3931	8870	-	-	-	-	-	-	0.33	0.30
2D	North	317	5479	4559	10038	500	800	0.1959	0.2080	0.08	0.09	0.28	0.31
	South	232	4821	4128	8949	500	2000	0.2002	0.1705	0.09	0.08	0.30	0.28
3D	-	568	10628	9134	19762	1200	1200	0.2632	0.2192	0.10	0.09	0.32	0.30

Table 6.1: Summary of number of events, P-and S-phases, damping values and variance for the model and the relocated aftershocks for each step towards the three-dimensional model calculation. (*) As the 1D model was obtained using a different program, damping values were not included.

6.3.1 Two-dimensional modeling

To obtain the 2D velocity model (2DVM), we extended our minimum 1D model León-Ríos et al. (2019) in a 2D grid with a minimum lateral spacing of 15 km to resolve velocity structure in west-east direction. In depth, we used the layers of the reference 1D model (see Figure B2 in Appendix B) to set the nodes separation. Distance between nodes varies from 2.5 km at shallower layers to 10 km at greater depths (see Figure B1 in Appendix B). To have a better constraint of the area, with a seismicity better distributed and a large amount of P- and S-onsets, we increased the number of events in the 1D catalog León-Ríos et al. (2019) from 227 to 549 earthquakes ($\geq$10 P-onsets, $\geq$5 S-onsets and gap <210° (Haberland et al., 2009; Hicks et al., 2014); see Table 6.1). The structural differences between areas located north and south to the equator forced us to split the calculation in two sections to obtain robust earthquake locations in this initial stage. For the inversion to the north (2D-N), we used 317 events with 5479 P- and 4559 S-onset phases (see Table 6.1). For the south section (2D-S), a total of 232 aftershocks containing 4821 P- and 4128 S-onset phases were used. Several damping values were tested, as described in Eberhart-Phillips (1986), to select the best one to perform the inversions (see Figure B3 in Appendix B). A rough 2D model was calculated and used as input for the following inversions. For both north and south sections, we applied a smoothing technique (Haberland et al., 2009; Collings et al., 2012; Hicks et al., 2014) by shifting nodes by a third of the minimum spacing to improve our lateral resolution. The resulting averaged Vp model was used as the new starting model to invert for Vp/Vs.

6.3.2 Three-dimensional modeling

Using the results from the previous stage, we continued to calculate a 3D velocity model (3DVM). We added 19 more events (Ml $\geq$2.5 and gap <230°) that filled blank spaces left in the 2D modeling. In total, we inverted 568 earthquakes with 10628 P- and 9134 S-phases (see Table 6.1). The nodes distribution for this stage is shown in Figure B1 in Appendix B. The 3D grid comprises 11 profiles distributed in a volume with a minimum spacing, of 15 km, 20 km and 2.5 km, for the x (east), y (north) and z (down) axis, respectively. With this setting, we incorporated 2D-N and 2D-S arrival times and estimated the optimal damping values (see Figure B3 in Appendix B). Our preferred solution avoids along strike smearing by performing the Vp inversion over a smooth 2D initial model extended along the described grid (see Figure B4 in Appendix B). Subsequently, we inverted

for Vp/Vs ratios following the same procedure conducted for the 2D modeling.

6.4 Resolution

Although the setting of our amphibious experiment ensures a good coverage for recording the aftershocks, the irregular distribution of both stations and earthquakes raises the problem of resolution heterogenity within the 3D volume. To identify areas that are well resolved and to distinguish them for areas that are poorly resolved, we inspected critical parameters from the model resolution matrix and also conducted checkerboard tests. Finally, to estimate the standard deviation and analyze the restoring capability of our 3D model, we performed bootstrap and synthetic recovery tests.

6.4.1 Model resolution matrix (MRM)

We investigated in detail the MRM to provide insights on how well resolved the model parameters (seismic velocities) are. By taking the ratio between off-diagonal and diagonal elements of the MRM, we derived the spread function (SF, Toomey and Foulger (1989)) helping to identify areas with good and poor ray coverage. We also inspected the size and orientation of the smearing by contouring the 70% value of the diagonal elements at each row of the MRM (eg. Haberland et al. (2009); Collings et al. (2012); Hicks et al. (2014)). In general, large diagonal elements of the MRM, small SF and rounded 70% contour lines around the grid node are related to well resolved areas.
Cross sections in Figure 6.2 and 6.3 show the resolution of our 2DVM and 3DVM for both Vp and Vp/Vs. We consider well recovered areas when the SF is <65% of its maximum value (eg. Haberland et al. (2009); Collings et al. (2012); Hicks et al. (2014)). The 2DVM show a well resolved Vp in both, north and south, segments. The Vp/Vs ratios show a less constrained area, mainly because of reduction on the number of S-phase onsets.
For our 3DVM, Figure 6.3 shows a representative sample for the inverted profiles (see Figures B5 and B6 in Appendix B for MRM in all profiles). From north to south, we observed how the central profiles area better resolved. At ~1°N, in profile 1, the lack of seismicity and data from OBS at this latitude confines the resolution contour to an area with data coming from a seismic cluster in the upper crust. In contrast, the rest of the profiles show wider resolution contours. In terms of MRM, the small SF and rounded-like shape of the 70% resolution kernels indicate well resolved areas. Although some areas in the marine forearc can show lateral smearing (P5-P6, see Figures B5 and B6 in Appendix B), it is important to highlight how the resolved areas were increased trenchward thanks to the presence of the OBS distributed offshore. The portion of the marine forearc devoid of OBSs (P1) is not resolved at shallow depths (<5-7 km). For Vp/Vs (Figure 6.3), the resolution contours are smaller due to the number of S-phases detected; however, we were able to resolve the central part in all of them. In terms of smearing, we see a transition in the shape of the 70% resolution kernels that goes from small in the central part (around 0 km in the x-axis) to large-elongated shape near the edges limiting the resolution in these areas (see Figures B5 and B6 in Appendix B).

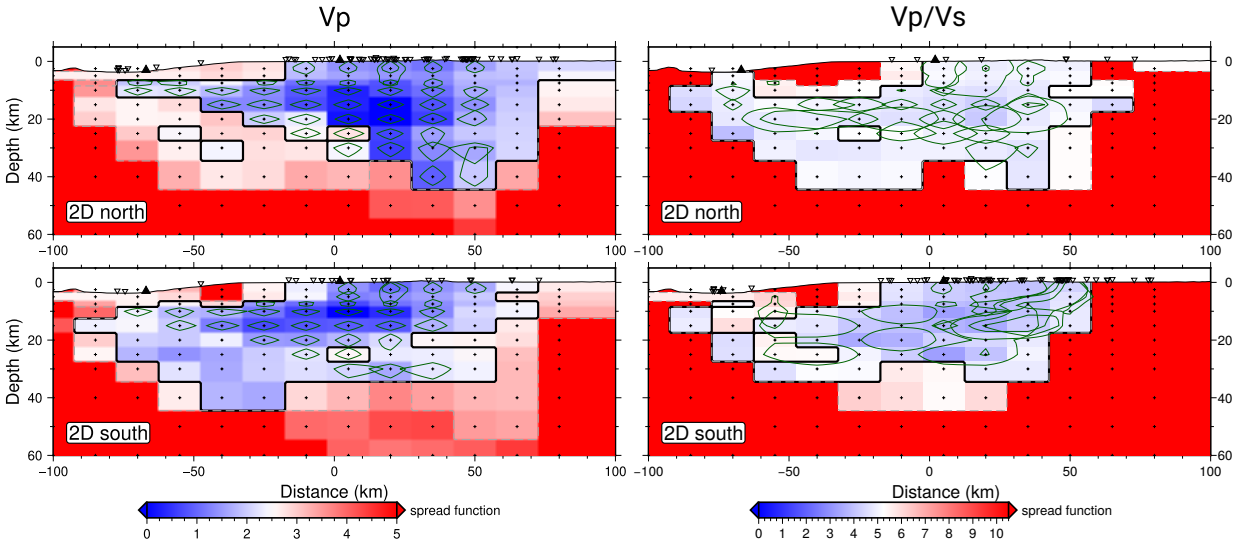

Figure 6.2: 2D model resolution matrix (MRM). Resolution contour estimation for the 2D Vp and Vp/Vs models in the north and south segments. Based on the MRM analysis, calculation of the spread function is displayed in a red/blue scale. Green lines show the 70% contour for the diagonal elements of the MRM.

6.4.2 Checkerboard test

To analyze the resolution capability of our dataset we evaluate synthetic reconstruction tests. A classical tool to explore this matter is by performing a checkerboard test (Spakman and Nolet, 1988). This type of analysis helps us to estimate how well resolved are different sizes of anomalies in our model and how well amplitudes are recovered. Synthetic travel times were calculated using the observations from our final 3D inversion over an alternating pattern of positive and negative anomalies of 5% of the inverted model. Different sizes of anomalies (15 km and 30 km) were tested. Then, the inversion method was applied to recover the original structure. Finally, we evaluated the agreements (dv) between the anomalies in the initial and final models to assess the resolution capability of our dataset. Anomalies of 30 km wide (see Figures 6.4 and B7) show well recovered velocities (dv $\sim$5%) down to $\sim$40 km depth. Lateral and vertical extension of the recovered anomalies show a recovery <2% deeper and on the edges of the profiles. For small-scale perturbations (15 km), areas of good recovery are similar to those from larger anomalies, showing a reduction of recovered velocities (dv <2%) when deeper than $\sim$30km. We observe a reduction in the recovering capacity in P1 where the lack of seismicity limits the resolution only to a small region at shallower depths (<20 km) below the coastline. P2 shows a good recovery reaching dv $\sim$4% in its central region although the edges still show the effects of reduced seismicity. Profiles P4-P8 are well recovered (dv $\sim$5%) in the central areas, reaching good resolution up to the trench. Finally, the southermost profile P10 also shows well recovered areas although the reduced seismicity in that region limits the in-depth restoring capacity to <2% down to 20 km.

6.4.3 Synthetic recovery test

We also performed synthetic restoring tests to assess the imaging capability of the 3DVM. We focused on the analysis of a subducting seamount shaped with a low Vp anomaly and located close

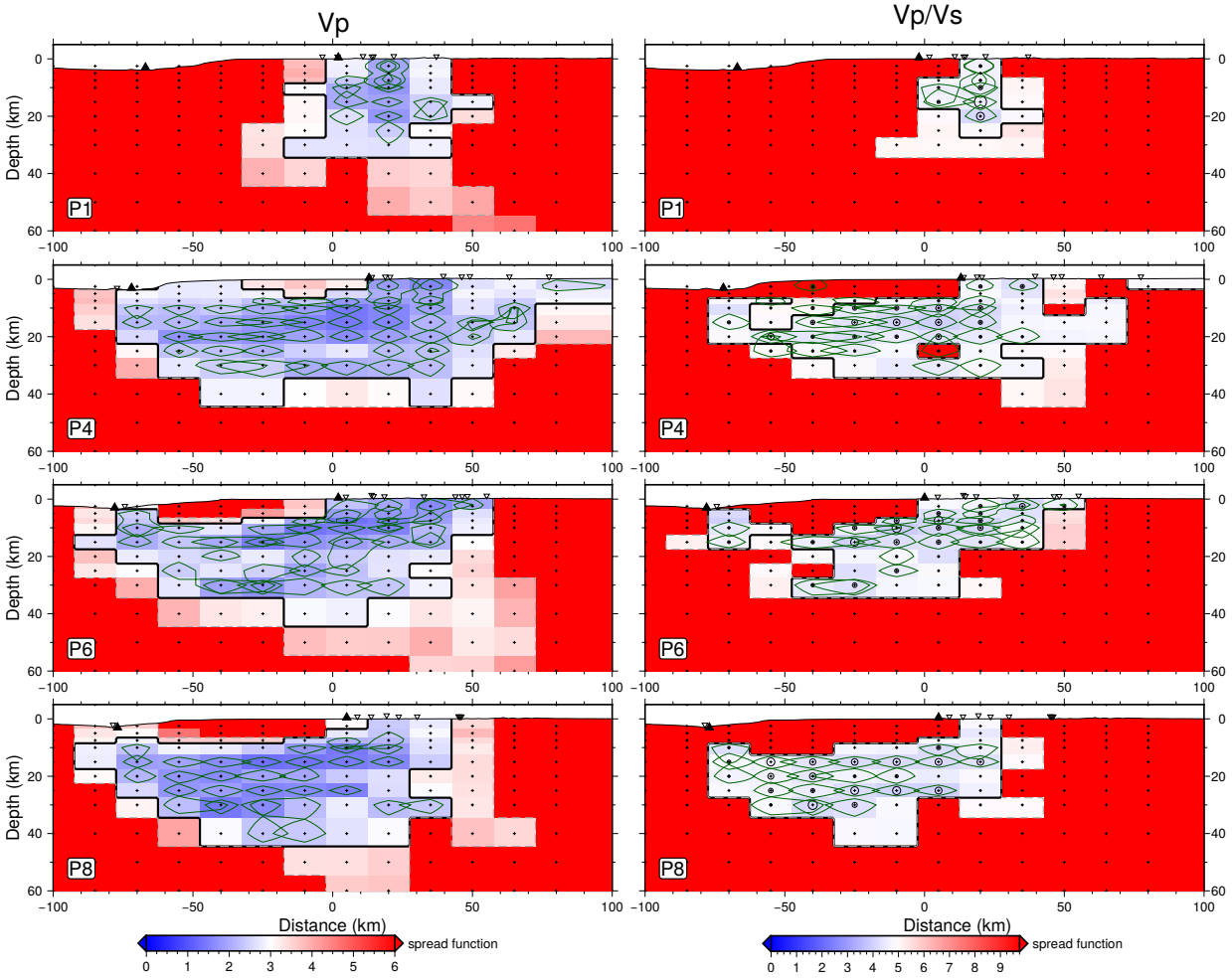

Figure 6.3: 3D model resolution matrix (MRM). Resolution contour estimation for the 3D Vp and Vp/Vs along representative profiles for the northern, central and southern parts of the area of study. Based on the MRM analysis, calculation of the spread function is shown by a red/blue scale. Green ellipses show the 70% contour for the diagonal elements of the MRM. See text for further information.

to the trench in profiles P4 and P5. The synthetic model also includes a low Vp feature at ~20 km depth, located in P7 (see Figures 6.4c and B8). Synthetic travel times were computed as described above and subsequently inverted over the 2D initial model. Profiles where the low Vp anomalies were included recovered similar shapes and values. We observe that P4 is more likely to restore the low Vp by getting values ~5 km/s down to 5 km depth. P5 restored reduced velocities (~5.5 km/s) with the tested Vp=5 km/s anomaly observed only with a small size (see Figure B8 in Appendix B). In terms of the low Vp anomaly at ~20 km depth in profile P7, the model can recover the anomaly although with a reduced amplitude. Figure 6.4c shows profiles P4 and P7 for this test while Figure B8 in Appendix B presents the recovered velocities for the central profiles (P3-P8).

To check the influence of the initial model on our obtained Vp velocities, especially for the slab crust at depth >30 km, we conducted a second synthetic test based on the 2D-N Vp model. The 2D-N model, with a low Vp feature near the trench and without plunging slab crust deeper than the upper plate's Moho, was projected along all grid nodes and synthetic arrival times were calculated. Similar to the previous test, arrival times were subsequently inverted over a smooth initial model (see Figure B9 in Appendix B). In general, the recovered velocities agree with the

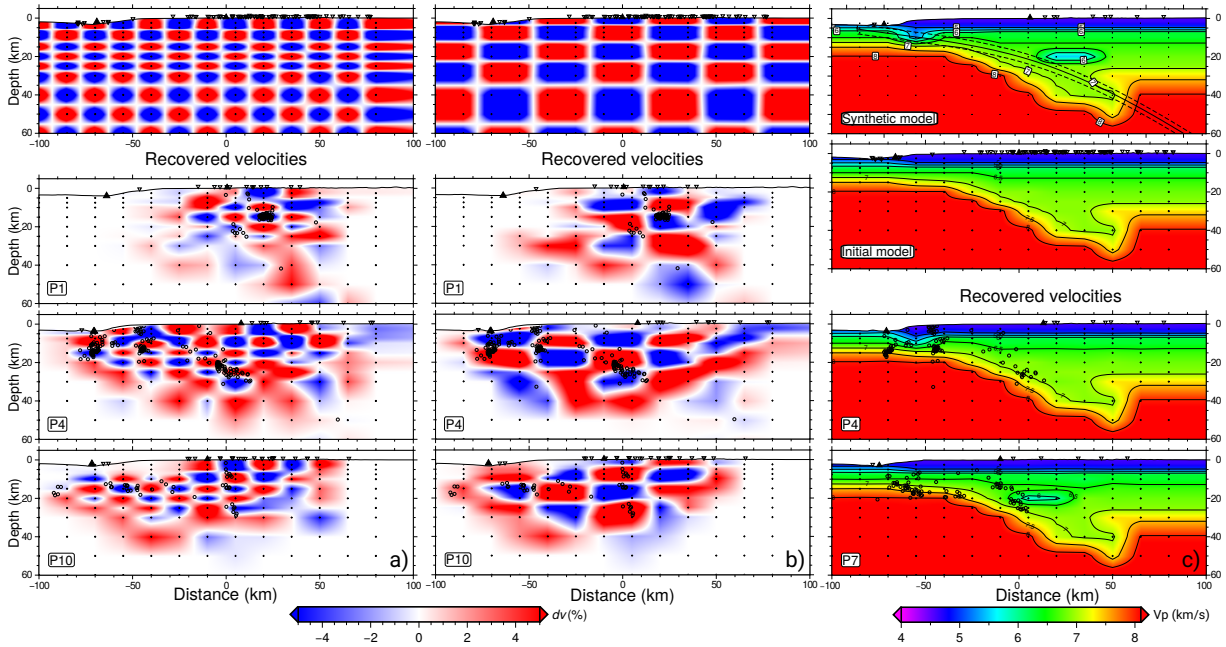

Figure 6.4: Synthetic recovery tests. Checkerboard test for **a)** small, 15km and **b)** medium, 30 km anomalies. Top image show the input model comprised by alternated positive and negative anomalies of ±5% of the inverted model. Bottom images show the recovered velocities along representative profiles for the northern, central and southern segments in our region of interest. **c)** Restoring test for a synthetic model that includes a seamount represented by a low Vp (5.0 km/s) anomaly added in P4 and a low Vp anomaly (5.5 km/s) at 20 km depth in P7. The initial model for the inversion is shown in the central panel. Lower panels show the restored velocites in P4 and P7. See Figure B7, B8 and B9 in Appendix B for the full profiles and further tests.

initial 2D-N model, with major features present in almost all profiles. However, this test highlights the segmentation of the margin by showing how the restored model varies as we move south. Close to the trench, we observe how the low Vp anomaly disappears in P5-P6, to then reappears in P7 and P8 but with a broader and deeper extension.

To further analyze possible artifacts and check the robustness for our final model, we computed a 3D inversion based on the merged 2D-N and 2D-S models. The inversion followed same procedure described for our staggered 3D inversion. Results for this inversion are shown in Figures B10 and B11, in Appendix B, for horizontal and vertical slices, respectively. In general, the velocities imaged by the merged 2D-N and 2D-S models are similar to those obtained by the smooth initial model. Main features at the surface are well resolved; however, along strike smearing is observed, especially for the features close to the trench. This suggest that the merged modeling strategy can add possible artifacts to the inversion and confirms the robustness of our 3D model based on high quality arrival times inverted over a smooth initial 2D model.

6.4.4 Bootstrap

A last sensitivity test was performed to estimate the standard deviation for the obtained velocities. We conducted a bootstrap test by creating a subset of data comprising 80% of the actual catalog which was subsequently inverted. Aftershocks included in the tested catalog were randomly selected and the inversion parameters were the same as the descibed for the 3D velocity model.

We repeated this process 100 times and calculated the standard deviation at each node of the grid (see Figure B12 in Appendix B). Finally, the overall mean value was calculated to estimate the error of our obtained Vp and Vp/Vs models. Maximum estimated standard deviation for Vp is $\sim$0.3 km/s and $\sim$0.01 for Vp/Vs.

6.5 Results

The 2DVM and 3DVM highlight the main structural features for the central Ecuadorian subduction zone. Based on the inspections of both, SF and checkerboard tests, we estimated regions with good resolution that, in general, extend $\sim$130 eastward from the trench axis. In depth, we can resolve velocities down to $\sim$35 km. The following sections describe the results shown in Figures 6.5, 6.6, 6.7, 6.8 and 6.9. Cross sections were produced for 2DVM and 3DVM (see Figures 6.5, 6.8 and 6.9). We used slab1.0 (Hayes et al., 2012) as a reference the interface at depths greater than 15 km and modified the shallower part by using the trench location from (Collot et al., 2005) and our obtained aftershock distribution. Also, horizontal slices for Vp and Vp/Vs were taken at 2, 5, 10 and 20 km depth to observe velocity changes in depth (see Figures 6.6 and 6.7). The margin shows Vp/Vs ratios ranging from 1.74 to 1.94 in agreement with Hyndman (1979) and Christensen (1996, 2004) that suggested typical Vp/Vs values in the upper oceanic crust of 1.78 to 2.11 depending on the percentage of serpentine, fluids or lithology.

6.5.1 Two-dimensional velocity models

From the resulting 2DVM, we can identify first order features in both, north and south, segments. Figure 6.5 shows cross sections for Vp and Vp/Vs where the Vp=7.5 km/s isocontour images the geometry of the crustal part of the downgoing plate. We also observed elevated Vp/Vs ratios ($\sim$1.90) close to the trench. In the overriding plate, velocity anomalies correspond to major geological structures, such as basins, faults and geological formations distributed along the margin. North and south profiles in Figure 6.5 show prominent low Vp anomalies ($\sim$4 km/s) and alternated distribution of Vp/Vs ratios, with low ($\sim$1.75) and high ($\sim$1.90) values, extending eastward at shallow depths. Geological features associated with these anomalies have been mapped at the surface by Reyes and Michaud (2012) and will be discussed later. Finally, in terms of seismicity, we observe that most of the aftershocks are located along the slab interface. However, we observe a change from a more interface-aligned organization of aftershocks in the north to a more disperse distribution of events in the south.

6.5.2 Three-dimensional velocity model

Figures 6.6, 6.7, 6.8 and 6.9 show our resulting Vp and Vp/Vs 3DVM together with the relocated seismicity, displayed in horizontal slices and cross sections, respectively. At shallow depths (z=2 km and z=5 km, see Figure 6.6), we imaged a prominent elongated N-S feature ($\sim$30 x 150 km) along the coast, having Vp ranging from $\sim$ 5.0 km/s to $\sim$ 5.5 km/s. We also observe low velocites (Vp$\sim$4.5 km/s) south and east of the high Vp anomaly, suggesting a high velocity contrast at

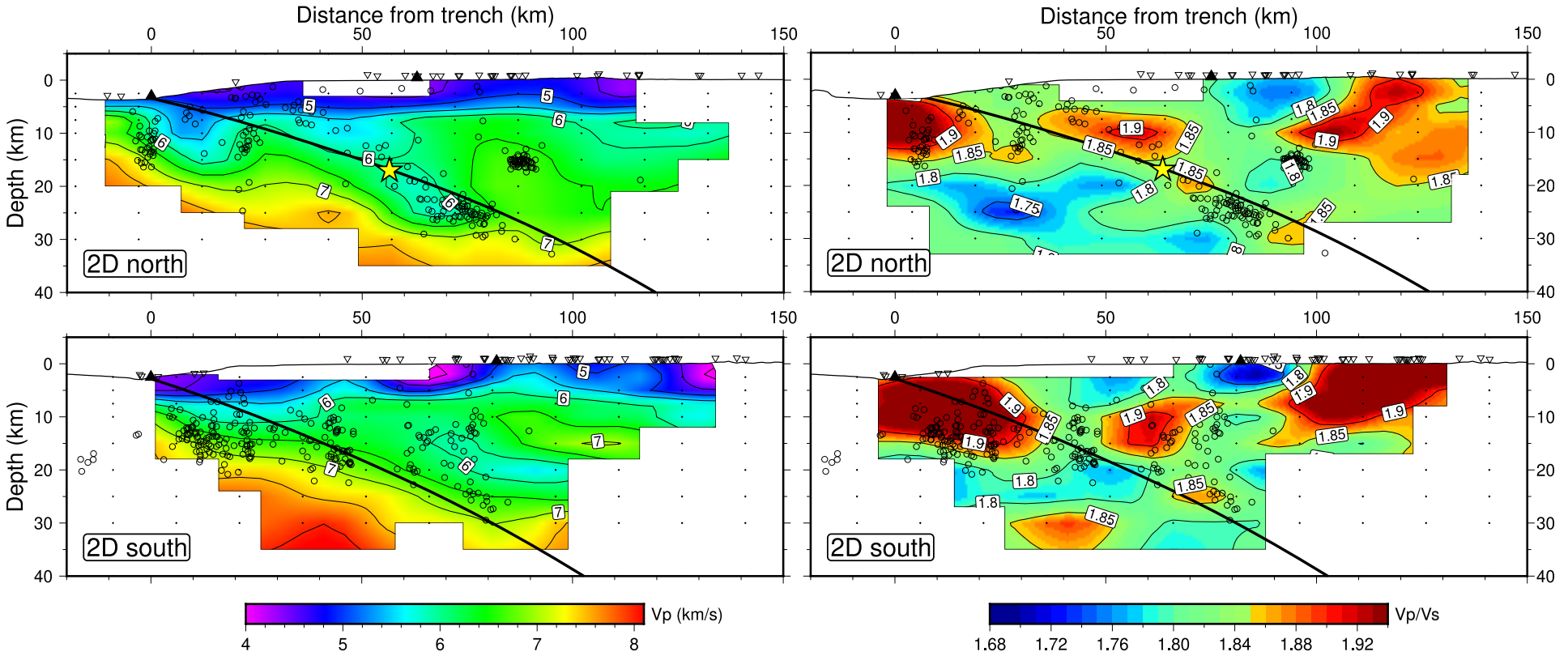

Figure 6.5: 2D velocity model. Two-dimensional models for both north (top) and south (bottom), Vp (left) and Vp/Vs (right). Velocities and Vp/Vs ratios are color coded and iso-contours are plotted every 0.5 km/s and 0.05 for Vp and Vp/Vs, respectively. Also, based on resolution estimated by the MRM and checkerboard test, results for non resolved areas are shown faded or blank. Relocated hypocenters are plotted in black circles, and grid nodes are shown in black crosses. Yellow star in north, Vp and Vp/Vs, profiles indicates the hypocenter for the 2016 Pedernales earthquake (Nocquet et al., 2017). Solid black triangles represent the projection of the trench and coastline. Finally, inverted triangles are the stations contained on each profile.

shallow depths in the area. At the same depth (z=2 and z=5 km), high and low Vp/Vs ratio anomalies(>1.85 and <1.80) are observed at the location of the high and low Vp regions.
Cross sections in Figures 6.8 and 6.9 image in detail the uppermost part of the subducting oceanic Nazca plate. By comparing the depth of the Vp 7.2-7.5 km/s iso-contour at ∼20 km eastward of the trench, we observe a thick crust ∼15 km which is consistent with previous observations for the Nazca plate thickness (Sallarès et al., 2003; Gailler et al., 2007; Cano et al., 2014). In terms of Vp/Vs ratios, we find values ∼1.90 close to the trench in profiles P2-P9 (see Figures 6.8 and 6.9). Close to the trench, a prominent low Vp anomaly (∼5.5 km/s) is observed in the oceanic crust. Horizontal slices at z=10 km, in Figure 6.6, show the along strike extension where three low Vp patches are illuminated. Moreover, a detailed inspection of the cross sections (see Figures 6.8 and 6.9), show a prominent low Vp feature of ∼20 km in P4. Also, this low Vp anomaly shows a broader extension to the south from P5-P9. In terms of Vp/Vs, it is also possible to observe a N-S variation in the area where the low Vp anomaly is described. We image Vp/Vs ratios ∼1.75 in P4-P5 that change to ∼1.85 from P6-P9 close to the trench.
Finally, from the relocated aftershocks displayed in vertical and horizontal profiles, we observe a clustered distribution mainly organized along the slab interface, as described by Agurto-Detzel et al. (2019), Meltzer et al. (2019) and Soto-Cordero et al. (2020) but also at shallower depths (<20 km) in the upper crust as discussed by Hoskins et al. (2018) and León-Ríos et al. (2019). We found a group of seismicity in profile P1 that corresponds to the Esmeraldas activity occurred in July 2016.
Cross sections in profiles P2-P5 show the seismicity mostly aligned along the slab interface at depths > 15 km. In contrast, close to the trench in P4, we observe a prominent sub-vertical organization of events showing a depth range between 5 to 10 km. Aftershocks in profiles P6-P7 appear with a more disperse distribution. However, it is still possible to identify some clusters of earthquakes lying close to the trench (∼10-15 km depth). P8 shows clustered activity in the oceanic crust, located ∼10-15 km east from the trench. Finally, in profiles P9 and P10, the observed seismicity reduces significantly with a few events in the slab interface, and also clustered activity in the upper crust with a vertical distribution occurring at shallower depths (∼10-15 km) in P9.

6.6 Interpretation and discussion

Upper plate crust (UC)

P-wave velocities in the UC can be associated with geological structures described by Reyes and Michaud (2012) and showed in Figure 6.1. Observations from horizontal slices at shallow depths (z=2 and z=5 km) are labeled in Figure 6.6 relating the high Vp (∼5.5 km/s) feature to outcrops of the Piñon formation (P). The same structure is well imaged in Vp/Vs profiles P4-P6 in Figures 6.8 and 6.9. This formation is clearly imaged by relatively low Vp/Vs ratios (1.75-1.80) distributed along the coastline between 0.5°S and ∼0.1°N, and it is part of the oceanic terranes in the overriding plate (Reynaud et al., 1999; Luzieux et al., 2006; Reyes and Michaud, 2012). We

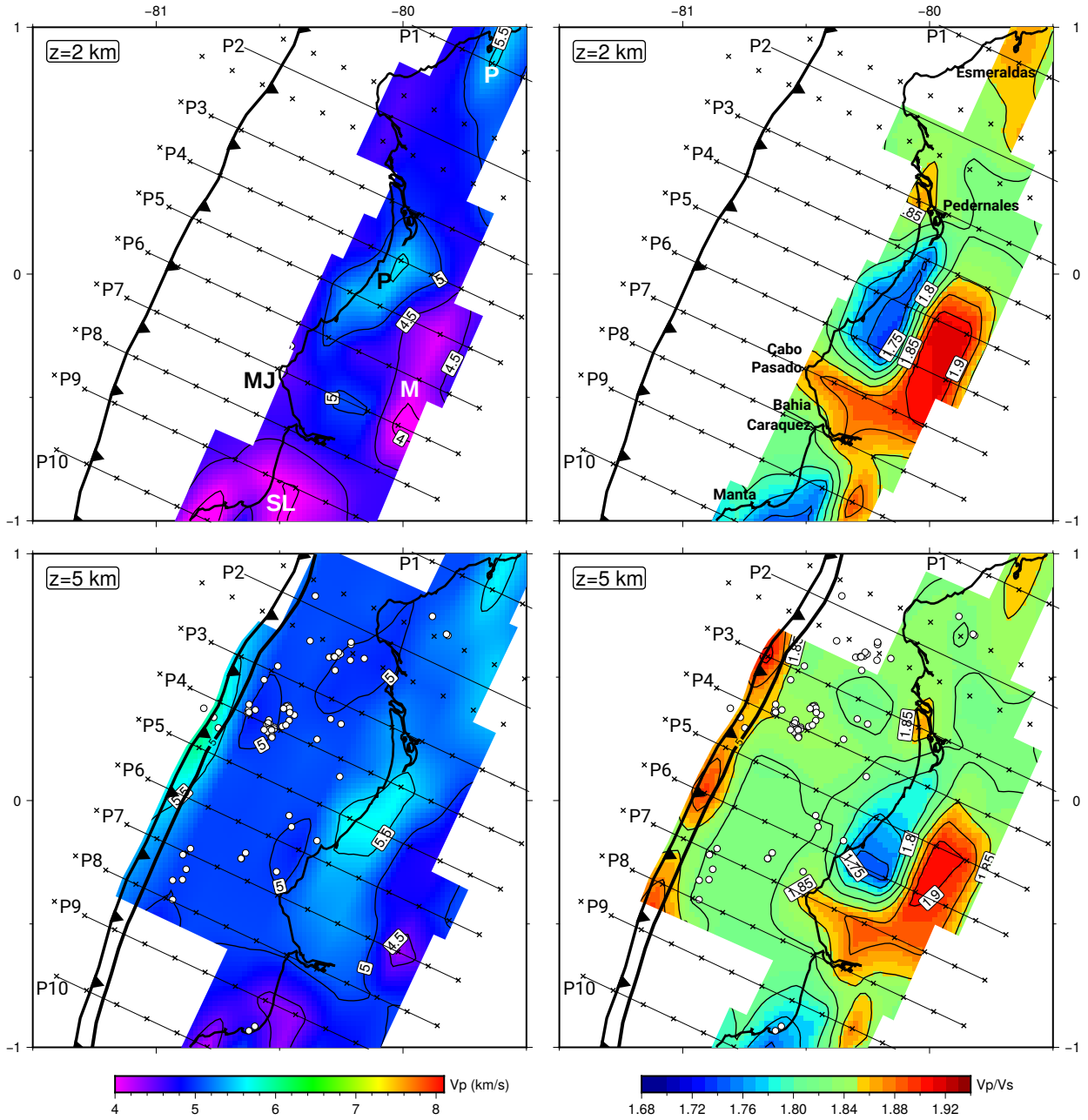

Figure 6.6: 3D velocity model, horizontal slices at 2 km and 5 km depth. Vp (left) and Vp/Vs (right) horizontal slices at 2, 5, 10 and 20 km depth. Velocities and Vp/Vs ratios are color coded and iso-contours are plotted every 0.5 km/s and 0.05 for Vp and Vp/Vs, respectively. Also, based on resolution estimated by the MRM and checkerboard test, results for non resolved areas are blank. For reference, name of the mentioned cities in text are shown in the 2 km depth Vp/Vs slice. Profile and grid nodes locations are displayed by solid line and crosses, respectively. P: Piñon formation, M: Manabi basin, MJ: Manta-Jama basin and SL: San Lorenzo block.

can estimate its lateral extent up to ∼25 km. In contrast, at 2 km depth, we observe an elongated N-S orientated low Vp (∼4 km/s) body that extends southward. This feature can be associated with the northern part of a sedimentary basin, namely the Manabi basin (M; Reyes and Michaud (2012)). The Manabi basin is well identified by a large scale (∼80 km x 27 km) NNE high Vp/Vs (1.85–1.90) anomaly associated to non-consolidated and hydrated rocks. We also imaged what might be the basin depocenter by identifying a region of reduced Vp (∼4.5 km/s) and elevated ratios (∼1.85) down to 5 km depth (see Figure 6.6).

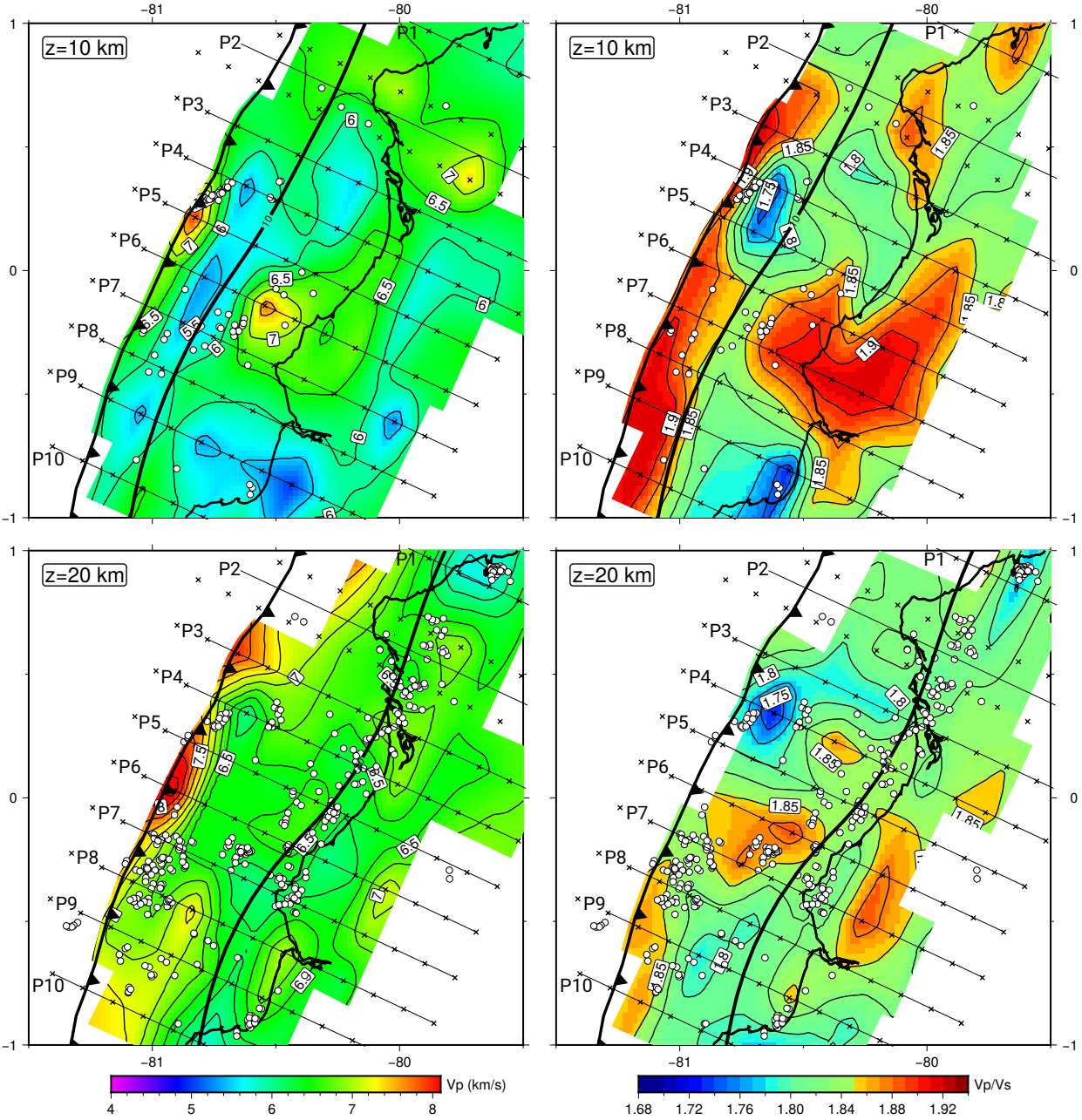

Figure 6.7: 3D velocity model, horizontal slices at 10 km and 20 km depth. Vp (left) and Vp/Vs (right) horizontal slices at 2, 5, 10 and 20 km depth. For reference, name of the mentioned cities in text are shown in the 2 km depth Vp/Vs slice. Profile and grid nodes locations are displayed by solid line and crosses, respectively. See caption in Figure 6.6 for more details.

The Manabi basin is a large structure that extends for about 200 km along strike and its north-east boundary is controlled by the Jama Fault System (JFS) which separates the basin from the Cretaceous Piñon formation. The contrasted nature of these formations could be related to the high constrast imaged in the horizontal slices of both Vp and Vp/Vs models. This fact has been previously described based on station correction terms from our derived 1D velocity model (León-Ríos et al., 2019). Moreover, Vp/Vs cross sections P4-P7 (see Figures 6.8 and 6.9) highlighted this contrast of Vp/Vs ratios, around 100 km eastward from the trench, up to 5-10 km depth. Collot et al. (2004) and Michaud et al. (2015) have suggested that the JFS extends offshore

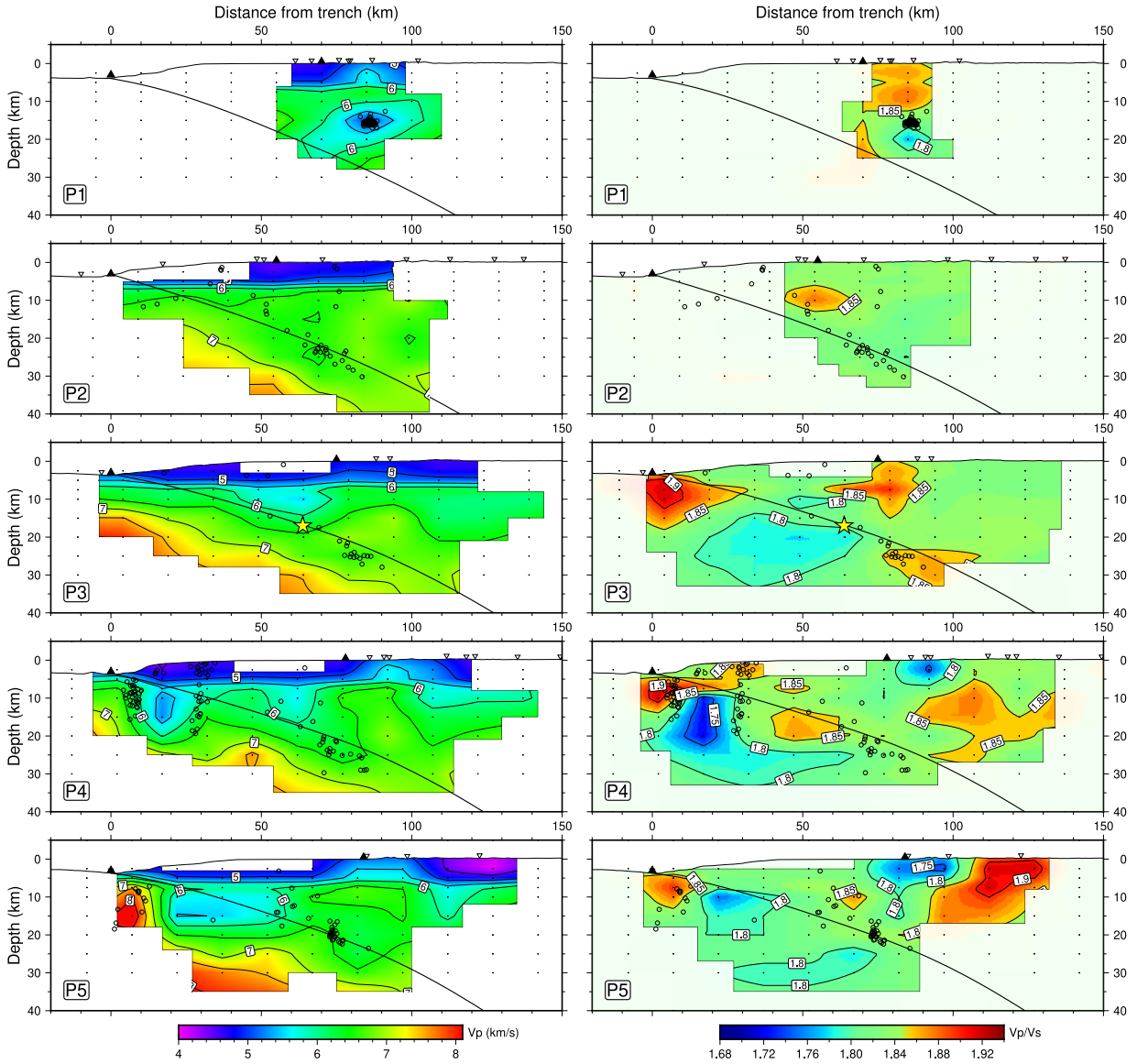

Figure 6.8: 3D velocity model, cross sections P1-P5. Three-dimensional models for both Vp (left) and Vp/Vs (right) along W-E profiles. Velocities and Vp/Vs ratios are color coded and iso-contours are plotted every 0.5 km/s and 0.05 for Vp and Vp/Vs, respectively. Also, based on resolution estimated by the MRM and checkerboard test, results for non resolved areas are faded. Location of the profiles is shown in Figures 6.6 and 6.7. Width for projection of hypocenters and stations is 22 km. Relocated hypocenters are plotted in black circles, and stations are shown by inverted triangles. Grid nodes are displayed in black crosses and solid black triangles represent the projection of the trench and coastline. Finally, yellow star in P3 indicates the hypocenter for the 2016 Pedernales earthquake (Nocquet et al., 2017).

forming an active flower-like fault structure in the marine forearc; however, our model does not show clear evidence to support that hypothesis. Southermost profiles P9 and P10 image reduced ratios covering a large area in the overrding plate. These anomalies can be associated with the San Lorenzo formation (SL –Figure 6.6) mapped by (Reyes and Michaud, 2012) and also observed by Lynner et al. (2020) and Koch et al. (2020).

Iso-velocity contours of Vp ∼6.0-6.2 km/s in cross sections (see Figures 6.8 and 6.9) also contribute to imaging a transtion zone in the marine forearc at depth above the interplate, which separates a wide deformed, eroded and fractured trenchward region of accreted oceanic

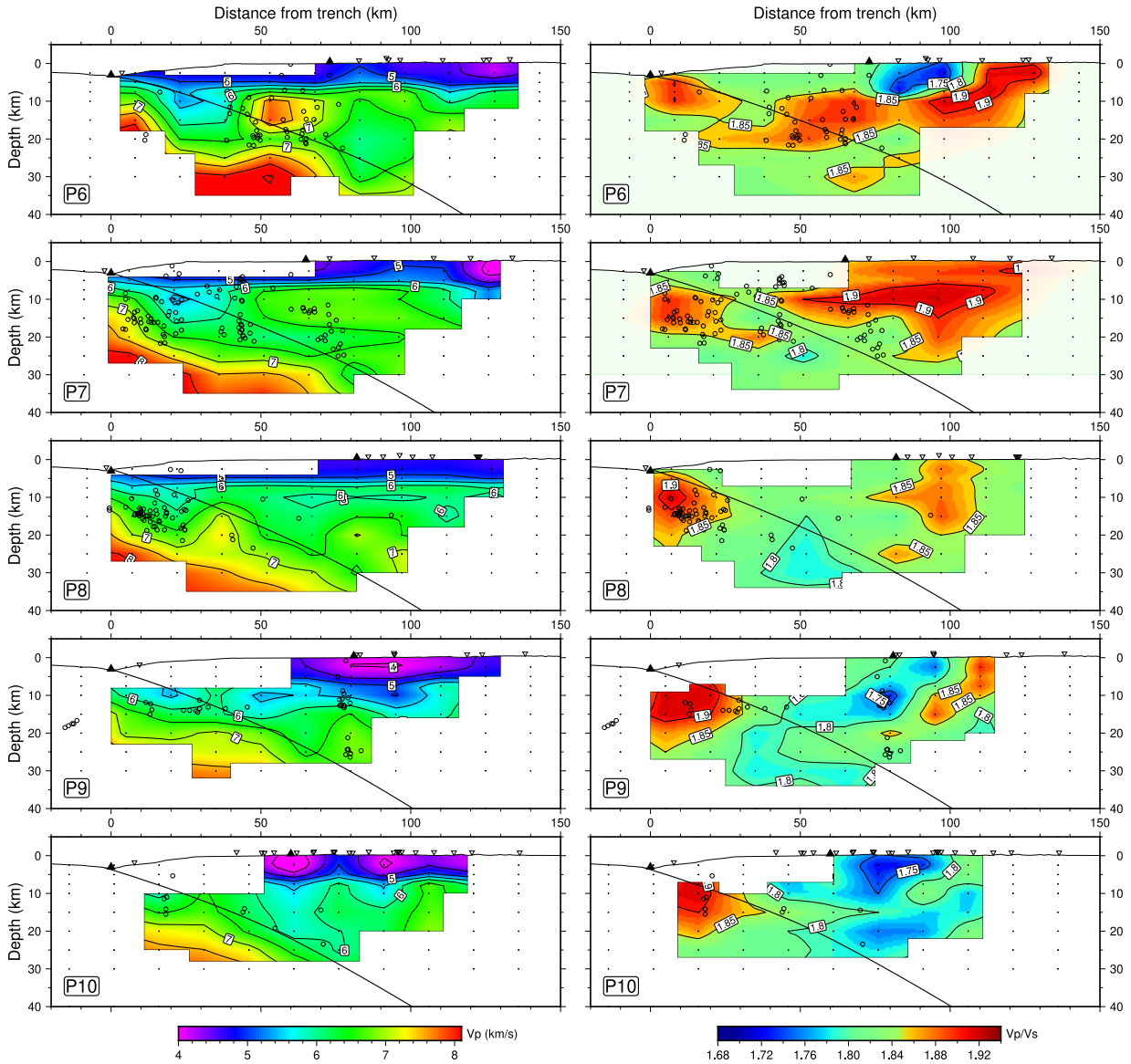

Figure 6.9: 3D velocity model, cross sections P6-P10. Three-dimensional models for both Vp (left) and Vp/Vs (right) along W-E profiles. Based on resolution estimated by the MRM and checkerboard test, results for non resolved areas are faded. Relocated hypocenters are plotted in black circles, and stations are shown by inverted triangles. Grid nodes are displayed in black crosses and solid black triangles represent the projection of the trench and coastline. See Figure 6.8 for further details.

Cretaceous rocks, with Vp ~5.5 km/s, from a deeper more consolidated, less deformed and more mechanically resistant area to the east (Vp>6 km/s and depth > 7 km; Gailler et al. (2007); Cano et al. (2014)). Following this iso-velocity contours (Vp ~6.0-6.2 km/s) along the vertical sections (see Figures 6.8 and 6.9), we observe that in profiles P3-P5, the transition zone is located between 50 to 60 km eastward of the trench and might be related to the west limit of the Piñon formation imaged at shallower depths by reduced Vp/Vs ratios (~1.75). As suggested by Wang and Bilek (2011) and Marcaillou et al. (2016), this possible highly damaged frontal zone can prevent seismic rupture to nucleate at shallow depths on the megathrust fault. The eastern limit of this frontal domain could indicate a major feature controlling the up-dip rupture extension of moderate-magnitude megathrust earthquakes such as the Mw 7.8 in 1942 and the Mw 7.8 in 2016

occurring on the deeper portion of the fault. Similar behavior has been proposed by Cano et al. (2014) for the northern Esmeraldas region and the Mw 7.7 earthquake in 1958 (see Figure 6.1). As the ∼50-60 km wide low velocity wedge is directly affected by the subducting plate and the possible frontal erosion caused by the incoming topography (Dominguez et al., 1998; von Huene et al., 2000; Sage et al., 2006), it is expected that the accreted volcanic rocks that shaped the oceanic terranes in the outermost forearc on this region are fluid-saturated, altered and disaggregated (Contreras-Reyes et al., 2012; Cano et al., 2014; Marcaillou et al., 2016). Finally, towards southern profiles (P6-P8), the described transition zone reduces its extension to less than 40 km (at ∼10 km depth) leading to a margin with Vp ∼6 km/s, consistent with the observations made by Gailler et al. (2007).

Subducting Oceanic Lithosphere

In general, as it is shown in Figures 6.8 and 6.9, Vp velocities resulting from our 3DVM image a predominant area of Vp ∼4.5-7.5 km/s dipping eastward associated to mid oceanic ridge basalts (MORB) and basaltic lavas formed at a spreading center that compose the oceanic crust (White et al., 1992), but also to serpentinized rocks that contribute to reduce Vp values (Marcaillou et al., 2008). Because of inherent limitations of our dataset and model, with in-depth grid node spacing of 5 km (down to 30 km depth), we cannot assess an exact value for the oceanic crustal thickness. Considering the iso-velocity contour of Vp 7.5 km/s that mimics the Moho, we have some insights on the downgoing plate characteristics. On average, we observe no significant changes in oceanic crustal thickness that appears to be around 15 km (see Figure B13). An abnormally thick oceanic crust has been previously observed by marine seismic experiments (Sallarès et al., 2003, 2005; Gailler et al., 2007) in the area that is related to the presence of the CR. Our tomography shows similar velocites for the upper crust from previous studies (Sallarès et al., 2005; Graindorge et al., 2004) and the presence of the CR is on all profiles where the base of the oceanic crust is resolved from P3-P9, highlighting its extension under the margin. The CR resulted from the cooling of mantle melted material originated ∼15-20 Myr B.P. by the interaction between the Galapagos hot spot and the Cocos-Nazca spreading center (Lonsdale, 1978; Sallarès et al., 2003; Gailler et al., 2007), adding material to the lower layers of the oceanic crust and shifting the Moho location to greater depths (see z=20 km in Figure 6.7, Figure 6.8 and 6.9). Furthermore, looking at the along strike variations of the 7.5 km/s iso-velocity contour on profiles P4 to P7 (see Figure B13 in Appendix B), the flattening of the contour at ∼40 km from the trench shows a thinning of the downgoing crust that could be interpreted as the eastern border of the CR or strong variations of the CR structure (see Figure 6.10). If indeed we observe the eastern border of the CR, it seems to be close to the coast, not having reached it yet. This position of the eastern border of the CR is consistent with the extension of the Malpelo ridge, as both were part of the same ridge (Lonsdale, 1978). Such interpretation implies a prior process that resulted in the coastal Cordillera uplift such as stripping events at the base of the forearc crust (Menant et al., 2020) and/or deep slab folding at depth (Cerpa et al., 2015).

In terms of Vp/Vs, we image elevated ratios of ∼1.85 dipping eastward, close to the trench. This feature is intersected with Vp/Vs ratios ∼1.80 related to the oceanic terranes (see profiles P3-P5

in Figure 6.8). We observe differences in the Vp/Vs ratios betweeen north (P2-P5) and south (P6-P10) segments along the downgoing plate. The CR shows high Vp/Vs ratio anomaly (>1.85) that changes to normal oceanic values when the slab reaches 10 km depth (P6-P10), associated with seismicity on P7-P9. To the north, this feature seems affected by the low Vp anomaly observed on P4-P5, and shows a low Vp/Vs value.

Elevated Vp/Vs close to the trench

Our 2DVM (see Figure 6.5) shows for the north and south segments elevated Vp/Vs ratio contours (>1.85), illuminating the subducting oceanic crust close to the trench. However, both profiles reached values > 1.90 indicating a highly hydrated region. More in detail, the 3DVM helps us to identify the areas where these highs in Vp/Vs ratio are located. Horizontal slices, at z=5 km, in Figure 6.6, show two small patches of Vp/Vs $\sim$1.85 located at 0°and 0.5°N. Similarly, slice at z=10 km (see Figure 6.7) imaged two N-S elongated anomalies of elevated ratios (>1.85) that extend for $\sim$50 km in the north, and $\sim$100 km in the south, respectively. High Vp/Vs ratios along the trench axis have been observed along other subduction zones (e.g. northeastern Japan (Nakajima et al., 2001), central Chile (Haberland et al., 2009; Hicks et al., 2014) and Costa Rica (Bangs et al., 2015). This feature is associated with the lithology of the oceanic crust, the presence of fluids from dehydrating subducted sediments (Husen et al., 2000), and hydrated oceanic crust with extensional faults formed before subduction in the outer-rise (von Huene et al., 2004). The central Ecuadorian subduction zone has been described as an erosive margin with a low input of sediments (Collot et al., 2002; Gailler et al., 2007; Marcaillou et al., 2016), and therefore other mechanisms explaining the elevated Vp/Vs along the trench are needed. Cross sections P4-P5, in Figure 6.8, suggest a positive relation between subducting topography and elevated Vp/Vs ratios (>1.85) on the edges of these features. Moreover, the seismicity distributed with a sub-vertical disposition of $\sim$10 km length inside the oceanic crust gives us insights about possible deformed and fractured areas caused either by the collision of bathymetric features with the overriding plate and/or the reactivation of extensional faults on the Nazca plate, created by the outer rise bending prior subducting (Von Huene and Culotta, 1989; von Huene et al., 2004). In Figure 6.10, we suggest that the high ratios imaged by our Vp/Vs model are also associated to the subduction of bathymetric features, such as the Atacames seamounts, which cause deformation and generation of weakness areas close to the trench. This process contributes to have high rates of fluids migration by increasing the porosity and permeability on both plates involved. On the other hand, the broader extension of elevated Vp/Vs ratios >1.85 in the southern segment (P6-P10) are mainly related to the presence of the CR and its sharp topography (see Figure B14). This bathymetric feature and the previously mentioned outer rise bending contribute to a pervasively fractured and highly hydrated oceanic crust.

Low velocities in the oceanic crust

Our 3DVM illuminates a highly heterogeneous margin which is largely affected by the presence of topographic features on the seafloor. Horizontal slices at z=10 km (see Figure 6.7) show a

prominent elongated N-S feature with Vp ~5.5 km/s located ~10 km eastward of the trench axis. Restoring and inversion tests (see Figures B8, B9, B10 and B11 in Appendix B) support the robustness of this intriguing feature. Moreover, the inspection of the MRM along strike (see Figure B15) show small SF and rounded 70% contour lines indicating a reduced along strike smearing and therefore a well resolved area. The along strike length of this anomaly (~130 km) is consistent with the incoming bathymetric structures in the area (see Figure B14). Moreover, lower Vp (~5.0 km/s) anomalies are confined to smaller areas in P4, P6-P7 and P9. These observations can be complemented by collocating the observed Vp to the imaged Vp/Vs ratios. Horizontal slices in Figures 6.6 and 6.7 allow us to estimate the dimension of the observed features by imaging a rounded, ~15 x 25 km2 (at z=10 km), relatively low Vp/Vs ratios anomalies (~1.80), located around P4.

Cross sections in Figure 6.8 and 6.9 help us to discuss the in-depth extension of the observed anomalies. Here we focus on P4 which shows a promiment low Vp body (~5.0-5.5 km/s) at ~20 km from the trench that it is flanked by two areas Vp ~6.0 km/s on the sides. This feature agrees in shape and location with the observations described by Marcaillou et al. (2016) who estimated a ~2.5 km high seamount through an active seismic experiment. It also matches with the residual bathymetry derived by Agurto-Detzel et al. (2019) (see Figure B14). Therefore, we interpret the observed low Vp anomaly as a seamount coming from the Atacames seamount chain, in the northern edge of the CR (P4, Vp ~5.0 km/s) surrounded by Vp ~5.5 km/s that could be related to possible thermal anomalies associated to the origin of these structures and/or possible serpentinization as observed farther north by Marcaillou et al. (2008).

The seismicity distribution also contributes to reinforce our interpretation. In P4 (see Figure 6.8), we observe two vertical clusters of aftershocks suggesting that the flanks of the seamount are under a high stress regime promoting faulting and seismic stress release. The clustered seismicity allows us to estimate a ~15-20 km lateral extension of this feature.

In relation to the origin of the observed low velocities, studies in young seamounts have shown that it is possible to observe low Vp in its structure (eg. Caplan-Auerbach and Duennebier (2001); Kopp et al. (2004)). In the case of the Ecuadorian margin, it has been estimated that the Atacames seamounts were created around ~15-20 Myr ago in the Galapagos hot-spot (Lonsdale, 1978; Sallarès et al., 2003) which fits with the young age hypothesis. Moreover, the erosive margin might have contributed to increasing the pressure along the seamount axis creating weaker areas in its base leading to the observed reduced velocities.

Further south, the negative relation between low Vp (~5.5 km/s) and high Vp/Vs (~1.85) suggest a different interpretation for this segment. Between P6-P8, we observe a broader low Vp (~5.5 km/s) anomaly that might correspond to material of the CR. Moreover, the elevated Vp/Vs ratios (~1.85) imaged along P6-P10 might point to a deeply fractured and highly hydrated incoming CR.

Structures controlling the seismicity

Figures 6.6, 6.7, 6.8 and 6.9 show the distribution of the seismicity contrasted by the Vp and Vp/Vs 3DVM. Although, most of the relocated aftershocks are distributed along the plate interface, we identified several clusters of seismicity that can be related to structural features imaged by our 3D

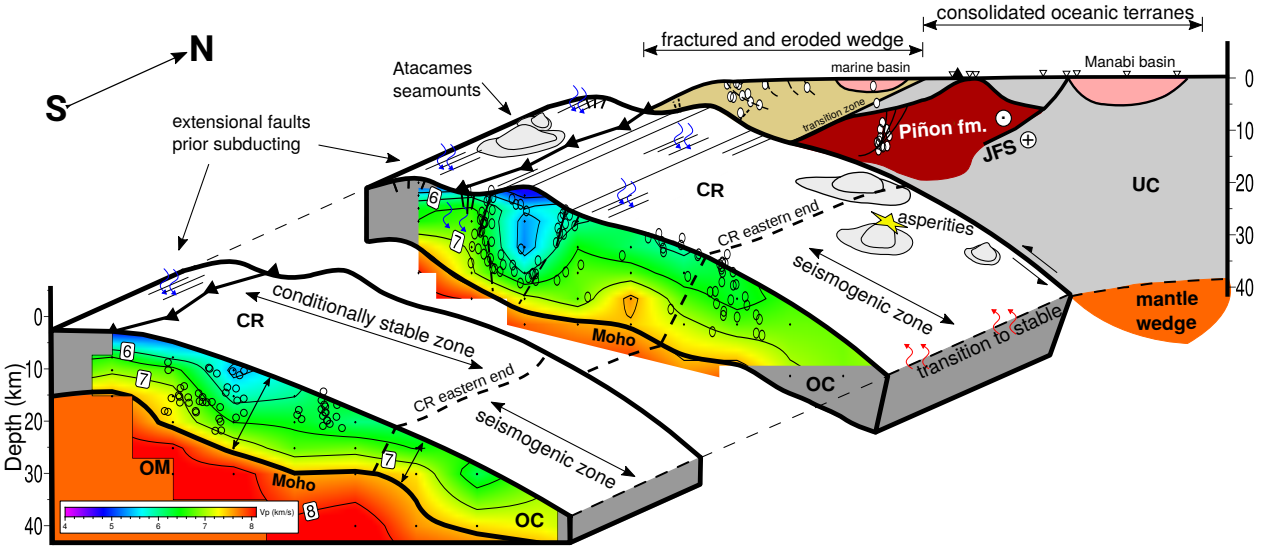

Figure 6.10: Interpretative scheme of the Ecuadorian margin. Structural synthesis based on the main findings of this work around profile P4. UC: upper crust, OC: oceanic crust, OM: oceanic mantle, JFS: Jama fault system, with strike-slip displacement indicated by the dot and cross. Transition betweeen the marine wedge and continental basement is indicated by a master fault represented by a solid black line dipping trenchward. Vp velocities at P4 are projected on the front side of the image. Hypocenters are shown in circles. Black triangles represent the trench axis and the coastline. Inverted triangles indicate station locations. Yellow star represents the epicentre of the 2016 Pedernales earthquake (Nocquet et al., 2017). Vertical scale exaggeration 1:1.5.

velocity model.

As we mentioned before, between latitudes ∼1°N and ∼2°S, the Atacames seamounts and the CR contribute to increase deformation and therefore to create and/or reactivate extensional faults in the Nazca plate. This process, plus the bending of the plate prior subducting that causes extensional faulting, facilitates the occurrence of clustered seismicity along small-scale faults in the oceanic crust (see Figure 6.10). In the case of the Atacames seamounts, its influence on the Ecuadorian margin can be observed in the bathymetry of the marine forearc (von Huene et al., 2004; Collot et al., 2005; Barnes et al., 2010; Marcaillou et al., 2016), and also inferred by the seismicity detected at shallow depths in the marine eroded wedge suggesting a highly fractured region. Subducted seamounts can also act as asperities/barriers at greater depths (>15 km) contributing to the nucleation and/or stop of intermediate-magnitude (M 7.5-8.0, Bilek et al. (2003)) megathrust earthquakes (Watts et al., 2010; Wang and Bilek, 2011).

The CR seems to be the main feature controlling the seismicity in the margin between P3-P10. Several studies have suggested that ridges may act aseismically and/or promote creep on the megathrust fault accompanied with small events (eg. Wang and Bilek (2014)). For the CR, Gutscher et al. (1999) described how large earthquakes have not rupture across this feature. Graindorge et al. (2004) suggested a greater period of recurrence of large earthquakes in that region in comparison with the northern segment. Recently, Agurto-Detzel et al. (2019) also proposed differences on the slip behavior for North and South segments. Based on the imaged Vp and Vp/Vs models, we suggest that this large-scale marine feature might contribute to a deeply fractured and highly hydrated oceanic crust promoting the circulation of fluids to greater depths (∼20-30 km). Fluids would change the local behavior on the slab interface from unstable slip to

conditionally stable (Kodaira et al., 2004) and therefore impede the occurrence of large megathrust earthquakes. These conditionally stable parts seem also favorable for SSE (e.g. Tokai segment in Nankai trench) and has been described in the area by Rolandone et al. (2018).
In the upper crust, several small- to large-scale faults might have been activated after the 2016 Pedernales earthquake. The shallow clustered seismicity observed close to the Esmeraldas city (∼1°N) is related to extensional mechanism (Hoskins et al., 2018; Agurto-Detzel et al., 2019) and can be associated to the activation of the Tanigüe fault (Michaud et al. (2015) –see Figure 6.1) which may extend down to ∼15 km reaching a low Vp/Vs rounded-like body (∼1.80) capable to produce this type of confined aftershocks. To the south (∼1°S), we observe clustered vertically-aligned seismicity, at ∼10-15 km depth, in the southernmost profile P9. Figure 6.1 helps us to relate these events with the surface projection of the El Aromo fault (F6 in Figure **??**) which has been previously described as an active structure by Segovia et al. (2018) and it is well imaged in our Vp/Vs model by a strong contrast between elevated and reduced ratios (see P9 in Figure 6.9).

6.7 Conclusion

Using the unprecedented rapid deployment that recorded the aftershock sequence unfolded by the 2016 Pedernales earthquake, we built a high-quality dataset of manually picked, P- and S-phases which were used to derive a 3DVM for Vp and Vp/Vs. We imaged the velocity structure of the central Ecuadorian subduction zone and associated with the geological and seismotectonics contexte of the region. P-wave velocities (∼4.5-7.5 km/s) in the downgoing plate highlight the roughness of the incoming oceanic crust. Moreover, the observed Vp/Vs anomalies ranging from 1.74 to 1.95 suggest a heterogeneous and hydrated margin. We imaged the subduction of large-scale bathymetric features, such as the Atacames seamounts and the CR, which seems to contribute to the high circulation of fluids, especially close to the trench.
These features also play an important role in controlling the seismic behavior of the margin. We identified a subducting seamount, part of the Atacames chain, which is imaged by Vp ∼5.0 km/s and Vp/Vs ratios ∼1.75 that we related to young magmatic material. The Carnegie Ridge seems to be the main feature controlling the seismicity in the region, by promoting creeping and SSE caused by fluids migrating from a deeply fractured and highly hydrated oceanic crust. This fact is directly linked to the updip rupture limit of large megathrust earthquakes in the northern segment and the absence of large megathrust earthquakes in the southern region over the instrumental period.
Finally, our observations show the relevance of having well resolved Vp and Vp/Vs models that complement each other in order to give a full interpretation, especially in highly heteregeneous and segmented regions such as the Ecuadorian margin.

Acknowledgments

This study was supported by IGEPN, IRD, the INSU-CNRS and the ANR grant REMAKE ANR-15-CE04-0004. The UK portion of the temporary deployment was supported by NERC grant NE/P008828/1. The US portion of the temporary deployment was supported by IRIS PASSCAL and NSF RAPID Program Award EAR-1642498. SLR acknowledges partial support from ANID under Programa Formación de Capital Humano Avanzado, Becas Chile (Grant 8068/2015). HAD acknowledges support from ANR project ANR-15-CE04-0004 and UCA/JEDI project ANR-15-IDEX-01. We are also indebted to the people at Geoazur laboratories and INOCAR by its contribution in the installation of OBSs at sea in very harsh environments. Also we extend the acknowledgment to the staff at IGEPN for the continuous support during the deployment and service of the inland stations. Data available at IRIS website http://www.iris.edu/dms/nodes/dmc/ using the network code 8G (Meltzer and Beck, 2016), EC (Alvarado et al., 2018) and G (Institut de Physique du Globe de Paris , IPGP). Data from the emergency deployment XE available through Regnier et al. (2016). Aftershocks catalog is available through Agurto-Detzel et al. (2019). Model data will be available in the KIT open repository. Finally, the authors want to thank all the people in Ecuador who allowed us to install our stations in their houses, big thanks for your hospitality, patience and help when it was needed.

Chapter 7

Physical properties controlling the rupture of the Pedernales earthquake

In this chapter, I focus on describing the relation between the seismic velocity structures imaged along the Ecuadorian margin and the rupture process of the 2016 Pedernales earthquake. Based on our recently derived three-dimensional seismic velocity model (3DVM), I investigate how changes in the seismic velocity structure of the rock material might be associated with the slip behavior along the slab interface during the coseismic stage. This chapter is under preparation to be submitted as a research article.

Abstract

Limits of coseismic slip along the plate interface have been usually associated to areas acting as barriers that stop the rupture propagation. For large earthquakes (M>8.5), the velocity structure along rupture areas shows that coseismic slip spread along the margin without discriminate changes in velocities. At a smaller scale, a negative relation has been observed between Poisson's ratio and seismic coupling. However, variations of the physical properties, such as body wave velocities, along the slab interface and its influence on the extent of coseismic slip have been overlooked. Based on the 3D seismic velocity model derived for the central Ecuadorian margin, we study the links between variations of the Vp/Vs ratios along the megathrust and the rupture limits of the 2016 Mw 7.8 Pedernales earthquake. We check rupture-scaling relations and applied a grid search approach to explore the Vp/Vs distribution across multiple rupture scenarios. Furthermore, by relating the observed Vp/Vs ratios to the frictional properties of the margin, we estimated a range for the critical slip distance D_c of the 2016 rupture. Our findings show that the mainshock occurred in the only possible area capable of hosting an earthquake with the observed size. Moreover, the up- and down-dip limits of the event are controlled by elevated Vp/Vs (>1.84) surrounding the rupture. Finally, the estimated range for D_c is in the same order of magnitude as that observed by geodectic inversions during the coseismic stage of the Pedernales rupture.

7.1 Introduction

Observations along seismogenic zones in megathrust environments have discussed that the limits of the seismogenic zone are defined by unconsolidated sediments (Byrne et al., 1988) and stable sliding clays (Vrolijk, 1990) in the updip portion, and thermally limited (Tichelaar and Ruff, 1993; Hyndman and Wang, 1993) or controlled by the interaction of the megathrust with the forearc Moho (Ruff and Tichelaar, 1996) at the downdip edge. Lay et al. (2012) suggested areas for stabe sliding for the updip limit of the seismogenic zone and areas prone to creep and/or produce slow slip events in the downdip limit. For rupture extending along the seismogenic region, local bathymetric features such as ridges, seamounts and peninsulas have been identified as features capable of controlling the slip propagation (Bilek et al., 2003; Bilek, 2010; Watts et al., 2010; Wang and Bilek, 2011; Collot et al., 2017). On this matter, the local heterogenities of each margin have shown links between the distribution of Vp/Vs ratios and the rupture boundaries along the slab interface. The difficulties to study the oceanic-continental margin (e.g. lack of observations and coarse resolution offshore) have prevented to further constrain this link for moderate-magnitude (M 7.5-8.5) earthquakes.

A direct method to analyze the seismic properties in subduction areas are tomographic images of travel time arrivals which allow us to obtain the variation of P- and S- wave velocities and its corresponding ratios (Vp/Vs) in certain region of interest (Anderson and Dziewonski, 1984). For the 2012 Nicoya earthquake in Costa Rica, Audet and Schwartz (2013) associated the south-eastern limit of the coseismic slip with areas of elevated Vp/Vs ratios. Similar results are observed for the 2015 Illapel, Chile earthquake, where the rupture was unable to cross a region with high Vp/Vs ratios located in the southern part of the mainshock Liu et al. (2018). These observations suggest that the distribution of Vp/Vs ratios might be indicative for areas of stable sliding (or no stress accummulation). The image of the distribution of Vp and Vp/Vs ratios along the slab interface can also help us to investigate how physical properties affect frictional behaviors of the seismogenic megathrust, such as the loading system stiffness (k, fault surrounding rocks) and the critical slip distance (D_c). These parameters are related by the rate-and-state law (Marone, 1998) which for unstable stick-slip behavior (i.e. earthquake rupture) needs to be less than the critical rheologic stiffness (k_c; Leeman et al. (2016))

$$k < k_c = \frac{\sigma_{n'}(b-a)}{D_c} \tag{7.1}$$

Here, the frictional rate parameter $(b-a)$ is roughly consistent between laboratory and filed/modelling-based estimation (Marone, 1998). The critical slip distance D_c, defined by Dieterich (1979) as the slip necessary to renew surface contacts, however, shows many orders of discrepancy between lab-measurements and those from dynamic rupture modelling. Thus, there are still no concensus on its value, range and physical interpretation and the D_c is imposed a priori and then assumed constant and uniformly distributed on the fault plane.

The b-value has been widely used to describe the stress regime and the tectonic characteristics of a region of interest (Jin and Aki (1989); Wiemer and Katsumata (1999); Schorlemmer et al. (2005); Sobiesiak et al. (2007); Tassara et al. (2016); among others). Although the b-value can be

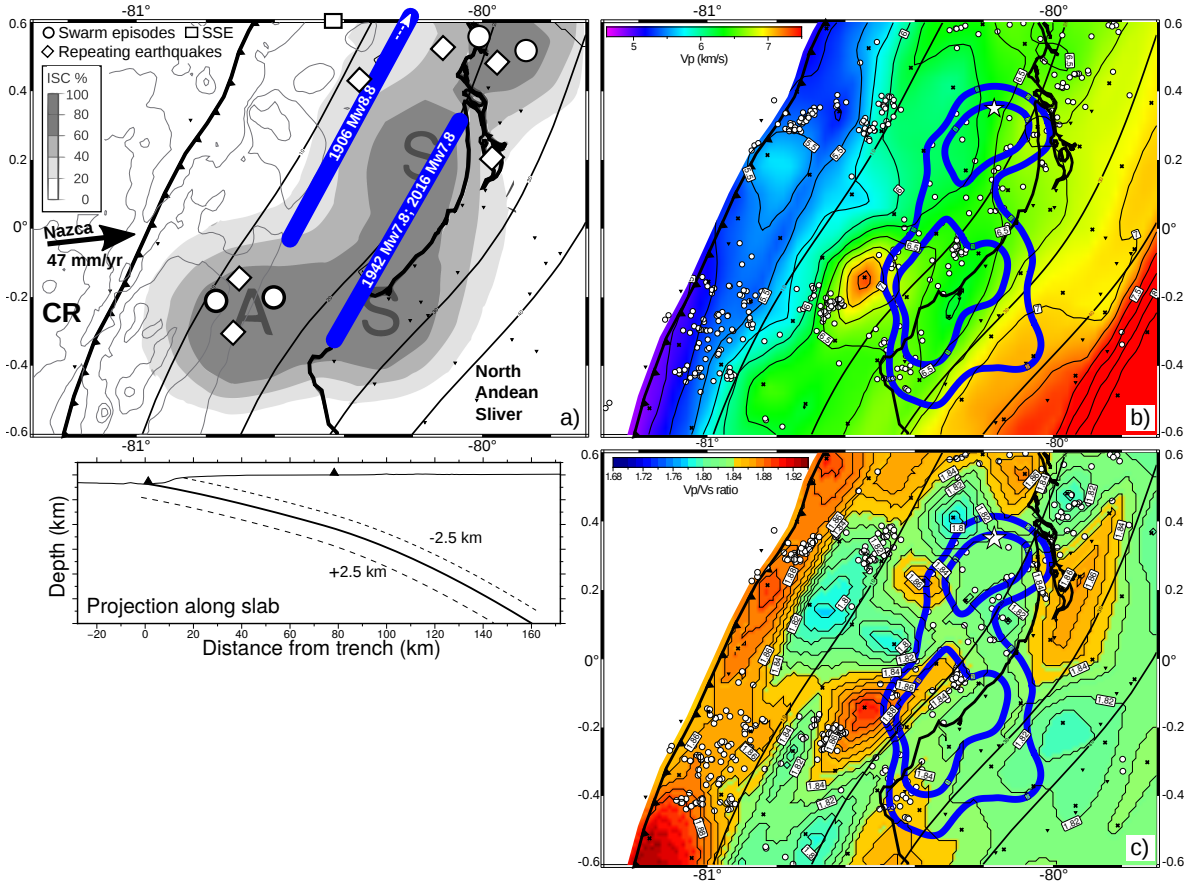

Figure 7.1: **a)** Seismotectonic setting of the study area. Solid blue lines represent the extension of the 1906 Mw 8.8, 1942 Mw 7.8 and 2016 Mw 7.8 earthquakes occurred in the area. The convergence rate between the Nazca plate and the North Andean Sliver is ∼47 mm/yr (Nocquet et al., 2014). Circles, diamonds and squares indicate swarm episodes (Segovia, 2001; Segovia et al., 2009; Vaca et al., 2009), repeating earthquakes (Rolandone et al., 2018) and slow slip events (SSE, Mothes et al. (2013); Vallée et al. (2013); Chlieh et al. (2014); Collot et al. (2017); Segovia et al. (2018); Vaca et al. (2018); Rolandone et al. (2018)) that have been identified along the margin. Interseismic coupling from (Nocquet et al., 2014) is shown in gray colorscale. Residual batimetry from Agurto-Detzel et al. (2019) is plotted for the offshore region. A: Aseismic zone, S: seismic zone, CR: Carnegie ridge. **b)-c)** Vp and Vp/Vs structures projected along a ±2.5 km region around the slab interface (see inset). White star represents the epicenter of the 2016 Mw 7.8 Pedernales earthquake (Nocquet et al., 2017) and solid blue line shows its corresponding 2 m and 3 m coseismic slip contour derived by (Gombert et al., 2018).

related to physical and mechanical properties, it cannot be interpreted as a direct observation as it requires certain assumptions (e.g. fault geometry, roughness, stress change, among others) that are still under debate. The recently three-dimensional velocity model (3DVM) derived using local earthquake tomography based on the aftershock sequence of the Mw 7.8 2016 Pedernales, Ecuador earthquake (León-Ríos et al., 2020) provides such opportunity to constrain the physical properties of the rocks surrounding the plate interface. We investigate how the distribution of the Vp/Vs ratios along the slab influenced the rupture of the 2016 earthquake in Pedernales. Furthermore, by using the observed Vp and Vp/Vs ratios, we determine the possible range of D_c of seismic rupture in nature. The tomographic results shed light on the seismic velocity structure along the megathrust, while the study of the 2016 rupture and its physical properties provide relevant information for the estimation of seismic hazard.

7.2 Characteristics of the Ecuadorian margin

7.2.1 Seismotectonic setting

The central coastal region of Ecuador between 1°N and 1°S is characterized by rapid convergence (∼47 mm/yr) of the oceanic Nazca plate and the North Andean Sliver (NAS; Kendrick et al. (2003); Nocquet et al. (2009, 2014)), part of the South American continental plate (Figure 7.1). The low input of sediments and rough bathymetry leads to an erosive margin (Collot et al., 2002; Marcaillou et al., 2016) with a high degree of segmentation along strike Gailler et al. (2007). It is suggested that the region is mainly controlled by the aseismic Carnegie Ridge (CR; e.g. Gailler et al. (2007); Agurto-Detzel et al. (2019); León-Ríos et al. (2020)). This feature adds roughness to the incoming bathymetry, acting as a barrier for megathrust ruptures to the north (lat$\gtrsim$0°) and preventing the occurrence of moderate-magnitude (M>7.5) earthquakes to the south (lat$\lesssim$0°). The CR contributes also to diversifying the seismic behavior (Agurto-Detzel et al., 2019) by promoting slow slip events (SSE, Mothes et al. (2013); Vallée et al. (2013); Chlieh et al. (2014); Collot et al. (2017); Segovia et al. (2018); Vaca et al. (2018); Rolandone et al. (2018)), repeating earthquakes (Rolandone et al., 2018) and seismic swarms (Segovia, 2001; Segovia et al., 2009; Vaca et al., 2009) which are mainly located south of the equator between 0°and 2°S (Figure 7.1).

7.2.2 Seismic velocity model

Based on our 3DVM (León-Ríos et al., 2020), we further explore the seismic velocity distribution along the plate interface and its relation with the rupture area of the 2016 Pedernales earthquake. We check the degree of dependency between the solution and the grid node configuration, and obtain averaged Vp and Vp/Vs models that are subsequently projected along the slab interface (see Methods). The imaged P-wave velocities range between 4.5-7.2 km/s along the plate interface. We identified a low Vp (∼5.5 km/s) area, located close to the trench at ∼0.2°N, that we interpreted either as thermal anomalies produced at the Galapagos Hot Spot or shallow serpentinization (León-Ríos et al., 2020; Marcaillou et al., 2008). At the northern end of the CR (∼0.2-0.4°N), an isolated offshore feature with P-wave velocities ∼5.0 km/s was associated with a seamount part of the Atacames seamount chain (León-Ríos et al., 2020; Marcaillou et al., 2016). The eastern end of the CR is still under discussion, however the imaged Vp structures (León-Ríos et al., 2020) suggest that the CR ends close to the coastline. The eastern end of the CR can be associated to the slab depths observed along the margin which shows a wider and smoother dipping region north of the ∼0.2°N and a narrower and steeper slab in the southern area (∼0.2°N- ∼0.6°S; see Figure 7.1). The region between the 10 km and 40 km slab-depth contour shows Vp ∼6.0-7.0 km/s which suggests a more mechanically stable region in agreement with the typical extent of seismogenic zones (Ruff and Tichelaar, 1996; Hyndman et al., 1997). Below the 40 km slab-depth contour, Vp>7.2-7.5 km/s are consistent with upper mantle velocities described in the area (e.g. Gailler et al. (2007); Cano et al. (2014); Figure 7.1).

Tomographic images along the slab interface also show a region that is mainly dominated by areas around Vp/Vs ∼1.80-1.84. This is consistent with the average value derived by León-Ríos et al.

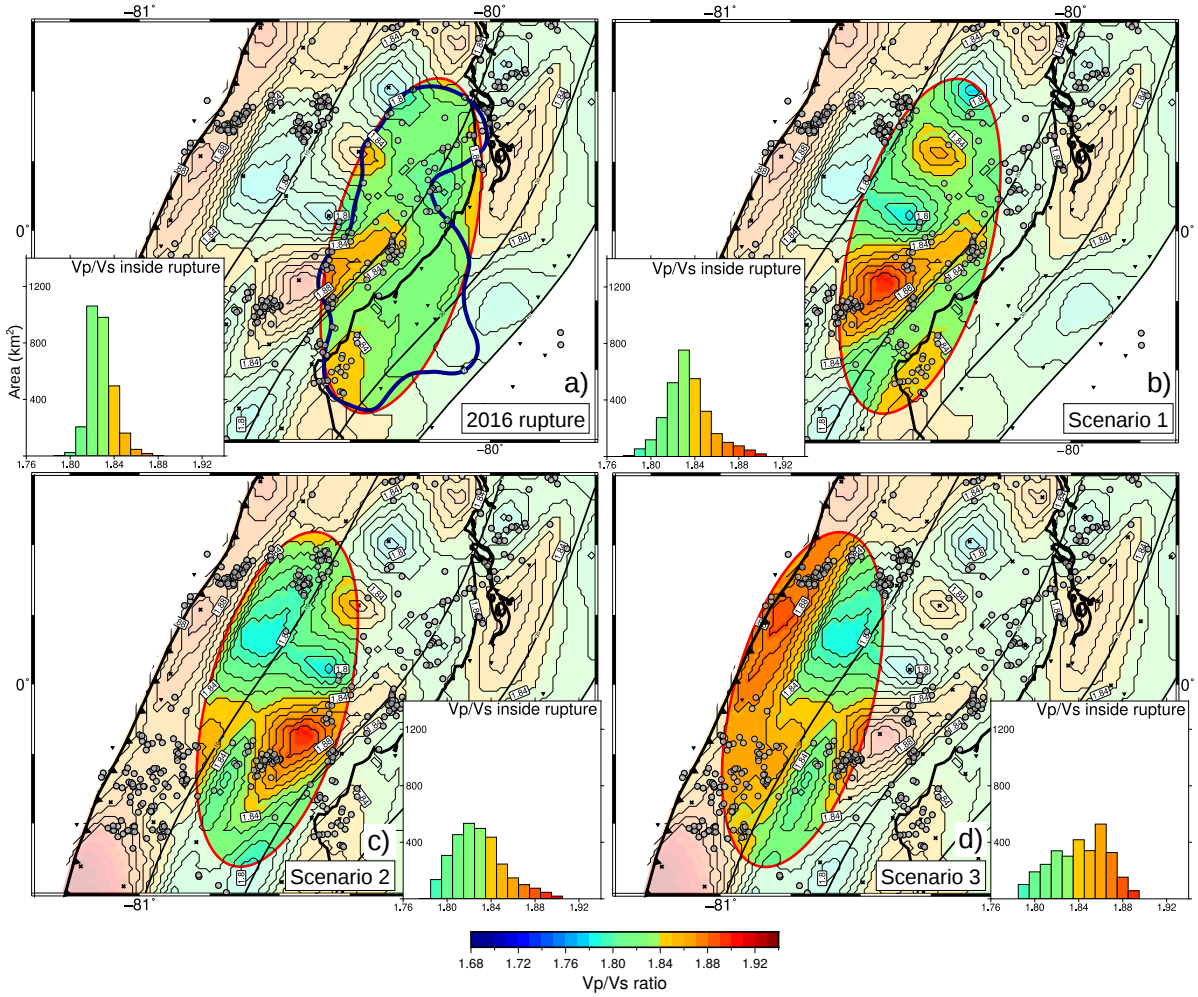

Figure 7.2: **a)** 2016 Pedernales rupture represented in blue by its 2 m coseismic slip contour (Gombert et al., 2018). Red ellipse shows the simplified rupture area estimated by rupture-scaling relations. **b)-d)** Scenarios for three different Mw 7.8 earthquake locations producing a rupture area within the range of the area estimated (A_e). For each case, the center of the ellipse was shifted by 20, 40 and 60 km towards the trench axis. Inset histograms are color coded using the Vp/Vs colorscale and represent the distribution of the Vp/Vs ratios inside the ellipse.

(2019) with a minimum 1D velocity model. In details, we observe elevated Vp/Vs ratios (>1.84) suggesting a highly hydrated area close to the trench and down to the 10 km slab-depth contour. Between the 10 km and 30 km slab-depth contour, the mixture distribution of low (<1.80) and high (>1.84) Vp/Vs ratios indicates a heterogenous forearc. At greater depths along the slab interface (>30 km), the Vp/Vs ratios show values ∼1.82 indicating a less hydrated slab (Figure 7.1). The coseismic slip model (Gombert et al., 2018) show that the 2016 Pedernales earthquake propagated along a region with Vp ∼6.5 km/s and Vp/Vs ratios between 1.80-1.84. The latter values are in agreement with the range given for accreted oceanic rocks (Hyndman, 1979; Christensen, 1996, 2004). In contrast, elevated Vp/Vs ratios (>1.84) fit with areas where aseismic behavior has been identified (Rolandone et al. (2018); Vaca et al. (2018); see Figure 7.1). Moreover, these patches of high Vp/Vs bound the north-eastern and south-western edges of the 2 m coseismic slip contour and might have contributed to stop the rupture extent of the 2016 Pedernales earthquake.

7.3 Quantifying the relation between Vp/Vs and coseismic slip

Based on the hypothesis that the elevated Vp/Vs ratios (>1.84) could have controlled the rupture, we analyzed the Vp/Vs ratios along the slab interface against, under the knowledge of the authors, the coseismic slip models available for the Pedernales earthquake (Nocquet et al., 2017; Gombert et al., 2018; Yi et al., 2018). Using the 2 m coseismic slip contour, we estimated an area (A_{2m}) of 5660 km^2. Subsequently, based on the N-S elongated ruptures observed along the South American subduction zone (Bilek, 2010), we simplified the 2016 coseismic slip to an elliptical shape that follows the (W/L) relation of 0.4 (see Figure 7.2). Subsequently, by considering the rupture-scaling parameters from Allen and Hayes (2017), we calculated the range area expected for Mw 7.8 event (A_e). Values varies from 7211 km^2 to 7870 km^2, which in comparison to A_{2m} are larger by 20-30% (see Methods). We then analyse three scenarios in which the rupture was shifted by 20 km, 40 km and 60 km towards the trench (see Methods). For all the cases, histogram for the Vp/Vs distribution inside the ellipse were produced. We observe that the Pedernales earthquake occurred in a region that it is mostly covered by Vp/Vs values (1.80-1.84). The scenario 1 and 2 show a more disperse distribution of Vp/Vs ratios, with values ranging from 1.78 to 1.88. Finally, the histogram for scenario 3 present a region mainly covered by elevated Vp/Vs ratios ($\sim$1.86, see Figure 7.2).

To further extend the possible scenarios, we explore the whole area affected by the 2016 Pedernales earthquake by following a grid search approach. Here, the simplified elliptical rupture of area A_e varies in its centroid location and striking angle to fully cover the region (see Methods). Based on the overall Vp/Vs ratio of the margin (1.82) and a $\pm$ $\sim$0.02 range for regular ratios (e.g. Husen et al. (2000); Reyners et al. (2006); Nakajima et al. (2001), among others), we defined Vp/Vs>1.84 as high ratios and subsequently map their distribution inside the ellipse (A_{vpvs}). We compare the sizes of A_e and A_{vpvs} by introducing a normalized area coefficient A_N as follows

$$A_N = 1 - \frac{A_{vpvs}}{A_e} \tag{7.2}$$

Thus, the cases where A_N is large will illuminate the regions most likely to host a Mw 7.8 rupture (see Methods). We find that the distribution of the maximum values of A_N coincides with the location of the 2016 Pedernales rupture (see Figure 7.3). For the rest of the cases tested, A_N shows a notorious reduction indicating that a large portion of the ellipse is covered by elevated Vp/Vs (>1.84), which together with the stress state might contribute to reduce the chances of a potential earthquake to propagate (see inset in Figure 7.3). To evaluate if our findings vary depending on the chosen Vp/Vs, we applied the same procedure for Vp/Vs>1.85. Findings show a similar region for a potential rupture (see Figure C5) with the best 20% rupture scenarios having A_N>0.97. These results suggest that the Mw 7.8 Pedernales earthquake occurred in the only area where the margin is, according to the seismic velocity distribution, mechanically capable to nucleate and propagate a megathrust earthquake with the observed characteristics. For large megathrust earthquakes (M>8.5), the velocity structure derived after the 2010 Mw 8.8 Maule, Chile earthquake (Hicks et al., 2014) or the 2011 Mw 9.0 Tohoku-Oki earthquake (Yamamoto

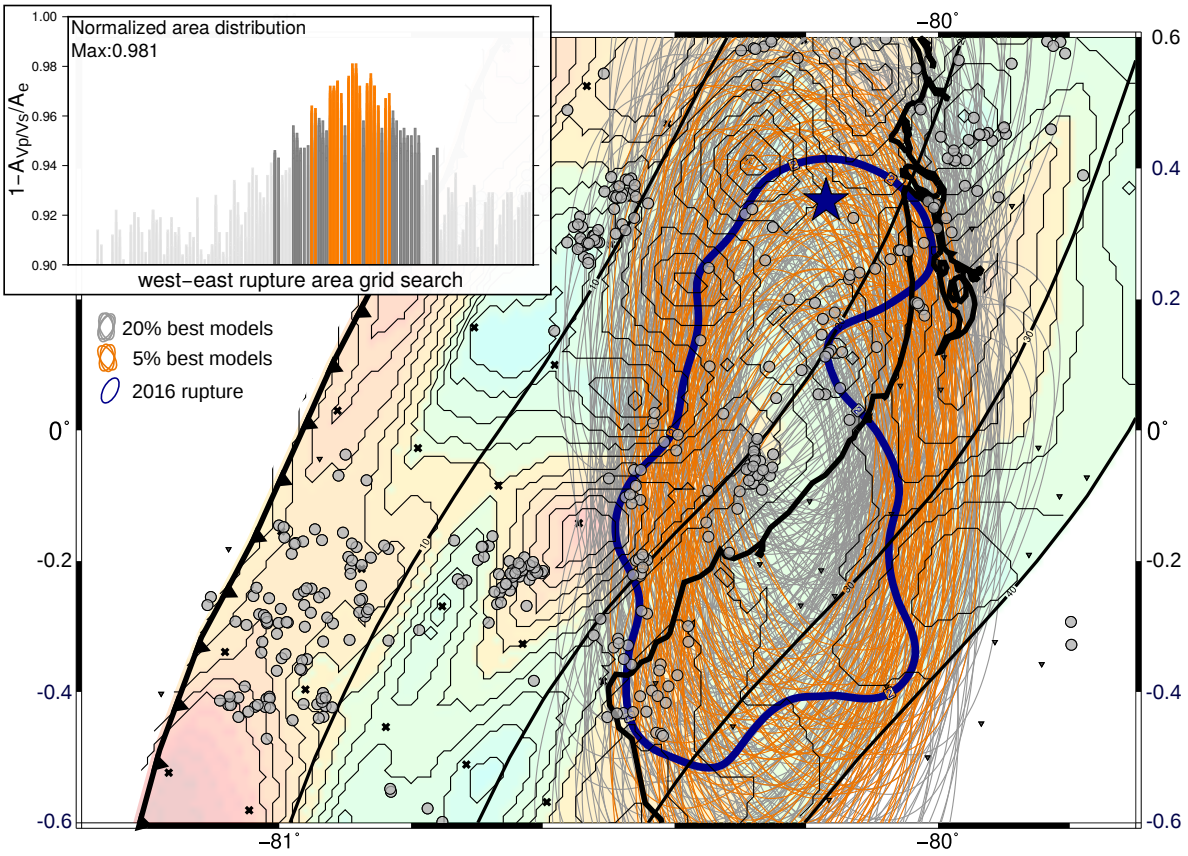

Figure 7.3: Mapview of the rupture area grid search showing the best 20% solutions in gray and the best 5% in orange and its comparison with the 2 m coseismic slip contour (solid blue line) derived by Gombert et al. (2018). The star represents the epicenter of the 2016 Pedernales earthquake (Nocquet et al., 2017) and the solid black lines shown the 10 km depth slab. The inset plot shows a west-east stacked histogram with the 1625 ellipses tested in the region with gray and orange bars representing the 20% and 5% best models, respectively.

et al., 2014) shows that the largest amplitudes of coseismic slip spread along the margin without discriminate specific changes in seismic velocities. In both cases the large magnitude of the events (>8.5) and therefore the amount of energy released suggests that changes in the velocity structure are not sufficient to control the limits of the rupture. The observations in large earthquakes could help to set a threshold for the validity of our method.

7.4 Frictional properties of the seismogenic megathrust

The Vp and Vp/Vs ratios distribution imaged by the local earthquake tomography can also be used to determine the frictional properties in the region. Here we focused on the estimation of the critical slip distance D_c which is a key parameter for numerical simulations of dynamic earthquake rupture propagation (e.g. Andrews (1976a,b); Fukuyama et al. (2003)). D_c cannot be easily inferred from seismological observations (Cocco et al., 2009) and has been mainly measured by laboratory experiments (e.g Okubo and Dieterich (1984); Ohnaka et al. (1987)). However, the latter estimations show many orders of discrepancy between those from dynamic rupture modelling. By combining equation 7.7 (Marone, 1998) and the equations from Goodman and Sundaram (1978) (see Methods), we can obtain a relation for D_c as follows

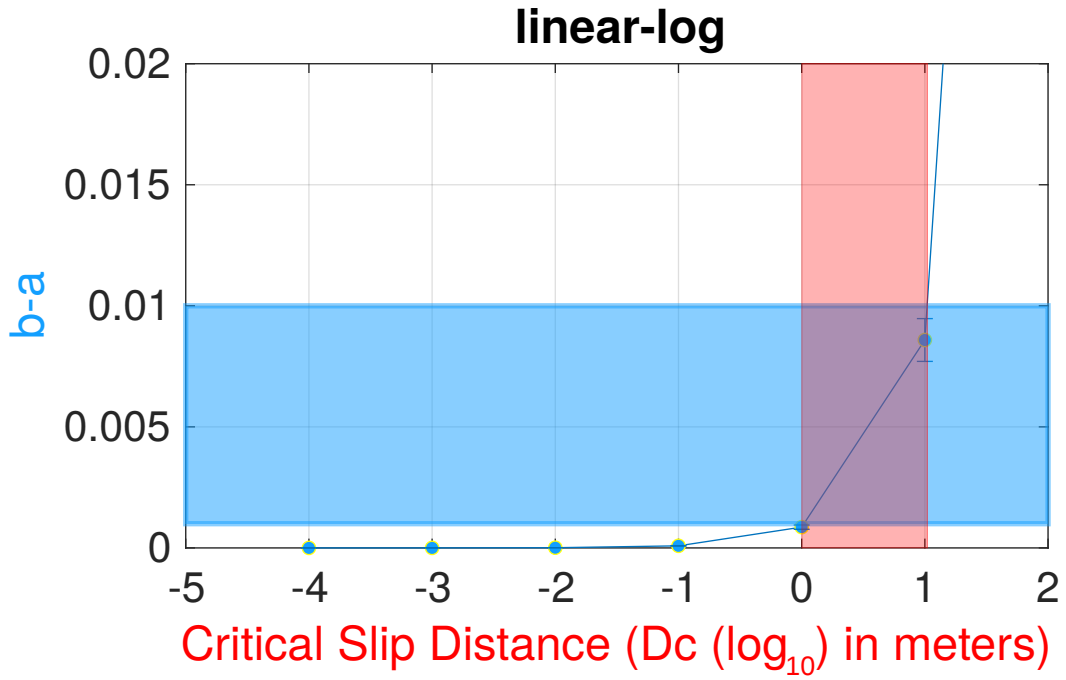

Figure 7.4: Linear-log plot of $(b-a)$ versus the critical slip distance D_c. The light-blue area shows the appropriate range of 10^{-3} to 10^{-2} for $(b-a)$, while the light-red area shows corresponding range for D_c between 1 and 10 m.

$$D_c < \frac{2\sigma_{n'}(b-a)(1-\upsilon^2)}{C \cdot E} \tag{7.3}$$

Here, we can assume the effective normal stress ($\sigma_{n'}$) is equal to the difference of lithostatic and hydrostatic stresses at seismogenic depth of 30 km. For stick-slip behavior, the frictional rate parameter $(b-a)$ ranges from 10^{-3} to 10^{-2} and is roughly consistent from laboratory and filed/modelling-based estimation (Marone, 1998). Our tomographic model of the Vp and Vp/Vs and the characteristics of the Pedernales rupture provide the opportunity to constrain the surrounding rock stiffness (k) by using a relation between the inverse fault length, the Young's modulus and Poisson's ratio (Goodman and Sundaram (1978); Methods). We then can estimate a possible range for the critical slip distance D_c of seismic rupture in nature (see Figure 7.4).
We note that this value for D_c represents an upper bound so that the critical stiffness is larger than off-fault rock stiffness, a condition that allows the velocity-weakening behavior as seen from the coseismic rupture of the Pedernales earthquake. We conclude that, in natural megathrust fault like the one failed in 2016 Pedernales earthquake, the critical slip distance D_c on fault during rupture propagation is at meter-level, at the same order of magnitude as the slip amplitude constrained by joint and geodetic inversions by Gombert et al. (2018). Our observations contribute to setting a control value, from nature, and therefore improve the validity of numerical simulations for earthquake dynamics.

7.5 Conclusion

The association of our tomographic images with geodetic observations and rupture-scaling relations, together with the grid search approach, led us to characterize the plate interface along the Ecuadorian margin. By exploring the distribution of the Vp/Vs ratios along the slab interface and the coseismic slip derived after the 2016 Pedernales earthquake, we observe that the rupture is bounded by regions of elevated Vp/Vs ratios (>1.84) which might have contribute to stopping the propagation of the coseismic slip. To evaluate if the rupture could have occurred in a different region of the margin, we sistematically tested different rupture scenarios following a grid search approach. Our findings show that the areas where Vp/Vs>1.84 is prevalent are less likely to propagate a moderate-magnitude earthquake. By introducing the normalized area A_N, we find that their maximum values collocate with the 2 m coseismic slip contour derived after the earthquake. This observation strongly suggest that the area which failed during the 2016 Pedernales was the only region capable to host an Mw 7.8 earthquake within the region of interest. The Vp and Vp/Vs models also allowed us to estimate the critical slip distance D_c which is in the same order of magnitude as the observed slip amplitude for the Pedernales event. Oue work provides, to our knowledge, the first estimation of this parameter based on the direct observations of the velocity weakening along a megathrust fault. Finally, weather the link between the seismic velocities and the coseismic slip of the Pedernales earthquake is observed in other moderate-magnitude earthquake, the analysis of the distribution of Vp/Vs ratios along the megathrust might shed light on possible areas prone to rupture and the likely size of potential earthquakes, providing relevant information for the estimation of seismic hazard.

Methods

Grid nodes configuration

The node locations in the inversion grid were shifted by 1/3 of its minimum spacing in the north and east direction and by ±2 km in the vertical component (see Table C1 in Appendix C). Each configuration was inverted first for Vp and subsequently for Vp/Vs (León-Ríos et al., 2020). The final models were obtained by respectively averaging the P-wave velocities and Vp/Vs ratios calculated for each grid node setting. Bootstrap performed for a subset of data of our 3DVM shows a standard deviation of 0.3 km/s for Vp and 0.01 for Vp/Vs, while the differences observed between the Vp and Vp/Vs models obtained by the inversions with different node settings also falls in that range.

3DVM projected along the slab interface

To derived the P-wave velocities and Vp/Vs ratios in the seismogenic zone, we used different a range of volumes that vary in thickness from ±0.5 km to ±4km along a slab interface produced by combining the trench location derived by (Collot et al., 2005), the relocated seismicity for depths <15 km (León-Ríos et al., 2020) and slab1.0 (Hayes et al., 2012) and slab2.0 (Hayes et al., 2018)

models for depths > 15km (see Figure C3 in Appendix C). Based on the in-depth resolution of our 3DVM that shows the capability to resolve features of ∼5 km, together with the averaged models from the different grid nodes configuration and an estimated earthquake error of ± 2.15 km (León-Ríos et al., 2020), we chose the ±2.5 km projection for further analysis. Figure C3 in Appendix C shows the results for all the projected volumes along the slab interface.

Rupture-scaling relations

A rupture area of 5660 km^2 (A_{2m}) was calculated for the 2016 Pedernales earthquake by following the 2 m coseismic slip contour (Gombert et al., 2018). In contrast, rupture-scaling relations (Equation 7.4 and 7.5)(Allen and Hayes, 2017) led to an expected area (A_e) ranging from 7211 km^2 to 7870 km^2.

$$log(A_{AH1}) = a + blog(Mw); a = -3.63, b = 0.63, Mw = 7.8 \tag{7.4}$$

$$log(A_{AH2}) = a + blog(Mw); a = -5.62, b = 1.22, Mw = 7.8 \tag{7.5}$$

By dividing A_{2m} over A_{AHi}, we obtained a ∼20-30% underestimation that can be translated to a difference of ∼15-20 km in length and ∼6-8 km in width. Then, using a W/L of 0.4 and preserving A_e, we can estimate a rupture length ranging from 134 km to 141 km, and a rupture width that varies between 53 km and 56 km.

Rupture scenarios and grid search

Using a simplified elliptic rupture that follows the rupture-scaling relations with a length of 138 km and a width of 55 km, and a NE striking angle of 15°, we produce three scenarios in which the center of the ellipse was shifted seaward by 20 km, 40 km and 60 km. By gridding the study area with 1x1 km^2 bins, we observe the distribution of the Vp/Vs ratios inside the ellipse and relate this value to a percentage of the total expected area A_e. Subsequently, following a grid search approach, we designed a rupture area grid search that sistematically explores the whole region of interest. Ellipses of area within the range of the expected area A_e were produced based on the W/L relation of 0.4 and moved every 10 km and 15 km in the east-west and north-south direction, respectively. Also, to inspect different rupture scenarios, we randomly varied the NE striking angle in a range of -10°to 30°using a 10°step. The areas with no resolution at depths >40 km were not considered in the analysis. Using the 1x1 km^2 bins we estimated the area covered by Vp/Vs>1.84 (A_{vpvs}) inside the ellipse. These values were normalized by the expected area A_e to obtain the normalized area as follow

$$A_N = 1 - \frac{A_{vpvs}}{A_e} \tag{7.6}$$

with A_N representing the portion of the rupture occupied by Vp/Vs>1.84. The region where A_N is maximum (i.e. small A_{vpvs}) can be associated to areas where a M 7.8 earthquake is more likely to occur.

Frictional properties of the seismogenic megathrust

Based on the rate-and-state law (Marone, 1998) for unstable stick-slip behavior (i.e. earthquake rupture), the loading system stiffness (k, fault surrounding rocks) needs to be less than the critical rheologic stiffness (k_c); Leeman et al. (2016))

$$k < k_c = \frac{\sigma_{n'}(b-a)}{D_c} \tag{7.7}$$

with $\sigma_{n'}$ as the effective normal stress, $(b-a)$ frictional rate parameter and D_c critical slip distance. By assuming an unstable sliding scenario (i.e., earthquake rupture) $\sigma_{n'}$ can be estimated by the difference between the lithostatic and hydrostatic stresses at seismogenic depth of 30 km. The value of $(b-a)$ needs to be positive within the velocity-weakening regime, where the fault surface frictional resistance decreases (Ruina, 1983). For stick-slip behavior, the typical $(b-a)$ value falls in the range of 10^{-3}–10^{-2} (Boulton et al., 2014; Scholz, 2002). On the left side, the stiffness of loading system (k) can be derived by

$$k = \frac{C \cdot E}{2(1-\upsilon^2)} \tag{7.8}$$

Here, C is the inverse of fault length, E and υ are elastic parameters for Young's modulus and Possion's ratio, respectively (Goodman and Sundaram, 1978). The latter two can be derived from Vp and Vp/Vs as

$$V_p = \sqrt{\frac{1}{\rho}\frac{E(1-\upsilon)}{(1+\upsilon)(1-2\upsilon)}}; V_s = \sqrt{\frac{1}{\rho}\frac{E}{2(1+\upsilon)}} \tag{7.9}$$

Combining the equations 7.8 and 7.9, we can derive the elastic stiffness of off-fault rocks. According to equation 7.7, the critical stiffness of the fault should then be larger than that of off-fault rock. Finally, given the appropriate range for $(b-a)$, we obtain the possible range of the critical slip distance D_c.

Chapter 8

Conclusions

Seismic data recorded by the large emergency network deployed shortly after the Mw 7.8 Pedernales earthquake was used to image the velocity structure for the Ecuadorian margin based on local earthquake tomography. Manually picked P- and S-onset times were subsequently inverted with a gradual increase in complexity from 1D to 3D Vp and Vp/Vs models. Resulting velocities were contrasted with both geological and tectonics setting, and also with the coseismic slip produced by the mainshock. Finally, our observations show the relevance of having well resolved Vp and Vp/Vs models that complement each other in order to give a full interpretation, especially in a highly heteregeneous and segmented regions such as the Ecuadorian margin. Major findings can be summarize as follow:

I inferred a **Minimum 1D velocity model** for the Pedernales segment based on the aftershock sequence (Ml>3.5) of the Mw 7.8 Pedernales earthquake. The velocity structure for both P- and S-phases shows good resolution down to 40 km depth constrained with the ray paths and the earthquake distribution. The area has an average Vp/Vs ratio of 1.82 which varies with depth that may be related to hydration and serpentinization in the downgoing plate. The seismicity is distributed in streaks which align perpendicular to the trench. Shallow seismicity (<15 km) observed in both northern and southern segments of the rupture area suggests the (re)activation of faults in the overriding plate. Also, seismicity reaching the trench indicates the absence of a frontal accretionary prism and possible activity on the downgoing plate.

Regional moment tensors were calculated to analyze the source mechanism of 14 events offshore. Although the majority of the events show focal mechanisms consistent with the subduction geometry, I also observe extensional faulting in the marine forearc that can be associated to the subduction of already-mapped seamounts. I also found strike-slip faulting which might be related to the reactivation of a strike-slip structure after the 2016 Mw 7.8 Pedernales earthquake that, in combination with the subduction of the crest of the CR, might contribute to generate the observed seismicity along the marine forearc. The observation of this type of activity suggests the need to reevaluate the geological structures in the marine forearc and to update the seismic hazard map for this region including the possible scenario of a large strike-slip event.

By adding manually picked events with M>2.5 and using the minimum 1D model as starting

reference model, I derived a **three-dimensional velocity model for Vp and Vp/Vs ratios**. I imaged with high resolution the velocity structure of the central Ecuadorian subduction zone. P-wave velocities (Vp $\sim$4.5 - 7.5 km/s) in the downgoing plate highlight the roughness of the incoming oceanic crust. Moreover, the observed mixture of low ($\sim$1.80) and high ($\sim$1.85) Vp/Vs ratios suggest a heterogeneous and hydrated margin. I imaged the subduction of large-scale bathymetric features, such as the Carnegie Ridge (CR) and the Atacames seamounts, which contribute to the high circulation of fluids, especially close to the trench. The CR seems to be the main structure controlling the seismicity along the margin by promoting creeping and slow slip events caused by fluids migrating from a deeply fractured and highly hydrated oceanic crust. This fact is directly linked to the updip rupture limit of large megathrust earthquakes in the northern segment and the absence of large megathrust earthquakes in the southern region over the instrumental period.

I also projected the **velocity structure along the slab interface** to quantify the relation between the Vp/Vs ratios and the coseismic slip of the 2016 Pedernales earthquake. By following a rupture area grid search approach, I explored the distribution of Vp/Vs ratios >1.84. The results reveal that the 2016 Pedernales earthquake occurred in the only portion of the margin with the physical conditions (Vp/Vs $\sim$1.78-1.84) to nucleate and propagate the rupture. Moreover, the Vp/Vs ratios distribution along the slab interface suggests that the up- and down-dip limits of the Pedernales earthquake was controlled by areas of elevated Vp/Vs ratios (>1.84). The Vp and Vp/Vs ratios were also used to estimate the upper bound of the critical slip distance (D_c). The calculated range for D_c is between 1 and 10, and is in agreement with the slip amplitudes observed during the Pedernales earthquake.

The results of this study remark the importance of large collaboration projects that facilitate a rapid response after the occurrence of a large megathrust earthquake. The dense network installed in Ecuador, provided us with high quality data that was used to derive the three-dimensional velocity structure of the Ecuadorian margin. These seismic velocity models, together with the seismotectonical and geological information available, conform a powerful combination that contributes to a better understanding of the South American subduction zone and the intrinsic seismic hazard in the region.

Finally, the **Future work** should focus on the integration of the results coming from the different studies that have been carried after the installation of the Pedernales emergency network. The comparison and complement of the different observations will, undoubtedly, raise the bar on our comprehension of the central Ecuadorian margin. Furthermore, it is relevant to address the influence of the 3D structures interacting in the different seismic processes, especially along the marine forearc. On this matter, a large project is planned for the upcoming years to image with high resolution the trench location, the circulation of fluids along the interface and the P- and S-wave velocity structures in the offshore region.

Bibliography

K. Abe. Size of great earthquakes of 1837–1974 inferred from tsunami data. *Journal of Geophysical Research: Solid Earth*, 84(B4):1561–1568, 1979.

W. Agudelo, A. Ribodetti, J.-Y. Collot, and S. Operto. Joint inversion of multichannel seismic reflection and wide-angle seismic data: Improved imaging and refined velocity model of the crustal structure of the North Ecuador–South Colombia convergent margin. *Journal of Geophysical Research: Solid Earth*, 114(B2), 2009.

H. Agurto, A. Rietbrock, S. Barrientos, K. Bataille, and D. Legrand. Seismo-tectonic structure of the Aysén Region, Southern Chile, inferred from the 2007 M w= 6.2 Aysén earthquake sequence. *Geophysical Journal International*, 190(1):116–130, 2012.

H. Agurto-Detzel, Y. Font, P. Charvis, M. Régnier, A. Rietbrock, D. Ambrois, M. Paulatto, A. Alvarado, S. Beck, F. Courboulex, et al. Ridge subduction and afterslip control aftershock distribution of the 2016 Mw 7.8 Ecuador earthquake. *Earth and Planetary Science Letters*, 520: 63–76, 2019.

K. Aki and W. Lee. Determination of three-dimensional velocity anomalies under a seismic array using first P arrival times from local earthquakes: 1. A homogeneous initial model. *Journal of Geophysical research*, 81(23):4381–4399, 1976.

K. Aki and P. G. Richards. *Quantitative seismology*. 2002.

K. Aki, A. Christoffersson, and E. S. Husebye. Determination of the three-dimensional seismic structure of the lithosphere. *Journal of Geophysical Research*, 82(2):277–296, 1977.

T. I. Allen and G. P. Hayes. Alternative rupture-scaling relationships for subduction interface and other offshore environments. *Bulletin of the Seismological Society of America*, 107(3):1240–1253, 2017.

A. Alvarado, L. Audin, J.-M. Nocquet, E. Jaillard, P. Mothes, P. Jarrín, M. Segovia, F. Rolandone, and D. Cisneros. Partitioning of oblique convergence in the Northern Andes subduction zone: Migration history and the present-day boundary of the North Andean Sliver in Ecuador. *Tectonics*, 35(5):1048–1065, 2016.

A. Alvarado, M. Ruiz, P. Mothes, H. Yepes, M. Segovia, M. Vaca, C. Ramos, W. Enríquez, G. Ponce, P. Jarrín, et al. Seismic, volcanic, and geodetic networks in Ecuador: Building capacity for monitoring and research. *Seismological Research Letters*, 89(2A):432–439, 2018.

D. L. Anderson and A. M. Dziewonski. Seismic tomography. *Scientific American*, 251(4):60–71, 1984.

H. Anderson and T. Webb. New Zealand seismicity: patterns revealed by the upgraded National Seismograph Network. *New Zealand journal of geology and geophysics*, 37(4):477–493, 1994.

D. Andrews. Rupture propagation with finite stress in antiplane strain. *Journal of Geophysical Research*, 81(20):3575–3582, 1976a.

D. Andrews. Rupture velocity of plane strain shear cracks. *Journal of Geophysical Research*, 81 (32):5679–5687, 1976b.

S. Araujo. *Travel time tomography of the crust and the mantle beneath Ecuador from data of the national seismic network.* PhD thesis, Grenoble Alpes, 2016.

Y. Asano, T. Saito, Y. Ito, K. Shiomi, H. Hirose, T. Matsumoto, S. Aoi, S. Hori, and S. Sekiguchi. Spatial distribution and focal mechanisms of aftershocks of the 2011 off the Pacific coast of Tohoku earthquake. *Earth, planets and space*, 63(7):29, 2011.

P. Audet and S. Y. Schwartz. Hydrologic control of forearc strength and seismicity in the costa rican subduction zone. *Nature Geoscience*, 6(10):852–855, 2013.

G. Backus and F. Gilbert. The resolving power of gross earth data. *Geophysical Journal International*, 16(2):169–205, 1968.

G. Backus and F. Gilbert. Constructing P-velocity models to fit restricted sets of travel-time data. *Bulletin of the Seismological Society of America*, 59(3):1407–1414, 1969.

G. Backus and F. Gilbert. Uniqueness in the inversion of inaccurate gross earth data. *Philosophical Transactions of the Royal Society of London. Series A, Mathematical and Physical Sciences*, 266 (1173):123–192, 1970.

G. E. Backus and J. Gilbert. Numerical applications of a formalism for geophysical inverse problems. *Geophysical Journal International*, 13(1-3):247–276, 1967.

N. L. Bangs, K. D. McIntosh, E. A. Silver, J. W. Kluesner, and C. R. Ranero. Fluid accumulation along the Costa Rica subduction thrust and development of the seismogenic zone. *Journal of Geophysical Research: Solid Earth*, 120(1):67–86, 2015.

P. M. Barnes, G. Lamarche, J. Bialas, S. Henrys, I. Pecher, G. L. Netzeband, J. Greinert, J. J.

Mountjoy, K. Pedley, and G. Crutchley. Tectonic and geological framework for gas hydrates and cold seeps on the Hikurangi subduction margin, New Zealand. *Marine Geology*, 272(1-4): 26–48, 2010.

C. Beauval, H. Yepes, W. H. Bakun, J. Egred, A. Alvarado, and J.-C. Singaucho. Locations and magnitudes of historical earthquakes in the Sierra of Ecuador (1587–1996). *Geophysical Journal International*, 181(3):1613–1633, 2010.

S. L. Beck and L. J. Ruff. The rupture process of the great 1979 Colombia earthquake: Evidence for the asperity model. *Journal of Geophysical Research: Solid Earth*, 89(B11):9281–9291, 1984.

S. L. Bilek. Invited review paper: Seismicity along the South American subduction zone: Review of large earthquakes, tsunamis, and subduction zone complexity. *Tectonophysics*, 495(1-2):2–14, 2010.

S. L. Bilek, S. Y. Schwartz, and H. R. DeShon. Control of seafloor roughness on earthquake rupture behavior. *Geology*, 31(5):455–458, 2003.

P. Bird. An updated digital model of plate boundaries. *Geochemistry, Geophysics, Geosystems*, 4 (3), 2003.

W. Bloch, T. John, J. Kummerow, P. Salazar, O. S. Krüger, and S. A. Shapiro. Watching dehydration: Seismic indication for transient fluid pathways in the oceanic mantle of the subducting Nazca slab. *Geochemistry, Geophysics, Geosystems*, 19(9):3189–3207, 2018.

P. Bolton. Local level economic and social consequences. *The March 5, 1987, Ecuador earthquakes: mass wasting and socioeconomic effects*, page 100, 1991.

M. Bouchon. A simple method to calculate Green's functions for elastic layered media. *Bulletin of the Seismological Society of America*, 71(4):959–971, 1981.

C. Boulton, D. E. Moore, D. A. Lockner, V. G. Toy, J. Townend, and R. Sutherland. Frictional properties of exhumed fault gouges in DFDP-1 cores, Alpine Fault, New Zealand. *Geophysical Research Letters*, 41(2):356–362, 2014.

C. Bristow. *Mapa Geologico Parcial Del Ecuador (basado en Los Mapas de la DGGM), 1: 2 900 000: In: CR Bristow & R. Hoffstetter. Ecuador. Lexique Stratigraphique International, Vol. 5, Amerique Latine, Fasc. 5a2.-Paris: Centre National de la Recherche Scientifique, 1977.* Centre National de la recherche scientifique, 1977.

S. Burdick, R. D. Van der Hilst, F. L. Vernon, V. Martynov, T. Cox, J. Eakins, G. H. Karasu, J. Tylell, L. Astiz, and G. L. Pavlis. Model update january 2013: Upper mantle heterogeneity beneath north america from travel-time tomography with global and usarray transportable array

data. *Seismological Research Letters*, 85(1):77–81, 2014.

D. E. Byrne, D. M. Davis, and L. R. Sykes. Loci and maximum size of thrust earthquakes and the mechanics of the shallow region of subduction zones. *Tectonics*, 7(4):833–857, 1988.

T. Cahill and B. L. Isacks. Seismicity and shape of the subducted Nazca plate. *Journal of Geophysical Research: Solid Earth*, 97(B12):17503–17529, 1992.

A. Calahorrano. Estudio del origen del enjambre sísmico de la zona norte de la ciudad de Quito, durante 1998–1999. *Escuela Politecnica Nacional, Quito*, 2001.

A. Calahorrano, V. Sallarès, J.-Y. Collot, F. Sage, and C. R. Ranero. Nonlinear variations of the physical properties along the southern Ecuador subduction channel: Results from depth-migrated seismic data. *Earth and Planetary Science Letters*, 267(3-4):453–467, 2008.

J. A. Cañas and A. Ledesma. Método de inversión generalizada: aplicación en sismología y posibilidad en ingeniería civil. *Universidad Politécnica de Cataluña (España), ISSN*, pages 0213–1315, 1984.

L. C. G. Cano, A. Galve, P. Charvis, and B. Marcaillou. Three-dimensional velocity structure of the outer fore arc of the Colombia-Ecuador subduction zone and implications for the 1958 megathrust earthquake rupture zone. *Journal of Geophysical Research: Solid Earth*, 119(2): 1041–1060, 2014.

G. Cantalamessa and C. Di Celma. Sedimentary features of tsunami backwash deposits in a shallow marine Miocene setting, Mejillones Peninsula, northern Chile. *Sedimentary Geology*, 178(3-4): 259–273, 2005.

G. Cantalamessa, C. Di Celma, L. Ragaini, G. Valleri, and W. Landini. Sedimentology and high-resolution sequence stratigraphy of the late middle to late Miocene Angostura Formation (western Borbón Basin, northwestern Ecuador). *Journal of the Geological Society*, 164(3):653–665, 2007.

J. Caplan-Auerbach and F. Duennebier. Seismicity and velocity structure of Loihi Seamount from the 1996 earthquake swarm. *Bulletin of the Seismological Society of America*, 91(2):178–190, 2001.

N. G. Cerpa, R. Araya, M. Gerbault, and R. Hassani. Relationship between slab dip and topography segmentation in an oblique subduction zone: Insights from numerical modeling. *Geophysical Research Letters*, 42(14):5786–5795, 2015.

M. Chlieh, P. Mothes, J.-M. Nocquet, P. Jarrin, P. Charvis, D. Cisneros, Y. Font, J.-Y. Collot, J.-C. Villegas-Lanza, F. Rolandone, et al. Distribution of discrete seismic asperities and aseismic slip

along the Ecuadorian megathrust. *Earth and Planetary Science Letters*, 400:292–301, 2014.

N. I. Christensen. Poisson's ratio and crustal seismology. *Journal of Geophysical Research: Solid Earth*, 101(B2):3139–3156, 1996.

N. I. Christensen. Serpentinites, peridotites, and seismology. *International Geology Review*, 46(9): 795–816, 2004.

M. Cocco, E. Tinti, C. Marone, and A. Piatanesi. Scaling of slip weakening distance with final slip during dynamic earthquake rupture. *International Geophysics*, 94:163–186, 2009.

R. Collings, D. Lange, A. Rietbrock, F. Tilmann, D. Natawidjaja, B. Suwargadi, M. Miller, and J. Saul. Structure and seismogenic properties of the Mentawai segment of the sumatra subduction zone revealed by local earthquake traveltime tomography. *Journal of Geophysical Research: Solid Earth*, 117(B1), 2012.

R. E. Collings. *The Sumatra subduction zone: seismicity, velocity structure and seismic anisotropy*. PhD thesis, University of Liverpool, 2012.

J.-Y. Collot, P. Charvis, M.-A. Gutscher, and S. Operto. Exploring the Ecuador-Colombia active margin and interplate seismogenic zone. *EOS, Transactions American Geophysical Union*, 83 (17):185–190, 2002.

J.-Y. Collot, B. Marcaillou, F. Sage, F. Michaud, W. Agudelo, P. Charvis, D. Graindorge, M.-A. Gutscher, and G. Spence. Are rupture zone limits of great subduction earthquakes controlled by upper plate structures? Evidence from multichannel seismic reflection data acquired across the northern Ecuador–southwest Colombia margin. *Journal of Geophysical Research: Solid Earth*, 109(B11), 2004.

J.-Y. Collot, S. Migeon, G. Spence, Y. Legonidec, B. Marcaillou, J.-L. Schneider, F. Michaud, A. Alvarado, J.-F. Lebrun, M. Sosson, et al. Seafloor margin map helps in understanding subduction earthquakes. *Eos, Transactions American Geophysical Union*, 86(46):463–465, 2005.

J.-Y. Collot, F. Michaud, A. Alvarado, B. Marcaillou, M. Sosson, G. Ratzov, S. Migeon, A. Calahorrano, and A. Pazmino. Visión general de la morfología submarina del margen convergente de Ecuador-Sur de Colombia: implicaciones sobre la transferencia de masa y la edad de la subducción de la Cordillera de Carnegie. *Geologia y Geofisica Marina y Terestre del Ecuador. Publicacion CNDM-INOCAR-IRD, PSE001-09, Guayaquil, Ecuador*, pages 47–74, 2009.

J.-Y. Collot, E. Sanclemente, J.-M. Nocquet, A. Leprêtre, A. Ribodetti, P. Jarrin, M. Chlieh, D. Graindorge, and P. Charvis. Subducted oceanic relief locks the shallow megathrust in central

Ecuador. *Journal of Geophysical Research: Solid Earth*, 122(5):3286–3305, 2017.

E. Contreras-Reyes, J. Jara, I. Grevemeyer, S. Ruiz, and D. Carrizo. Abrupt change in the dip of the subducting plate beneath north Chile. *Nature Geoscience*, 5(5):342–345, 2012.

O. Coutant. Numerical study of the diffraction of elastic waves by fluid-filled cracks. *Journal of Geophysical Research: Solid Earth*, 94(B12):17805–17818, 1989.

T. Dahm and F. Krüger. Moment tensor inversion and moment tensor interpretation. In *New Manual of Seismological Observatory Practice 2 (NMSOP-2)*, pages 1–37. Deutsches GeoForschungsZentrum GFZ, 2014.

M. C. Daly. Correlations between Nazca/Farallon plate kinematics and forearc basin evolution in Ecuador. *Tectonics*, 8(4):769–790, 1989.

J. H. Dieterich. Modeling of rock friction: 1. Experimental results and constitutive equations. *Journal of Geophysical Research: Solid Earth*, 84(B5):2161–2168, 1979.

Domdomegg. *Oceanic-continental destructive*. Wikimedia commons, Dec 2015. URL https://commons.wikimedia.org/wiki/File:Oceanic-continental_destructive_plate_boundary.svg.

S. Dominguez, S. Lallemand, J. Malavieille, and R. von Huene. Upper plate deformation associated with seamount subduction. *Tectonophysics*, 293(3-4):207–224, 1998.

L. Dorbath, A. Cisternas, and C. Dorbath. Assessment of the size of large and great historical earthquakes in Peru. *Bulletin of the Seismological Society of America*, 80(3):551–576, 1990.

D. S. Dreger and D. V. Helmberger. Determination of source parameters at regional distances with three-component sparse network data. *Journal of Geophysical Research: Solid Earth*, 98(B5): 8107–8125, 1993.

A. M. Dziewonski and J. H. Woodhouse. An experiment in systematic study of global seismicity: Centroid-moment tensor solutions for 201 moderate and large earthquakes of 1981. *Journal of Geophysical Research: Solid Earth*, 88(B4):3247–3271, 1983.

D. Eberhart-Phillips. Three-dimensional velocity structure in northern California Coast Ranges from inversion of local earthquake arrival times. *Bulletin of the Seismological Society of America*, 76(4):1025–1052, 1986.

D. Eberhart-Phillips. Three-dimensional P and S velocity structure in the Coalinga region, California. *Journal of Geophysical Research: Solid Earth*, 95(B10):15343–15363, 1990.

D. Eberhart-Phillips. Local earthquake tomography: earthquake source regions. *Seismic*

Tomography: Theory and Practice, 1993.

J. Egred. Breve historia sísmica de la República del Ecuador (1534-1965). *Bol. Bibl. Geofís. Oceanogr. Am*, 1968.

G. Ekström, M. Nettles, and A. Dziewoński. The global CMT project 2004–2010: Centroid-moment tensors for 13,017 earthquakes. *Physics of the Earth and Planetary Interiors*, 200:1–9, 2012.

J. R. Evans, D. Eberhart-Phillips, and C. Thurber. User's manual for SIMULPS12 for imaging Vp and Vp/Vs; a derivative of the" Thurber" tomographic inversion SIMUL3 for local earthquakes and explosions. Technical report, US Geological Survey,, 1994.

M. Farías, D. Comte, S. Roecker, D. Carrizo, and M. Pardo. Crustal extensional faulting triggered by the 2010 Chilean earthquake: The Pichilemu seismic sequence. *Tectonics*, 30(6), 2011.

Y. Font, M. Segovia, S. Vaca, and T. Theunissen. Seismicity patterns along the Ecuadorian subduction zone: new constraints from earthquake location in a 3-D a priori velocity model. *Geophysical Journal International*, 193(1):263–286, 2013.

E. Fukuyama, T. Mikumo, and K. B. Olsen. Estimation of the critical slip-weakening distance: Theoretical background. *Bulletin of the Seismological Society of America*, 93(4):1835–1840, 2003.

A. Gailler, P. Charvis, and E. R. Flueh. Segmentation of the Nazca and South American plates along the Ecuador subduction zone from wide angle seismic profiles. *Earth and Planetary Science Letters*, 260(3-4):444–464, 2007.

F. Gilbert and G. E. Backus. Propagator matrices in elastic wave and vibration problems. *Geophysics*, 31(2):326–332, 1966.

F. Gilbert and A. M. Dziewonski. An application of normal mode theory to the retrieval of structural parameters and source mechanisms from seismic spectra. *Philosophical Transactions of the Royal Society of London. Series A, Mathematical and Physical Sciences*, 278(1280):187–269, 1975.

B. Gombert, Z. Duputel, R. Jolivet, M. Simons, J. Jiang, C. Liang, E. J. Fielding, and L. Rivera. Strain budget of the Ecuador–Colombia subduction zone: A stochastic view. *Earth and Planetary Science Letters*, 498:288–299, 2018.

R. E. Goodman and P. Sundaram. Fault and system stiffnesses and stick-slip phenomena. *pure and applied geophysics*, 116(4-5):873–887, 1978.

D. Graindorge, A. Calahorrano, P. Charvis, J.-Y. Collot, and N. Bethoux. Deep structures of the Ecuador convergent margin and the Carnegie Ridge, possible consequence on great earthquakes recurrence interval. *Geophysical Research Letters*, 31(4), 2004.

M.-A. Gutscher, J. Malavieille, S. Lallemand, and J.-Y. Collot. Tectonic segmentation of the North Andean margin: impact of the Carnegie Ridge collision. *Earth and Planetary Science Letters*, 168(3-4):255–270, 1999.

C. Haberland, A. Rietbrock, D. Lange, K. Bataille, and T. Dahm. Structure of the seismogenic zone of the southcentral Chilean margin revealed by local earthquake traveltime tomography. *Journal of Geophysical Research: Solid Earth*, 114(B1), 2009.

B. R. Hacker, G. A. Abers, and S. M. Peacock. Subduction factory 1. Theoretical mineralogy, densities, seismic wave speeds, and H2O contents. *Journal of Geophysical Research: Solid Earth*, 108(B1), 2003.

N. Hardy. Tectonic evolution of the easternmost Panama Basin: Some new data and inferences. *Journal of South American earth sciences*, 4(3):261–269, 1991.

G. P. Hayes, D. J. Wald, and R. L. Johnson. Slab1. 0: A three-dimensional model of global subduction zone geometries. *Journal of Geophysical Research: Solid Earth*, 117(B1), 2012.

G. P. Hayes, G. L. Moore, D. E. Portner, M. Hearne, H. Flamme, M. Furtney, and G. M. Smoczyk. Slab2, a comprehensive subduction zone geometry model. *Science*, 362(6410):58–61, 2018.

C. Heine. Plate boundaries for GMT5's psxy, Sep 2019. URL https://wiki.paleoearthlabs.org/scientificdata/platetectonics/birdplateboundaries.

D. G. Herd, T. L. Youd, H. Meyer, W. J. Person, C. Mendoza, et al. The great Tumaco, Colombia earthquake of 12 december 1979. *Science*, 211(4481):441–445, 1981.

M. Hernández, F. Michaud, M. Rivadeneira, D. Barba, and J.-Y. Collot. El sistema de fallas de Jama en la plataforma continental (off-shore) del margen ecuatoriano: resultados preliminares a partir de la interpretación de perfiles sísmicos de reflexión. 2011.

R. B. Herrmann. Computer programs in seismology: An evolving tool for instruction and research. *Seismological Research Letters*, 84(6):1081–1088, 2013.

S. P. Hicks, A. Rietbrock, I. M. Ryder, C.-S. Lee, and M. Miller. Anatomy of a megathrust: The 2010 M8. 8 Maule, Chile earthquake rupture zone imaged using seismic tomography. *Earth and Planetary Science Letters*, 405:142–155, 2014.

M. Hoskins, A. Meltzer, L. Soto-Cordero, J. Stachnik, S. L. Beck, C. Lynner, M. C. Ruiz, A. P. Alvarado, S. Hernandez, P. Charvis, et al. Variable slip modes in postseismic deformation north of the April 16, 2016 M w 7.8 Pedernales, Ecuador megathrust earthquake. *AGUFM*, 2018: T43E–0444, 2018.

S. Husen and E. Kissling. Postseismic fluid flow after the large subduction earthquake of Antofagasta, Chile. *Geology*, 29(9):847–850, 2001.

S. Husen, E. Kissling, E. Flueh, and G. Asch. Accurate hypocentre determination in the seismogenic zone of the subducting Nazca Plate in northern Chile using a combined on-/offshore network. *Geophysical Journal International*, 138(3):687–701, 1999.

S. Husen, E. Kissling, and E. R. Flueh. Local earthquake tomography of shallow subduction in north Chile: A combined onshore and offshore study. *Journal of Geophysical Research: Solid Earth*, 105(B12):28183–28198, 2000.

R. Hyndman. Poisson's ratio in the oceanic crust—a review. *Tectonophysics*, 59(1-4):321–333, 1979.

R. D. Hyndman and K. Wang. Thermal constraints on the zone of major thrust earthquake failure: The cascadia subduction zone. *Journal of Geophysical Research: Solid Earth*, 98(B2):2039–2060, 1993.

R. D. Hyndman, M. Yamano, and D. A. Oleskevich. The seismogenic zone of subduction thrust faults. *Island Arc*, 6(3):244–260, 1997.

G. A. Ichinose, K. D. Smith, and J. G. Anderson. Moment tensor solutions of the 1994 to 1996 Double Spring Flat, Nevada, earthquake sequence and implications for local tectonic models. *Bulletin of the Seismological Society of America*, 88(6):1363–1378, 1998.

E. e. O. d. S. d. l. T. d. S. E. Institut de Physique du Globe de Paris (IPGP). GEOSCOPE, French Global Network of broad band seismic stations, 1982.

H. Iyer and K. Hirahara. *Seismic tomography: Theory and practice*. Springer Science & Business Media, 1993.

E. Jaillard, G. Hérail, T. Monfret, E. Díaz-Martínez, P. Baby, A. Lavenu, and J. Dumont. Tectonic evolution of the Andes of Ecuador, Peru, Bolivia and northernmost Chile. *Tectonic Evolution of South America*, 31:481–559, 2000.

E. Jaillard, H. Lapierre, M. Ordonez, J. T. Alava, A. Amortegui, and J. Vanmelle. Accreted oceanic terranes in Ecuador: southern edge of the Caribbean Plate? *Geological Society, London, Special Publications*, 328(1):469–485, 2009.

A. Jin and K. Aki. Spatial and temporal correlation between coda Q- 1 and seismicity and its physical mechanism. *Journal of Geophysical Research: Solid Earth*, 94(B10):14041–14059, 1989.

M. u. Jost and R. Herrmann. A student's guide to and review of moment tensors. *Seismological Research Letters*, 60(2):37–57, 1989.

H. Kanamori and J. W. Given. Use of long-period surface waves for rapid determination of earthquake-source parameters. *Physics of the Earth and Planetary interiors*, 27(1):8–31, 1981.

H. Kanamori and K. C. McNally. Variable rupture mode of the subduction zone along the Ecuador-Colombia coast. *Bulletin of the Seismological Society of America*, 72(4):1241–1253, 1982.

A. Kato, T. Iidaka, R. Ikuta, Y. Yoshida, K. Katsumata, T. Iwasaki, S. Sakai, C. Thurber, N. Tsumura, K. Yamaoka, et al. Variations of fluid pressure within the subducting oceanic crust and slow earthquakes. *Geophysical Research Letters*, 37(14), 2010.

A. Kato, S. Sakai, and K. Obara. A normal-faulting seismic sequence triggered by the 2011 off the Pacific coast of Tohoku earthquake: Wholesale stress regime changes in the upper plate. *Earth, planets and space*, 63(7):43, 2011.

V. Keilis-Borok and T. Yanovskaja. Inverse problems of seismology (structural review). *Geophysical Journal International*, 13(1-3):223–234, 1967.

J. A. Kelleher. Rupture zones of large South American earthquakes and some predictions. *Journal of Geophysical Research*, 77(11):2087–2103, 1972.

E. Kendrick, M. Bevis, R. Smalley Jr, B. Brooks, R. B. Vargas, E. Laurıa, and L. P. S. Fortes. The Nazca–South America Euler vector and its rate of change. *Journal of South American Earth Sciences*, 16(2):125–131, 2003.

M. Kikuchi and H. Kanamori. Inversion of complex body waves—III. *Bulletin of the Seismological Society of America*, 81(6):2335–2350, 1991.

E. Kissling, W. Ellsworth, D. Eberhart-Phillips, and U. Kradolfer. Initial reference models in local earthquake tomography. *Journal of Geophysical Research: Solid Earth*, 99(B10):19635–19646, 1994.

C. D. Koch, C. Lynner, J. Delph, S. L. Beck, A. Meltzer, Y. Font, L. Soto-Cordero, M. Hoskins, J. C. Stachnik, M. Ruiz, et al. Structure of the Ecuadorian forearc from the joint inversion of receiver functions and ambient noise surface waves. *Geophysical Journal International*, 2020.

S. Kodaira, T. Iidaka, A. Kato, J.-O. Park, T. Iwasaki, and Y. Kaneda. High pore fluid pressure may

cause silent slip in the Nankai Trough. *Science*, 304(5675):1295–1298, 2004.

H. Kopp, E. R. Flueh, C. Papenberg, and D. Klaeschen. Seismic investigations of the O'Higgins Seamount Group and Juan Fernández Ridge: aseismic ridge emplacement and lithosphere hydration. *Tectonics*, 23(2), 2004.

D. Lange, F. Tilmann, S. E. Barrientos, E. Contreras-Reyes, P. Methe, M. Moreno, B. Heit, H. Agurto, P. Bernard, J.-P. Vilotte, et al. Aftershock seismicity of the 27 February 2010 Mw 8.8 Maule earthquake rupture zone. *Earth and Planetary Science Letters*, 317:413–425, 2012.

F. Lanning, A. G. Haro, M. K. Liu, A. Monzón, H. Monzón-Despang, A. Schultz, A. Tola, G. Diaz-Fanas, N. Antonaki, S. Nikolaou, et al. EERI Earthquake Reconnaissance Team Report: M7. 8 Muisne, Ecuador earthquake on April 16, 2016. 2016.

T. Lay and T. C. Wallace. *Modern global seismology*. Elsevier, 1995.

T. Lay, H. Kanamori, C. J. Ammon, K. D. Koper, A. R. Hutko, L. Ye, H. Yue, and T. M. Rushing. Depth-varying rupture properties of subduction zone megathrust faults. *Journal of Geophysical Research: Solid Earth*, 117(B4), 2012.

W. H. K. Lee and J. C. Lahr. HYPO71: A computer program for determining hypocenter, magnitude, and first motion pattern of local earthquakes. Technical report, US Geological Survey,, 1972.

J. Leeman, R. Valdez, R. Alley, S. Anandakrishnan, and D. Saffer. Mechanical and hydrologic properties of Whillans Ice Stream till: Implications for basal strength and stick-slip failure. *Journal of Geophysical Research: Earth Surface*, 121(7):1295–1309, 2016.

S. León-Ríos, S. Ruiz, A. Maksymowicz, F. Leyton, A. Fuenzalida, and R. Madariaga. Diversity of the 2014 Iquique's foreshocks and aftershocks: clues about the complex rupture process of a Mw 8.1 earthquake. *Journal of Seismology*, 20(4):1059–1073, 2016.

S. León-Ríos, H. Agurto-Detzel, A. Rietbrock, A. Alvarado, S. Beck, P. Charvis, B. Edwards, Y. Font, T. Garth, M. Hoskins, et al. 1D-velocity structure and seismotectonics of the Ecuadorian margin inferred from the 2016 Mw7. 8 Pedernales aftershock sequence. *Tectonophysics*, 767: 228165, 2019.

S. León-Ríos, L. Bie, H. Agurto-Detzel, A. Rietbrock, A. Galve, A. P. Alvarado, S. L. Beck, P. Charvis, Y. Font, S. Hidalgo, et al. 3D local earthquake tomography of the Ecuadorian margin in the source area of the 2016 Mw 7.8 Pedernales earthquake. 2020.

J.-J. Lévěque, L. Rivera, and G. Wittlinger. On the use of the checker-board test to assess the resolution of tomographic inversions. *Geophysical Journal International*, 115(1):313–318, 1993.

M. Litherland. The metamorphic belts of Ecuador. *British Geological Survey, Overseas Memoir.*, 11, 1994.

C. Liu, C. An, B. Shan, X. Xiong, and X. Chen. Insights into the kinematic rupture of the 2015 mw 8.3 illapel, chile, earthquake from joint analysis of geodetic, seismological, tsunami, and superconductive gravimeter observations. *Journal of Geophysical Research: Solid Earth*, 123 (11):9778–9799, 2018.

P. Lonsdale. Ecuadorian subduction system. *AAPG Bulletin*, 62(12):2454–2477, 1978.

P. Lonsdale. Creation of the Cocos and Nazca plates by fission of the Farallon plate. *Tectonophysics*, 404(3-4):237–264, 2005.

L. Luzieux, F. Heller, R. Spikings, C. Vallejo, and W. Winkler. Origin and Cretaceous tectonic history of the coastal Ecuadorian forearc between 1 N and 3 S: Paleomagnetic, radiometric and fossil evidence. *Earth and Planetary Science Letters*, 249(3-4):400–414, 2006.

C. Lynner, C. Koch, S. L. Beck, A. Meltzer, L. Soto-Cordero, M. C. Hoskins, J. C. Stachnik, M. Ruiz, A. Alvarado, P. Charvis, et al. Upper-plate structure in Ecuador coincident with the subduction of the Carnegie Ridge and the southern extent of large mega-thrust earthquakes. *Geophysical Journal International*, 220(3):1965–1977, 2020.

W. Mao, G. Panza, and P. Suhadolc. Linearized waveform inversion of local and near-regional events for source mechanism and rupturing processes. *Geophysical Journal International*, 116 (3):784–798, 1994.

B. Marcaillou, G. Spence, J.-Y. Collot, and K. Wang. Thermal regime from bottom simulating reflectors along the north Ecuador–south Colombia margin: Relation to margin segmentation and great subduction earthquakes. *Journal of Geophysical Research: Solid Earth*, 111(B12), 2006.

B. Marcaillou, G. Spence, K. Wang, J.-Y. Collot, and A. Ribodetti. Thermal segmentation along the N. Ecuador–S. Colombia margin (1–4 N): Prominent influence of sedimentation rate in the trench. *Earth and Planetary Science Letters*, 272(1-2):296–308, 2008.

B. Marcaillou, J.-Y. Collot, A. Ribodetti, E. d'Acremont, A.-A. Mahamat, and A. Alvarado. Seamount subduction at the North-Ecuadorian convergent margin: Effects on structures, interseismic coupling and seismogenesis. *Earth and Planetary Science Letters*, 433:146–158, 2016.

C. Marone. The effect of loading rate on static friction and the rate of fault healing during the earthquake cycle. *Nature*, 391(6662):69–72, 1998.

R. Meissnar, E. Flueh, F. Stibane, and E. Berg. Dynamics of the active plate boundary in southwest

Colombia according to recent geophysical measurements. *Tectonophysics*, 35(1-3):115–136, 1976.

A. Meltzer and S. Beck. Pedernales earthquake aftershock deployment Ecuador. *International Federation of Digital Seismograph Networks, Other/Seismic Network, doi*, 10, 2016.

A. Meltzer, S. Beck, M. Ruiz, M. Hoskins, L. Soto-Cordero, J. C. Stachnik, C. Lynner, R. Porritt, D. Portner, A. Alvarado, et al. The 2016 M w 7.8 Pedernales, Ecuador, earthquake: Rapid response deployment. *Seismological Research Letters*, 90(3):1346–1354, 2019.

A. Menant, S. Angiboust, T. Gerya, R. Lacassin, M. Simoes, and R. Grandin. Transient stripping of subducting slabs controls periodic forearc uplift. *Nature communications*, 11(1):1–10, 2020.

C. Mendoza and J. W. Dewey. Seismicity associated with the great Colombia-Ecuador earthquakes of 1942, 1958, and 1979: Implications for barrier models of earthquake rupture. *Bulletin of the seismological society of America*, 74(2):577–593, 1984.

F. Michaud, J. Collot, A. Alvarado, E. Lopez, and y el personal científico y técnico del INOCAR. Repùblica del Ecuador, batimetria y relieve continental. Technical report, publicacion IOA-CVM-02-Post. INOCAR, Guayaquil, Ecuador, 2006.

F. Michaud, J.-N. Proust, J.-Y. Collot, J.-F. Lebrun, C. Witt, G. Ratzov, H. Pouderoux, C. Martillo, M. Hernández, G. Loayza, et al. Quaternary sedimentation and active faulting along the Ecuadorian shelf: preliminary results of the ATACAMES Cruise (2012). *Marine Geophysical Research*, 36(1):81–98, 2015.

P. A. Mothes, J.-M. Nocquet, and P. Jarrín. Continuous GPS network operating throughout Ecuador. *Eos, Transactions American Geophysical Union*, 94(26):229–231, 2013.

J. Nakajima, T. Matsuzawa, A. Hasegawa, and D. Zhao. Three-dimensional structure of Vp, Vs, and Vp/Vs beneath northeastern Japan: Implications for arc magmatism and fluids. *Journal of Geophysical Research: Solid Earth*, 106(B10):21843–21857, 2001.

J.-M. Nocquet, P. Mothes, and A. Alvarado. Geodesia, geodinámica y ciclo sísmico en Ecuador. *Geologia y Geofisica Marina y Terrestre del Ecuador*, pages 83–95, 2009.

J.-M. Nocquet, J. Villegas-Lanza, M. Chlieh, P. Mothes, F. Rolandone, P. Jarrin, D. Cisneros, A. Alvarado, L. Audin, F. Bondoux, et al. Motion of continental slivers and creeping subduction in the northern Andes. *Nature Geoscience*, 7(4):287, 2014.

J.-M. Nocquet, P. Jarrin, M. Vallée, P. Mothes, R. Grandin, F. Rolandone, B. Delouis, H. Yepes, Y. Font, D. Fuentes, et al. Supercycle at the Ecuadorian subduction zone revealed after the 2016 Pedernales earthquake. *Nature Geoscience*, 10(2):145–149, 2017.

S. J. Norton. Iterative seismic inversion. *Geophysical Journal International*, 94(3):457–468, 1988.

M. Ohnaka, Y. Kuwahara, and K. Yamamoto. Constitutive relations between dynamic physical parameters near a tip of the propagating slip zone during stick-slip shear failure. *Tectonophysics*, 144(1-3):109–125, 1987.

P. G. Okubo and J. H. Dieterich. Effects of physical fault properties on frictional instabilities produced on simulated faults. *Journal of Geophysical Research: Solid Earth*, 89(B7):5817–5827, 1984.

F. Pasten-Araya, P. Salazar, S. Ruiz, E. Rivera, B. Potin, A. Maksymowicz, E. Torres, J. Villarroel, E. Cruz, J. Valenzuela, et al. Fluids along the plate interface influencing the frictional regime of the Chilean subduction zone, northern Chile. *Geophysical Research Letters*, 45(19):10–378, 2018.

S. M. Peacock. Are the lower planes of double seismic zones caused by serpentine dehydration in subducting oceanic mantle? *Geology*, 29(4):299–302, 2001.

R. H. Pilger. Cenozoic plate kinematics, subduction and magmatism: South American Andes. *Journal of the Geological Society*, 141(5):793–802, 1984.

J. E. Ramírez. *Historia de los Terremotos*. Bogotá: Instituto Geográfico Agustín Codazzi, 1975.

N. Rawlinson, S. Pozgay, and S. Fishwick. Seismic tomography: a window into deep earth. *Physics of the Earth and Planetary Interiors*, 178(3-4):101–135, 2010.

N. Rawlinson, A. Fichtner, M. Sambridge, and M. K. Young. Seismic tomography and the assessment of uncertainty. In *Advances in Geophysics*, volume 55, pages 1–76. Elsevier, 2014.

M. Regnier, Y. Font, P. Charvis, D. Mercerat, A. Rietbrock, M. Ruiz, and A. Alvarado. Pedernales. *International Federation of Digital Seismograph Networks. Dataset/Seismic Network. doi*, 10, 2016.

P. Reyes and F. Michaud. Mapa geologica de la margen costera ecuatoriana (1: 500000), 2012.

C. Reynaud, É. Jaillard, H. Lapierre, M. Mamberti, and G. H. Mascle. Oceanic plateau and island arcs of southwestern Ecuador: their place in the geodynamic evolution of northwestern South America. *Tectonophysics*, 307(3-4):235–254, 1999.

M. Reyners, D. Eberhart-Phillips, G. Stuart, and Y. Nishimura. Imaging subduction from the trench to 300 km depth beneath the central north island, new zealand, with vp and vp/vs. *Geophysical Journal International*, 165(2):565–583, 2006.

A. Rietbrock, I. Ryder, G. Hayes, C. Haberland, D. Comte, S. Roecker, and H. Lyon-Caen.

Aftershock seismicity of the 2010 Maule Mw= 8.8, Chile, earthquake: Correlation between co-seismic slip models and aftershock distribution? *Geophysical Research Letters*, 39(8), 2012.

F. Rolandone, J.-M. Nocquet, P. A. Mothes, P. Jarrin, M. Vallée, N. Cubas, S. Hernandez, M. Plain, S. Vaca, and Y. Font. Areas prone to slow slip events impede earthquake rupture propagation and promote afterslip. *Science advances*, 4(1):eaao6596, 2018.

J.-P. Rothé. *The Seismicity of the Earth, 1953-1965: La Séismicité Du Globe 1953, 1965*. Unesco, 1969.

L. J. Ruff and B. W. Tichelaar. What controls the seismogenic plate interface in subduction zones? *Subduction: Top to bottom*, 96:105–111, 1996.

A. Ruina. Slip instability and state variable friction laws. *Journal of Geophysical Research: Solid Earth*, 88(B12):10359–10370, 1983.

S. Ruiz, M. Metois, A. Fuenzalida, J. Ruiz, F. Leyton, R. Grandin, C. Vigny, R. Madariaga, and J. Campos. Intense foreshocks and a slow slip event preceded the 2014 Iquique Mw 8.1 earthquake. *Science*, 345(6201):1165–1169, 2014.

S. Ruiz, E. Klein, F. del Campo, E. Rivera, P. Poli, M. Metois, V. Christophe, J. C. Baez, G. Vargas, F. Leyton, et al. The seismic sequence of the 16 September 2015 M w 8.3 Illapel, Chile, earthquake. *Seismological Research Letters*, 87(4):789–799, 2016.

I. Ryder, A. Rietbrock, K. Kelson, R. Bürgmann, M. Floyd, A. Socquet, C. Vigny, and D. Carrizo. Large extensional aftershocks in the continental forearc triggered by the 2010 Maule earthquake, chile. *Geophysical Journal International*, 188(3):879–890, 2012.

F. Sage, J.-Y. Collot, and C. R. Ranero. Interplate patchiness and subduction-erosion mechanisms: Evidence from depth-migrated seismic images at the central Ecuador convergent margin. *Geology*, 34(12):997–1000, 2006.

V. Sallarès, P. Charvis, E. R. Flueh, and J. Bialas. Seismic structure of Cocos and Malpelo Volcanic Ridges and implications for hot spot-ridge interaction. *Journal of Geophysical Research: Solid Earth*, 108(B12), 2003.

V. Sallarès, P. Charvis, E. R. Flueh, J. Bialas, and S. S. Party. Seismic structure of the Carnegie Ridge and the nature of the Galapagos hotspot. *Geophysical Journal International*, 161(3):763–788, 2005.

M. Sambridge. Inverse problems in a nutshell. *Center for Advanced Data Inference, Research School of Earth Sciences, Australian National University, ACT*, 2006.

C. H. Scholz. The mechanics of earthquakes and faulting. *mef*, page 496, 2002.

D. Schorlemmer, S. Wiemer, and M. Wyss. Variations in earthquake-size distribution across different stress regimes. *Nature*, 437(7058):539–542, 2005.

M. Segovia. El sismo de Bahía del 4 de agosto de 1998: Caracterización del mecanismo de ruptura y análisis de la sismicidad en la zonacostera. *Titulo de Ingeniera Geologia tesis): Escuela Politecnica Nacional, Quito, Ecuador*, 2001.

M. Segovia, A. Alvarado, J. Collot, V. Sallares, and N. Pazmiño. Breve análisis de la sismicidad y del campo de esfuerzos en el Ecuador. *Geología y Geofísica Marina y Terrestre del Ecuador: desde la costa continental hasta las Islas Galápagos*, pages 131–149, 2009.

M. Segovia, Y. Font, M. Regnier, P. Charvis, J. Nocquet, A. Galve, Y. Hello, A. Ogé, P. Jarrin, and M. Ruiz. Intense microseismicity associated with a SSE at La Plata Island in the central subduction zone of Ecuador. In *AGU Fall Meeting Abstracts*, 2015.

M. Segovia, Y. Font, M. Régnier, P. Charvis, A. Galve, J.-M. Nocquet, P. Jarrín, Y. Hello, M. Ruiz, and A. Pazmiño. Seismicity distribution near a subducting seamount in the Central Ecuadorian subduction zone, space-time relation to a slow-slip event. *Tectonics*, 37(7):2106–2123, 2018.

J. L. Sennson and S. L. Beck. Historical 1942 Ecuador and 1942 Peru subduction earthquakes and earthquake cycles along Colombia-Ecuador and Peru subduction segments. *Pure and applied geophysics*, 146(1):67–101, 1996.

S. A. Sipkin. Estimation of earthquake source parameters by the inversion of waveform data: synthetic waveforms. *Physics of the Earth and Planetary interiors*, 30(2-3):242–259, 1982.

S. A. Sipkin. Moment tensor solutions estimated using optimal filter theory for 51 selected earthquakes, 1980–1984. *Physics of the earth and planetary interiors*, 47:67–79, 1987.

S. A. Sipkin and R. E. Needham. Moment-tensor solutions estimated using optimal filter theory: global seismicity, 1993. *Physics of the Earth and Planetary Interiors*, 86(4):245–252, 1994.

M. Sobiesiak, U. Meyer, S. Schmidt, H.-J. Götze, and C. Krawczyk. Asperity generating upper crustal sources revealed by b value and isostatic residual anomaly grids in the area of Antofagasta, Chile. *Journal of Geophysical Research: Solid Earth*, 112(B12), 2007.

E. Sokos and J. Zahradník. Evaluating centroid-moment-tensor uncertainty in the new version of ISOLA software. *Seismological Research Letters*, 84(4):656–665, 2013.

E. N. Sokos and J. Zahradnik. ISOLA a Fortran code and a Matlab GUI to perform multiple-point source inversion of seismic data. *Computers & Geosciences*, 34(8):967–977, 2008.

L. Soto-Cordero, A. Meltzer, E. Bergman, M. Hoskins, J. C. Stachnik, H. Agurto-Detzel, A. Alvarado, S. Beck, P. Charvis, Y. Font, et al. Structural control on megathrust rupture and slip behavior: Insights from the 2016 Mw 7.8 Pedernales Ecuador earthquake. *Journal of Geophysical Research: Solid Earth*, 125(2):e2019JB018001, 2020.

W. Spakman and G. Nolet. Imaging algorithms, accuracy and resolution in delay time tomography. In *Mathematical geophysics*, pages 155–187. Springer, 1988.

S. Stein and M. Wysession. An introduction to seismology. *Earthquakes, and Earth*, 2003.

D. A. Storchak, D. Di Giacomo, I. Bondár, E. R. Engdahl, J. Harris, W. H. Lee, A. Villaseñor, and P. Bormann. Public release of the ISC–GEM global instrumental earthquake catalogue (1900–2009). *Seismological Research Letters*, 84(5):810–815, 2013.

R. A. Strelitz. The fate of the downgoing slab: a study of the moment tensors from body waves of complex deep-focus earthquakes. *Physics of the Earth and Planetary Interiors*, 21(2-3):83–96, 1980.

A. Tarantola. Inversion of travel times and seismic waveforms. In *Seismic tomography*, pages 135–157. Springer, 1987.

A. Tassara, H. Soto, J. Bedford, M. Moreno, and J. C. Baez. Contrasting amount of fluids along the megathrust ruptured by the 2010 Maule earthquake as revealed by a combined analysis of aftershocks and afterslip. *Tectonophysics*, 671:95–109, 2016.

C. Thurber and D. Eberhart-Phillips. Local earthquake tomography with flexible gridding. *Computers & Geosciences*, 25(7):809–818, 1999.

C. H. Thurber. Earthquake locations and three-dimensional crustal structure in the Coyote Lake area, central California. *Journal of Geophysical Research: Solid Earth*, 88(B10):8226–8236, 1983.

C. H. Thurber and S. R. Atre. Three-dimensional Vp/Vs variations along the Loma Prieta rupture zone. *Bulletin of the Seismological Society of America*, 83(3):717–736, 1993.

B. W. Tichelaar and L. J. Ruff. Depth of seismic coupling along subduction zones. *Journal of Geophysical Research: Solid Earth*, 98(B2):2017–2037, 1993.

S. Toda and H. Tsutsumi. Simultaneous reactivation of two, subparallel, inland normal faults during the M w 6.6 11 April 2011 Iwaki earthquake triggered by the M w 9.0 Tohoku-oki, Japan, earthquake. *Bulletin of the Seismological Society of America*, 103(2B):1584–1602, 2013.

D. Toomey and G. Foulger. Tomographic inversion of local earthquake data from the Hengill-

Grensdalur central volcano complex, Iceland. *Journal of Geophysical Research: Solid Earth*, 94 (B12):17497–17510, 1989.

R. Trenkamp, J. N. Kellogg, J. T. Freymueller, and H. P. Mora. Wide plate margin deformation, southern Central America and northwestern South America, CASA GPS observations. *Journal of South American Earth Sciences*, 15(2):157–171, 2002.

J. Um and C. Thurber. A fast algorithm for two-point seismic ray tracing. *Bulletin of the Seismological Society of America*, 77(3):972–986, 1987.

S. Vaca, M. Régnier, N. Bethoux, V. Alvarez, and B. Pontoise. Sismicidad de la región de Manta: Enjambre sísmico de Manta-2005. *Geologia y Geofisica Marina y Terrestre del Ecuador Desde la Costa Continental Hasta las Islas Gapapagos*, pages 151–166, 2009.

S. Vaca, M. Vallée, J.-M. Nocquet, J. Battaglia, and M. Régnier. Recurrent slow slip events as a barrier to the northward rupture propagation of the 2016 Pedernales earthquake (Central Ecuador). *Tectonophysics*, 724:80–92, 2018.

M. Vallée, J.-M. Nocquet, J. Battaglia, Y. Font, M. Segovia, M. Regnier, P. Mothes, P. Jarrin, D. Cisneros, S. Vaca, et al. Intense interface seismicity triggered by a shallow slow slip event in the Central Ecuador subduction zone. *Journal of Geophysical Research: Solid Earth*, 118(6): 2965–2981, 2013.

R. Von Huene and R. Culotta. Tectonic erosion at the front of the Japan Trench convergent margin. *Tectonophysics*, 160(1-4):75–90, 1989.

R. von Huene, C. R. Ranero, W. Weinrebe, and K. Hinz. Quaternary convergent margin tectonics of Costa Rica, segmentation of the Cocos Plate, and Central American volcanism. *Tectonics*, 19 (2):314–334, 2000.

R. von Huene, C. R. Ranero, and P. Vannucchi. Generic model of subduction erosion. *Geology*, 32 (10):913–916, 2004.

P. Vrolijk. On the mechanical role of smectite in subduction zones. *Geology*, 18(8):703–707, 1990.

K. Wadati and S. Oki. On the travel time of earthquake waves.(part ii). *Journal of the Meteorological Society of Japan. Ser. II*, 11(1):14–28, 1933.

K. Wang and S. L. Bilek. Do subducting seamounts generate or stop large earthquakes? *Geology*, 39(9):819–822, 2011.

K. Wang and S. L. Bilek. Invited review paper: Fault creep caused by subduction of rough seafloor relief. *Tectonophysics*, 610:1–24, 2014.

A. B. Watts, A. A. Koppers, and D. P. Robinson. Seamount subduction and earthquakes. *Oceanography*, 23(1):166–173, 2010.

A. Wegener. Die herausbildung der grossformen der erdrinde (kontinente und ozeane), auf geophysikalischer grundlage. *Petermanns Geographische Mitteilungen*, 63:185–195, 1912.

R. S. White, D. McKenzie, and R. K. O'Nions. Oceanic crustal thickness from seismic measurements and rare earth element inversions. *Journal of Geophysical Research: Solid Earth*, 97(B13):19683–19715, 1992.

S. M. White, R. Trenkamp, and J. N. Kellogg. Recent crustal deformation and the earthquake cycle along the Ecuador–Colombia subduction zone. *Earth and Planetary Science Letters*, 216(3): 231–242, 2003.

S. Wiemer and K. Katsumata. Spatial variability of seismicity parameters in aftershock zones. *Journal of Geophysical Research: Solid Earth*, 104(B6):13135–13151, 1999.

Y. Yamamoto, K. Obana, S. Kodaira, R. Hino, and M. Shinohara. Structural heterogeneities around the megathrust zone of the 2011 Tohoku earthquake from tomographic inversion of onshore and offshore seismic observations. *Journal of Geophysical Research: Solid Earth*, 119(2):1165–1180, 2014.

L. Yi, C. Xu, Y. Wen, X. Zhang, and G. Jiang. Rupture process of the 2016 Mw 7.8 Ecuador earthquake from joint inversion of InSAR data and teleseismic p waveforms. *Tectonophysics*, 722:163–174, 2018.

M. Yoshimoto, H. Kumagai, W. Acero, G. Ponce, F. Vásconez, S. Arrais, M. Ruiz, A. Alvarado, P. Pedraza García, V. Dionicio, et al. Depth-dependent rupture mode along the Ecuador-Colombia subduction zone. *Geophysical Research Letters*, 44(5):2203–2210, 2017.

D. Zhao, A. Hasegawa, and S. Horiuchi. Tomographic imaging of p and s wave velocity structure beneath northeastern japan. *Journal of Geophysical Research: Solid Earth*, 97(B13):19909–19928, 1992.

Appendix A

This appendix contains the supplementary material for the article **1D velocity structure and seismotectonics of the Ecuadorian margin inferred from the 2016 Mw 7.8 Pedernales aftershock sequence** (León-Ríos et al., 2019) presented in Chapter 5.

- Supplementary Material 1: Selected data
- Supplementary Material 2: Number of observations
- Supplementary Material 3: Current 1D models in Ecuador
- Supplementary Material 4: Simplified velocity model for FWI
- Supplementary Material 5: Histogram of station residuals
- Supplementary Material 6: Comparison of initial/final aftershock localizations
- Supplementary Material 7: Stability test for relocated seismicity
- Supplementary Material 8: Comparison of slab1.0/slab2.0 and the relocated seismicity
- Supplementary Material 9: Statistics for RMT solution: event 4
- Supplementary Material 10: Statistics for RMT solution: event 3
- Supplementary Material 11: Statistics for RMT solution: event 15
- Supplementary Material 12: Depth differences between arrival times and FWI
- Supplementary Material 13: Interseismic and postseismic distribution of earthquakes

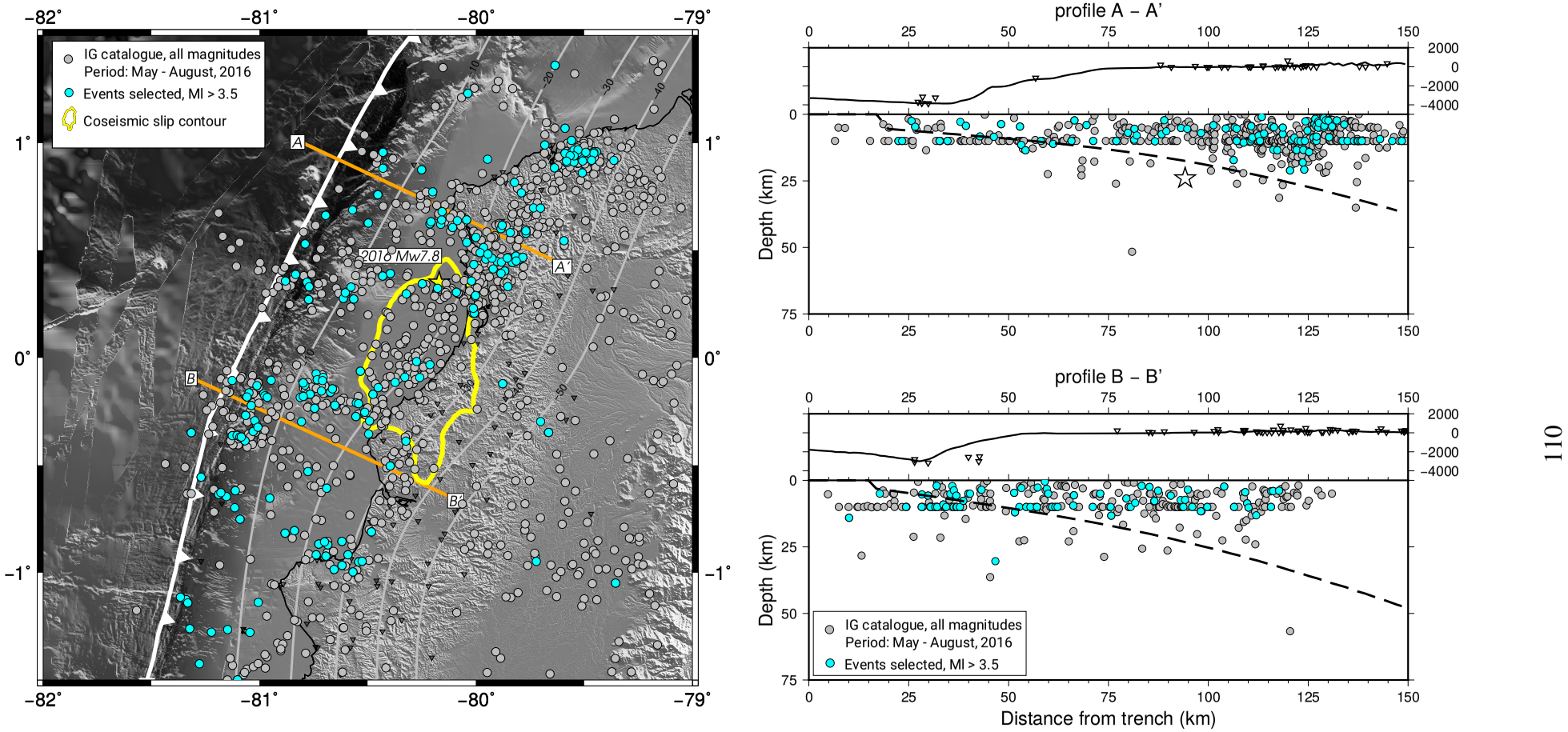

Supplementary Material A1: Hypocentral locations reported by the IGEPN for the period May-August 2016. Gray circles represent all the seismicity in the catalog. Light blue circles are the events with magnitude greater than 3.5 selected for the manual picking. Star represents the hypocenter for the 2016 Pedernales earthquake derived by Nocquet et al. (2017). Coseismic contour in yellow solid line was calculated by Nocquet et al. (2017). Segmented line is Slab1.0 from Hayes et al. (2012). Inland and seafloor topography was obtained by Michaud et al. (2006). Trench data from Collot et al. (2005).

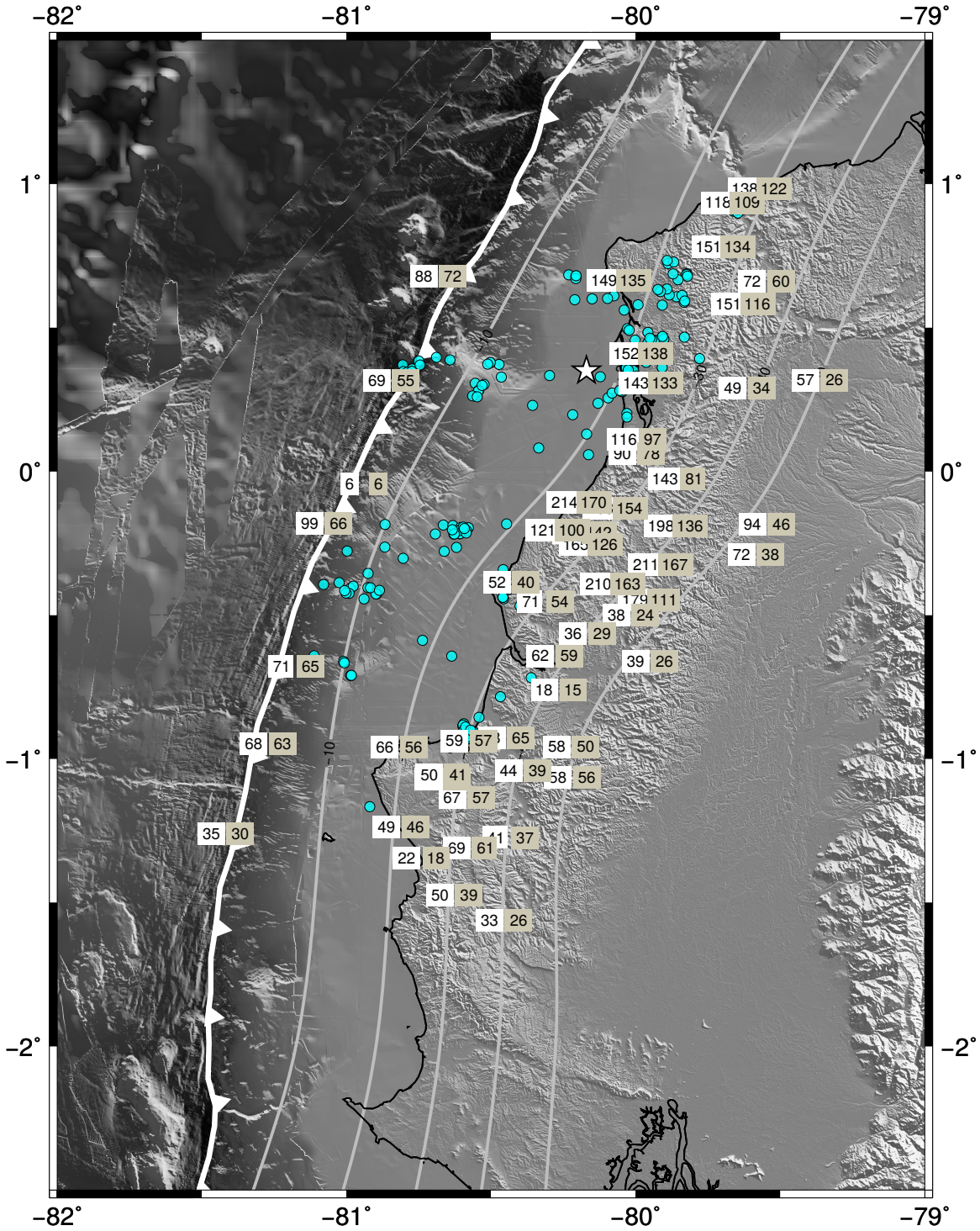

Supplementary Material A2: Distribution of the number of observations for the P- and S-phase obtained in each station used in this work. White and green boxes indicate P- and S- onsets, respectively. White star shows the epicenter of the 2016 Pedernales earthquake derived by Nocquet et al. (2017). Cyan circles are showing the locations obtained using our minimum 1D model. Inland and seafloor topography was obtained by Michaud et al. (2006). Trench data from Collot et al. (2005).

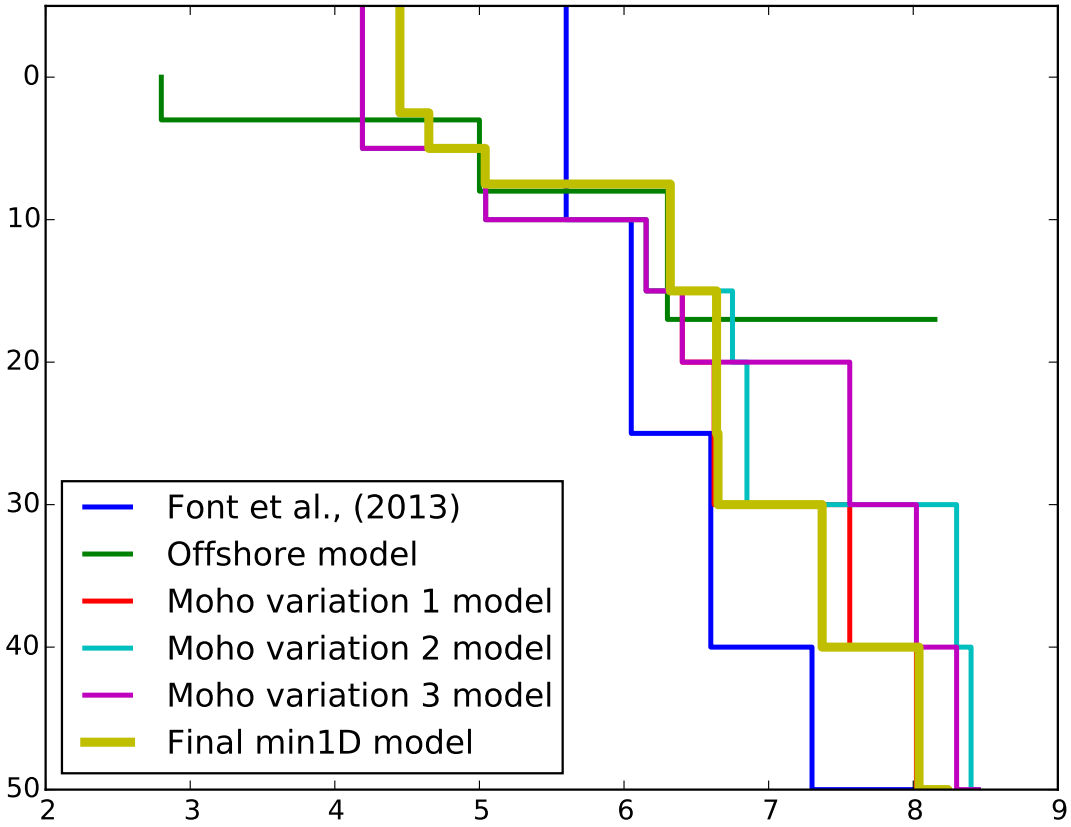

Supplementary Material A3: Reference models used as a starting point to build our minimum 1D velocity model. Blue line corresponds to the *a priori* model by Font et al., (2013). Green line is a representation for offshore Ecuador. Red, cyan and purple lines are combined models incluiding Font and offshore with variation in the Moho depth from 20 to 40 km. Finally, brown line shows our obtained minimum 1D model.

Depth (km)	Vp (km/s)	Vs (km/s)
0.0	4.45	2.26
5.0	5.04	2.59
10.0	6.32	3.42
20.0	6.64	3.69
25.0	6.65	3.80
30.0	7.37	3.81
40.0	8.04	4.64
50.0	8.24	4.64
60.0	8.45	4.71

Supplementary Material A3: Simplified velocity model used for the FWI using isola. The shallowest 8 layers from the original minimum 1D velocity model were merged into 4 layers.

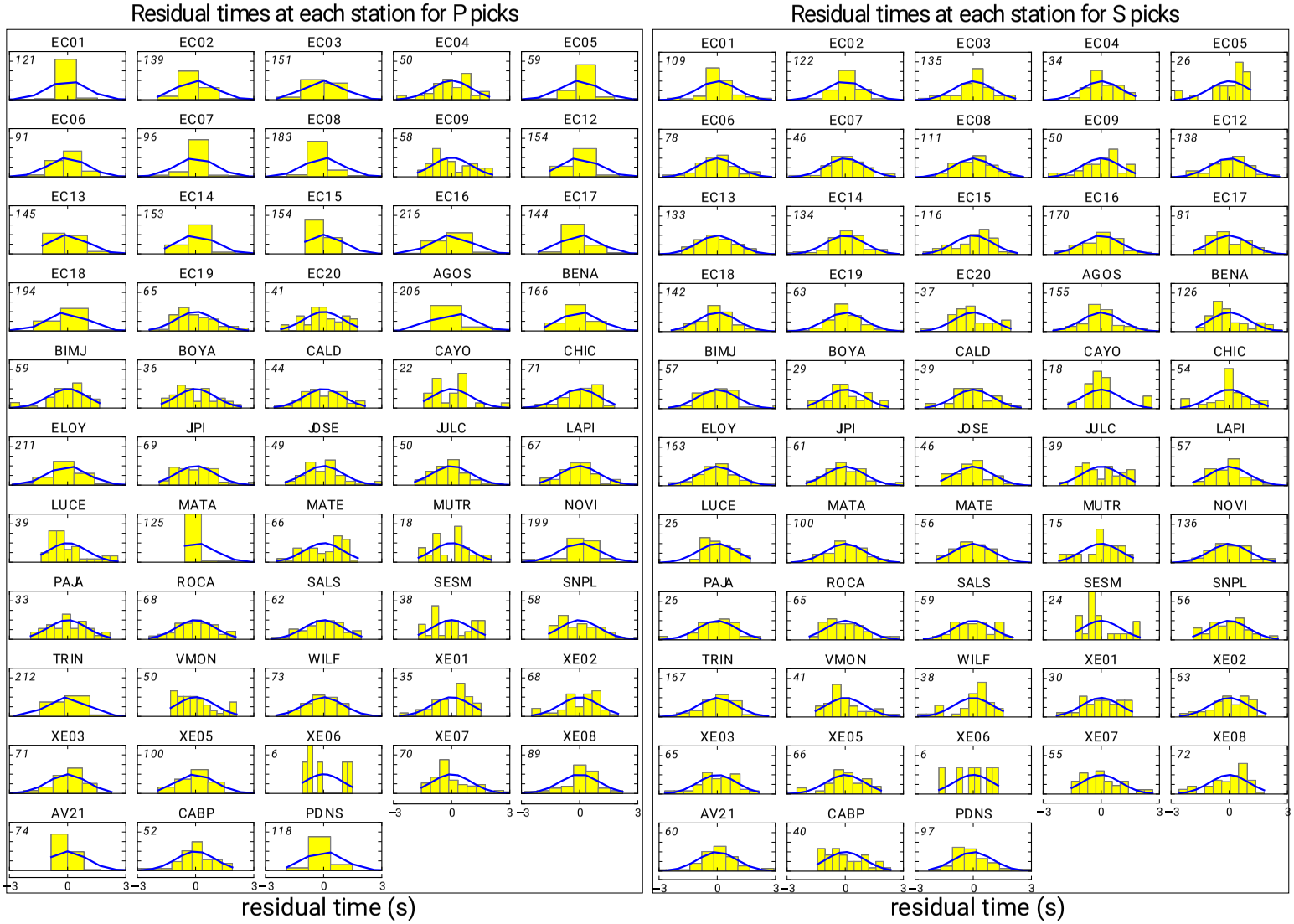

Supplementary Material A4: Histogram for the residual values for the P and S picks at each station. In the top right corner is indicated the number of observations for the corresponding phase at the station. Solid blue line corresponds to the standard deviation fitting.

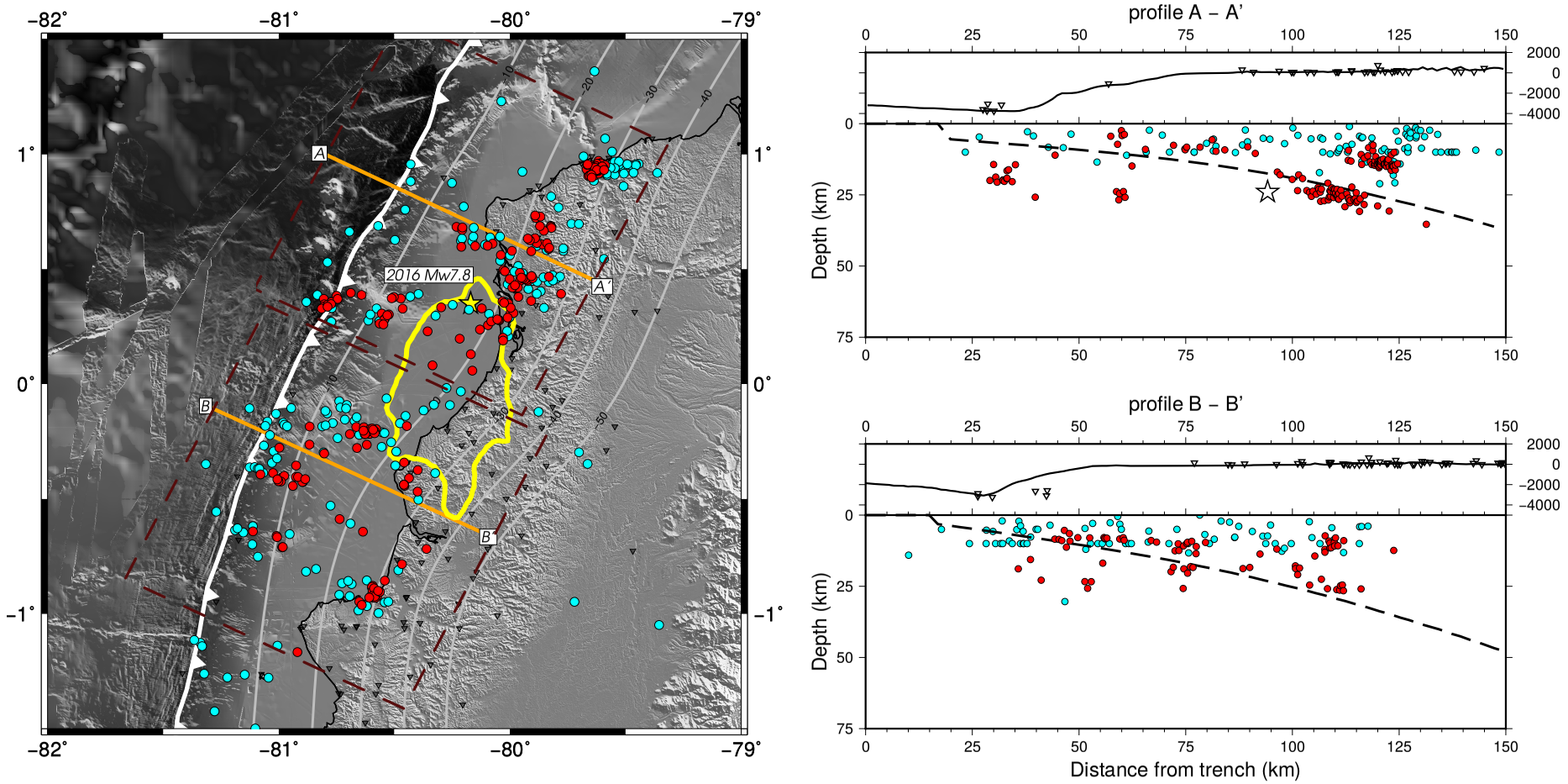

Supplementary Material A5: Comparison between the analized seismicity: location by IGEPN and locations obtained in this work. Cyan circles indicate the locations reported by IGEPN. Red circles show the locations obtained using our minimum 1D model. Star represents the hypocenter for the 2016 Pedernales earthquake derived by **??**. Segmented boxes indicate the area of the projected profiles. Segmented line is Slab1.0 from Hayes et al. (2012). Inland and seafloor topography was obtained by Michaud et al. (2006). Trench data from Collot et al. (2005).

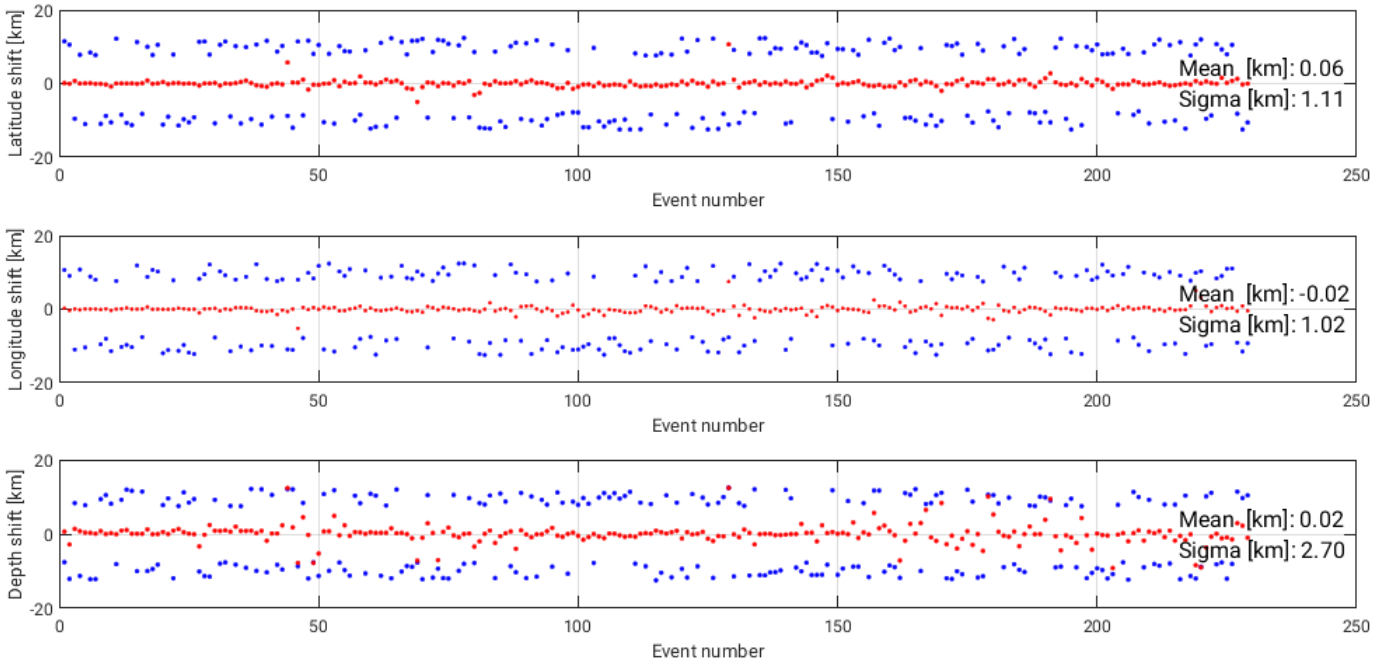

Supplementary Material A6: Stability test for the relocated seismicity. Blue circles indicate the random shift applied to the original locations. Red circles are the recovered locations of the events after been located using our minimum 1D velocity model.

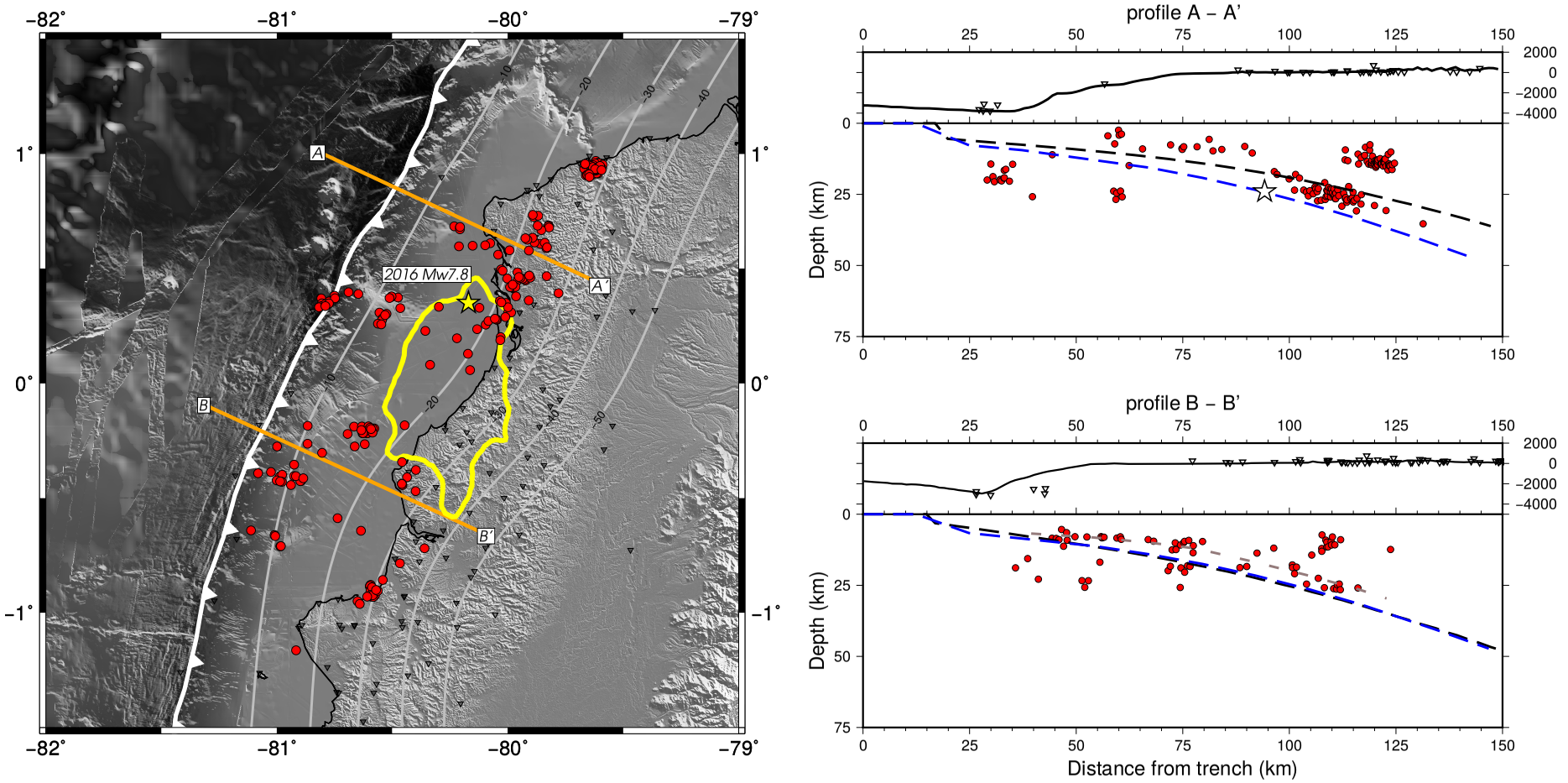

Supplementary Material A7: Comparison of the seismicity location regarding Slab1.0 (Hayes et al., 2012) and Slab2.0 (Hayes et al., 2018). Red circles show the locations obtained using our minimum 1D model. Star represents the hypocenter for the 2016 Pedernales earthquake derived by Nocquet et al. (2017). Segmented black line shows Slab1.0 from Hayes et al. (2012). Segmented blue line represents Slab2.0 from Hayes et al. (2018). Segmented gray line represents our proposed shallower slab. Inland and seafloor topography was obtained by Michaud et al. (2006). Trench data from Collot et al. (2005).

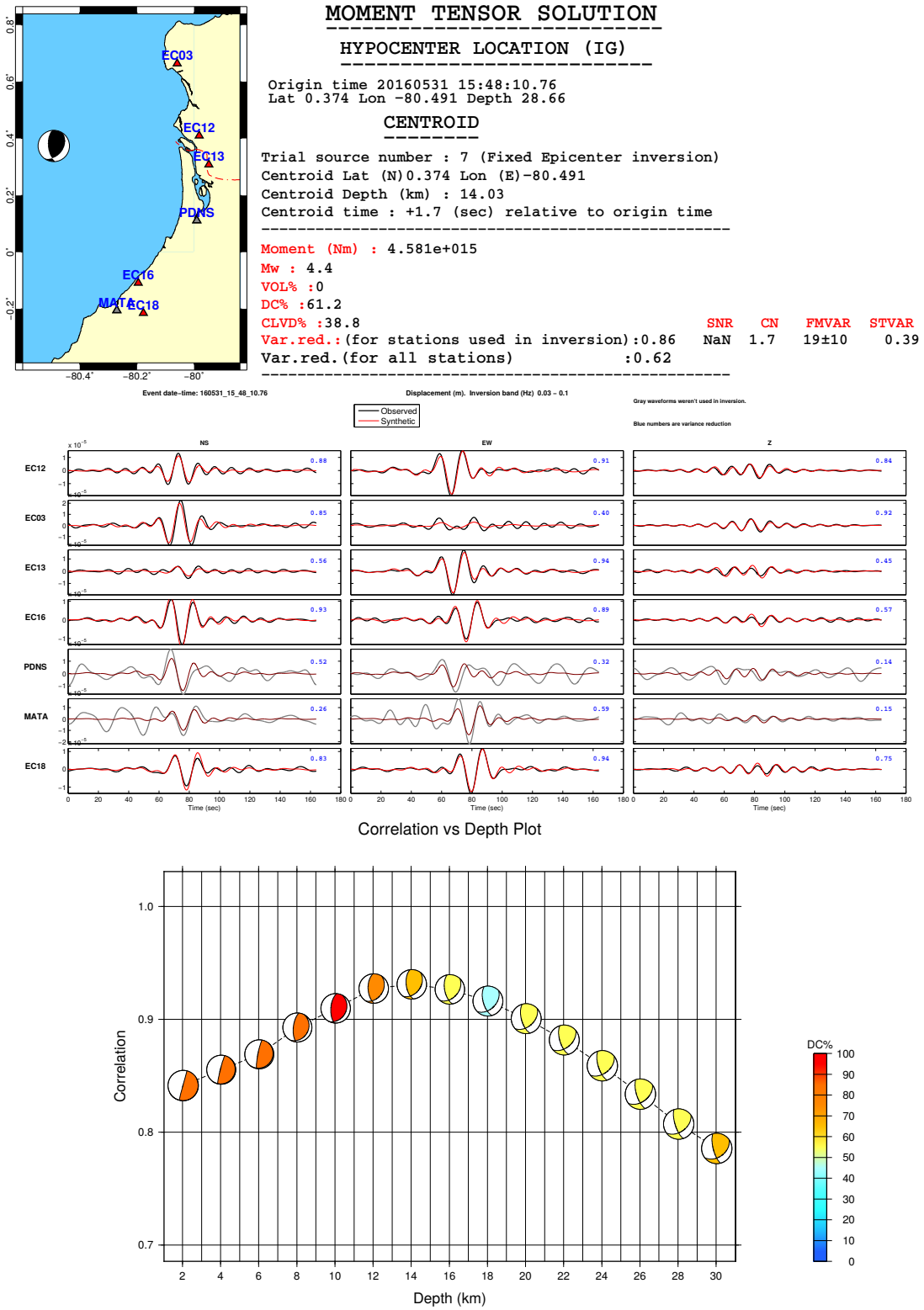

Supplementary Material A8: Waveform fitting after the FWI using *isola* for a reverse event (e4 in Table 2). (top) Beach ball shows the obtained focal mechanism. Red star indicates the event epicenter. Stations used are shown with red triangles. Insert is the MT solution from USGS catalog. Summary of the solution. (center) Synthetic signal is plot in solid red line over the observed trace in black. Frequency range used in the inversion is indicated at the top of each event. (bottom) Correlation plot.

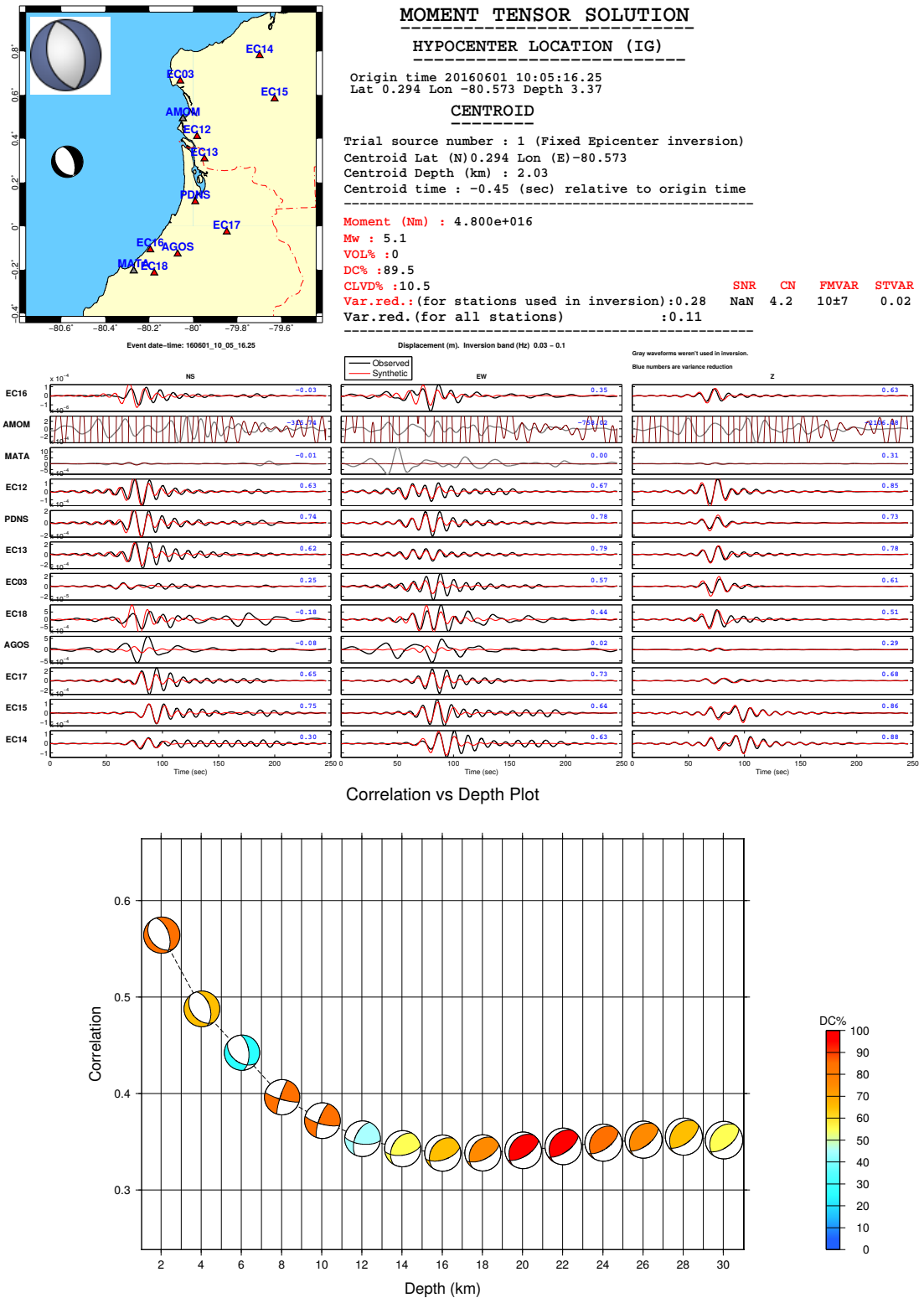

Supplementary Material A9: Waveform fitting after the FWI using *isola* for an extensional event (e3 in Table 2). (top) Beach ball shows the obtained focal mechanism. Red star indicates the event epicenter. Stations used are shown with red triangles. Insert is the MT solution from GFZ catalog. Summary of the solution. (center) Synthetic signal is plot in solid red line over the observed trace in black. Frequency range used in the inversion is indicated at the top of each event. (bottom) Correlation plot.

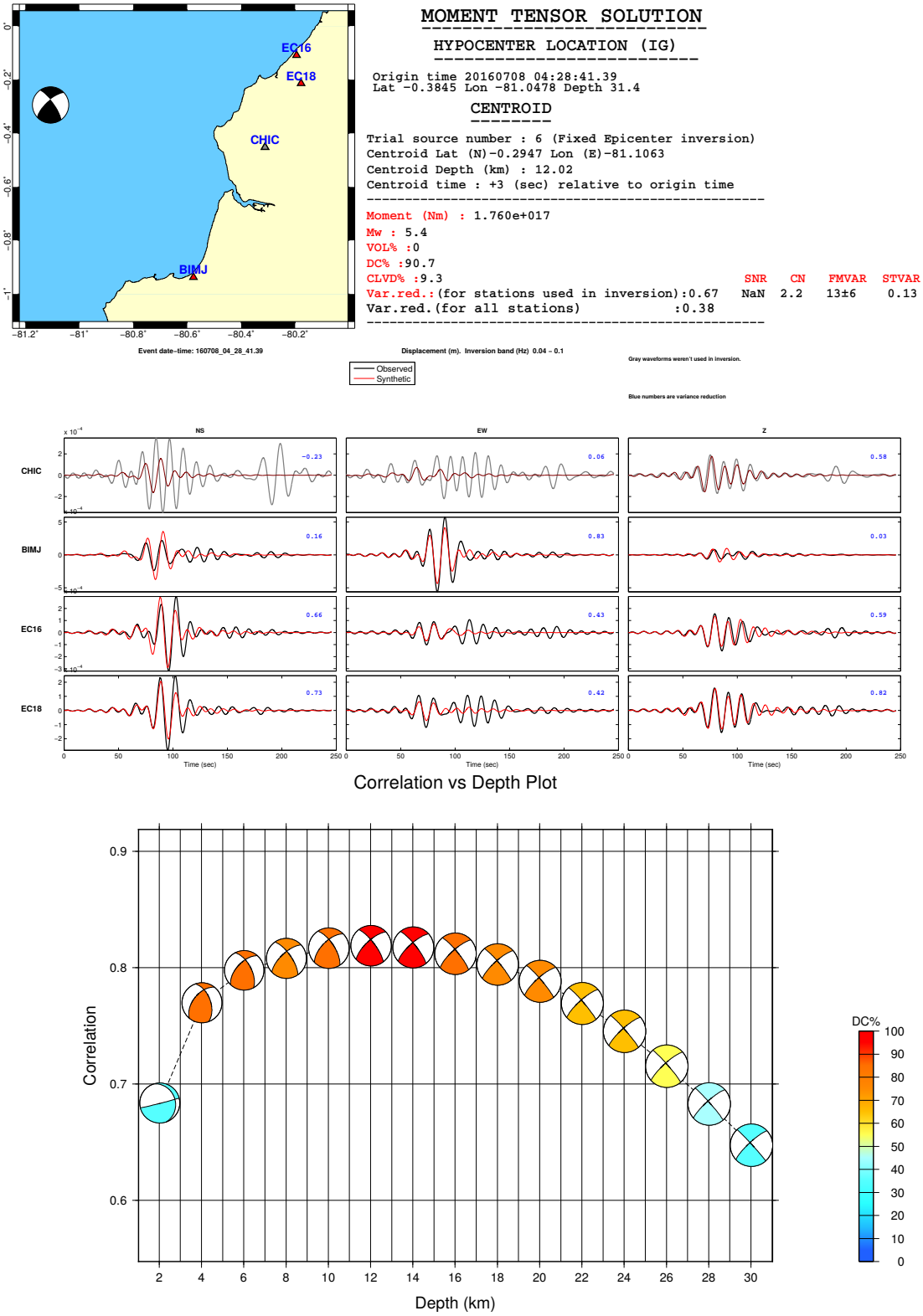

Supplementary Material A10: Waveform fitting after the FWI using *isola* for a strike-slip event (e15 in Table 2). (top) Beach ball shows the obtained focal mechanism. Red star indicates the event epicenter. Stations used are shown with red triangles. Summary of the solution. (center) Synthetic signal is plot in solid red line over the observed trace in black. Frequency range used in the inversion is indicated at the top of each event. (bottom) Correlation plot.

Event	ID	Arrival times depth (km)	ERZ (km)	Centroid depth (km)	Δ depth (km)
20160601.150052	e27	4.16	1.99	2.03	2.13
20160601.100515	e3	4.42	2.58	2.03	2.39
20160708.070348	e17	7.88	3.55	12.03	4.15
20160707.171013	e14	8.12	0.49	14.02	5.90
20160606.164508	e0	8.24	0.73	13.00	4.76
20160531.154810	e4	11.91	5.46	14.03	2.12
20160602.001859	e8	12.54	2.04	16.03	3.49
20160621.044024	e7	18.37	2.50	5.00	13.37
20160601.021221	e9	18.99	2.37	16.03	2.96
20160710.064434	e19	22.35	1.28	10.03	12.32
20160708.073516	e18	22.99	1.21	12.03	10.96
20160530.054856	e5	25.53	0.94	25.03	0.50
20160708.044136	e16	29.99	1.91	8.03	21.96
20160505.160640	e25	-	-	8.03	-

Supplementary Material A10: Comparison between depths obtained from arrival times inversion and FWI. Events are sorted by the depths calculated in our minimum 1D velocity model. Depths for the shallowest seismicity, down to 20 km, coincide with an average variation of 3.56 km.

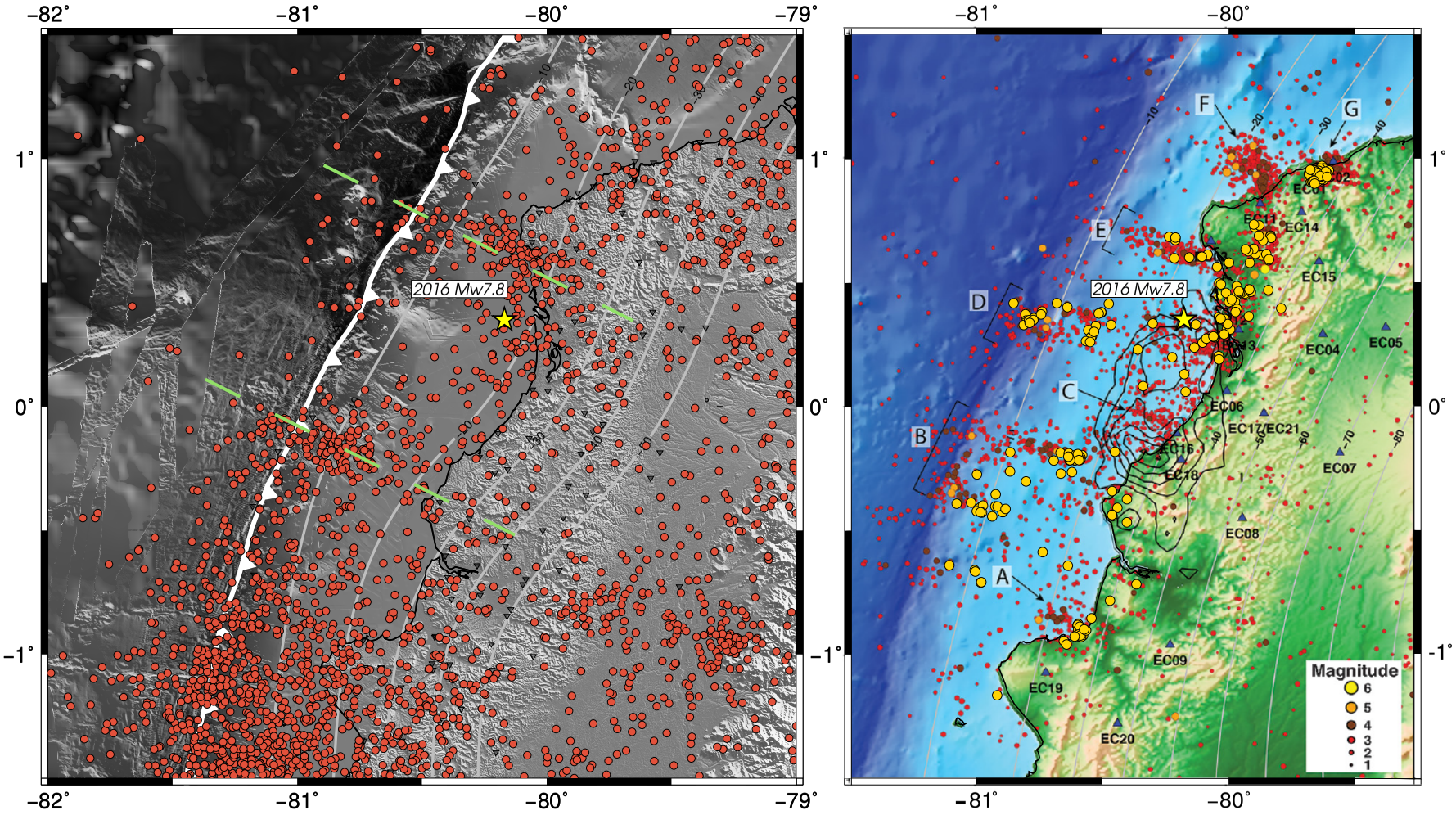

Supplementary Material A11: (Left) seismicity distribution during the interseismic period between 1950 –15 April 2016. Data retireved from the ISC website. (Right) Figure edited from (Meltzer and Beck, 2016) with our relocated seismicity (yellow circles) superimposed over their located aftershocks.

Appendix B

This appendix contains the supporting information for the article **3D local earthquake tomography of the Ecuadorian margin in the source area of the 2016 Mw 7.8 Pedernales earthquake** León-Ríos et al. (2020) which is part of the Chapter 6.

- Supporting Information 1: Inversion grid.
- Supporting Information 2: Minimum 1D velocity model.
- Supporting Information 3: Damping curves.
- Supporting Information 4: Initial 2D velocity model.
- Supporting Information 5: MRM analysis.
- Supporting Information 6: Checkerboard test.
- Supporting Information 7: Synthetic model. Testing anomalies on Vp model.
- Supporting Information 8: Synthetic model. Testing influence of 2D initial model.
- Supporting Information 9: 3D velocity model, merging modeling strategy. Horizontal slices.
- Supporting Information 10: 3D velocity model, merging modeling strategy. Cross sections.
- Supporting Information 11: Estimated standard deviation.
- Supporting Information 12: Analyzing Vp iso-velocity contours.
- Supporting Information 13: Constrasting residual bathymetry and Vp horizontal slice.
- Supporting Information 14: MRM analysis along strike.

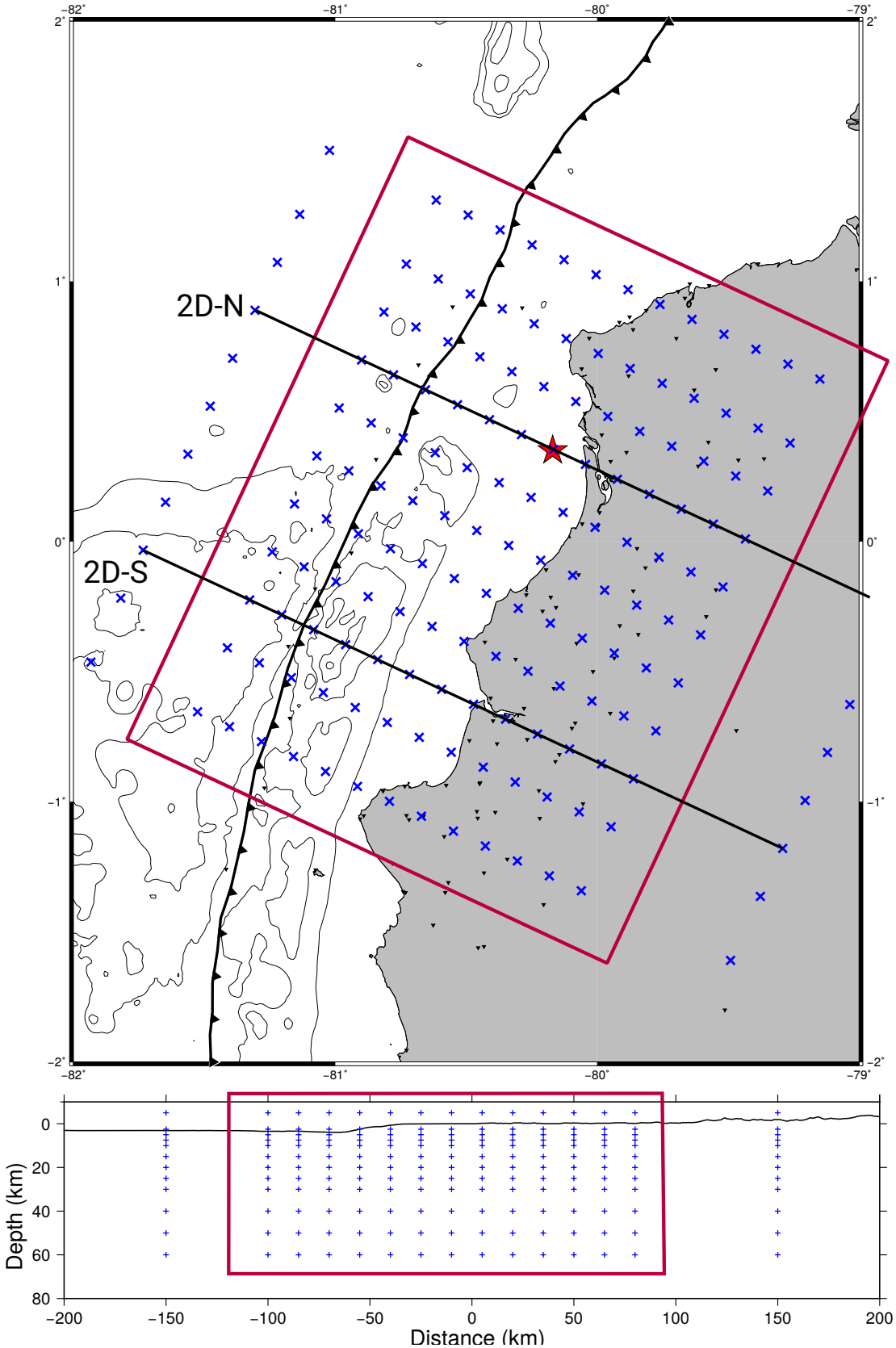

Supplementary Material B1: Inversion grid. Grid nodes distribution for the inversion process. Outer rectangle shows the distribution for the coarse grid, while inner rectangle represents the fine grid with a 15 km W-E nodes spacing and 22.5 km separation along strike. Bottom image shows the distribution in depth following the layering of the minimum 1D velocity model (León-Ríos et al., 2019).

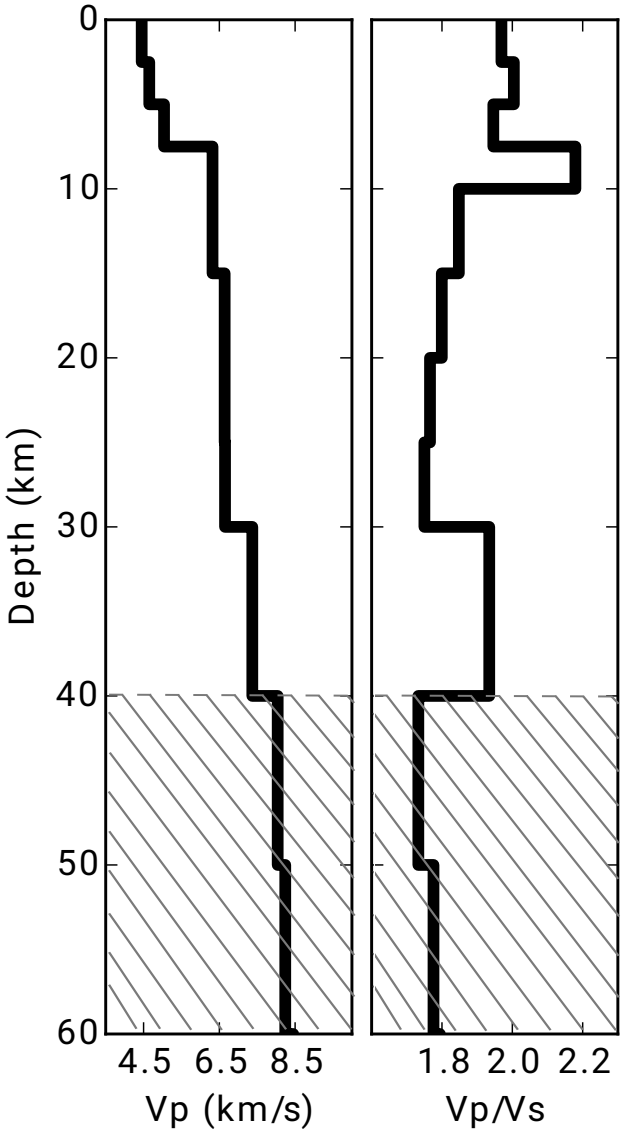

Depth (km)	Vp (km/s)	Vp/Vs
0	4.45	1.96
2.5	4.65	2.00
5.0	5.04	1.94
7.5	6.32	2.18
10.0	6.32	1.84
15.0	6.64	1.80
20.0	6.64	1.76
25.0	6.65	1.75
30.0	7.37	1.93
40.0	8.04	1.73
50.0	8.24	1.77
60.0	8.45	1.79

Supplementary Material B2: Vp (left) and Vp/Vs (right) one-dimensional structure derived by León-Ríos et al. (2019). Inset table details the values at each layer. The average Vp/Vs ratio is 1.82.

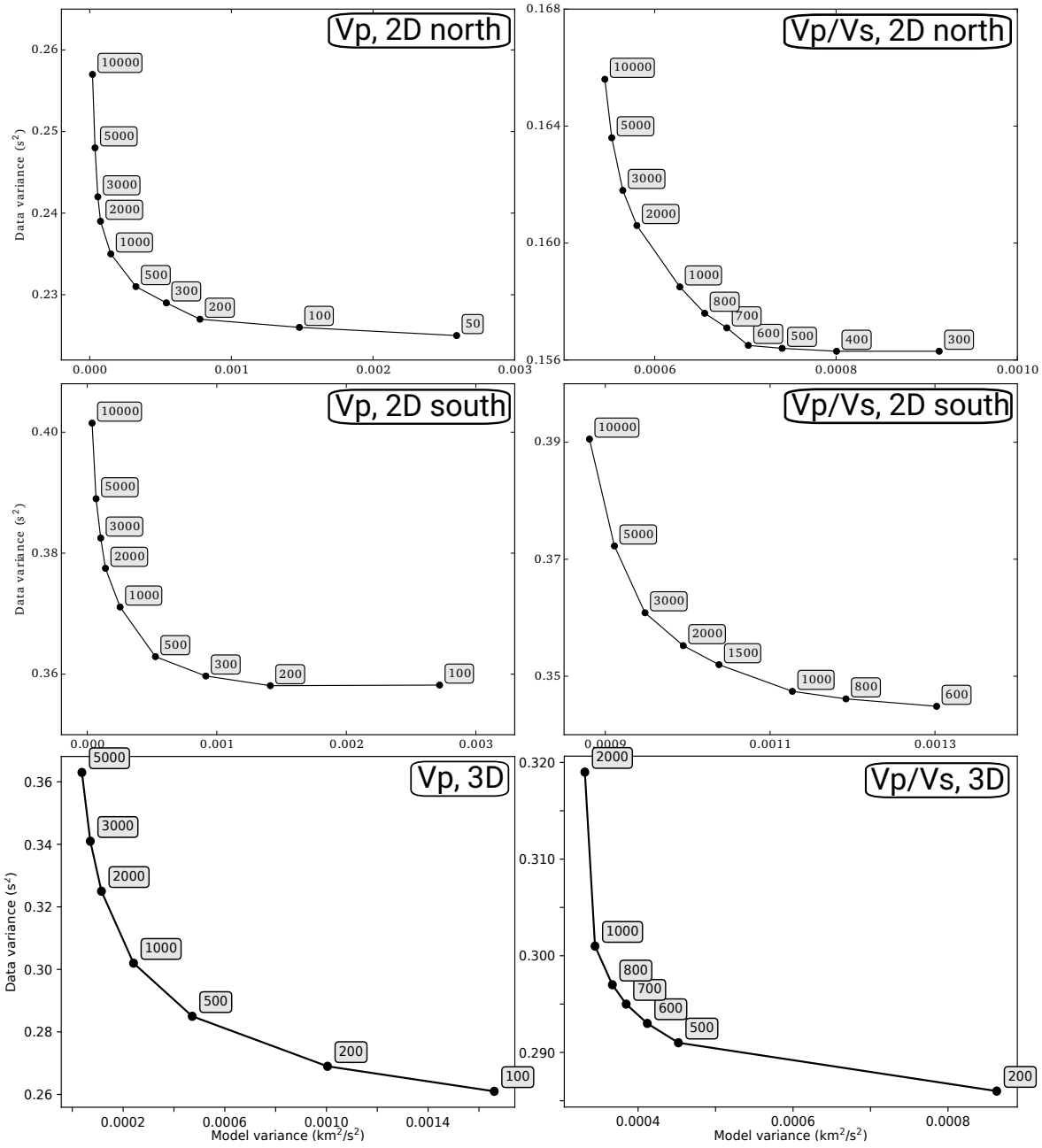

Supplementary Material B3: Damping curves. Trade-off curves analysis for the different stages of this work. Left side shows the Vp and right side the Vp/Vs ratio. Damping curves were calculated for north and south segments in the 2D inversion, and for the complete dataset in the 3D inversion stage.

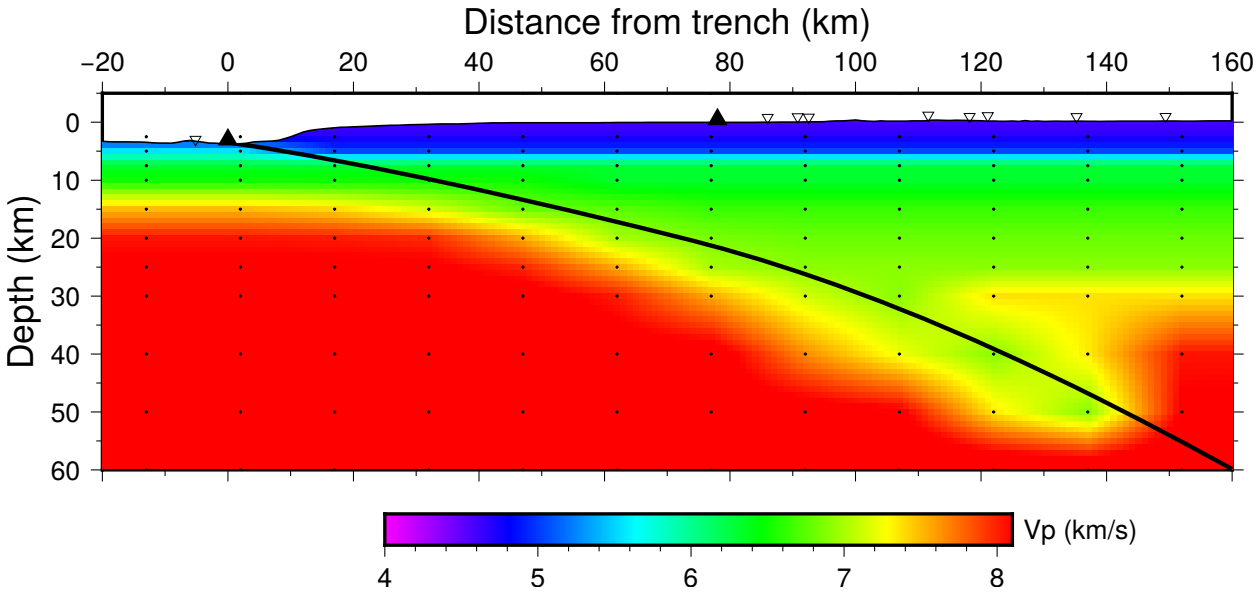

Supplementary Material B4: Initial 2D P-wave velocity model based on the slab geometry. Solid black triangles represent the projection of the trench (Collot et al., 2005) and coastline. The inverted triangles are the stations projected on each profile in a region of $\pm$12 km.

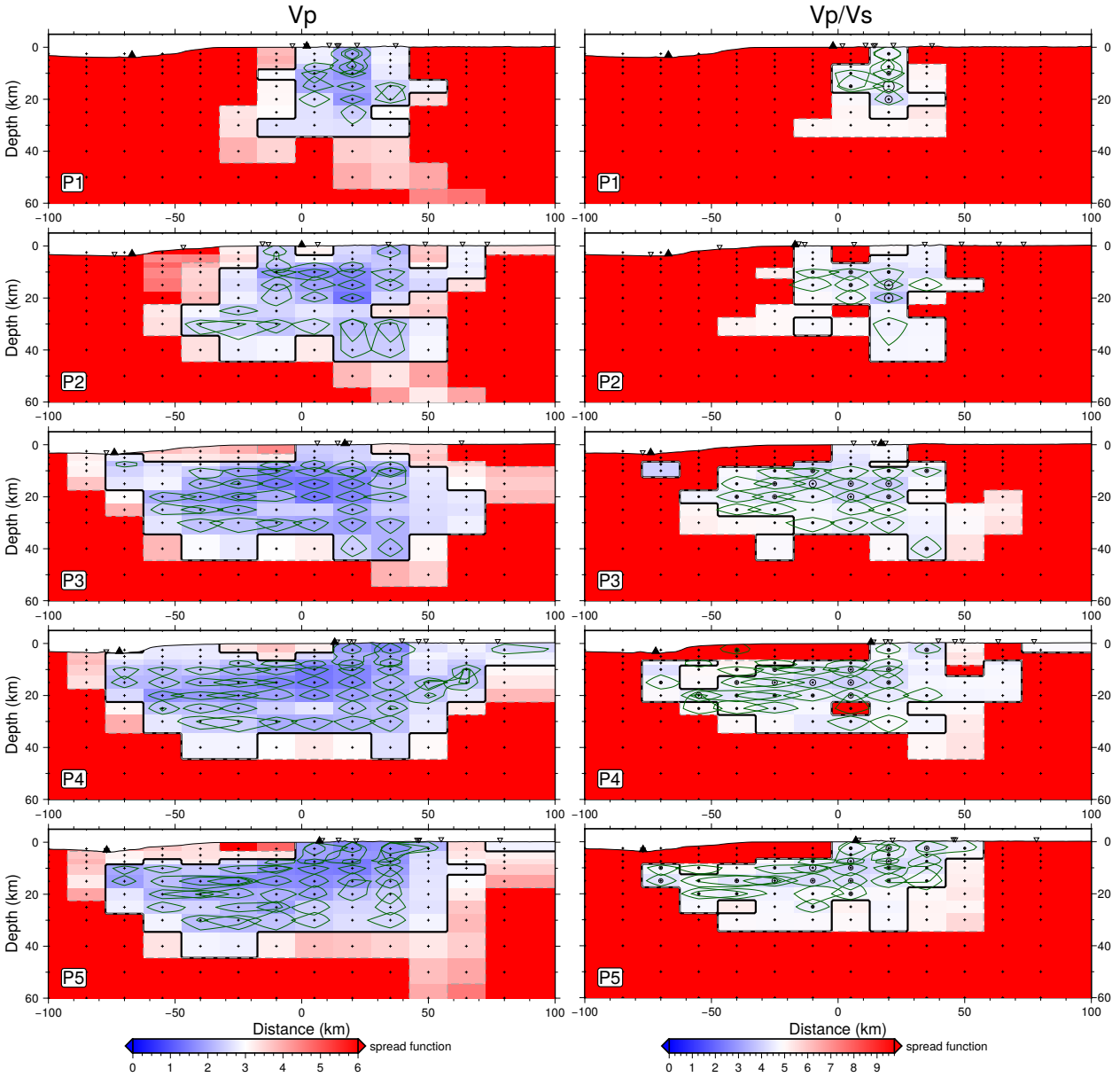

Supplementary Material B5: 3D MRM analysis. Model resolution matrix analysis using the spread function and the 70% of the diagonal elements of the MRM. Spread function is color coded with a blue-red with blue colors representing well resolved regions.

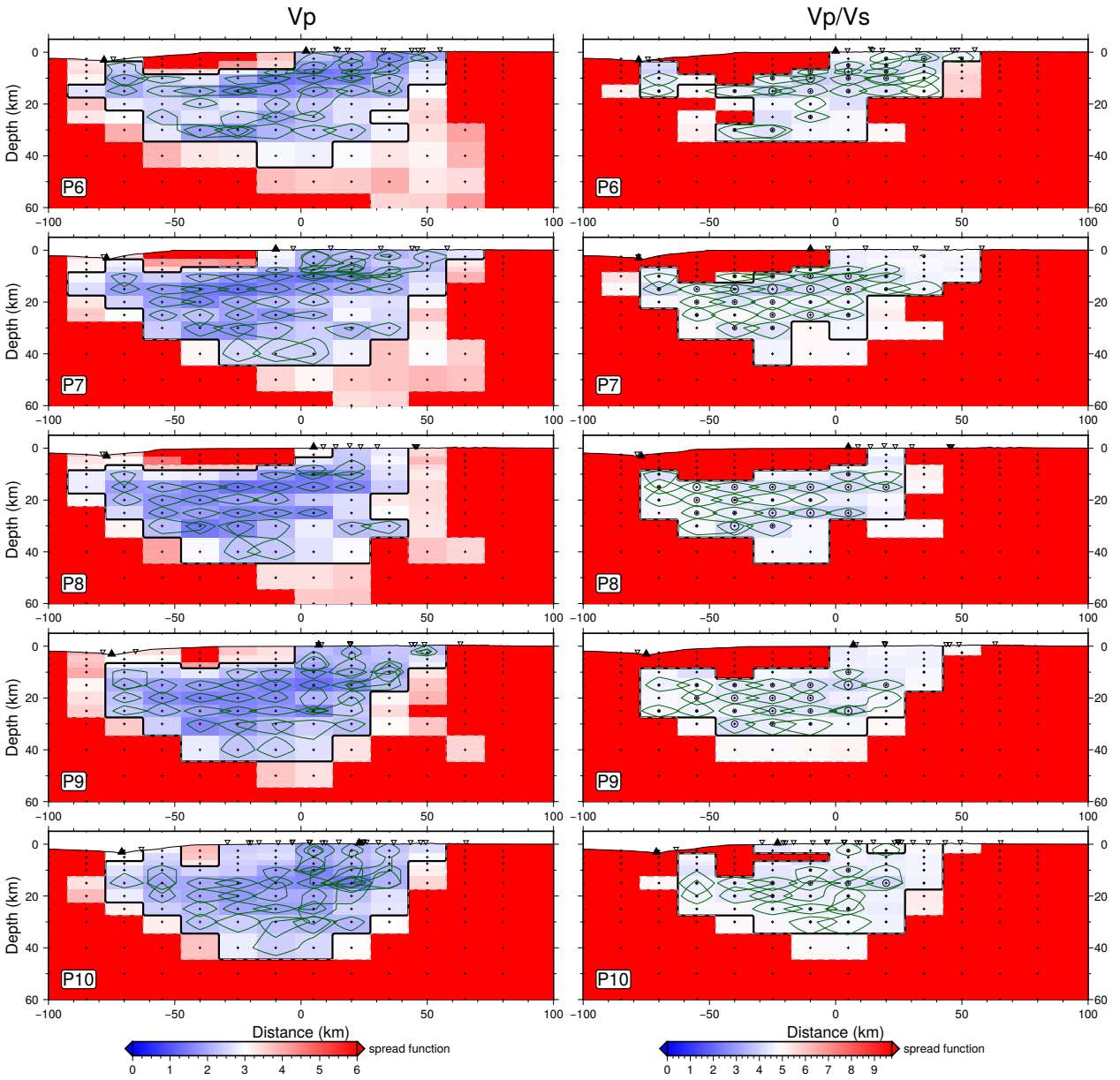

Supplementary Material B6: 3D MRM analysis. Model resolution matrix analysis using the spread function and the 70% of the diagonal elements of the MRM. Spread function is color coded with a blue-red with blue colors representing well resolved regions.

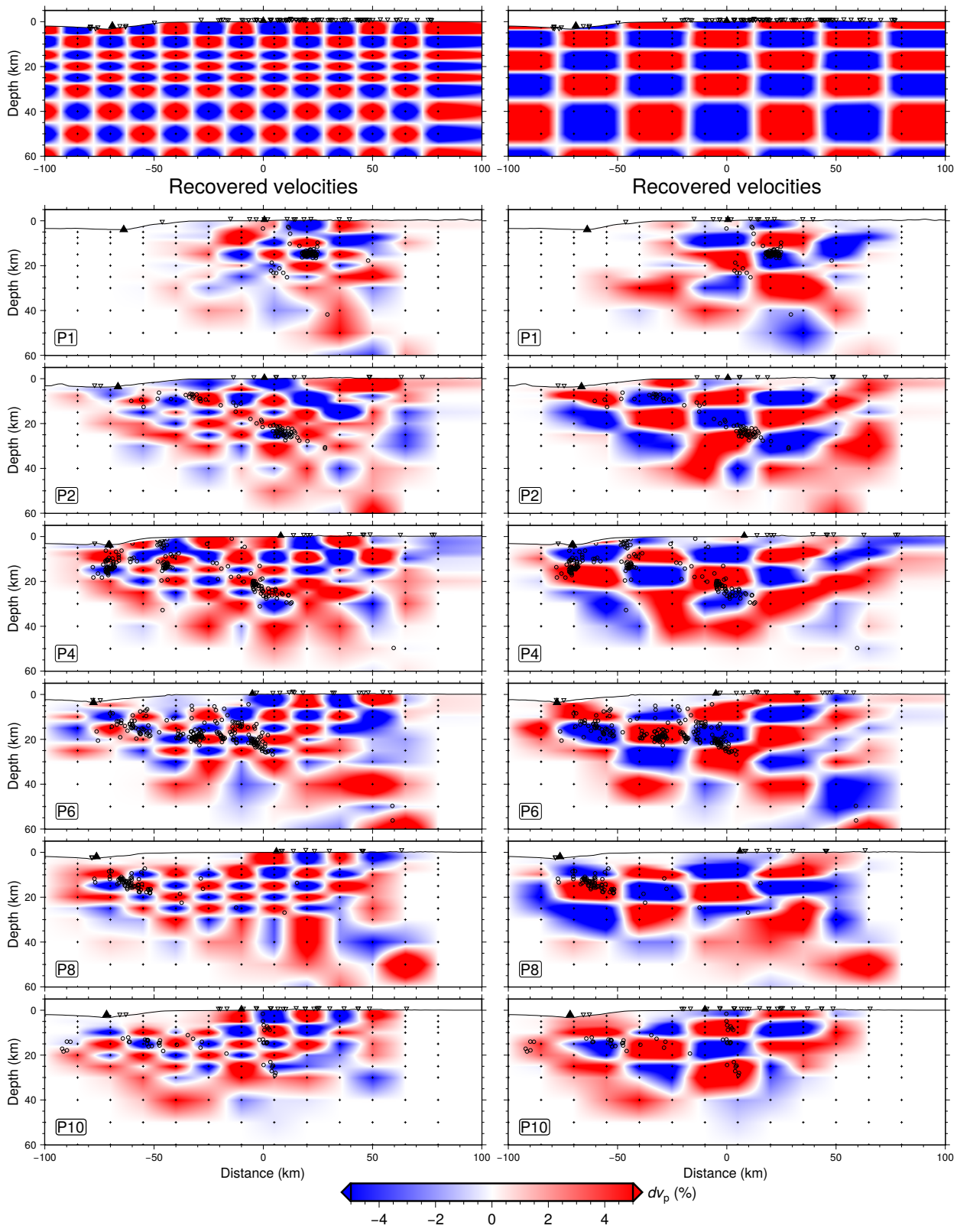

Supplementary Material B7: Testing influence of 2D initial model. Synthetic model. Synthetic restoring test to evaluate the influence of our 2D Vp northern segment model (2D-N), over a homogeneous subduction zone. Synthetic arrival times were generated using the synthetic model (2D-N) and then tested over the homogeneous initial model. Recovered velocities are shown for central profiles (P3-P8).

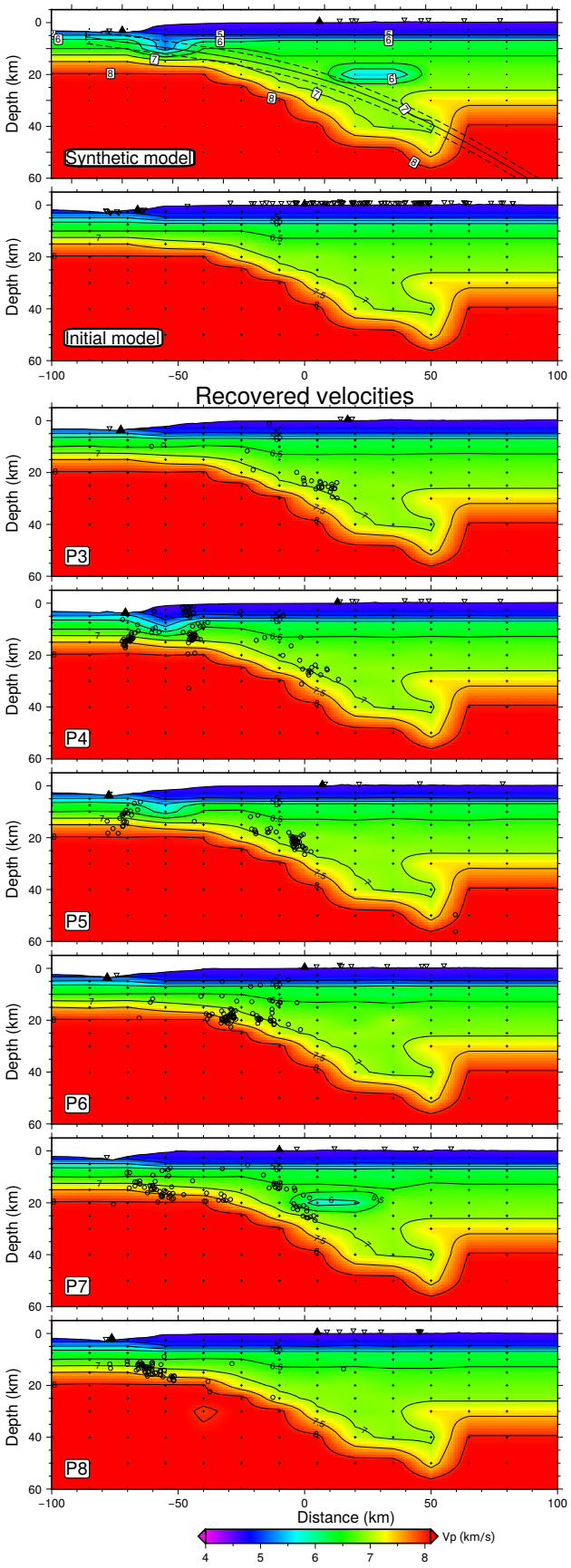

Supplementary Material B8: Synthetic model. Testing influence of 2D initial model. Synthetic recovery test for a seamount represented by low Vp anomalies added in P4-P5. Also, a low velocity anomaly was included at 20 km depth in P7. Projection of the input model is shown at the top.

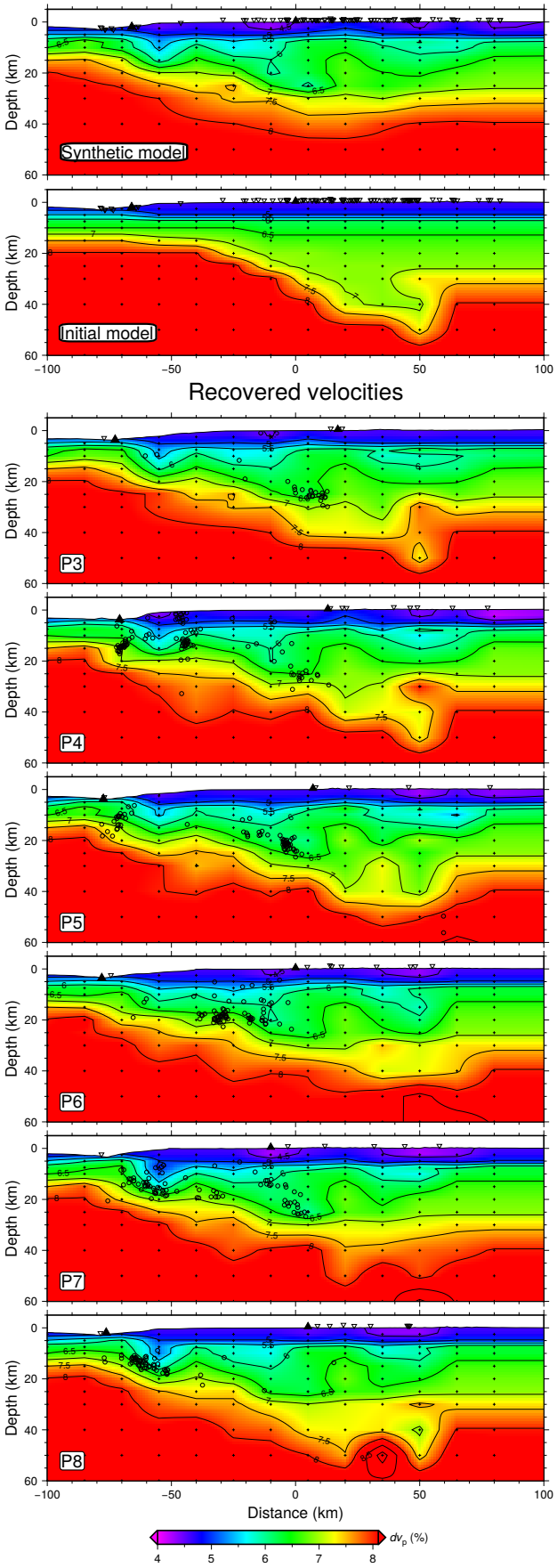

Supplementary Material B9: Testing influence of 2D initial model. Synthetic model. Synthetic restoring test to evaluate the influence of our 2D Vp northern segment model (2D-N), over a homogeneous subduction zone. Synthetic arrival times were generated using the synthetic model (2D-N) and then tested over the homogeneous initial model. Recovered velocities are shown for central profiles (P3-P8).

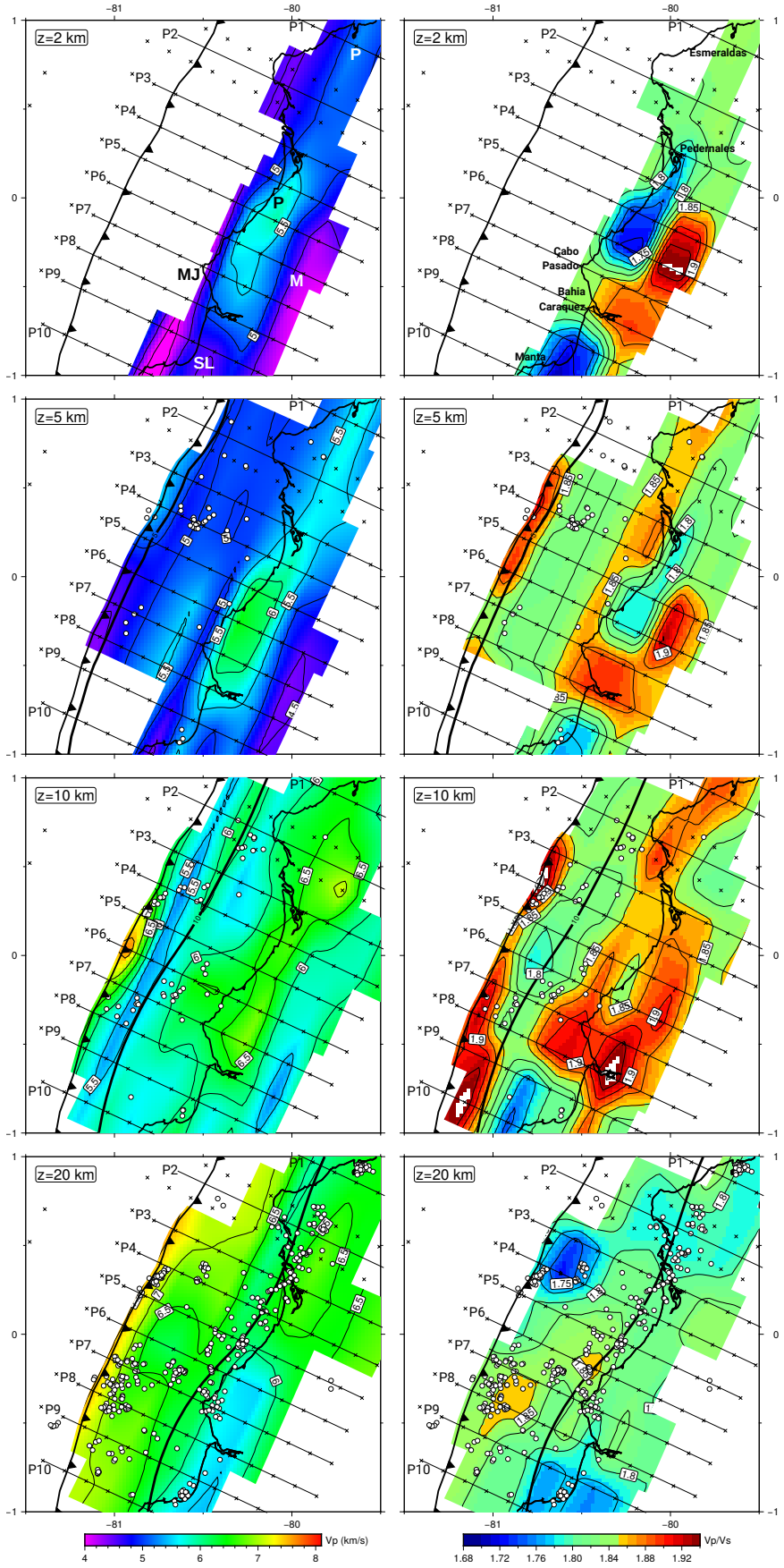

Supplementary Material B10: 3DVM for both Vp (left) and Vp/Vs (right) based on the inversion of a smooth initial 2D initial model and 2D-N and 2D-S arrival times. Results are shown by horizontal slices at 2, 5, 10 and 20 km depth. See Figure 6.6 for further details.

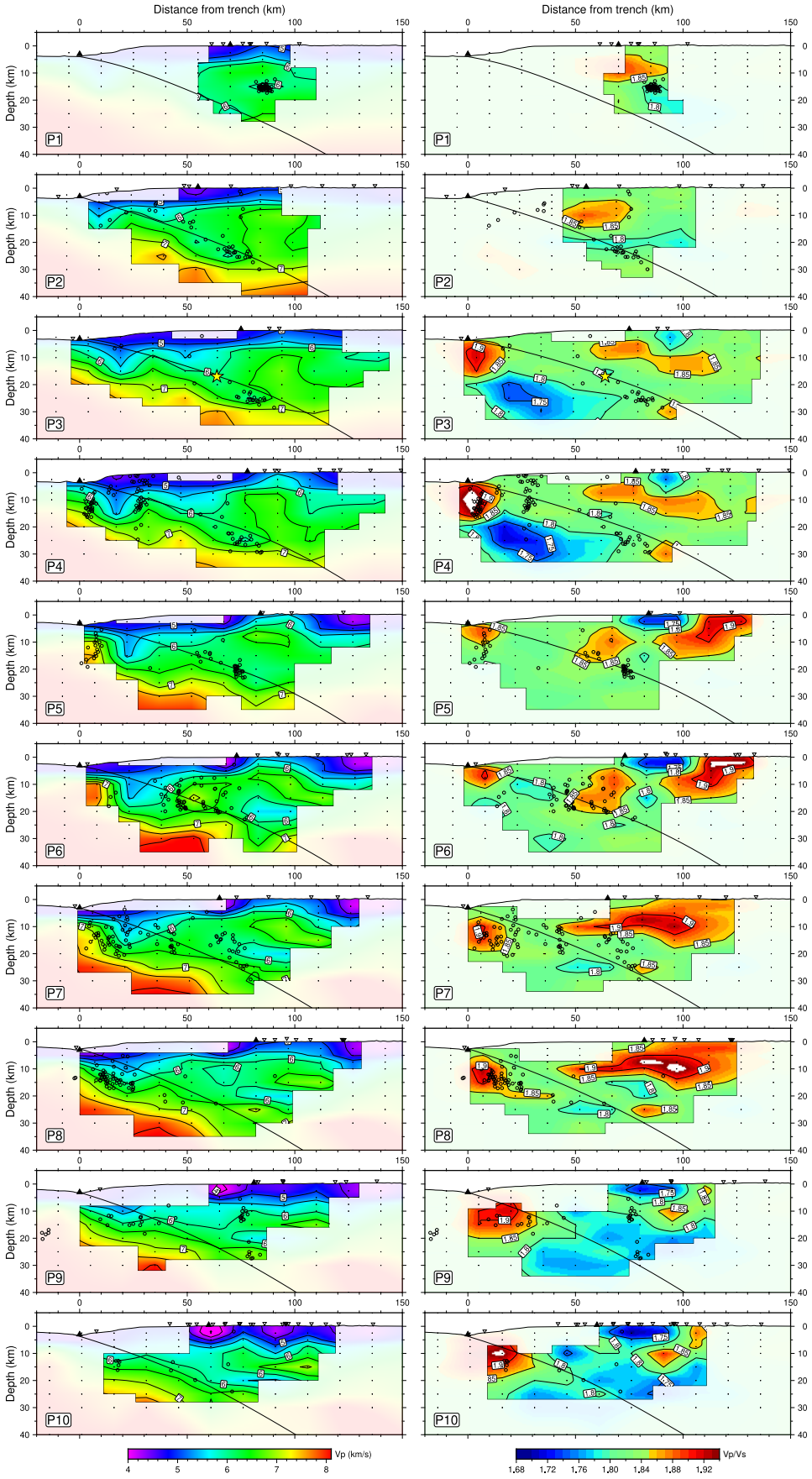

Supplementary Material B11: 3DVM for both Vp (left) and Vp/Vs (right) based on the inversion of a smooth initial 2D initial model and 2D-N and 2D-S arrival times. Results are shown along 10 W-E cross sections profiles. See Figure 6.8 for further details.

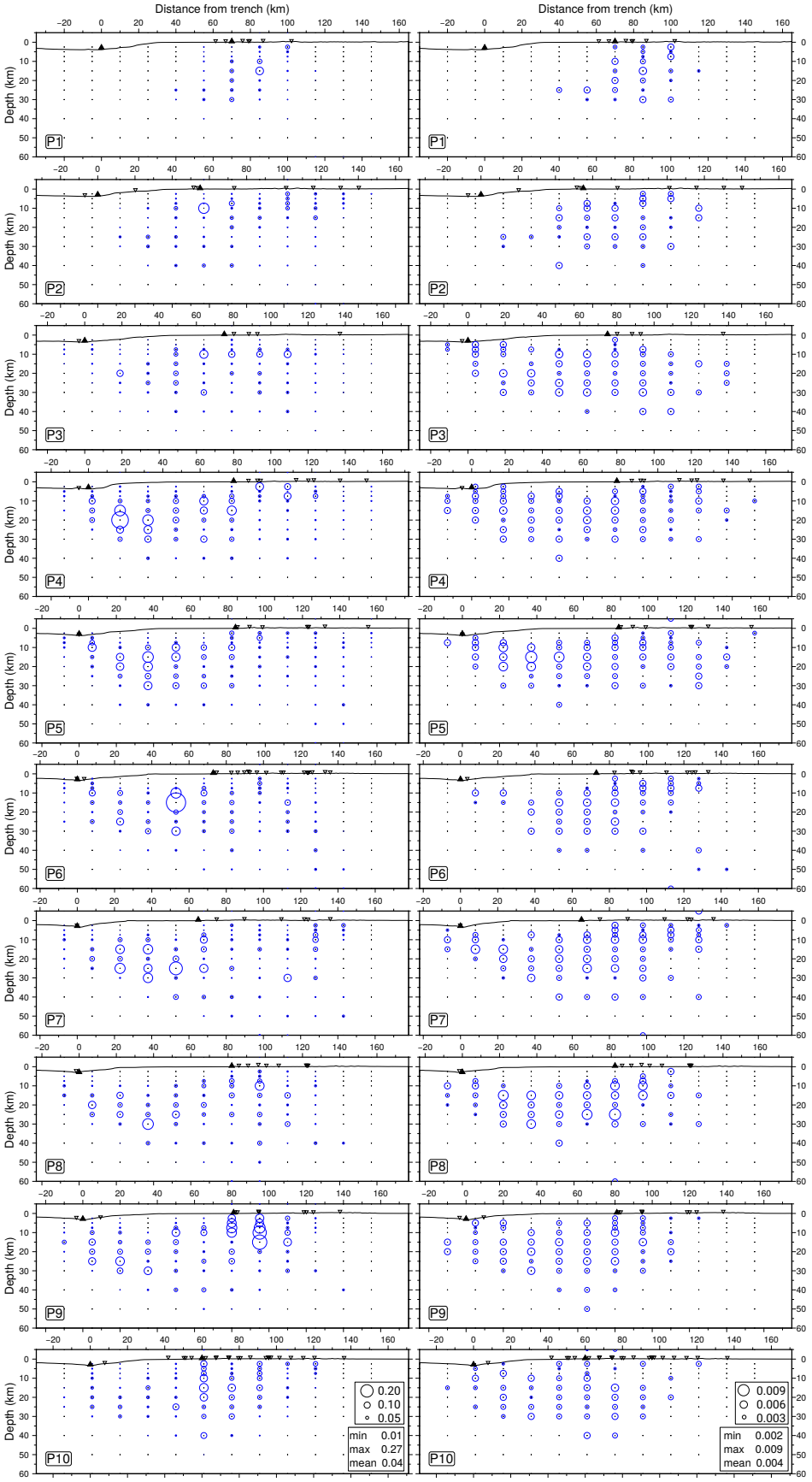

Supplementary Material B12: Bootstrap results for an inversion based on a randomly selected subset of aftershocks comprising 80% of the events in our actual catalogue. Blue cirles indicate the size of the standard deviation at each profile. (left) Vp, (right) Vp/Vs.

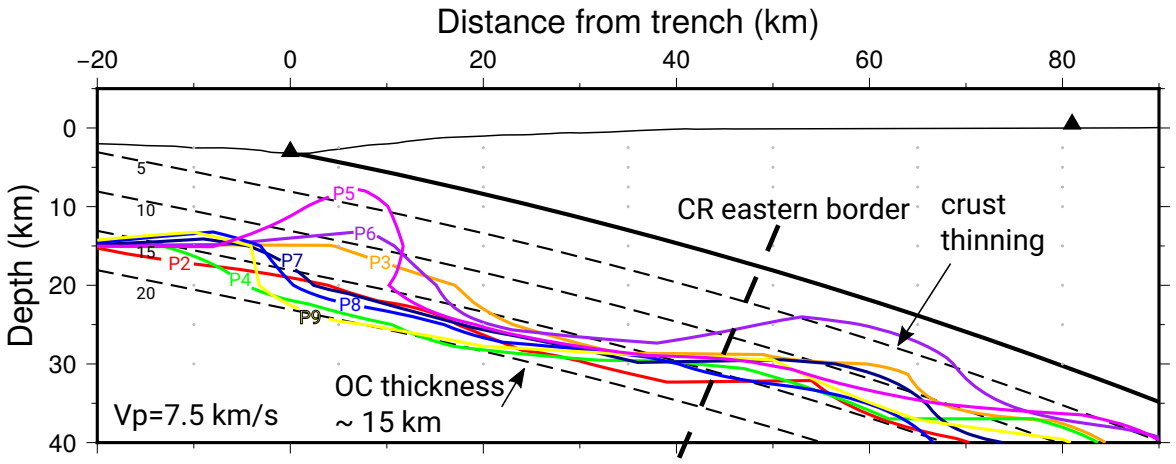

Supplementary Material B13: Analyzing Vp iso-velocity contours. Vp velocities associated to the lower part of the oceanic crust (top) and to the oceanic upper mantle (bottom). Cross sections compare the depth of profiles P2-P8 identified by colored solid lines. Slab interface and its projection at 5, 10 , 15 and 20 km are plotted for reference. Lightblue shaded area indicates the area of analysis. Black triangle represents the trench.

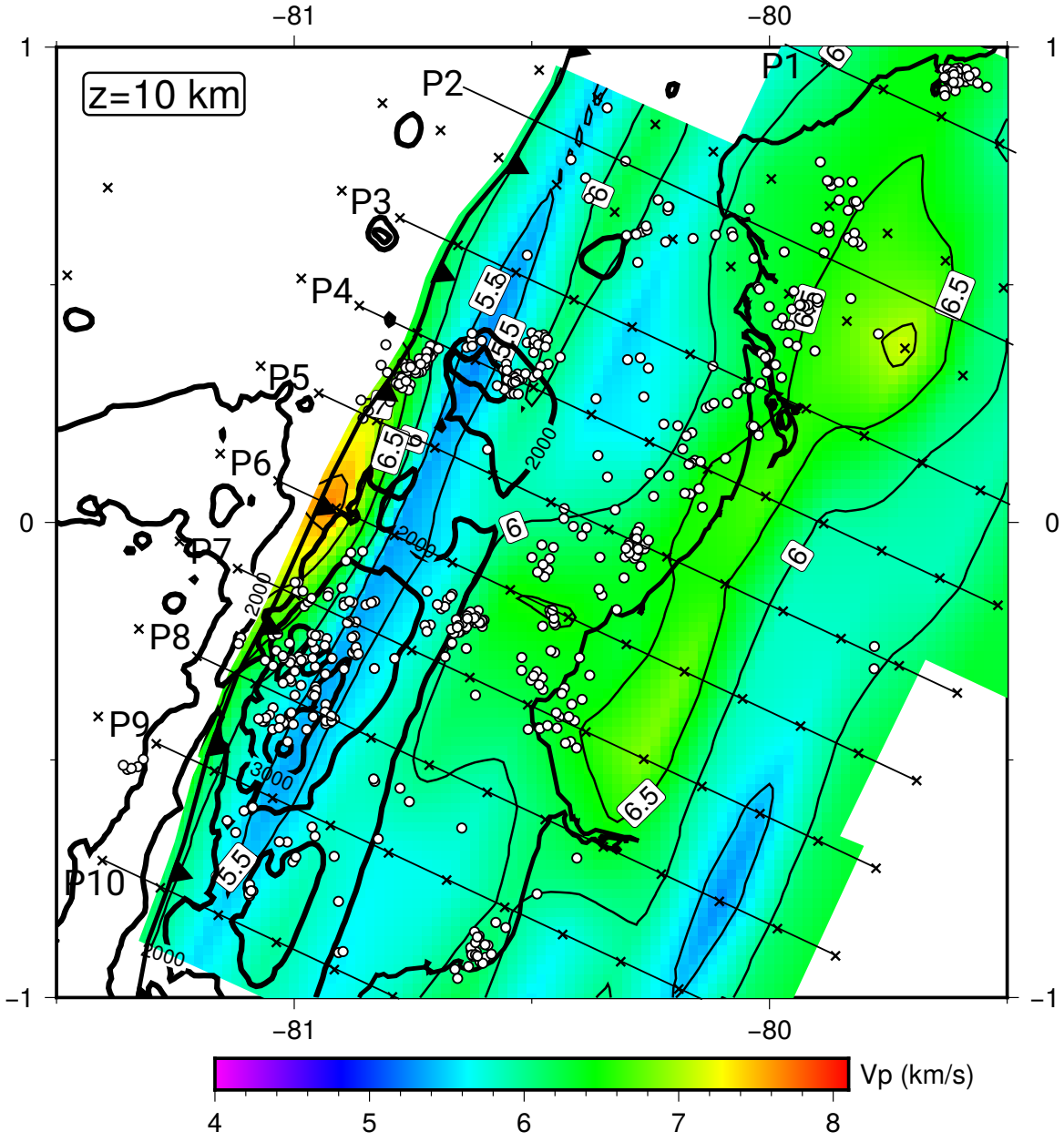

Supplementary Material B14: Constrasting residual bathymetry and Vp horizontal slice. Residual bathymetry derived by Agurto-Detzel et al. (2019) superimposed over our 3D Vp velocities obtained for a horizontal slice at 10 km depth.

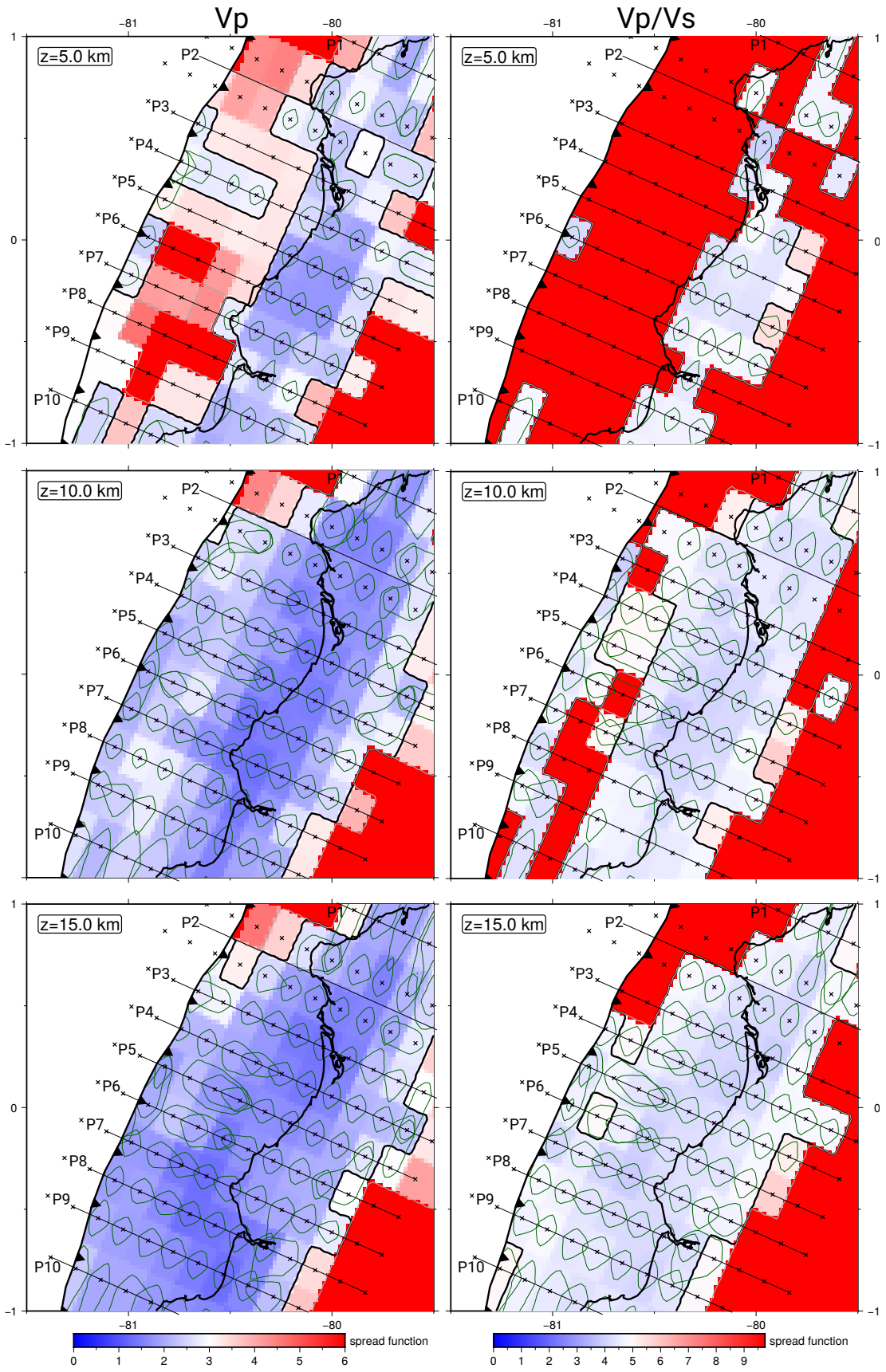

Supplementary Material B15: 3D MRM analysis along strike. Horizontal slices for the obtained 3D Vp (left) and Vp/Vs (right) models at 5, 10 and 15 km depth to estimate the sentivity of the solution along strike.

Appendix C

This appendix contains the Extended data for Chapter 7.

- Extended Data 1: Summary for the shifted grid nodes
- Extended Data 2: MRM along the slab interface
- Extended Data 3: Averaged Vp/Vs projection along the slab interface
- Extended Data 4: Ellipse grid search, samples
- Extended Data 5: Rupture area gird search for Vp/Vs>1.85

	mod 1	mod 2	mod 3	mod 4	mod 5	mod 6	mod 7
Δx (east, km)	0	5	10	0	0	0	0
Δy (north, km)	0	0	0	7	14	0	0
Δz (depth, km)	0	0	0	0	0	-2	2

Extended Data Table C1: Summary of node shifting for each model configuration. The x-axis is positive towards East, y-axis positive towards North and vertical component positive downward.

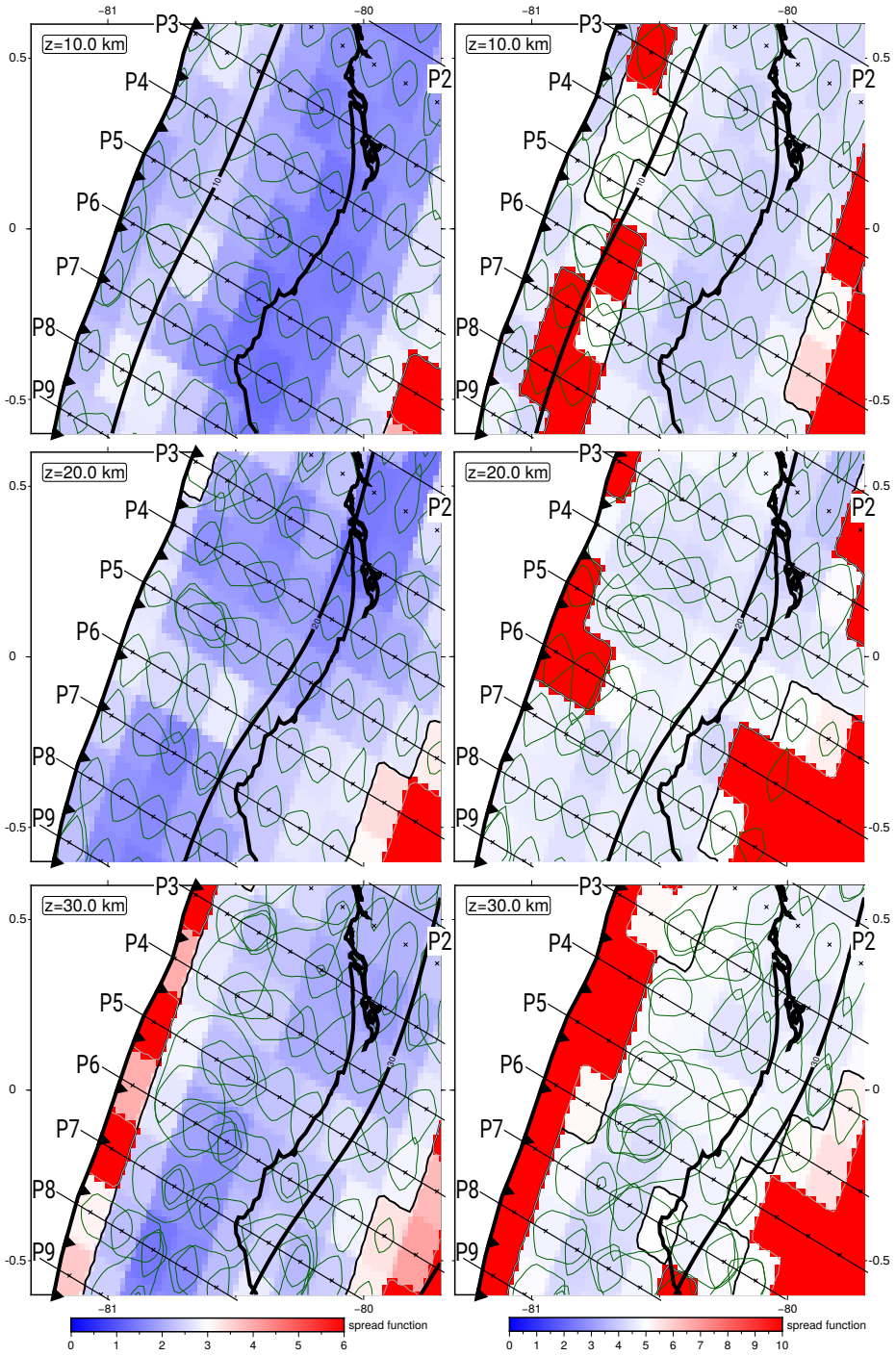

Extended Data Figure C2: Horizontal slices for MRM (blue-red color coded) and 70% contour lines of the elements ratio (green) at 10, 20 and 30 km depth. Solid black line representes the slab depth contour at 10, 20 and 30, respectively. **Left** Vp model, **right** Vp/Vs model.

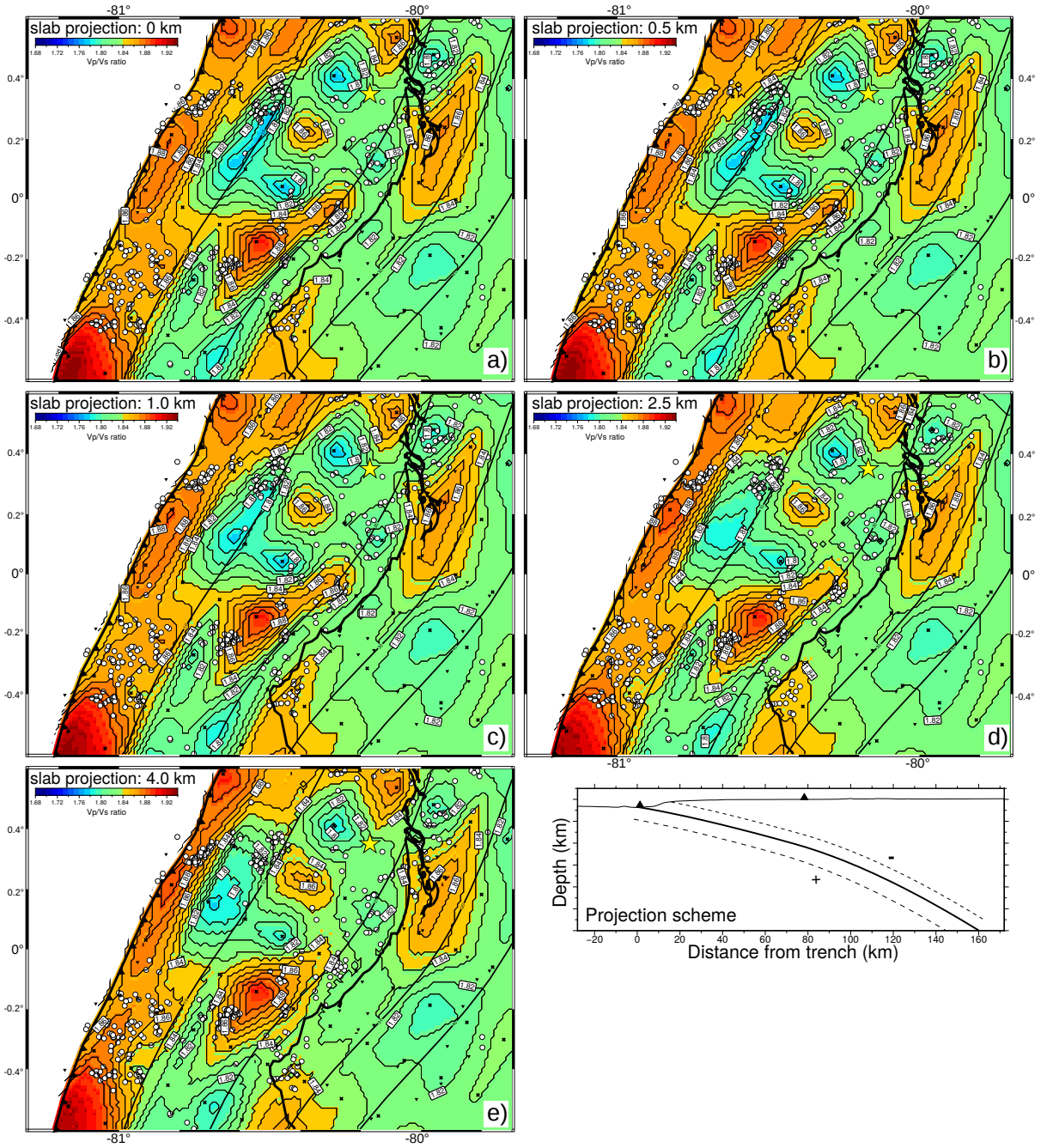

Extended Data Figure C3: Averaged Vp/Vs ratios projected along the different areas around the slab interface. **a)** 0 km, **b)** 0.5 km, **c)** 1.0 km, **d)** 2.5 km and **e)** 4.0 km. Inset plot at the bottom right corner shows the projection scheme used to produce each figure.

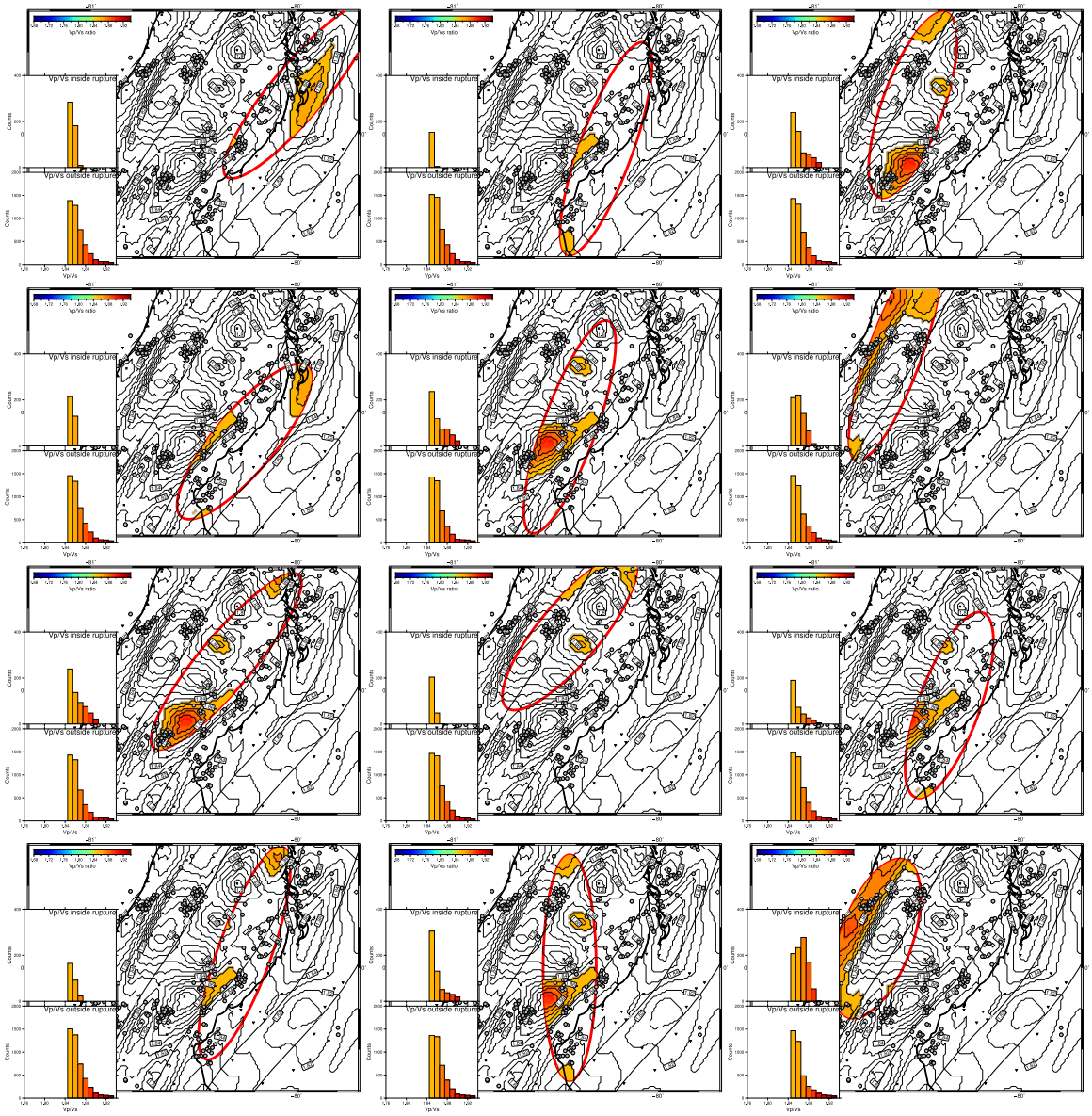

Extended Data Figure C4: Samples for the ellipse grid search performed along the study region. In total, 1625 cases were tested with the ellipse varying in its location (latitude, longitude), striking angle and length and width parameters (see Methods section for further details).

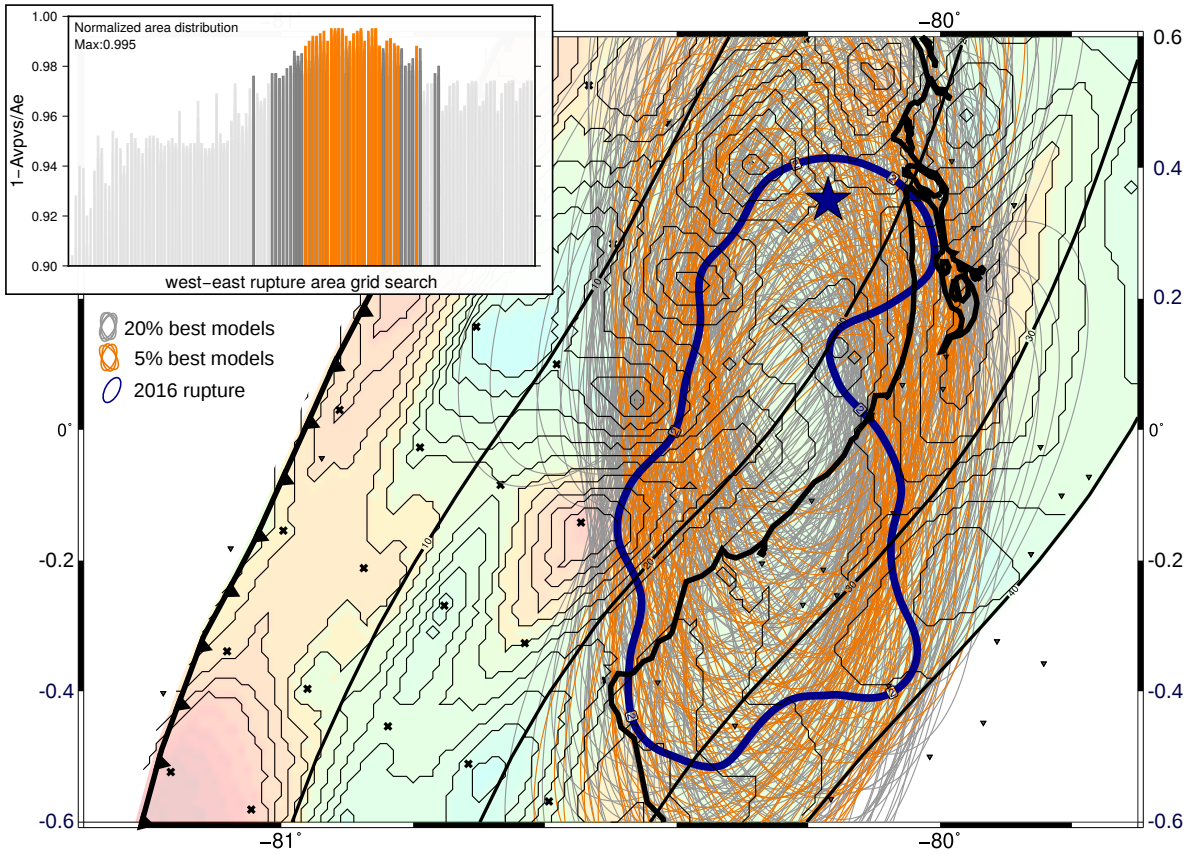

Extended Data Figure C5: Mapview of the rupture area grid search, for Vp/Vs>1.85, showing the best 20% solutions in gray and the best 5% in orange and its comparison with the 2 m coseismic slip contour (solid blue line) derived by Gombert et al. (2018). The star represents the epicenter of the 2016 Pedernales earthquake (Nocquet et al., 2017) and the solid black lines shown the 10 km depth slab. The inset plot shows a west-east stacked histogram with the 1625 ellipses tested in the region with gray and orange bars representing the 20% and 5% best models, respectively.